

## ABSTRACT

Title of dissertation: SUPERCONDUCTING RADIO FREQUENCY  
MATERIALS SCIENCE THROUGH  
NEAR-FIELD MAGNETIC MICROSCOPY

Bakhrom Gafurovich Oripov  
Doctor of Philosophy, 2020

Dissertation directed by: Professor Steven M. Anlage  
Department of Physics

Superconducting Radio-Frequency (SRF) cavities are the backbone of a new generation of particle accelerators used by the high energy physics community. Nowadays, the applications of SRF cavities have expanded far beyond the needs of basic science. The proposed usages include waste treatment, water disinfection, material strengthening, medical applications and even use as high-Q resonators in quantum computers. A practical SRF cavity needs to operate at extremely high rf fields while remaining in the low-loss superconducting state. State of the art Nb cavities can easily reach quality factors  $Q > 2 \times 10^{10}$  at 1.3 GHz.

Currently, the performance of the SRF cavities is limited by surface defects which lead to cavity breakdown at high accelerating gradients. Also, there are efforts to reduce the cost of manufacturing SRF cavities, and the cost of operation. This will require an R&D effort to go beyond bulk Nb cavities. Alternatives to bulk Nb are Nb-coated Copper and Nb<sub>3</sub>Sn cavities. When a new SRF surface treatment, coating technique, or surface optimization method is being tested, it is usually very costly

and time consuming to fabricate a full cavity. A rapid rf characterization technique is needed to identify deleterious defects on Nb surfaces and to compare the surface response of materials fabricated by different surface treatments. In this thesis a local rf characterization technique that could fulfill this requirement is presented.

First, a scanning magnetic microwave microscopy technique was used to study SRF grade Nb samples. Using this novel microscope the existence of surface weak-links was confirmed through their local nonlinear response. Time-Dependent Ginzburg-Landau (TDGL) simulations were used to reveal that vortex semiloops are created by the inhomogeneous magnetic field of the magnetic probe, and contribute to the measured response.

Also, a system was put in place to measure the surface resistance of SRF cavities at extremely low temperatures, down to  $T = 70$  mK, where the predictions for the surface resistance from various theoretical models diverge. SRF cavities require special treatment during the cooldown and measurement. This includes cooling the cavity down at a rate greater than  $1K/\text{minute}$ , and very low ambient magnetic field  $B < 50$  nT. I present solutions to both of these challenges.

SUPERCONDUCTING RADIO FREQUENCY MATERIALS SCIENCE  
THROUGH NEAR-FIELD MAGNETIC MICROSCOPY

by

Bakhrom Gafurovich Oripov

Dissertation submitted to the Faculty of the Graduate School of the  
University of Maryland, College Park in partial fulfillment  
of the requirements for the degree of  
Doctor of Philosophy  
2020

Advisory Committee:

Professor Steven M. Anlage, Chair/Advisor

Professor Gianluigi Ciovati

Professor Christopher Lobb

Professor Benjamin Palmer

Professor Ichiro Takeuchi

© Copyright by  
Bakhrom Oripov  
2020

## Dedication

To all educators who scattered around the globe in God's name with a mission to teach tolerance and serve humanity by making science and wisdom accessible to all.

## Acknowledgments

Today, I have reached a significant milestone in my life; I have finally received my Ph.D. degree, the highest academic degree anyone can earn. It was a journey of my life that started 16 years ago when I was selected for the National Physics Olympiad Team. While I am excited and proud of this achievement, none of this would be possible without the enormous support I have received from several mentors, friends, and family members; whose contribution I would like to recognize here.

Firstly, I want to extend my deepest gratitude to my advisor and mentor, Prof. Steven Mark Anlage. Steven is an energetic and passionate researcher who always had a distinctive perspective on the research problems that we encountered. Steven is a renowned and prominent scientist, but I attribute this project's success and to Steven's unique qualities as a mentor. Steven is one of the most humble and down to earth people I have ever met. Steven and I held weekly project meetings where he would treat me as a colleague, although it was a meeting between a distinguished scholar and a rookie scientist. Steven had never dismissed any idea that I brought to the table and always commended me on my efforts while providing critical feedback. Whenever we met with collaborators, Steven would allow me to take the lead and answer any outstanding questions jumping in only when I needed him. By doing so, Steven instilled in me the confidence and inspiration needed to conduct proper research. At the same time, he genuinely cared about his student's well-being asking about our life outside the lab before each meeting. I thank Steven for turning this rookie scientist into a real one!

I thank Prof. Gianluigi Ciovati for advising me on the SRF aspect of this project. I still remember the first time I met him back in 2015 in Whistler, Canada, at the tutorial that he gave during the International Conference on RF Superconductivity. Only after that tutorial, I realized the importance of this project and acquired all relevant knowledge about the superconductors and microwave fields. Over the years, whenever Steve and I needed feedback on freshly acquired data or needed advice on the future direction of the project, Prof. Ciovati was there for us. I feel incredibly fortunate to have Prof. Anlage and Prof. Ciovati as my mentors.

I thank the other committee members, Prof. Christopher Lobb, Prof. Ichiro Takeuchi, and Prof. Benjamin Palmer for generously offering their time and overseeing this dissertation work and the defense. Their support and guidance, especially Prof. Lobb's comments and suggestions, significantly improved this dissertation.

I want to thank the faculty members of the Maryland Quantum Materials Center, Prof. Frederick Wellstood, Prof. Johnpierre Paglione, Prof. Richard Greene, and everyone else who participated in weekly Center seminars for their critical feedback on my presentations. I want to apologize to Dr. Sudeep Dutta for the discomfort caused by the noise of my liquid nitrogen pre-cooling system and thank him for several enlightening discussions about Quantum Computing, Academia, Politics, and life. I also want to thank UMD physics staff, Brian Straughn, Douglas Benson, Jack Touart, Mary Sutton, and Kristin Stenson. These people made sure that every device we had was well maintained, and everyone gets paid on time.

I thank my labmates Tamin Tai, Bo Xiao, Daimeng Zhang, Melissa Trepanier, Yuewen Tan, Seokjin Bae, Ziyuan Fu, Shukai Ma, Min Zhou, Cougar Garcia, Jingnan

Cai, and Lei Chen. I will miss my daily lunches with Jingnan, which I forced him to attend. I thank Seokjin for being there for me when I needed to vent out my frustration. I thank Cougar for sharing his networking skills with me. I will miss our weekly group lunches, occasional board games, and nights out during the annual APS March meetings. Thank you all for making research fun. And I am sure that you guys will be missing my Dad jokes.

I thank Uğur Çetiner, Cem Aydın Keser, Ali Yapıcı and Amit Nag for their friendship and for hosting spontaneous coffee breaks and picnics. I especially thank Ali Yapıcı and Helen Borisova-Yapıcı for welcoming my wife and me into their house. I also thank all the members and volunteers of the Tajik American Cultural Association for creating and maintaining a welcoming community.

The seeds of scholarly curiosity were instilled in me long before I went off to college. I want to acknowledge my high school teachers and colleagues: Mustafa Altun, Nuri Bayram, Ünal Aslan, Veysel Bigeç, Maruf Çelebi and Ilhom Hotami. These people played a significant role in shaping my priorities in life. Special thanks to Nurullah Seçuk and Prof. Fayz Normurodov, who trained me for Physics Olympiads and convinced me to pursue a career in research. I thank Prof. Taylan Akdoğan for giving me the first taste of actual academic research and teaching us Matlab and Latex. I also thank my academic brother Ozarfar Gafarov who helped me with my graduate school application.

I thank my daughters, Maryam and Asiya, who provided me with my daily dosage of happiness. My wife, my best friend, and the love of my life, Niso deserve my gratitude as she was the one who shared the entire emotional burden of the graduate



school with me. She made sacrifices so that I could pursue my passion. I am very fortunate to have such a wonderful person as my wife.

I want to thank my family: my parents Sanavbar and Gafur, my brother Gufron, and my sister Nargis for their love, for encouraging me to follow my passion, and for supporting my decision to attend a graduate school, even though it meant that they rarely have a chance to see me or their grandkids/nieces.

I am very grateful to my parents-in-law, Abdujabor and Nargis, for the emotional support offered to me when I needed it most. They semi-annually endured a 14-hour flight to the USA only to help us with kids, giving my wife and me a chance to enjoy a full night sleep once in a while.

It is impossible to remember all, and I apologize to those I've inadvertently left out.

Lastly, I thank the Lord, the Creator and the Sustainer of the universe for giving me life.

---

# Table of Contents

---

<b>Table of Contents</b>	<b>vii</b>
<b>List of Tables</b>	<b>xi</b>
<b>List of Figures</b>	<b>xii</b>
<b>List of Symbols and Units</b>	<b>xxviii</b>
<b>List of Abbreviations</b>	<b>xxx</b>
<b>Chapter 1 Introduction to Superconductivity</b>	<b>1</b>
1.1 History and Hallmarks . . . . .	1
1.1.1 Discovery of “practically zero” resistance . . . . .	1
1.1.2 The Meissner Effect . . . . .	3
1.2 Phenomenological Theories of Superconductivity . . . . .	5
1.2.1 Gorter-Casimir Two Fluid Model . . . . .	5
1.2.2 London Equations . . . . .	6
1.2.3 Ginzburg-Landau (GL) Theory . . . . .	8
1.2.4 Coherence Length . . . . .	10
1.2.5 Flux quantization . . . . .	11
1.2.6 Superconducting Vortices . . . . .	12
1.2.7 The Josephson effect . . . . .	13
1.3 Bardeen, Cooper and Schrieffer (BCS) Microscopic Theory of Superconductivity . . . . .	16
1.4 Applications . . . . .	21
<b>Chapter 2 Superconducting Radio-Frequency Cavities</b>	<b>22</b>
2.1 The International Linear Collider . . . . .	22
2.2 Superconducting Radio Frequency (SRF) Cavity . . . . .	24
2.3 Surface Resistance . . . . .	25
2.4 Q-factor . . . . .	27
2.5 Residual Resistance . . . . .	28
2.6 Q-disease . . . . .	29
2.7 Trapped Magnetic Flux . . . . .	31
2.8 Surface Defects and Vortices . . . . .	32
2.9 Beyond Nb . . . . .	34

<b>Chapter 3 SRF Cavity Measurements at mK Temperatures</b>	<b>35</b>
3.1 Motivation . . . . .	35
3.2 Mounting an SRF cavity in a dilution refrigerator . . . . .	38
3.3 Liquid Nitrogen Precooling . . . . .	39
3.4 Magnetic Shielding . . . . .	45
3.5 Phase Locked Loop . . . . .	49
3.6 Operating Procedure . . . . .	52
3.7 Summary of the measurements . . . . .	59
<b>Chapter 4 Magnetic Microwave Microscopy</b>	<b>63</b>
4.1 Overview of Scanning Probe Microscopy . . . . .	63
4.2 Near-Field Microwave Microscopy . . . . .	65
4.3 Nonlinear response . . . . .	66
4.4 Previous generations of Magnetic Microwave Microscopes . . . . .	69
4.5 Magnetic Probe from Hard Disk Drive . . . . .	72
4.5.1 HFSS Simulations . . . . .	76
4.5.2 Numerical simulation by Seagate . . . . .	80
4.6 Experimental setup . . . . .	81
4.6.1 Advantages of this method . . . . .	87
<b>Chapter 5 Data from the Magnetic Microscope</b>	<b>88</b>
5.1 Sample 1 – Nb film on copper from CERN . . . . .	89
5.2 Sample 2 – Bulk Nb from MSU . . . . .	95
5.3 Sample 3 – Bulk Nb from Jefferson Lab . . . . .	101
5.4 Sample 4 – Nb film on copper from ASTeC . . . . .	101
5.5 Sample 5 – Nb film on sapphire from Jefferson lab . . . . .	103
5.6 Discussion . . . . .	104
<b>Chapter 6 Modeling of Harmonic Response</b>	<b>107</b>
6.1 Resistively Shunted Junction (RSJ) Model . . . . .	107
6.1.1 Weak-links on the surface of Nb . . . . .	107
6.1.2 The response of a weak-link to RF stimulus . . . . .	108
6.1.3 Weak-link harmonic response . . . . .	112
6.1.4 Fitting the measured third harmonic data . . . . .	115
6.1.5 Extracting BCS superconducting gap value . . . . .	119
6.1.6 Discussion . . . . .	120
<b>Chapter 7 Ginzburg-Landau Simulations</b>	<b>122</b>
7.1 Ginzburg-Landau Theory . . . . .	122
7.1.1 Ginzburg-Landau Free Energy Functional . . . . .	122
7.1.2 Gor'kov's validation of GL theory . . . . .	127
7.2 Time-dependent GL model . . . . .	135
7.3 TDGL simulations . . . . .	138
7.3.1 Gauge invariance, boundary conditions and normalization . . . . .	138
7.3.2 Material parameters . . . . .	141

7.3.3	Introduction and Treatment of Defects . . . . .	147
7.3.4	TDGL in COMSOL . . . . .	151
7.4	Two-Domain TDGL and Inclusion of Superconducting Screening . . . . .	155
7.4.1	Superconducting sphere in a uniform magnetic field . . . . .	157
7.4.2	Point magnetic dipole above a semi-infinite superconductor . . . . .	161
<b>Chapter 8 TDGL Modeling of the Near-Field Magnetic Microwave Microscope</b>		<b>163</b>
8.1	Magnetic Dipole . . . . .	164
8.2	Vortex semiloops . . . . .	166
8.3	The evolution of vortex semiloops with time . . . . .	169
8.4	The evolution of vortex semiloops with rf field amplitude . . . . .	171
8.5	The dependence of rf vortex dynamics on the friction coefficient $\eta$ . . . . .	172
8.6	The effect of localized defects on rf vortex semiloops . . . . .	174
8.7	Fitting the third harmonic data . . . . .	176
<b>Chapter 9 Vortex-Semiloops inside SRF cavities</b>		<b>180</b>
9.1	Numerical simulation of SRF cavity surface fields . . . . .	180
9.2	"Slow" TDGL . . . . .	183
9.3	Generalized TDGL (gTDGL) equations . . . . .	184
9.4	Relaxation times for amplitude and phase of $\Delta$ . . . . .	188
9.5	The dependence of Vortex Dynamics on Inelastic Scattering $\Gamma$ . . . . .	194
<b>Chapter 10 Surface Imaging Efforts</b>		<b>197</b>
10.1	2D scans of the $Bi_2Sr_2CaCu_2O_{8+x}$ sample . . . . .	198
10.2	Attocube positioning system . . . . .	202
10.3	Probe Z-scan over Sample . . . . .	203
10.4	XZ-scan . . . . .	208
10.5	Line Scans over a grain boundary in Bulk Nb . . . . .	210
10.6	Conclusion . . . . .	214
<b>Chapter 11 Microwave Surface Impedance measurements using the Parallel Plate Resonator</b>		<b>215</b>
11.1	Parallel Plate Resonator . . . . .	217
11.2	Experimental Setup . . . . .	220
11.3	Boron doped diamond sample . . . . .	223
11.4	Extracting $f_{res}$ and Q from the transmission data . . . . .	227
11.4.1	Phase vs frequency fit . . . . .	229
11.4.2	Multi-peak fit . . . . .	231
11.5	Results . . . . .	233
11.5.1	Penetration depth . . . . .	233
11.5.2	Surface resistance . . . . .	240
11.6	Conclusion . . . . .	240
<b>Chapter 12 Conclusion and Outlook</b>		<b>244</b>

<b>Appendix A Magnetic Microscope Operation Manual</b>	<b>247</b>
A.1 Connecting to the writer head . . . . .	247
A.2 Choosing the measurement frequency . . . . .	248
A.3 Finding optimal parameters . . . . .	251
<b>Appendix B Tuning Fork based Probe-Sample Distance Control</b>	<b>253</b>
<b>Bibliography</b>	<b>256</b>
<b>Curriculum vitae</b>	<b>294</b>

---

## List of Tables

---

Table 3.1	The list of components used in the PLL shown in <a href="#">Fig. 3.8</a> . . . . .	51
Table 3.2	Summary of the 2.2GHz elliptical Nb SRF cavity measurements at UMD and JLab. . . . .	60
Table 5.1	The list of samples measured for this thesis with their type, origin and references where further details can be found. . . . .	88
Table 6.1	Summary of RSJ model fit parameters extracted from third-harmonic data on two Nb samples. Weak-link number indicates the family number in the data. . . . .	121
Table 7.1	Measured values of SRF quality bulk Nb parameters used for numerical simulations. . . . .	142
Table 8.1	Values of parameters used for TDGL simulations of the oscillating magnetic dipole above the superconductor. . . . .	168
Table 11.1	The variance $\langle (f_{meas}(T) - f_{fit}(T))^2 \rangle$ of the fits shown in <a href="#">Fig. 11.8</a> . <a href="#">235</a>	
Table 11.2	Summary of fits to data taken with PPR measurements on Boron-doped diamond films. † Low temperature limit part of the data only. . . . .	237

---

## List of Figures

---

Fig. 1.1	The resistance of mercury (Hg) as a function of absolute temperature, reproduced from Table.IV of [3] . . . . .	2
Fig. 1.2	Meissner effect in a superconductor, a superconductor cylinder inside a magnetic field. Superconductors completely expel magnetic flux. (Source: The Feynman Lectures on Physics, Volume III [11]) . . . . .	4
Fig. 1.3	The structure of an Abrikosov vortex in a thin film superconductor under the influence of magnetic field perpendicular to the surface of the film. The order parameter is suppressed in the core which has the size of $\approx \xi$ and magnetic field penetrates laterally through the superconductor on a length scale $\approx \lambda$ . The total magnetic flux in a vortex is exactly $\Phi = \Phi_0$ . The supercurrent flows in the region between the normal core and the rest of the superconductor. Source: Applied Superconductivity and Cryoscience Group, University of Cambridge, Department of Materials Science and Metallurgy [25]. . . . .	12
Fig. 1.4	Schematic of a Josephson Junction (JJ): Two superconductors are separated by a thin insulator of thickness $L \leq \xi$ . . . . .	14
Fig. 1.5	An electron (red circle ●) moving through the ion lattice (blue circle ● with + signs) distorts the lattice. Because of the slow ion dynamics the distorted lattice then attracts the second electron moving in the opposite direction later in time, resulting in net attractive electron-electron interaction. . . . .	17
Fig. 1.6	The temperature dependence of BCS superconducting gap $\Delta_{BCS}$ calculated from Eq. (1.13). . . . .	19
Fig. 2.1	A superconducting TESLA cavity made from bulk Nb. Source: Fermilab ILC–SRF R&D webpage [49]. . . . .	24
Fig. 2.2	Cross section of a single cell cylindrical Superconducting Radio Frequency (SRF) cavity resonator. The fundamental mode of this resonator corresponds to the case where rf magnetic field amplitude peaks at the equator and the rf electric field amplitude peaks along the symmetry axis of the cavity. . . . .	25
Fig. 2.3	The surface resistance of an SRF cavity at 1.3 GHz frequency as a function of temperature. The $T \rightarrow 0$ limit shows a saturation of resistance contrary to what is predicted by Eq. (2.1). This figure is reproduced from [51]. . . . .	27

Fig. 2.4	The quality factor as a function of accelerating gradient for a cavity which is held at $T = 60K$ , $T = 75K$ , $T = 100K$ , $T = 125K$ and $T = 175K$ for 24 hours and then cooled down for testing. The quality factor of the cavity has severely degraded after being held at $T = 75K$ or $T = 100K$ , while holding the cavity at $T = 60K$ , $T = 125K$ or $T = 175K$ seems to have no effect on the cavity performance. This figure is reproduced from [67]. . . . .	31
Fig. 3.1	Surface resistance (in units of $R_0 = \frac{\mu_0^2 \sigma_n \omega \lambda^3 \Delta}{2\hbar}$ ) as a function of temperature calculated for several values of $\Gamma_{Dynes} = 0.06\Delta_{BCS}$ (red), $\Gamma_{Dynes} = 0.03\Delta_{BCS}$ (black) and $\Gamma_{Dynes} = 0.01\Delta_{BCS}$ (blue). The vertical dashed line indicates the lowest temperature accessible in a conventional liquid helium testing. This figure is reproduced from Ref. [64]. . . . .	37
Fig. 3.2	3-dimensional drawing of the 2.2 GHz Nb cavity (silver) and the copper support structure (orange). . . . .	39
Fig. 3.3	(a) Nb SRF Cavity mounted below the mixing chamber plate of the dilution Fridge. Note the stainless steel flanges on the Nb cavity. (b) Steel clamps replaced by OFHC Copper equivalents. . . . .	40
Fig. 3.4	The first generation version of the LN precooling system. (a) The top part of the LN precooling system is supported by a bellows mounted on the top of the cryostat. Blue arrows indicate the path of the cold LN and the red arrows indicate the path of the warmer nitrogen vapour returning from the heat bath. (b) The heat link between the mixing chamber plate and room temperature can be disabled by slightly raising the whole structure. (c) The heat bath rests on the mixing chamber plate and the thermal connection can be broken using the bellows on the top of the cryostat. (d) The cross section longitudinal view of the heat exchanger. The color gradient represent the relative temperature of LN, with blue being cold and red being warm. White arrows indicate the direction of the flow. . . . .	41
Fig. 3.5	a) Schematic of the LN precooling system (2 <sup>nd</sup> generation). LN (blue arrows →) is supplied through the inner tube of 2 coaxial SS tubes and the nitrogen vapour (red arrows →) is extracted via the outer tube. b) Picture of the input and output lines on the top of the cryostat. A safety pressure relief valve is installed in the return path. c) Picture of the LN precooling system (highlighted by a yellow box) inside the dilution fridge. . . . .	42
Fig. 3.6	a) The temperature measured at the mixing chamber of an empty cryostat. LN precooling started at $T = 205K$ b) The temperature measured at the equator of the cavity vs time when no LN precooling is used (blue) and with LN precooling started at $T = 160K$ (red). Time is measured from the moment the cooldown is started. . . . .	45



Fig. 3.7	(a) High- $\mu$ alloy metal foil wrapped around the cavity. (b) METGLAS foil wrapped around the Still Can. (c) METGLAS foil wrapped around the 4K Can. (d) Helmholtz-coils for active magnetic field cancellation with the cavity equator positioned at the center of the two coils. (e) Summary of the magnetic shielding shown in a cross-section view of the lower part of the cryostat. Three 2mm-thick cylindrical $\mu$ metal shields that are sitting inside the Still can are shown here. <b>Red lines</b> correspond to the location of METGLAS foil. . . . .	48
Fig. 3.8	Schematic of the PLL setup. The MW signal from the source and that from the cavity are mixed to produce a dc signal that depends on the phase difference between the two. The signal is amplified and sent to the frequency modulation input of the MW source, providing the feedback needed to keep the frequency of the MW source locked to the resonant frequency of the cavity. Measured quantities are shown in red. . . . .	50
Fig. 3.9	Pictures of the PLL setup. (a) The reflected signal is divided into two and sent to RF Switches 1 and 2. Similarly the unamplified part of the transmitted power coming from the directional couplers is sent to switch 1 and the part of the transmitted power that is amplified by the low noise amplifier is sent to switch 2. The output of switch 1 goes to the power meter, enabling measurement of either transmitted and or reflected power depending on the switch setting. The output of switch 2 goes to the high gain amplifier followed by a Schottky diode. This signal is sent to the oscilloscope to measure the decay time of $P_t(t)$ and $P_r(t)$ . The loop amplifier amplifies the output of the mixer and feeds it into the FM modulation port of the MW source. (b) The main circuit of the PLL. The operation is described in the text. (c) Picture of the MW equipment used in the PLL circuit. . . . .	53
Fig. 3.10	Transmission through the cavity $ S_{12} $ as a function of frequency measured by the VNA. The data was taken with an IF bandwidth of 10Hz and 0 dBm applied power. The resonant frequency is $f_0 = 2,266,858,113Hz$ . . . . .	54
Fig. 3.11	(a) <b>(blue)</b> Transmitted power as a function of time after the input power is turned off. <b>(red)</b> Exponential fit according to Eq. (3.6) with $\tau_d = 197.1ms$ . The measurement is averaged over 10 cycles. (b) <b>(blue)</b> Reflected power as a function of time. The input power is off for $t < 0$ . The peak at $t_{off} = 0.25s$ is smaller than the peak at $t_{on} = 0$ indicating and that the input antenna is undercoupled ( $\beta_{in} < 1$ ). Dashed lines indicate the moments RF power is turned ON ( <b>green dashed line</b> ) or turned OFF ( <b>red dashed line</b> ). Note that a) and b) do not correspond to the same measurement. . . . .	57

Fig. 4.1	Schematic of a scanning probe microscope (SPM). A probe is scanned over the sample, by either moving the probe or the sample itself. The probe-sample interaction, which is different depending on the type of microscope, produces a feedback signal which is used to adjust the probe-sample separation distance $d$ . Both the interaction signal and the position are recorded and analyzed. . . . .	64
Fig. 4.2	(a) Schematic representation of a capacitively coupled probe and an inductively coupled probe. A capacitively coupled probe can be formed by connecting an STM tip to the inner conductor of a coaxial cable. An inductively coupled probe can be created by forming a loop using the inner conductor of a coaxial cable and shorting it with the outer conductor. (b) Top view of surface current distribution ( $K$ ) induced on the surface of a superconductor by a coaxial loop probe placed $12\mu m$ above the sample. The computations have been performed with CST-Microwave Studio for an input power of $1W$ . This figure is reproduced from [98]. . . . .	66
Fig. 4.3	Intermodulation distortion (IMD) response ( $\square$ ) and surface resistance ( $\circ$ ) vs the circulating power inside the resonator. The data is measured on a $MgB_2$ stripline resonator at $T = 2.5K$ (Blue) and $T = 20K$ (Red). Note that the IMD is presented in a log scale while the surface resistance is presented on a linear scale. This figure is reproduced from Ref. [107]. . . . .	70
Fig. 4.4	(a) Gapped-ring core writer head and recording medium structure for longitudinal magnetic recording. (b) Single pole writer head and recording medium structure with a magnetic underlayer for perpendicular magnetic recording. A reading head that utilizes the giant magneto-resistance (GMR) effect to measure the magnetization of the recording layer is used in both cases. This figure is reproduced from Ref. [111]. . . . .	73
Fig. 4.5	(a) A picture of a Seagate magnetic writer probe, with glider and transmission line. (b) The close-up view of the pads at the end of transmission line that are used to make electrical connection to the writer head. Pads 3 – 4 are connected to the writer head. (c) A close up view of the writer head, the red area highlighted in (d). (d) the top view of the glider where the magnetic writer head is deposited. (e) A close-up view of the glider. . . . .	75
Fig. 4.6	(a) SEM image of the Western Digital Dragonfly probe's glider. (b) Magnified view of the read and write heads shown with a red box in (a). The reader and writer heads are separated by several layers of magnetic shielding. . . . .	77

Fig. 4.7	(a) HFSS simulation of a magnetic writer a height $d$ above a perfectly conducting sample. We model the probe as a $200nm \times 200nm \times 3\mu m$ ferrite rod perpendicular to the surface, driven by a 10 turn gold wire. This rod is part of a bigger magnetic yoke structure. The diameter of the coil is $1.2\mu m$ and the probe is $d = 200nm$ away from the surface of the sample. Yellow arrows indicate the direction of current flow. (b) Distribution of the magnitude of surface current density $ \vec{J}_{surf} $ on the sample surface. The colorbar indicates the magnitude of surface current density in a linear scale. The loop is excited by a $I = 50mA$ RF current at $f = 1.5GHz$ frequency. The $x$ and $y$ axes are the same as the ones defined in Fig. 4.5. . . . . .	77
Fig. 4.8	(a) The shape of the main pole of the writer head as deduced from [117] and [118]. (b) Schematic of the HFSS simulation. The main pole and the return pole, both of which are simulated as ferrites, are located 50nm above the superconductor, which is modeled as a perfect conductor. (c) The full design of the writer head as done in our HFSS simulation. The $x$ and $y$ axes are same as those defined in Fig. 4.5. . . . . .	79
Fig. 4.9	The spatial distribution on the surface of the superconductor simulated by the HFSS model shown in Fig. 4.8. The contour plot of magnitude of the magnetic fields component normal to the surface. The $x$ and $y$ axes are same with the ones defined in Fig. 4.5.	79
Fig. 4.10	(a) The spatial distribution of the magnetic field normal to the surface under the writer probe, calculated using the Stoner–Wohlfarth model for our type of write head. The probe is positioned 17nm above the magnetic medium with no soft magnetic underlayer. (b) The $y$ –line cut at $x = 0$ . (c) The $x$ –line cut at $y = 0$ . The $x$ and $y$ axes are same with the ones defined in Fig. 4.5. . . . . .	81
Fig. 4.11	(a) Schematic of the dry pulsed-tube cryostat manufactured by Entropy Cryogenics. (b) Picture of the fully closed cryostat. (c) Picture of the cryostat when vacuum can is taken off (d) Picture of the cryostat with only 4K can. (e) Picture of the top plate of the cryostat which houses the pulsed-tube, rf feed-through, dc wiring feed-through and the pressure sensor. (f) Inside of the cryostat, both rf conections and dc wiring are thermalized at each stage. .	82
Fig. 4.12	Photograph of the Experimental setup. The magnetic writer head is connected to an SMA coaxial connector by directly soldering it to the pads on the end of writer probe’s transmission line. The Nb sample is attached to the cold plate of the cryostat. The probe is in direct contact with the sample in this fixed-point measurement case. . . . . .	84

Fig. 4.13	(a) Schematic of experimental setup. A microwave (MW) source is used to generate an rf signal and feed it to the magnetic writer probe. The sample response magnetic field is coupled back to the probe and measured with a spectrum analyzer. (b) The picture of the measurement setup on the rack. (c) Sketch of the probe-sample interaction. The magnetic probe is approximated as a current loop producing perpendicular magnetic field inducing screening currents on the surface of the sample. This current generates a response magnetic field that is coupled back to the same probe. . . . .	86
Fig. 5.1	Picture of Sample 1, Nb film on copper from CERN. . . . .	89
Fig. 5.2	Temperature dependence of third-harmonic response $P_{3f}$ from Sample 1 for $f = 2.2GHz$ input frequency. (a) High input power limit with input powers $P_{rf} = -25dBm$ (blue), $P_{rf} = -22dBm$ (red), $P_{rf} = -19dBm$ (green). (b) Low input power limit with input powers $P_{rf} = -39dBm$ (blue), $P_{rf} = -36dBm$ (red), $P_{rf} = -33dBm$ (green), $P_{rf} = -30dBm$ (cyan). A peak in $P_{3f}(T)$ around $T_c$ is expected from the Ginzburg-Landau (GL) model. Note the periodicity as a function of temperature between $5K < T < 7K$ . . . . .	90
Fig. 5.3	Third-harmonic response $P_{3f}$ from Sample 1 as a function of temperature while cooling down (blue) and warming up (green and red). The data is taken at input frequency $f = 2.2 GHz$ and input power $P_{rf} = -40 dBm$ . The data shown in green color is acquired 1 week before the other two. . . . .	92
Fig. 5.4	(a) Third-harmonic response power $P_{3f}$ data (logarithmic scale) from Sample 1 as a function of temperature $T$ and applied rf power $P_{rf}$ . (b) Third-harmonic voltage response $V_{3f}$ data (on a linear scale) vs temperature and applied rf field amplitude $H_{rf}$ from Sample 1. The white dashed line shows the onset of non-linear response that we attribute to vortex nucleation as will be discussed in Chapter 8. The black dashed line shows the onset of periodic response. The response is measured at input frequency of $f = 2.2GHz$ . . . . .	94
Fig. 5.5	(a) Third-harmonic response $V_{3f}$ data at $T = 5.1K$ and $f = 2.2GHz$ measured on Sample 1. (b) $H_{p1}$ (blue $\square$ ), $H_{p2}$ (red $\circ$ ), $H_{p3}$ (green $\diamond$ ), $H_{p4}$ (cyan $+$ ), $H_{p5}$ (red $\square$ ), $H_{p6}$ (blue $\times$ ) and onset of nonlinearity $H_v$ (black $\times$ markers) vs temperature. . . . .	96
Fig. 5.6	Temperature dependence of third-harmonic response $P_{3f}$ from Sample 2 for $f = 1.49GHz$ input frequency with input powers $P_{rf} = -10dBm$ (blue), $P_{rf} = -5dBm$ (red), $P_{rf} = 0dBm$ (green), $P_{rf} = 5dBm$ (cyan) and $P_{rf} = 10dBm$ (magenta). The measurement is taken with video bandwidth and resolution bandwidth of $3Hz$ with 5 times averaging. The noise floor of the spectrum analyzer with these settings is $-155dBm$ . . . . .	97

Fig. 5.7	Third-harmonic voltage $V_{3f}$ data vs temperature and applied rf field amplitude from sample 2 measured at a $4.38GHz$ rf input frequency. A temperature-independent probe background non-linearity (Eq. (5.3)) has been subtracted, resulting in some negative values of $V_{3f}$ . . . . .	98
Fig. 5.8	Third-harmonic response $V_{3f}$ data at $T = 9.0K$ and $f = 4.38GHz$ measured on Sample 2. The probe background measured above $T_c$ is shown as the green dashed line. . . . .	99
Fig. 5.9	The first few $H_{pn}$ and the onset of periodicity $H_{p0}$ (black dashed line) vs temperature for sample 2. Three separate families of dips (blue, red, green) can be attributed to 3 separate weak-links. . .	100
Fig. 5.10	$H_{pn}$ vs $n$ for the sample 2 at $T = 9.0K$ . The solid line is a linear fit to the data. $H_{p0}$ is defined as the y-intercept of this fit. The "period" is defined as the slope of the fit line. In this particular example, $H_{p0} = 70.1 a.u.$ and the period is $31.54 a.u.$ . . . . .	100
Fig. 5.11	(a) Third-harmonic data $V_{3f}$ vs temperature and applied rf field amplitude $H_{rf}$ measured on Sample 3 at $f = 5.07GHz$ rf input frequency. (b) Vertical line cut through this image ( $V_{3f}$ vs $H_{rf}$ ) at a constant temperature of $T = 5.0K$ . . . . .	102
Fig. 5.12	Third-harmonic response $V_{3f}$ vs input rf field amplitude $H_{rf}$ data measured on Sample 4 at $T = 7.5K$ and $f = 4.855GHz$ rf input frequency. . . . .	103
Fig. 5.13	Fifth-harmonic response $V_{5f}$ vs input rf field amplitude $H_{rf}$ data measured on Sample 5 at $T = 4.2K$ and $f = 1.361GHz$ rf input frequency on Nb thin-film. . . . .	104
Fig. 6.1	Illustration of oxidation in air of a smooth, single crystal Nb. Metallic $NbO_x$ and $Nb_2O_5$ , which is an insulator, form at the surface when Nb is exposed to air for 30 minutes. RF magnetic field applied to such a surface will drive rf currents through this junction. Parts of this figure are reproduced from [133]. . . . .	108
Fig. 6.2	The simplest circuit model for a Josephson Junction. The driving current flows through 3 parallel branches: a capacitive branch due to an Insulating layer, an idealized Junction, and a resistive branch. . . . .	109
Fig. 6.3	Calculated gauge-invariant phase difference $\delta$ (top) and voltage (bottom) across an RSJ as a function of normalized time $\omega t$ for one RF period in steady state. The calculation is done using Eq. (6.2) with frequency of $\omega/2\pi = 1GHz$ , $I_c R = 20\mu V$ and $I_\omega R = 20\mu V$ (red), $I_\omega R = 25\mu V$ (green) and $I_\omega R = 30\mu V$ (blue). Note that the $2\pi$ phase slips in $\delta(\omega t)$ produce voltage spikes across the junction, leading to harmonic response. . . . .	111

Fig. 6.4	Calculated magnitude (top) and phase (bottom) of third harmonic voltage across an RSJ junction vs $I_\omega R$ for $I_c R = 20\mu V$ . The markers correspond to three curves shown in Fig. 6.3: $\diamond$ -red line, $\times$ -green line, and $\circ$ -blue line. Each periodic feature in $V_{3\omega}$ and $\Theta_{3\omega}$ correspond to an additional $2\pi$ phase slip in the junction during each rf period. . . . .	113
Fig. 6.5	(a) Solid lines: $H_{p1}, H_{p2}, H_{p3}, H_{p4}, H_{p5}, H_{p6}, H_{p7}, H_{p8}, H_{p9}, H_{p10}$ and $H_{p0}$ (dashed line) vs $I_c R$ calculated from the RSJ model. (b) Period of the dips $H_{pn}$ vs $I_c R$ . (c) Onset-to-period ratio $\frac{H_{p0}}{Period}$ vs $I_c R$ . . . . .	114
Fig. 6.6	Third-harmonic response $V_{3f}$ data at $T = 9.0K$ and $f = 4.38GHz$ measured on Sample 2 (black $\times$ markers). The probe background measured above $T_c$ is shown as the green dashed line. The RSJ fit with $I_c R = 49.4\mu V$ is shown as the red solid line. . . . .	116
Fig. 6.7	Third-harmonic response $V_{3f}$ data from Sample 1 at $T = 5.1K$ and $f = 2.2GHz$ (black $\times$ markers). Also shown are the RSJ fit with $I_c R = 58.3\mu V$ (green dashed-dotted line), time-dependent Ginzburg-Landau fit with $H_{dp} = 12$ (blue dashed line) (see Sec. 8.7), probe background (cyan dotted line) and complete fit obtained by vector complex addition (red solid line). . . . .	118
Fig. 6.8	(a) $I_c R(T)$ values extracted from the RSJ fit to the sample 1 data (black $\circ$ markers) and weak-link 1 (blue $\diamond$ markers), weak-link 2 (green $\times$ markers) and weak-link 3 (red $\star$ markers) of sample 2. (b) Calculated superconducting gap from sample 1 data (black $\circ$ markers-dash-dotted line) and weak-link 1 (blue $\diamond$ markers-solid line), weak-link 2 (green $\times$ markers-dashed line) and weak-link 3 (red $\star$ markers-dotted line) of sample 2. . . . .	120
Fig. 7.1	$\mathcal{F}_L$ vs $ \Psi ^2$ for several $\alpha$ values ( $\beta = 1$ ). Note the existence of a minimum in $\mathcal{F}_L$ at finite non-zero $ \Psi ^2$ when $\alpha < 0$ . . . . .	124
Fig. 7.2	Blue solid line: Gorkov function $\chi(\rho)$ vs $\rho$ using Eq. (7.12). Red dashed line: is the large- $\rho$ asymptotic behaviour $\frac{\pi^2}{7\zeta(3)\rho}$ . . . . .	128
Fig. 7.3	Magnetic penetration depth $\lambda(T)$ (blue) and coherence length $\xi(T)$ (red) vs mean-free path $l$ , calculated using Eq. (7.26) and Eq. (7.29) where $\gamma$ is calculated using Eq. (7.21) with $n_s^* = 8.54 \times 10^{27} m^{-3}$ for Nb. Both quantities are multiplied by $f_\alpha(T) = \sqrt{1 - T/T_c}$ to show the temperature independent dependence on the mean free path. . . . .	146
Fig. 7.4	Schematic view of the superconductor and vacuum domains and boundary conditions in my COMSOL simulations. . . . .	156

- Fig. 7.5 Plot of TDGL two-domain solution for z component of magnetic field in a plane through the center of the sphere in and around a superconducting sphere in the Meissner state subjected to a uniform static external magnetic field in the z-direction. The dashed lines show the boundaries of the spheres, with the smaller sphere being the superconducting sphere with diameter  $10\xi(0)$  and the larger sphere being the vacuum domain with diameter  $40\xi(0)$ . The solution is obtained for temperature  $T = 0$ , GL parameter  $\kappa = 1$  and external magnetic field  $\vec{B}_{applied} = 10 \times 10^{-3} B_{c2} \hat{z}$ . Black lines show the streamline plot of magnetic field, while the color represents the value of magnetic field component  $B_z$ . The white line indicates the equator, and the magnetic field along the white line is shown in Fig. 7.6. . . . . . 158
- Fig. 7.6 Top: Magnetic field  $\hat{z}$ -component ( $B_z$ ) profile through the center of sphere (white line in Fig. 7.5). The results of a single domain TDGL model are shown in red, a two-domain TDGL model in green, and the analytic solution is shown as a blue solid line. Bottom: The difference between a two-domain TDGL model and the analytic solution is shown in green and the difference between single domain TDGL model and the analytic solution is shown in red. The biggest difference is observed at the surface. . . . . 160
- Fig. 7.7 The magnitude of the superconducting screening current density at the surface  $J_{screening}$  as a result of a perpendicular magnetic dipole placed  $h_{dp} = 1\xi(0)$  above the superconductor vs the horizontal distance from the dipole location obtained from GL simulation (blue  $\times$ ) and numerical solution for the same scenario obtained from Ref. [221] (red solid line). Left inset shows a schematic of the dipole over the superconductor, while the right inset shows the top view of the surface current distribution calculated by GL, which is azimuthally symmetric. . . . . 162
- Fig. 8.1 TDGL simulation setup for an oscillating horizontal magnetic dipole  $\vec{M}_{dp}$  at fixed height  $h_{dp}$  above the superconductor surface. The magnetic probe is approximated as an oscillating point magnetic dipole parallel to the surface. Red Arrows: Surface currents on the horizontal (xy) superconductor/vacuum interface as calculated from the self-consistent TDGL equations. Black Arrows: Externally applied magnetic field on a vertical plane (xz) perpendicular to the superconductor surface and including the dipole. 165



- Fig. 8.2 Snapshot of 3 vortex semiloops at time  $t = 73\tau_j$  during the rf cycle of period  $200\tau_j$ . In this view, one is looking from inside the superconducting domain into the vacuum domain. Plots of  $|\Delta|^2$  are evaluated at the superconductor surface for an oscillating parallel magnetic dipole above the superconductor. The three-dimensional silver surfaces (corresponding to  $|\Delta|^2 = 0.005$ ) show the emergence of vortex semiloops. The simulation parameters are given in Table 8.1. . . . . 167
- Fig. 8.3 Summary of TDGL solution for an oscillating parallel magnetic dipole above a superconducting surface. (a)-(f) Plots of  $|\Delta|^2$  evaluated at the superconductor surface at different times for an oscillating parallel magnetic dipole above the superconductor. In the top part of each panel, one is looking from inside the superconducting domain into the vacuum domain, whereas in the bottom part of each panel, one is looking at the x-z cross-section plane towards the +y axis.  $\vec{M}_{dp}(t)$  is chosen such that  $\vec{B}_0(t) = 0.55\sin(\omega t)\hat{x}$ . The three-dimensional silver surfaces (corresponding to  $|\Delta|^2 = 0.005$ ) show the emergence of vortex semiloops. (g)  $|\vec{B}_0|$  at the surface vs time during the first half of the rf cycle. Red crosses correspond to field values for snapshots (a)-(f). The simulation parameters are given in Table 8.1. . . . . 169
- Fig. 8.4 Plots of  $|\Delta|^2$  (color) and  $\vec{J}_{surf}$  (arrows) evaluated at the two dimensional  $x = 0$  plane inside the superconductor at  $t = 50\tau_j$  for an oscillating parallel magnetic dipole above the superconductor. White arrows indicate the currents induced inside the superconducting domain. The three-dimensional silver surfaces (corresponding to  $|\Delta|^2 = 0.005$ ) show the emergence of vortex semiloops and the suppressed superconducting domain. All model parameters are listed in Table 8.1 . . . . . 171
- Fig. 8.5 a-h) Plots of  $|\Delta|^2$  evaluated at the superconductor surface at  $t = 50\tau_j$  for an oscillating parallel magnetic dipole above the superconductor as a function of dipole strength. In this view, one is looking from inside the superconducting domain into the vacuum domain. The maximum amplitude of applied rf field is shown as  $|\vec{B}_0|$ . The silver three-dimensional surfaces correspond to  $|\Delta|^2 = 0.005$  and show the suppressed order parameter domain and the vortex semiloops. The parameters of the simulation are listed in Table 8.1. . . . . 172
- Fig. 8.6 Plot of the maximum extent (in units of  $\xi(0)$ ) of excursion for the vortex semiloop  $d_v$  and the maximum extent for the suppressed superconductor domain  $d_n$  in an rf cycle as a function of friction coefficient  $\eta$  (log scale). The TDGL equations are solved at  $T = 0.9T_c$  for a parallel magnetic dipole above the superconductor. The full list of simulation parameters is given in Table 8.1. . . . . 173



Fig. 8.7	<p>Summary of TDGL solutions for an oscillating parallel magnetic dipole above a superconducting surface in the presence of a localized defect at <math>\vec{r}_d = 0\hat{x} + y_d\hat{y} - 12\hat{z}</math>, where <math>y_d</math> is varied from 0 to <math>16\xi(0)</math>. (a)-(e) Plots of vortex semiloops in the y-z cross-section plane below the dipole illustrated with a three-dimensional silver surface (corresponding to <math> \Delta ^2 = 0.003</math>) at time <math>t = 150\tau_j</math>, when the applied magnetic field reaches its peak amplitude. (f)-(j) Plots of vortex semiloops at time <math>t = 180\tau_j</math>. The defect is denoted by the red dot to the right of the center. <math>\vec{M}_{dp}(t)</math> is chosen such that <math>\vec{B}_0(t) = 0.30\sin(\omega t)\hat{x}</math>. The full list of simulation parameters is given in Table 8.1. . . . .</p>	175
Fig. 8.8	<p>The third harmonic response <math>B_{3\omega}(B_0)</math> normalized by the maximum value vs the radius of the simulation domain <math>R</math>. Note that <math>h_{sc}</math> and <math>h_{vac}</math> are varied proportionally with <math>R</math>. The parameters of the simulation are listed in Table 8.1. . . . .</p>	177
Fig. 8.9	<p>Third-harmonic response <math>V_{3f}</math> data from Sample 1 at <math>T = 5.1K</math> and <math>f = 2.2GHz</math> (black <math>\times</math> markers). Also shown are the time-dependent Ginzburg-Landau fit with <math>H_{dp} = 12</math> (blue dashed line), probe background (cyan dotted line), RSJ fit with <math>I_c R = 58.3\mu V</math> (green dashed-dotted line) (see Sec. 6.1), and complete fit obtained by vector complex addition (red solid line). . . . .</p>	178
Fig. 9.1	<p>(a)-(h) Plots of vortex semiloops illustrated with a silver surface (corresponding to <math> \Delta ^2 = 0.005</math>) at different times for parallel rf magnetic field in the <math>\hat{x}</math> direction above the superconductor. A localized defect is placed at the origin (<math>\vec{r}_d = 0\hat{x} + 0\hat{y} + 0\hat{z}</math>) and defined using Eq. (8.2) with <math>\sigma_x = 6</math> and <math>\sigma_y = \sigma_z = 1</math> and <math>T_{cd} = 0.1</math>. The color shows the order parameter magnitude <math> \Delta ^2</math> on the superconducting surface. (i) <math> \vec{B}_0 </math> at the surface vs time during the first half of the rf cycle. Red crosses correspond to field values for snapshots (a)-(h). The simulation was performed for <math>\kappa = 1</math>, <math>\eta = 1</math>, <math>B_0 = 0.3B_{c2}</math> and <math>2\pi/\omega = 1000\tau_j</math>. Note that this is a transient solution rather than a steady state solution. . .</p>	181
Fig. 9.2	<p>Relaxation times <math>\tau_{ \Delta }</math> (blue) and <math>\tau_\theta</math> (red) vs normalized gap <math> \Delta </math>, for the case of Nb in the dirty limit with <math>\eta = 1.78</math> and <math>\Gamma = 30.78</math>. Inset shows the same plot vs linear <math> \Delta </math>. This illustrates that the phase of the order parameter will relax more quickly than the amplitude whenever <math> \Delta </math> is large. Note that as <math> \Delta  \rightarrow 1</math>, <math>\tau_{ \Delta }/\tau_\theta \rightarrow 1 + \Gamma^2 \sim 10^3</math>. . . . .</p>	189
Fig. 9.3	<p>Relaxation times <math>\tau_{GL}</math> (blue), <math>\tau_{ \Delta }</math> (red) and <math>\tau_j</math> (green) vs temperature for Nb with <math>T_c = 9.2 K</math>. Also shown are periods corresponding to rf excitations with 200 MHz, 1GHz and 5 GHz frequencies. . . . .</p>	191

Fig. 9.4	<p>The frequency dependence of the critical field <math>H_{c1}(\omega)</math> calculated using Eq. (9.8) for <math>T/T_c = 0.75, 0.80, 0.85, 0.90</math> and <math>0.95</math>. Here <math>\tau_j(0)/\tau_{ \Delta }(T) = 0.027, 0.031, 0.038, 0.053</math> and <math>0.097</math> with <math>\Delta(T)/\Delta(0) = \frac{1.74}{2} [1 - (T/T_c)^4]</math>. This calculation is performed for <math>\Gamma = 30.78</math> and <math>\eta = 1.78</math>. . . . .</p>	193
Fig. 9.5	<p>Snapshots at <math>t = 4200\tau_0</math> of vortex semiloops illustrated with a silver surface (corresponding to <math> \Delta ^2 = 0.075</math>) simulated with different values of <math>\Gamma = \frac{2\tau_E\Delta_\infty(0)}{\hbar}</math> for parallel rf magnetic field in the <math>\hat{x}</math> direction above the superconductor. The blue line represents the free superconducting surface. The green line represents the boundaries of each simulation. A localized defect is placed on the surface at the origin (<math>\vec{r}_d = 0\hat{x} + 0\hat{y} + 0\hat{z}</math>) and defined using Eq. (8.2) with <math>\sigma_x = 4</math> and <math>\sigma_y = \sigma_z = 2</math> and <math>T_{cd} = 0.2</math>. The simulation was performed for <math>\kappa = 1.5</math>, <math>\eta = 1</math>, <math>B_0 = 0.35B_{c2}</math>, <math>T = 0.7T_c</math> and <math>2\pi/\omega = 5000\tau_0</math>. . . . .</p>	195
Fig. 10.1	<p>Schematic illustration of the variation in nonlinear scaling current density <math>J_{NL}</math> (blue) and third-harmonic response <math>P_{3f}</math> (red) due to the local surface defects. The schematic hierarchy of <math>J_{NL}</math> attributed to some well-known defects is shown on the right side arrow. This figure is partially reproduced from [104]. . . . .</p>	197
Fig. 10.2	<p>Optical microscope image of the measured BSCCO flake sample. The scanned area is shown by a black box in the inset, and the third-harmonic power image is shown in Fig. 10.3. . . . .</p>	199
Fig. 10.3	<p>Scanned Image of BSCCO sample at <math>T = 89K</math> at applied power <math>P_f = -6dBm</math> and frequency <math>f = 4.975</math> GHz. Colorbar shows the third-harmonic response <math>P_{3f}</math> in dBm. The scanned area is shown as a black box in Fig. 10.2. . . . .</p>	199
Fig. 10.4	<p>Schematic of the experimental setup for raster scanning and imaging of nonlinear response. The probe is attached to an Attocube z-axis cryogenic piezo scanner, directly above the superconducting sample which rests on top of a Cold Base attached to an Attocube xy cryogenic scanner. The coldbase is thermally anchored to the cold plate of the cryostat. The eye icon indicates the point from which images shown in Fig. 10.9 are captured. As described in Chapter 4, a microwave (MW) source is used to generate an rf signal and feed it to the magnetic writer probe. The sample response magnetic field is coupled back to the probe and measured with a spectrum analyzer. . . . .</p>	200

- Fig. 10.5 A picture of the experimental setup for raster scanning and imaging of nonlinear response. The probe is attached to an Attocube z-axis cryogenic piezo scanner, directly above the superconducting sample, which rests on top of a Cold Base attached to an Attocube xy cryogenic scanner. The coldbase is thermally anchored to the cold plate of the cryostat by means of copper braids. To strengthen the thermal link vacuum grease (Apiezon N Grease) is applied between the sample and the Cold Base, and also between the Y-scanner and the Cold Finger. . . . . 201
- Fig. 10.6 Optical images of the probe as it approaches the sample: (a) when probe is away from the sample; (b),(c),(d) when probe is barely touching the sample; (e) when probe is laying flat on the sample; and (f) when the Z-scanner is pushed too far and the front of the probe where the writer pole is located moves away from the sample. Reflection of the probe from the sample can be used to infer the probe-sample separation. The surface of the sample is shown by the red line in (e). . . . . 204
- Fig. 10.7 Third-harmonic response  $P_{3f}$  vs the position of the Z-axis scanner measured in the superconducting state (blue curve measured at  $T = 6K$ ) and the normal state (red curve measured at  $T = 10K$ ). Below  $Z < 2000\mu m$  the probe is far away from the sample and the measured third-harmonic response can be attributed to the probe itself. For  $2000\mu m < Z < 2300\mu m$  the probe starts deforming and we have noisy spikes in  $P_{3f}(Z)$  both in the superconducting and normal states. Above  $Z > 2300\mu m$  the probe lays flat against the sample and we measure consistent and temperature dependent third-harmonic response. The data is measured on a Bulk Nb (Sample 2 in Chapter 5) at frequency of  $f = 1.49GHz$  and  $P_f = -5dBm$  input power. . . . . 205
- Fig. 10.8 Third-harmonic response  $P_{3f}$  vs the position of the Z-axis scanner measured in the superconducting state (blue curve measured at  $T = 6K$ ) and the normal state (red curve measured at  $T = 10K$ ). Below  $Z < 2000\mu m$  the probe is far away from the sample and the measured third-harmonic response can be attributed to the probe itself. For  $2000\mu m < Z < 2300\mu m$  the probe starts deforming and we have noisy spikes in  $P_{3f}(Z)$  both in the superconducting and normal states. Above  $Z > 2300\mu m$  the probe lays flat against the sample and we measure consistent and temperature dependent third-harmonic response. The data is measured on a Bulk Nb (Sample 2 in Chapter 5) at frequency of  $f = 1.8GHz$  and  $P_f = -5dBm$  input power. . . . . 206

- Fig. 10.9 Optical images of the probe as it approaches the sample at room temperature: (a) when  $Z = 1900\mu m$  and probe is away from the sample. (b) when  $Z = 2200\mu m$  and the probe is barely touching the sample. (c) when  $Z = 2600\mu m$  and the probe is laying flat on the sample. In these pictures one is looking from the location denoted with an eye icon in Fig. 10.4. . . . . . 207
- Fig. 10.10 2-dimensional (XZ) scan of the bulk Nb sample (Sample 2 in Chapter 5). The third-harmonic response  $P_{3f}$  is measured at a frequency of  $f = 1.49GHz$ , temperature of  $T = 6K$  and  $P_f = -5dBm$  input power. The image was taken by scanning in Z and rastering in X. The data in the area bounded by two white line was averaged and is plotted in Fig. 10.11. The inset show the picture of the sample where the location of the scan is shown with a red line. . . . . . 209
- Fig. 10.11 Third harmonic response averaged over the area bounded by the white lines in Fig. 10.10. The data is presented in a logarithmic scale in dBm units but the averaging is performed in the linear scale. . . . . . 209
- Fig. 10.12 Top: 2-dimensional (XZ) scan of the bulk Nb sample. The third-harmonic response  $P_{3f}$  is measured at frequency of  $f = 1.49GHz$ , temperature  $T = 6K$  and  $P_f = 0dBm$  input power. In this case the X value is scanned while the Z value is rastered. Bottom: Line scans along the lines shown in the top panel. The new Z-direction is  $13^\circ$  tilted compared to the top panel. Dips in  $P_{3f}(Z)$  around  $Z=0$  are the result of the destructive interference between the sample nonlinear response and that generated by the probe itself. . . . . . 211
- Fig. 10.13 (a) Picture of the bi-crystal bulk Nb tensile sample. Yellow line shows the location of the grain boundary and the red line shows an approximate location where the line scan shown in Fig. 10.14 was measured. (b) SEM image of the grain boundary. . . . . . 212
- Fig. 10.14 Third-harmonic response  $V_{3f}$  vs the position of the X-axis scanner measured at frequency of  $f = 5.845GHz$  and temperature  $T = 4.5K$ . The measurement is performed simultaneously at 3 different input rf amplitudes:  $H_{rf} = 200a.u.$  (blue),  $H_{rf} = 400a.u.$  (red) and  $H_{rf} = 600a.u.$  (green). . . . . . 213
- Fig. 11.1 Schematic of the Parallel Plate Resonator. A dielectric spacer is sandwiched between two nominally identical superconducting films. Arrows show the rf magnetic fields  $H_{rf}$  (black) and surface currents  $J_{rf}$  (white) corresponding to the  $TEM_{01}$  mode. The coupling to the PPR is achieved by bringing 2 antennas close to the edge of the PPR. The antennas are made by exposing a short part of the inner conductor and a portion of the outer conductor of a coaxial cable. Schematic diagram not to scale. . . . . . 217

Fig. 11.2	Picture of the experimental setup. (a) PPR inside the copper cavity. Two dielectric posts are used to keep the samples together. Coupling antennas enter the cavity from two small holes on the left side. A thermometer and a heater are installed to monitor and control the temperature. The cavity housing the PPR is attached to the end of the dipping probe. (b) The dipping probe is inserted into the liquid helium dewar. (c) Top part of the dipping probe. Micrometers are installed to precisely move the rf coaxial cables up or down, which moves the antennas away or towards the sample, hence tuning the coupling strength of the antennas to the PPR. A relief valve is installed to relieve the helium gas pressure build up. (d) The cavity housing the PPR is attached to the mixing chamber plate of the dilution fridge shown in Fig. 3.5 of Chapter 3. An aluminium holder is designed to hold the antennas at the desired position. Alternatively, the cavity can be attached to the cold plate of the dry pulsed-tube cryostat shown in Fig. 4.11 of Chapter 4. . . . .	221
Fig. 11.3	The shape of the B-diamond sample. . . . .	224
Fig. 11.4	Transmission through the cavity housing the B-diamond PPR, $ S_{12} $ as a function of frequency, measured by the VNA at $T = 4.38K$ , $T = 4.98K$ and $T = 5.32K$ in the dipping probe. . . . .	226
Fig. 11.5	(a) Complex plane plot of the ideal resonator transmission $S_{12}(f)$ (blue circle) calculated using Eq. (11.5). The diameter of this circle is equal to $S_{peak}$ . The length of the green arrow connecting the origin with a data point on the circle is equal to the measured amplitude of the transmission $ S_{21}(f) $ . The phase of the resonance $\phi$ which is defined as the angle between the real axis and the line connecting the origin with a particular point is shown in (b) (red solid line). At the resonant frequency $Re\{S_{21}(f_{res})\} = S_{peak}$ and $\phi(f_{res}) = 0$ . . . . .	228
Fig. 11.6	The steps of an Phase vs frequency fit method. Measured amplitude and phase of $S_{12}(f)$ is shown in (a) and (b) respectively. (c) shows the Phase of the $S_{12}(f)$ after unwinding and background subtraction. (d) Complex plane plot of $S_{12}(f)$ (blue) and a circle fit (red) to it after the phase unwinding. Yellow circle shows the coordinates of $S_{ref}$ and the arrows indicate the translation and rotation performed to arrive at the data shown in (e). (e) Complex plane plot of $S_{12}(f)$ after the translation to and rotation around the origin. (f) (Black) The phase of the "clean" $S_{12}(f)$ data shown in (e) and the Eq. (11.8) fit to this data with $Q = 78$ , $f_{res} = 6.444$ GHz and $\theta_0 = -0.048$ (red). . . . .	230
Fig. 11.7	Multi-peak fit to $S_{12}(f)$ data using Eq. (11.9) with $N = 3$ : $f_{res,peak1} = 6.443$ GHz and $Q_{peak1} = 69$ ; $f_{res,peak2} = 7.115$ GHz and $Q_{peak2} = 52$ ; $f_{res,peak3} = 8.532$ GHz and $Q_{peak3} = 5.2$ . Data collected from Boron-doped diamond PPR at $T = 4.38$ K in the dipping probe. . . . .	233

Fig. 11.8	Temperature dependence of the resonant frequency $f_{res}(T)$ extracted from PPR measurement on B-diamond films inside the (a),(b) Entropy cryostat with $500\mu m$ Quartz dielectric spacer (two modes measured simultaneously) and (c) dilution fridge with $430\mu m$ Sapphire dielectric spacer. Also shown are fits to the data using Eqs. (11.1) and (11.3) with $p = 2$ (blue), $p = 4$ (red), $p = 4/3$ (green). Inset in (c) shows the quantity $f_{res}(0)\Delta f_{res}(T)/f_{res}^2(T)$ vs temperature, which is proportional to $\Delta\lambda/\lambda(0)$ . Solid red line is the fit to the data using Eq. (11.10) with $\Delta(0) = 812\mu eV$ . . . . .	234
Fig. 11.9	Estimated zero temperature penetration depth $\lambda(0)$ for various B-diamond films calculated using Eq. (11.11) (black $\circ$ ). The normal state resistivity $\rho_n$ and the critical temperature $T_c$ was taken from the data published in Ref.[252]. The red $\times$ shows the value of the penetration depth extracted from my B-diamond PPR measurement inside the dilution fridge. . . . .	239
Fig. 11.10	Upper bound on the surface resistance $R_s$ of the boron doped diamond film. Data taken at a frequency of $f = 7.52$ GHz (black stars). Also shown is the $R_s(T) = R_{BCS}(T) + R_0$ fit to the low temperature part of the data ( $T < 5.4$ K) with $R_0 = 65.3m\Omega$ , $\sigma_n = 4.02 \times 10^5 S/m$ and $\Delta(0) = 1.34meV$ used as fitting parameters (red solid line). Here $\lambda(0) = 3.42\mu m$ from Sec. 11.5.1 was used for the value of the penetration depth. Inset shows the $R_s(T) - R_0$ vs $T_c/T$ in log-linear scale. . . . .	241
Fig. A.1	The reflection coefficient $S_{11}(f)$ of the probe measured with a VNA at room temperature. . . . .	248
Fig. A.2	The reflection coefficient $S_{11}(f)$ of the probe measured at $T = 88K$ (blue) and $T = 107K$ (red), below and above the $T_c$ of the sample. In this measurement the probe is in contact with the BSCCO sample described in Sec. 10.1. The inset shows the amplitude of the complex difference $\Delta S_{12}$ between these two measurements. . . . .	249
Fig. A.3	Third-harmonic response $P_{3f}(f)$ measured on a bulk Nb sample at $T = 8K$ (blue) and $T = 10K$ (orange) below and above $T_c$ . There is enhanced third harmonic response measured in the $4.3GHz < f < 5.5GHz$ frequency window when the sample goes into the superconducting state. . . . .	250
Fig. B.1	Magnetic writer head attached to a quartz Tuning Fork in a q-plus sensor design. . . . .	254
Fig. B.2	Fundamental tone of the sensor shown in Fig. B.1. Data shown in blue and a Lorentzian fit with $f_{res} = 21,018$ Hz and $Q = 106$ is shown in red. . . . .	255

## List of Symbols and Units

Symbol	Definition (units)	[SI base units]
$\alpha$	GL expansion parameter ( $J$ )	$[kg \cdot m^2 \cdot s^{-2}]$
$\alpha_{\Delta}$	GL expansion parameter ( $1/J \cdot Volume$ )	$[kg^{-1} \cdot m^{-5} \cdot s^2]$
$\beta$	GL expansion parameter ( $J/Volume$ )	$[kg \cdot m^5 \cdot s^{-2}]$
$\beta_{\Delta}$	GL expansion parameter ( $1/J^3 \cdot Volume$ )	$[kg^{-3} \cdot m^{-9} \cdot s^6]$
$\gamma$	GL phenomenological parameter ( $1/kgJ^2m^3$ )	$[kg^{-3} \cdot m^{-7} \cdot s^4]$
$\Gamma$	$2\tau_E/\hbar$ ( $1/J$ )	$[kg^{-1} \cdot m^{-2} \cdot s^2]$
$\Gamma_{Dynes}$	Dynes pair-breaking scattering rate ( $J$ )	$[kg \cdot m^2 \cdot s^{-2}]$
$\Delta$	BCS Superconducting Gap ( $J$ )	$[kg \cdot m^2 \cdot s^{-2}]$
$\zeta$	Riemann zeta function	[dimensionless]
$\eta$	Normalized friction coefficient	[dimensionless]
$\eta_0$	$\pi^4/14\zeta(3) = 5.79$	[dimensionless]
$\kappa$	GL constant	[dimensionless]
$\Lambda$	London constant ( $kgm^3/C^2$ )	$[kg \cdot m^3 \cdot A^{-2} \cdot s^{-2}]$
$\lambda_L$	London penetration depth ( $m$ )	$[m]$
$\lambda, \lambda_{eff}$	Effective penetration depth ( $m$ )	$[m]$
$\mu_0$	Permeability of free space ( $H/m$ )	$[kg \cdot m \cdot A^{-2} \cdot s^{-2}]$
$\nu(0)$	DOS at Fermi Energy ( $1/J \cdot Volume$ )	$[kg^{-1} \cdot m^{-5} \cdot s^2]$
$\xi$	GL coherence length ( $m$ )	$[m]$
$\xi_0$	Pippard (BCS) coherence length ( $m$ )	$[m]$
$\pi$	Mathematical constant	[dimensionless]
$\sigma_n$	Normal state conductivity ( $1/\Omega m$ )	$[kg^{-1} \cdot m^{-3} \cdot A^2 \cdot s^3]$
$\tau_E$	Electron-phonon scattering time ( $s$ )	$[s]$
$\tau_{GL}$	GL relaxation time ( $s$ )	$[s]$
$\Phi_0$	Magnetic flux quantum (Wb)	$[kg \cdot m^2 \cdot A^{-1} \cdot s^{-2}]$
$\Psi$	GL order parameter ( $1/Volume$ )	$[m^{-3}]$

## List of Symbols and Units

Symbol	Definition (units)	[SI base units]
$\vec{A}$	Magnetic vector potential ( $N/A$ )	$[kg \cdot m \cdot A^{-1} \cdot s^{-2}]$
$\vec{B}$	Magnetic flux density ( $Wb/m^2$ )	$[kg \cdot A^{-1} \cdot s^{-2}]$
$B_c$	Thermodynamic critical B-field (T)	$[kg \cdot A^{-1} \cdot s^{-2}]$
$B_{c1}$	Lower critical B-field (T)	$[kg \cdot A^{-1} \cdot s^{-2}]$
$B_{c2}$	Upper critical B-field (T)	$[kg \cdot A^{-1} \cdot s^{-2}]$
$c$	Speed of light, $3 \times 10^8 m/s$	$[m \cdot s^{-1}]$
$D$	Electron diffusion coefficient ( $Area/s$ )	$[m^2 \cdot s^{-1}]$
$E_F$	Fermi Energy ( $J$ )	$[kg \cdot m^2 \cdot s^{-2}]$
$e$	Charge of an electron ( $C$ )	$[A \cdot s]$
$e_*$	Charge of an electron pair ( $C$ )	$[A \cdot s]$
$\mathcal{F}$	Helmholtz free energy density ( $J/m^3$ )	$[kg \cdot m^{-1} \cdot s^{-2}]$
$J_c$	Critical current density ( $A/Area$ )	$[m^{-2} \cdot A]$
$h$	Planck constant ( $Js$ )	$[kg \cdot m^2 \cdot s^{-1}]$
$\hbar$	Reduced Planck constant ( $Js$ )	$[kg \cdot m^2 \cdot s^{-1}]$
$H_c$	Thermodynamic critical H-field ( $A/m$ )	$[m^{-1} \cdot A]$
$H_{c1}$	Lower critical H-field ( $A/m$ )	$[m^{-1} \cdot A]$
$H_{c2}$	Upper critical H-field ( $A/m$ )	$[m^{-1} \cdot A]$
$k_B$	Boltzmann constant ( $J/K$ )	$[kg \cdot m^2 \cdot s^{-2} \cdot K^{-1}]$
$l$	Electron mean free path ( $m$ )	$[m]$
$m_e$	Mass of an electron (kg)	$[kg]$
$m_*$	Mass of an electron pair (kg)	$[kg]$
$n_s$	Superfluid density ( $1/Volume$ )	$[m^{-3}]$
$P_f$	Fundamental power ( $W$ )	$[kg \cdot m^2 \cdot s^{-3}]$
$P_{3f}$	Third harmonic power ( $W$ )	$[kg \cdot m^2 \cdot s^{-3}]$
$Q$	Quality factor	[dimensionless]
$T$	Temperature ( $K$ )	$[K]$
$T_c$	Critical temperature ( $K$ )	$[K]$
$U$	total energy stored in the cavity ( $J$ )	$[kg \cdot m^2 \cdot s^{-2}]$
$V_{3f}$	Third harmonic voltage ( $V$ )	$[kg \cdot m^2 \cdot A^{-1} \cdot s^{-3}]$
$v_F$	Fermi velocity ( $m/s$ )	$[m \cdot s^{-1}]$
$Z_0$	Characteristic impedance of coax lines ( $\Omega$ )	$[kg \cdot m^2 \cdot A^{-2} \cdot s^{-3}]$



## List of Abbreviations

a.u.	Arbitrary unit
BCS	Bardeen-Cooper-Schrieffer
BSCCO	Bismuth strontium calcium copper oxide $Bi_2Sr_2CaCu_2O_{8+x}$
CVD	Chemical Vapor Deposition
dBm	Power ratio in decibels (dB) of the measured power referenced to one milliWatt (mW)
DOS	Density of states
DR	Dilution Refrigerator
GHz	GigaHertz, $10^9$ Hz
GL	Ginzburg-Landau
gTDGL	generalized Time-Dependent Ginzburg-Landau
HDDs	Hard disk drives
HFSS	High frequency structure simulator
ILC	International Linear Collider
IMD	Intermodulation Distortion
LN	Liquid nitrogen ( $N_2$ )
MSU	Michigan State University
MW	Microwave
MXC	Mixing chamber plate, the coldest plate of DR
Nb	Niobium
Nb <sub>3</sub> Sn	Tri-Niobium Tin
OFHC	Oxygen-free high thermal conductivity
PLL	Phase-locked loop
PID	Proportional-integral-derivative (Controller)
RF	Radio frequency
RRR	Residual-resistivity ratio defined as $\rho(T = 300K)/\rho(T = 0K)$
SEM	Scanning electron microscope
SIS	Superconductor-insulator-superconductor
SNS	Superconductor-normal metal-superconductor
SRF	Superconducting radio frequency
SS	Stainless steel
SQUID	Superconducting quantum interference device
TDGL	Time-Dependent Ginzburg-Landau
TM	Transverse Magnetic modes of a travelling wave
UMD	University of Maryland
VNA	Vector network analyzer
YBCO	Yttrium barium copper oxide $YBa_2Cu_3O_{7-x}$

# 1

---

## Introduction to Superconductivity

---

### 1.1 History and Hallmarks

#### 1.1.1 Discovery of “practically zero” resistance

Superconductivity is a macroscopic quantum state, a rare phenomena where a material exhibits dissipationless transport of electrical current. Superconductivity was discovered by Heike Kamerlingh Onnes, at Leiden University in the Netherlands. Onnes was the first scientist to successfully liquefy helium, in July, 1908 [1]. Later, he used his novel cooling capability to study the low temperature resistance of metals. The goal was to test whether a metal cooled down to absolute zero (or very cold temperatures, since absolute zero cannot be physically achieved) would have zero resistance (suggested by Dewar), some residual resistance (Matthiessen’s rule) or zero conductance, as Kelvin has suggested [2].

After performing several measurements with platinum, Onnes proceeded with a measurement of mercury (Hg), which ended up being the first ever confirmed super-

conductor [4, 5]. The historic entry in his laboratory notebook reads: “Kwik nagenoeg nul” which can be translated as “Mercury[’s resistance] practically zero [at 3 K]” [1]. Onnes found that the resistance of mercury drops by a factor of  $\approx 400$  below 4.2 K temperature (he later refined his measurement setup and measured much lower resistance, see Fig. 1.1). The emergence of zero resistance by itself wasn’t very surprising, in fact Onnes believed that Einstein’s theory of quantum oscillators [6] predicts such zero resistance, however the drop in resistance was too big to be explained by Einstein’s model [7]. Needless to say, Onnes made his team check for short circuits, but each time the same drop in resistance at 4.2 K temperature was observed [1]. Onnes presented the results at the first Solvay Conference [8, 9], and the field of “*Supercon-*

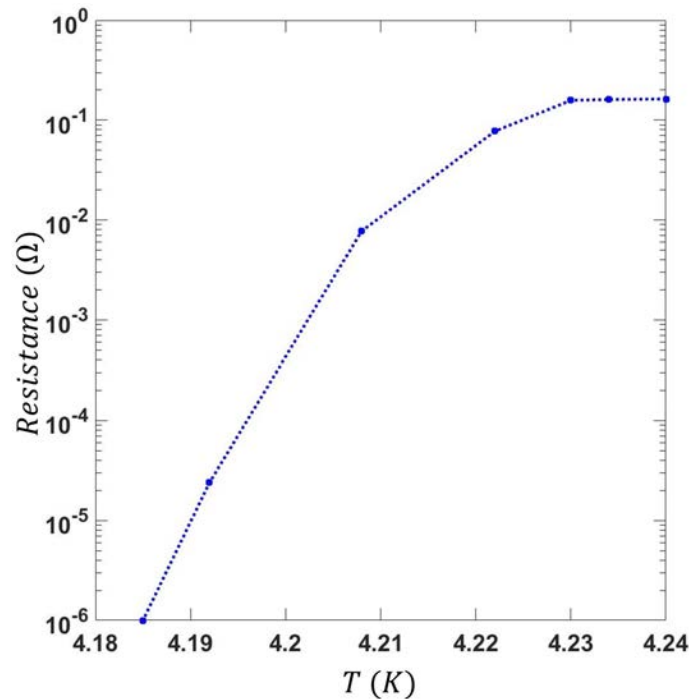


Fig. 1.1 The resistance of mercury (Hg) as a function of absolute temperature, reproduced from Table.IV of [3]

*ductivity*" was born, with *perfect dc conductance* being its first hallmark. Also the first parameter was defined, the superconducting critical temperature  $T_c$  below which the superconducting state emerges.

For the next 15 years after 1908, liquid helium was produced only in Onnes's lab in Leiden. Having a monopoly in helium liquefaction, the Onnes lab was the birth place of other superconductors like lead (Pb), tin (Sn), thallium (Tl), indium (In) [10] and became the mecca for physicists who wished to see the most advanced demonstration of superconductivity at the time: persistent current in a loop of superconducting wire. Onnes dreamed about possible applications of his game changing finding, like creating magnets which could generate 10 tesla magnetic fields, however he was disappointed to find out in 1914 that applying magnetic field, or high current, in that manner destroys the superconducting state. The field at which the superconducting state is lost is called the critical field  $H_c$  (or  $B_c = \mu_0 H_c$ ). The current density at which the superconducting state is lost is called the critical current density  $J_c$ , which is just the current density at which the wire generates  $H_c$  at the surface. Both of these parameters are temperature dependent.

### 1.1.2 The Meissner Effect

The next breakthrough in superconductivity came from Walther Meissner's lab in Germany, after they were successful in liquefying helium as well. While trying to study the nature of superconducting current, Meissner discovered that upon transition into the superconducting state, the material spontaneously expels a static magnetic

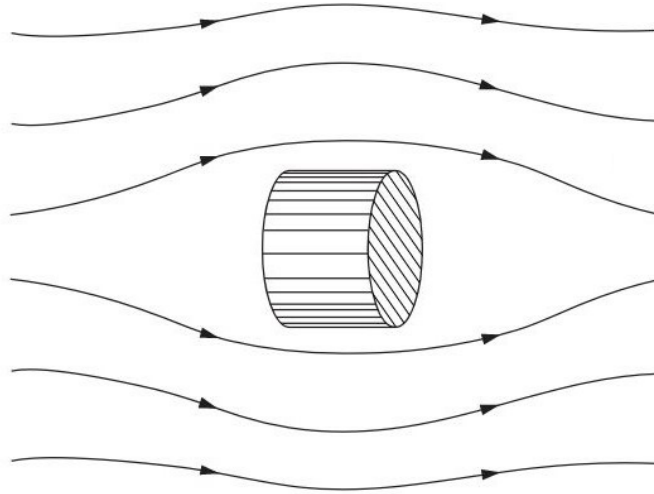


Fig. 1.2 Meissner effect in a superconductor, a superconductor cylinder inside a magnetic field. Superconductors completely expel magnetic flux. (Source: The Feynman Lectures on Physics, Volume III [11])

field [12] (Fig. 1.2). The perfect conductance already implied diamagnetism, but the common belief at the time was that a superconductor would seal any magnetic field present during the transition into the superconducting state, and screen any changes afterwards. Meissner's discovery, later dubbed the "Meissner effect", showed that superconductors exhibit *perfect diamagnetism*, which is now the second hallmark of superconductivity.

The third Hallmark of superconductivity is macroscopic quantum effects such as flux quantization. Before describing this effect some theoretical framework has to be introduced, therefore I postpone this discussion till [Sec. 1.2.5](#).

## 1.2 Phenomenological Theories of Superconductivity

### 1.2.1 Gorter-Casimir Two Fluid Model

Paul Ehrenfest believed that the transition into the superconducting state is a thermodynamic phase transition and treated it as such. The Meissner effect was the missing part of the puzzle, and led to the development of the Two Electron Fluids model by Cornelius Gorter and Ehrenfest's student Hendrik Casimir [13, 14]. This model postulates the existence of two mixed fluids inside a superconductor, each with its own velocity and inertia. The electron condensate behaves like superfluid and is in a completely ordered state (has no entropy). Only a fraction of the total electrons make up this condensate and are represented with  $n_s/n_e$ , where  $n_s$  is the superfluid electron density and  $n_e$  is the total electron density. This fraction equals 0 above and at the transition temperature (a.k.a critical temperature  $T_c$ ) and goes to 1 as  $T \rightarrow 0$ . The rest of the electrons ( $n_n = n_e - n_s$ ) behave as a normal electron gas would. Gorter and Casimir found that the following temperature dependence of  $n_s$  provides a fairly accurate representation of experimental results:

$$\frac{n_s}{n_e} = 1 - \frac{T^4}{T_c^4} \quad . \quad (1.1)$$

The Gorter-Casimir model gives an accurate and simple model for the thermodynamic properties of superconductors, like the jump in specific heat at  $T_c$  and its temperature dependence near  $T_c$ . Another important outcome was the temperature dependence

of  $H_c$ , again near  $T_c$  only.

### 1.2.2 London Equations

The Gorter-Casimir two-fluids model explained the thermodynamics of superconductors but not the electrodynamics. The first phenomenological model for that came from the London brothers (Heinz and Fritz London) who proposed two equations (known as the London equations) [15–17],

$$\vec{\mathbf{E}} = \frac{\partial}{\partial t}(\Lambda \vec{\mathbf{J}}_s) \quad \text{and} \quad (1.2)$$

$$\vec{\mathbf{B}} = -\vec{\nabla} \times (\Lambda \vec{\mathbf{J}}_s) \quad , \quad (1.3)$$

where  $\vec{\mathbf{E}}$  and  $\vec{\mathbf{B}}$  are electric and magnetic fields,  $\vec{\mathbf{J}}_s$  is the superfluid current density

and  $\Lambda = \frac{m}{n_s e^2}$  is a positive material-dependent constant. These two equations can be

combined into one using the definition of the magnetic vector potential ( $\vec{\mathbf{E}} = -\frac{\partial \vec{\mathbf{A}}}{\partial t}$  and  $\vec{\mathbf{B}} = \vec{\nabla} \times \vec{\mathbf{A}}$ ),

$$\vec{\mathbf{J}}_s = -\frac{1}{\Lambda} \vec{\mathbf{A}} \quad . \quad (1.4)$$

Note that Eq. (1.4) has an implicit gauge choice, namely the Coulomb gauge where  $\vec{\nabla} \cdot \vec{\mathbf{A}} = 0$ . A good motivation for Eq. (1.4) comes from quantum mechanics.

The canonical momentum can be written as  $\vec{\mathbf{P}} = (m\vec{\mathbf{v}} + e\vec{\mathbf{A}})$ . In order to get a zero-momentum state the average velocity of the condensate should be:

$$\langle \vec{\mathbf{v}}_s \rangle = -\frac{e}{m} \vec{\mathbf{A}} \quad . \quad (1.5)$$

Given  $\vec{\mathbf{J}}_s = n_s e \langle \vec{\mathbf{v}}_s \rangle$  you get [Eq. \(1.4\)](#). Using [Eq. \(1.4\)](#), Ampere's law ( $\vec{\nabla} \times \vec{\mathbf{B}} = \mu_0 \vec{\mathbf{J}}_s$ ) and the vector identity  $\vec{\nabla} \times \vec{\nabla} \times \vec{\mathbf{B}} = \vec{\nabla} \times (\vec{\nabla} \cdot \vec{\mathbf{B}}) - \nabla^2 \vec{\mathbf{B}} = -\nabla^2 \vec{\mathbf{B}}$  since  $\vec{\nabla} \cdot \vec{\mathbf{B}} = 0$  we get:

$$\nabla^2 \vec{\mathbf{B}} = \frac{1}{\lambda_L^2} \vec{\mathbf{B}} \quad \text{or} \quad \vec{\mathbf{B}}(z) = \vec{\mathbf{B}}(0) e^{-z/\lambda_L} \quad , \quad (1.6)$$

where  $\lambda_L = \sqrt{\Lambda/\mu_0} = \sqrt{\frac{m}{\mu_0 n_s e^2}}$  is the London penetration depth and  $\hat{z}$  is the normal to the surface of the superconductor ( $z = 0$ ). Physically the London equations imply that if a superconductor is exposed to magnetic field, it will generate surface currents which will shield the magnetic field from it's interior. The surface currents are concentrated on a length scale given by the penetration depth  $\lambda_L$ . The temperature dependence of the penetration depth comes from the temperature dependence of  $n_s$  as was introduced in [Sec. 1.2.1](#). As  $T \rightarrow T_c$ ,  $n_s \rightarrow 0$ , hence  $\lambda_L \rightarrow \infty$ , and the superconductor gradually loses it's ability to screen magnetic field. Note that the existence of Cooper pairs was unknown thus the values for mass, charge and number density in the equation of penetration are off by a factor of 2 as I will discuss in [Sec. 1.3](#).



### 1.2.3 Ginzburg-Landau (GL) Theory

In 1950, Soviet physicists Vitaly Ginzburg and Lev Landau proposed a phenomenological model of superconductivity [18]. The starting point of this theory was London's proposal that the superconducting state is a macroscopic coherent quantum state [19]. Both London theory and the Gorter-Casimir model failed to describe the destruction/suppression of superconductivity by currents/magnetic field (While the Gorter-Casimir model incorporates the existence of a critical field  $H_c$ , it can't explain the suppression of superconductivity at fields close to, but lower than,  $H_c$ ). Hence the goal of the GL model was to fix this shortcoming of London theory.

Ginzburg and Landau introduced a complex order parameter  $\Psi(\vec{r})$  which represents the superconducting state. The order parameter is a measure of the local strength of the superconducting state and is defined as  $|\Psi(\vec{r})|^2 = n_s(\vec{r})$  where  $n_s(\vec{r})$  is the superfluid density at position  $\vec{r}$ , as was introduced in Sec. 1.2.1. Near  $T_c$  the thermodynamic free energy density  $\mathcal{F}_{GL}$  can be expanded as a power series in  $|\Psi|$ .

Spatial variations in  $\Psi$  were introduced through  $\frac{\hbar^2}{2m} |\vec{\nabla}\Psi|^2$  and magnetic effects were

included by replacing  $\vec{\nabla} \rightarrow \vec{\nabla} - i\frac{e}{\hbar}\vec{\mathbf{A}}(\vec{r})$  as in the Schrödinger equation,

$$\mathcal{F}_{sc}(\vec{r}) = \mathcal{F}_n(\vec{r}) + \alpha(\vec{r}, T)|\Psi|^2 + \frac{\beta(\vec{r}, T)}{2}|\Psi|^4 + \frac{\hbar^2}{2m} \left| \left( \vec{\nabla} - \frac{ie}{\hbar}\vec{\mathbf{A}} \right) \Psi \right|^2 + \frac{1}{2\mu_0} |\vec{\nabla} \times \vec{\mathbf{A}} - \vec{\mathbf{B}}_a|^2, \quad (1.7)$$

where  $\mathcal{F}_{sc}$  is the free energy density of the superconducting state,  $\mathcal{F}_n$  is the free energy density of the normal state and  $\alpha(\vec{r}, T)$  and  $\beta(\vec{r}, T)$  are the temperature ( $T$ ) and position-dependent phenomenological expansion parameters,  $\vec{A}(\vec{r})$  is the magnetic vector potential,  $\vec{B}_a = \vec{B}_a(\vec{r}, t)$  is the externally applied magnetic field, and  $i = \sqrt{-1}$ . The GL equations can be obtained by minimizing the thermodynamic free energy density Eq. (1.7). This procedure is outlined in great detail in Sec. 7.1.1. In the GL model the superfluid current is given by [20]:

$$J_s = \frac{e^2}{m} |\Psi|^2 \left( \frac{\hbar}{e} \vec{\nabla} \theta - \vec{A} \right), \quad (1.8)$$

where  $\theta$  is the phase of the order parameter. This is the gauge-invariant version of Eq. (1.4).

While the Ginzburg-Landau model was derived as a phenomenological model, in 1959 Gor'kov was able to derive the same equation from BCS theory (to be introduced in Sec. 1.3) in the limit where the temperature is close to the superconducting critical temperature [21] (Described in more detail in Sec. 7.1.2). Due to the simplicity of the GL model, and its ability to analyze inhomogeneous superconductors with defects and interfaces, etc., researchers continue to use it to analyze complex phenomena in superconductors even after the introduction of the BCS theory.

## 1.2.4 Coherence Length

The London equations postulate that the value of the current density at a given point depends on the value of magnetic vector potential  $\vec{A}$  solely in that point. Pippard studied the effect of the mean free path on the London penetration depth and found that the addition of impurities considerably alters the penetration depth without producing a corresponding change in the thermodynamical properties of the material [22]. To account for the effect of mean-free path Pippard introduced the coherence length  $\xi$ , to quantify the length scale over which the superconducting wavefunction  $\Psi$  can vary. Inspired by Chamber's nonlocal generalization of Ohm's law, Pippard proposed the following replacement for Eq. (1.4):

$$\vec{J}_s(\vec{r}) = -\frac{3}{4\pi\xi_0\Lambda} \int_V \frac{[(\vec{r}-\vec{r}') \cdot \vec{A}(\vec{r}')] }{|\vec{r}-\vec{r}'|^4} (\vec{r}-\vec{r}') e^{-|\vec{r}-\vec{r}'|/\xi} d\vec{r}' \quad . \quad (1.9)$$

The coherence length  $\xi$  is related to mean-free-path  $l$  and the coherence length of the pure material  $\xi_0$  through  $\xi^{-1} = \xi_0^{-1} + l^{-1}$ . From the Heisenberg uncertainty principle Pippard estimated the pure material coherence length (usually called Pippard coherence length) to be  $\xi_0 \propto \hbar v_F / k_B T_c$ , where  $v_F$  is the Fermi velocity;  $\hbar$  and  $k_B$  are fundamental constants of nature.

### 1.2.5 Flux quantization

Flux quantization was first predicted by London in 1948 [19], although he had a missing factor of 2 since his prediction preceded the discovery of Cooper pairs (see Sec. 1.3), the electron pairs which are fundamental for superconductivity. The argument is very simple. Consider a closed superconducting ring. The current in any point within the ring is given by Eq. (1.8). The total magnetic flux through the ring can be calculated as follows:

$$\Phi \equiv \int_S \vec{\mathbf{B}} \cdot d\vec{s} = \oint_C \vec{\mathbf{A}} \cdot d\vec{l} = \oint_C \left[ \frac{\hbar}{e} \vec{\nabla} \theta - \frac{m\vec{J}_s}{e^2 |\Psi|^2} \right] \cdot d\vec{l} \quad , \quad (1.10)$$

where  $S$  is a surface that terminates on a closed loop  $C$ . If the contour for the integral is chosen deep inside the superconductor,  $J_s = 0$  and  $\oint \vec{\nabla} \theta \cdot d\vec{l} = 2\pi N$ , where  $N$  is a positive or negative integer, or zero. Hence total flux inside a superconductor has to be quantized in units of  $h/e$ . Later, when BCS theory was published it was thus clear that the charge  $e$  should be replaced by  $e^* = 2e$  due to the charge of a Cooper pair, giving a clear definition for a superconducting flux quantum  $\Phi_0 = h/2e$ .

Flux quantization was shown experimentally in two independent studies by Deaver and Fairbank [23], and Doll and Nabauer [24] both of which were done in 1961. It was the first demonstration of the influence of quantum mechanics on a macroscopic scale.

## 1.2.6 Superconducting Vortices

Right after the introduction of the GL model (Sec. 1.2.3) , one of Landau's students, Alexei Abrikosov, classified superconductors into Type I and Type II based on their response to an applied magnetic field. A type I superconductor completely expels magnetic field until a critical magnetic field  $H_c$  level is reached above which the superconducting state is lost. But when a type II superconductor is subjected to an external magnetic field above its lower critical field  $H_{c1}$ , it enters into the vortex state, and when the magnetic field amplitude reaches the upper critical field  $H_{c2}$ , the superconducting state is lost. The vortex state is a state where a mixture of superconducting

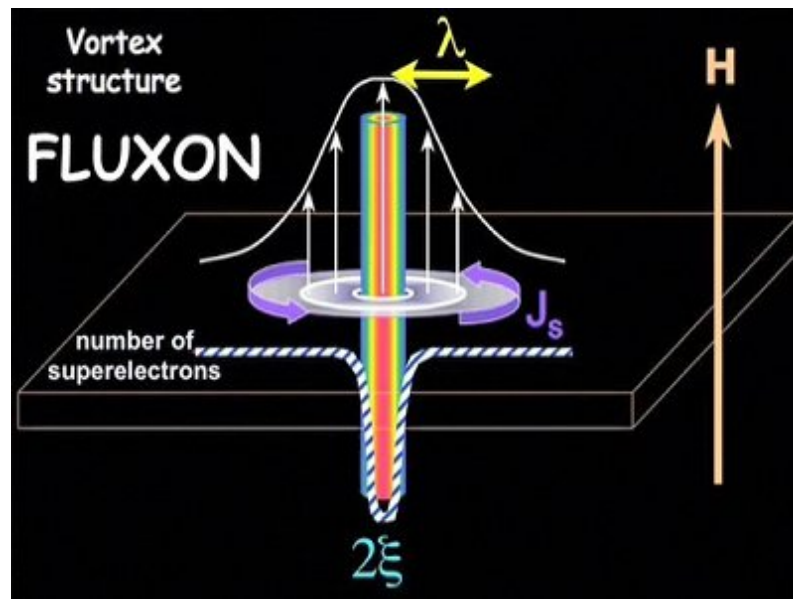


Fig. 1.3 The structure of an Abrikosov vortex in a thin film superconductor under the influence of magnetic field perpendicular to the surface of the film. The order parameter is suppressed in the core which has the size of  $\approx \xi$  and magnetic field penetrates laterally through the superconductor on a length scale  $\approx \lambda$ . The total magnetic flux in a vortex is exactly  $\Phi = \Phi_0$ . The supercurrent flows in the region between the normal core and the rest of the superconductor. Source: Applied Superconductivity and Cryoscience Group, University of Cambridge, Department of Materials Science and Metallurgy [25].

domains and Abrikosov vortices can coexist [26].

An Abrikosov vortex is made up of supercurrent circulating around a normal core (Fig. 1.3). When a superconducting vortex system is subjected to an electric current, it experiences a Lorentz force perpendicular to the direction of the current and magnetic field. The Lorentz force causes the vortex to move, creating an effective friction force due to flux motion [27]. The friction force is associated with quasiparticle excitations in the vortex core due to their interaction with the lattice, and generally increases with vortex velocity [28]. This friction force leads to a finite energy dissipation although the losses can be orders of magnitudes lower when compared to any normal state conductor.

### 1.2.7 The Josephson effect

In 1962, Brian Josephson, who was a graduate student at Cambridge University at the time, published his paper on tunneling between superconductors separated by an insulating barrier [29]. He postulated that since the superconducting state is a quantum state, it should be able to leak Cooper pairs through a thin barrier between two superconductors, resulting in a current which is proportional to the sine of the phase difference between the two superconductors, the effect which was later named "the Josephson effect".

Feynman has provided an elegant discussion of the Josephson effect based on quantum mechanics [11]. Given a junction with complex order parameters  $\Psi_L = |\Psi_L| e^{i\theta_L}$  on the left and  $\Psi_R = |\Psi_R| e^{i\theta_R}$  on the right (as in Fig. 1.4), the two supercon-

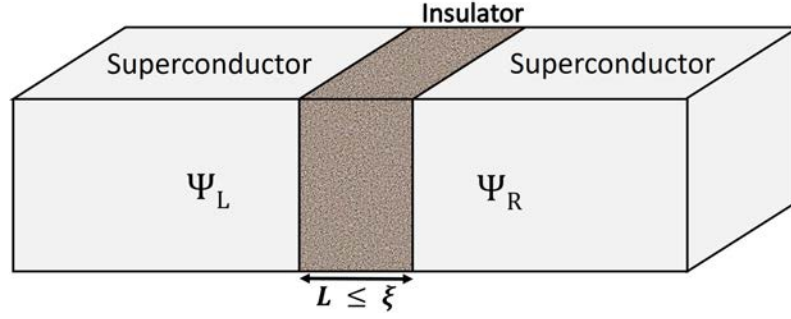


Fig. 1.4 Schematic of a Josephson Junction (JJ): Two superconductors are separated by a thin insulator of thickness  $L \leq \xi$ .

ducting order parameters can be related as follows:

$$i\hbar \frac{\partial \Psi_L}{\partial t} = U_L \Psi_L + K \Psi_R \quad \text{and} \quad (1.11)$$

$$i\hbar \frac{\partial \Psi_R}{\partial t} = U_R \Psi_R + K \Psi_L \quad ,$$

where  $K$  is the coupling constant depending on the geometry of the junction,  $U_L$  and  $U_R$  are the potential energies on two sides of the junction. Setting the phase difference across the junction as  $\delta(t) = \theta_R(t) - \theta_L(t)$  and the potential difference across the junction  $V = (U_R - U_L)/e^*$  one gets the Josephson equations for the current and voltage:

$$J = J_c \sin \delta \quad \text{and} \quad (1.12)$$

$$V = \Phi_0 \frac{\partial \delta}{\partial t} \quad ,$$

where  $J_c = \frac{2K}{\hbar} |\Psi_L| |\Psi_R|$  and K is the coupling constant which depends on the geometry of the junction (area, thickness).

Josephson tunneling is an example of a quantum mechanical phenomena of "tunneling through a potential barrier" on a macroscopic scale, hence it is a "macroscopic quantum effect". The discovery of JJs is as revolutionary as the invention of transistors was in semiconductor technology. Combining two or more JJs in a loop creates a superconducting quantum interference device (SQUID) which is one of the most sensitive magnetometers to date. Today JJ's are in the heart of superconducting qubits, the building blocks of superconducting quantum computers, and SQUIDs made of JJs are at the core of superconducting electronics, mainly rapid single flux quantum (RSFQ) devices. Feynman foresaw a future where the usage of quantum mechanics is mainstream, and concluded one of his lectures on superconductivity with the following quote [7]:

*"...this means that the quantum mechanical laws which have been buried in the esoteric works of theoretical physicists who deal only with atoms, must now become the common knowledge of technicians who are going to work with electric circuits and so forth."*

– Richard Feynman

I myself have already reaped the benefits of this technology. As I will mention in [Chapter 3](#), an extremely sensitive magnetometer based on JJs was used to survey the ambient magnetic field *in-situ* inside the dilution refrigerator at mK temperatures.



I will also be using the Josephson effects to model the nonlinear response produced by the weak links on the surface of Nb in [Chapter 6](#).

### 1.3 Bardeen, Cooper and Schrieffer (BCS) Microscopic Theory of Superconductivity

All the theories described in [Sec. 1.2](#) were "phenomenological", i.e. based on a minimum number of assumptions inspired by observed phenomena. The existence of an "order parameter" was postulated, but no microscopic justification was given. For almost 50 years after the discovery of the superconductivity, there was no microscopic theory capable of fully describing it. And it was definitely not for lack of trying, the most renowned physicists of the time, great names in science like Joseph John Thompson, Albert Einstein, Niels Bohr, L'eon Brillouin, Ralph Kronig, Felix Bloch, Lev Landau, Werner Heisenberg, Max Born, and Richard Feynman [[7](#)] have tried to postulate a microscopic theory, but failed [[30](#)]. Einstein famously said [[31](#)]:

*“Given our ignorance of quantum mechanics of composite systems we are far away from being able to convert these vague ideas into a theory.”*

– Albert Einstein

However each of these failed attempts provided an inspiration for the next step.

In 1950 Reynolds *et al.* [[32](#)] and Maxwell [[33](#)] independently studied several isotopes of mercury and found that the critical temperature  $T_c$  is a function of the

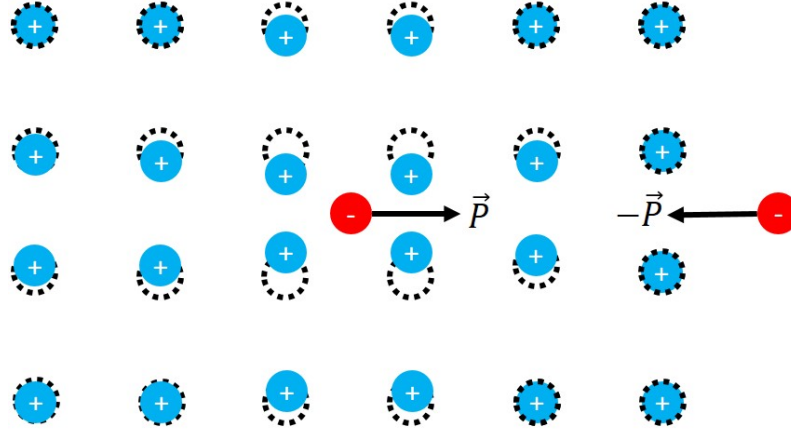


Fig. 1.5 An electron (red circle ●) moving through the ion lattice (blue circle ● with + signs) distorts the lattice. Because of the slow ion dynamics the distorted lattice then attracts the second electron moving in the opposite direction later in time, resulting in net attractive electron-electron interaction.

atomic mass  $M$ , with the lighter isotopes having higher critical temperatures  $T_c \propto M^{-1/2}$ . It was clear that any microscopic theory should include the effect of the lattice.

Bardeen and Pines studied the role of electron-electron interactions in determining the electron-phonon interaction in metals [34]. They found that there could exist a weak attractive phonon-induced interaction between electrons. If we put it simply, when an electron moves through the lattice, it would deform the lattice, by attracting positive ions. When the second electron passes through the lattice, it would be attracted to ions in the deformed lattice, resulting in net attraction between electrons Fig. 1.5. This is referred to as a retarded interaction.

In 1956, Cooper showed that if the interaction between two electrons near the Fermi level is attractive, and that interaction is considered on the background of the Fermi sea, those electrons can form a bound state, no matter how weak that interaction force is [35, 36]. The bound state means that the total energy of two electrons is

smaller than the energy of two independent free electrons, thus these electrons are bonded together in a pair, usually referred to as Cooper pair. The Cooper pair is the central ingredient of BCS Theory.

The next step in the development of the BCS theory came from Bardeen's student Schrieffer, who found the right wave function to describe the superconducting state. Now all ingredients were ready for the development of one of the most outstanding intellectual achievements in theoretical physics, the BCS theory.

According to BCS, electrons in the superconducting state form into Cooper pairs and condense into a coherent ground state. This behaviour is very similar to the behaviour of Bosons, but the onset starts at the critical temperature  $T_c$ . The ground state of the condensate and the energy of the quasiparticle excitation states with the lowest energy are separated by  $2\Delta_{BCS}$ , where  $\Delta_{BCS}$  is the BCS energy gap, which can be computed from the self-consistent gap equation

$$1 = \nu(0)V_{eff} \int_0^{\hbar\omega_D} \frac{d\epsilon}{\sqrt{\epsilon^2 + \Delta_{BCS}^2}} \tanh\left(\frac{\sqrt{\epsilon^2 + \Delta_{BCS}^2}}{2k_B T}\right), \quad (1.13)$$

where  $\nu(0)$  is the density of states (DOS) at the Fermi Energy,  $V_{eff}$  is the interaction potential (which is assumed to be constant) that creates Cooper pairs and  $\omega_D$  is the Debye frequency (cutoff frequency for the lattice vibrations). At  $T = 0$  Eq. (1.13) can be solved analytically,

$$\Delta_{BCS}(0) = \frac{\hbar\omega_D}{\sinh\left[1/\nu(0)V_{eff}\right]}. \quad (1.14)$$

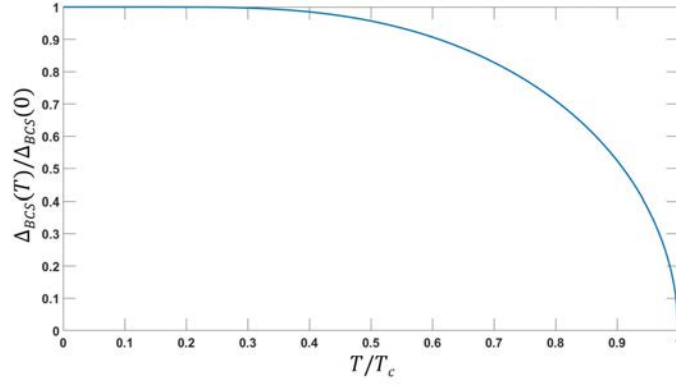


Fig. 1.6 The temperature dependence of BCS superconducting gap  $\Delta_{BCS}$  calculated from Eq. (1.13).

Clearly, the energy gap is related to the electron-phonon interaction, but not in a form that could be expanded in a power series, hence the perturbation theory that was used by many others failed.

The zero temperature BCS energy gap  $\Delta_{BCS}(0)$  can be related to the critical temperature  $T_c$  as follows:

$$\Delta_{BCS}(0) = 1.764k_B T_c \quad . \quad (1.15)$$

These results are universal (independent of material), but are derived under the weak-coupling approximation, i.e.  $\nu(0)V_{eff} \ll 1$ . Nevertheless, many materials have been experimentally tested to have  $\Delta_{BCS}(0)/k_B T_c$  ratio close to 1.764. The temperature dependence of the BCS gap is plotted in Fig. 1.6 and can be best approximated as

$$\Delta_{BCS}(T) \approx 1.74\Delta_{BCS}(0) \left(1 - \frac{T}{T_c}\right)^{1/2} \quad \text{near } T_c.$$

In reality BCS theory is very simplistic because it doesn't include much of the

details of a material's properties. In order to work with real materials, like Nb, one has to account for strong-coupling effects, which will result in slight modifications of the BCS equations. The strong coupling effects can be included in theory through the electron-phonon spectral function  $\alpha_\omega^2 F(\omega)$  which can be obtained from tunneling experiments. The spectral function  $\alpha_\omega^2 F(\omega)$  contains the essential information related to the electron-phonon coupling and characterizes the scattering of quasiparticles that is mediated by the exchange of a phonon with energy  $\hbar\omega$ . One of the proposed equations for the ratio of the order parameter to the critical temperature was derived by Mitrovic, Zarate and Carbotte [37] as follows:

$$\frac{2\Delta_{BCS}(0)}{k_B T_c} = 3.53 \left[ 1 + 12.5 \left( \frac{k_B T_c}{\hbar\omega_{ln}} \right)^2 \ln \left( \frac{\hbar\omega_{ln}}{k_B T_c} \right) \right], \quad (1.16)$$

where  $\frac{k_B T_c}{\hbar\omega_{ln}}$  is an indication of coupling strength and  $\omega_{ln}$  is the averaged phonon frequency:

$$\omega_{ln} \equiv \exp \left[ \frac{\int_0^\infty \frac{d\omega}{\omega} \alpha_\omega^2 F(\omega) \ln(\omega)}{\int_0^\infty \frac{d\omega}{\omega} \alpha_\omega^2 F(\omega)} \right]. \quad (1.17)$$

## 1.4 Applications

Superconductor technology is widely used in industrial applications where high current and low loss are required. With technological advancements in the fabrication of high-quality superconducting materials and significant reduction in cryocooler prices, superconductor-enabled devices like magnetic resonance imaging (MRI), high performance microwave and radio frequency (RF) filters, low-noise and quantum-limited amplifiers, or fast digital circuits based on rapid single flux quantum (RSFQ) logic devices became feasible [[38](#), [39](#)].

Another useful large-scale application of superconductors can be seen in particle accelerators. Extremely low losses in superconducting radio frequency (SRF) cavities allows one to use them to accelerate particles in continuous wave (cw) mode, rather than using copper cavities which are used in pulsed mode. SRF cavities will be discussed in great detail in [Chapter 2](#).

# 2

---

## Superconducting Radio-Frequency Cavities

---

### 2.1 The International Linear Collider

The biggest discovery in particle physics in the last decade was the discovery of the Higgs boson [40–42], a particle named after Peter Higgs who received the 2013 Nobel Prize in physics "for the theoretical discovery of a mechanism that contributes to our understanding of the origin of mass of subatomic particles". The Higgs boson was the final particle predicted by the Standard Model. The Standard Model of particle physics is the best self-consistent model that encapsulates our understanding of fundamental particles and fundamental forces (except gravity) [43]. However, the Standard Model leaves certain issues of particle physics (for example dark matter, the excess of matter over antimatter) unaddressed [44, 45].

The Higgs boson has a central role in the Standard Model and is responsible for the generation of the masses of all elementary particles [46]. The properties of the Higgs boson are precisely specified by the Standard Model, hence precise and detailed study of these properties is needed to validate these predictions, or to formulate exten-

sions that would account for any observed discrepancies between the experimentally observed properties and Standard Model predictions.

Currently the Higgs boson is being studied at the Large Hadron Collider (LHC) in Geneva, Switzerland. As the name suggests, it's a collider where protons are accelerated and set to a collision course. In reality, the subconstituents of the proton, quarks and gluons, are colliding. The true initial states of the colliding particles are thus unknown and model-dependent assumptions are needed to analyze the data, resulting in relatively low-precision analysis. Furthermore, there are a lot of Standard Model events in the background that have to be subtracted from the data, which adds to the noise [47].

The proposed International Linear Collider (ILC) is designed as a 200–500*GeV* linear electron-positron collider, both of which are fundamental particles with known properties. The ILC will be able to perform model-independent precise measurements of the Higgs boson's properties. The ILC can also be used to study some unique properties of the Higgs boson, for example one could measure and verify whether it is indeed a zero-spin particle, as the Standard Model predicts [44, 48].

Superconducting TESLA style cavities will be the heart of the ILC [50]. A superconducting TESLA cavity (see Fig. 2.1) is a 9-cell combination of Nb superconducting radio frequency (SRF) cavity resonators each having it's lowest TM mode resonating at 1.3 GHz [51]. These cavities will be kept at 2K by superfluid helium. Electrons will be accelerated via the radio-frequency (rf) electric fields inside these cavities. Approximately 16000 Nb SRF cavities will be employed in the ILC [52, 53].





Fig. 2.1 A superconducting TESLA cavity made from bulk Nb. Source: Fermilab ILC–SRF R&D webpage [49].

## 2.2 Superconducting Radio Frequency (SRF) Cavity

A Superconducting Radio Frequency (SRF) cavity is an rf resonator cell made of superconducting material. For the purposes of this thesis an SRF cavity refers to elliptical cells used in a TESLA cavity, [51] which are best suited for usage in high-energy linear accelerators (linacs) where charged particles move at nearly the speed of light. Nb is the most dominant material used in SRF applications because it has the highest superconducting critical temperature ( $T_c = 9.3K$ ) and super-heating field ( $B_{sh} \approx 240mT$ ) among the elemental superconductors at ambient pressure, while being a good heat conductor at typical SRF operating temperatures [54].

During normal operation an SRF cavity is subjected to high rf magnetic field parallel to the internal superconducting surface. The highest electric field is along the accelerating axis and the highest magnetic field on the equator of the cylindrical cavity as shown in Fig. 2.2. In a TESLA cavity 9 such cells are combined together and operated in a " $\pi$  mode" where the rf field oscillation phase shift between each adjacent

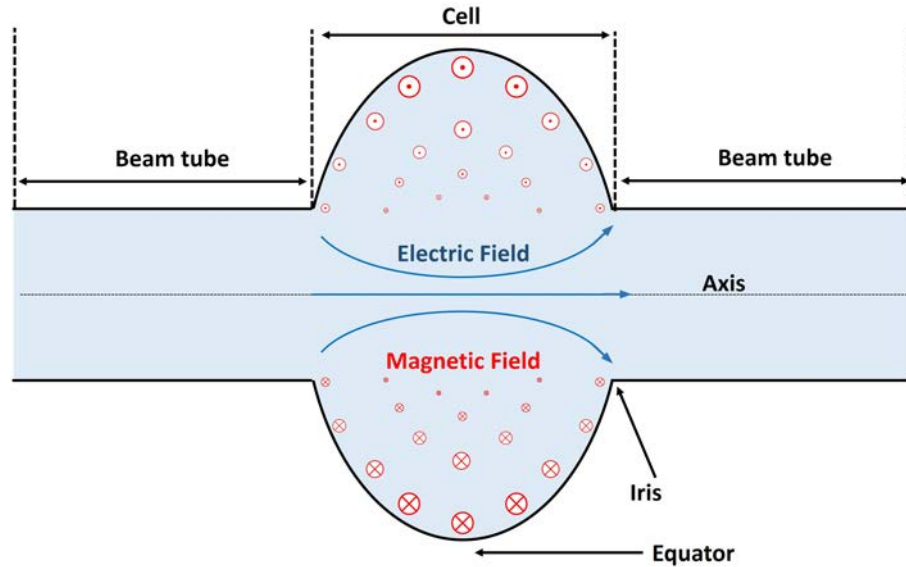


Fig. 2.2 Cross section of a single cell cylindrical Superconducting Radio Frequency (SRF) cavity resonator. The fundamental mode of this resonator corresponds to the case where rf magnetic field amplitude peaks at the equator and the rf electric field amplitude peaks along the symmetry axis of the cavity.

cell is  $\pi$  radians. This allows a charged particle bunch to continuously accelerate.

## 2.3 Surface Resistance

One of the key objectives in SRF cavity operation is to maximize the acceleration while minimizing the dissipated power in the cavities. Unfortunately, in a superconductor only the dc electrical resistance goes to zero. In [Sec. 1.2.1](#), I described the existence of the normal fluid, a portion of the electrons which remain in the normal state. The microscopic theory also describes the existence of some number of unpaired electrons which are called quasiparticles, the amount of which exponentially depends

on temperature, at least ideally. Any rf electromagnetic field will cause dissipation in a superconductor due to the finite inertia of the quasiparticles. For a conventional superconductor with a uniform gap on the Fermi-surface (s-wave superconductor) like Nb, the BCS surface resistance can be approximated at low temperatures as follows [55–57]

$$R_{BCS}(T) \approx \frac{\mu_0^2 \sigma_n \omega^2 \lambda^3 \Delta}{k_B T} \ln \left[ \frac{2.246 k_B T}{\hbar \omega} \right] \exp \left[ -\frac{\Delta}{k_B T} \right], \quad (2.1)$$

where  $\sigma_n$  is the normal state conductivity,  $\omega$  is the frequency of the rf field,  $\lambda$  is the effective penetration depth,  $\Delta$  is the BCS energy gap and  $T$  is temperature. This approximation is valid when  $T < T_c/2$  and  $\hbar\omega < \Delta$ .

Eq. (2.1) indicates that as  $T \rightarrow 0$  the resistance should go to zero exponentially. However, experimental evidence suggests that there is some temperature-independent residual resistance which never goes away, see Fig. 2.3. For this reason it is customary to split the experimentally measured surface resistance into a BCS resistance and a residual resistance,

$$R_s = R_{BCS} + R_{res} \quad . \quad (2.2)$$

This should not be interpreted as if  $R_{res}$  cannot be explained within the framework of BCS, per se, rather it is merely used to quantify the deviation of surface resistance from Eq. (2.1), independent of the physical reasons behind it.

Eq. (2.1) show the BCS surface resistance is proportional to  $\omega^2$  hence one could try to operate at lower frequencies to minimize loss. However, the internal surface

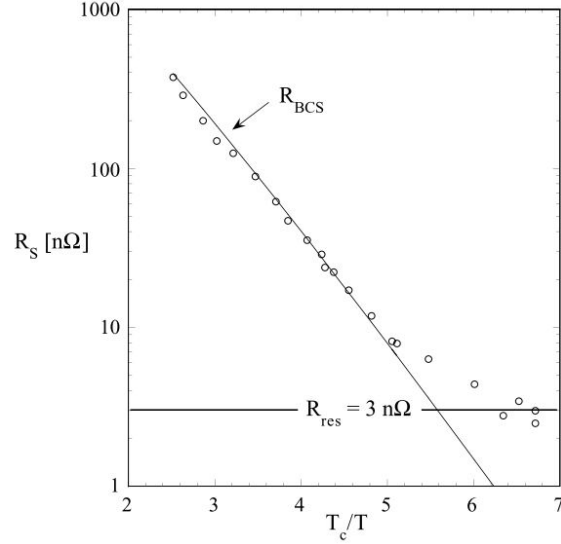


Fig. 2.3 The surface resistance of an SRF cavity at 1.3 GHz frequency as a function of temperature. The  $T \rightarrow 0$  limit shows a saturation of resistance contrary to what is predicted by Eq. (2.1). This figure is reproduced from [51].

area of the cavity ( $A$ ) is inversely proportional to the resonant frequency  $A \propto \omega_{res}^{-1}$ , and  $R_{res}$  is frequency independent, thus at lower frequencies  $R_{BCS} \ll R_{res}$ . To lower the resonant frequency  $\omega_{res}$ , one needs to increase the surface area  $A$ , consequently increasing the total loss. As a result, the optimal resonant frequency range for an SRF cavity is  $f = 0.3 - 3GHz$ .

## 2.4 Q-factor

The dissipation of the cavity is quantified through the "quality factor"  $Q$  defined as the number of rf cycles it takes to dissipate the energy stored in the cavity  $U$ , by a

factor of  $1/e$  [58, p.45]:

$$Q = \frac{\omega U}{P_d} = \frac{\omega \mu_0 \int_V |H(\vec{r})|^2 dV}{R_s \oint_S |H(\vec{r})|^2 ds} = \frac{G}{R_s} , \quad (2.3)$$

where  $P_d$  is the power dissipated in cavity walls,  $\omega$  is the resonant frequency,  $G$  is the geometry constant and the surface integral is taken over the interior surface of the cavity of volume  $V$ . For a 1.3GHz Nb SRF Tesla cavity  $G = 270\Omega$  [51] and given the fact that state of the art SRF cavities regularly reach  $Q > 2 \times 10^{10}$ , it corresponds to about  $R_s(\text{Nb}) = 15n\Omega$  surface resistance at  $T = 2K$ . For comparison the surface resistance of copper at  $T = 2K$  and  $f = 1GHz$  is about  $R_s(\text{Cu}) = 1m\Omega$  [59], which is about  $10^6$  times larger than  $R_s(\text{Nb})$ , demonstrating the superiority of superconducting rf cavities.

## 2.5 Residual Resistance

The residual resistance can be caused by several types of extrinsic sources such as trapped magnetic flux, magnetic impurities, dislocation tangles, non-equilibrium quasiparticles [60] or various types of surface defects. There are some efforts to explain the residual resistance within the framework of BCS theory by attributing it to the existence of sub-gap states due to nonideal surfaces [61]. Also the Fermilab group was able to show that at low powers the cavity loss can be attributed to the existence of two-level-systems (TLS) on the inner surface of the cavity [62, 63], most likely in

the native oxides of Nb.

Specifically, Gurevich and Kubo [64] calculated the surface impedance of a superconductor with a thin dirty layer on the surface. They assumed this dirty layer would broaden the gap peaks in the density of states (DOS) and create subgap states [65]. The Gurevich/Kubo model shows that as a result of gap broadening, the BCS surface resistance no longer has exponential dependence given by Eq. (2.1), even at  $T \ll T_c$ . According to this model, the temperature dependences of surface resistance calculated for different values of  $\Gamma_{Dynes}$ , which parametrizes the smearing of the gap (see Eq. (3.2)), overlap at higher temperatures and show measurable difference only at very low temperatures (see Fig. 3.1). Thus, measurement of Nb SRF cavity surface resistance at very low temperatures is needed to investigate the possible mechanisms responsible for the residual loss. This will be the topic of Chapter 3 where I describe the system I built to measure the surface resistance of SRF cavities down to mK temperatures.

## 2.6 Q-disease

In the early days of SRF research a Nb SRF cavity would be first tested in a vertical stand which could rapidly cool down the cavity, and then later installed horizontally in an accelerator module. It was observed that the quality factor measured in a vertical test and the quality factor measured in the accelerator module would be inconsistent, with the latter being much lossier. This effect is usually referred to as

"Q-disease" [66] by SRF scientists.

It was observed that high purity Nb is more susceptible to Q-disease. Also it was noted that Q-disease could be mitigated if the cavity is warmed up to room temperature and cooled down to cryogenic temperatures rapidly. Halbritter *et al.* performed one of the most consequential experiments: A cavity was cooled down and held at several different intermediate temperatures for 24 hours. It was found that not all intermediate temperatures can cause the Q-disease, but there exists a certain "Danger Zone" corresponding to  $T$  between 75K and 150K (see Fig. 2.4) [67] where the increase in losses occurred. To avoid Q-disease, one must perform rapid cooldown and try to avoid remaining in the danger zone for more than one hour [66].

Current agreement in the SRF community is that hydrogen migration is responsible for the Q-disease. At around  $T = 120K$  hydrogen is very mobile and can diffuse to a distance of about  $0.3mm$  in one hour. Hydride islands thus form near the surface of Nb adding to the surface loss. There are some recent experimental efforts to directly observe the formation of these hydrides [68]. The Q-disease can be avoided if the cavity is baked at  $T = 500 - 900^\circ C$  for several hours. A more detailed overview of the Q-disease is given in Ref. [66]. The Q-disease is of concern to me, because to cool down an SRF cavity to mK temperatures, I mount it inside a dry dilution refrigerator with limited cooling power. Without any modifications, at best, the cooling rate of  $8K/hour$  was achieved in the danger zone. To increase the cooling rate I built a custom liquid nitrogen precooling system that I will discuss in Chapter 3.

## 2.7 Trapped Magnetic Flux

Nb is a type II superconductor and can host magnetic vortices. One way vortices can form is due to the external magnetic field that is trapped during the cool down procedure. Although the cavities are usually shielded from ambient magnetic field, no shielding can produce exactly zero magnetic field. There always exists a small range near  $T_c$  where the ambient field  $H > H_{c2}(T)$ , offering the opportunities for vortices

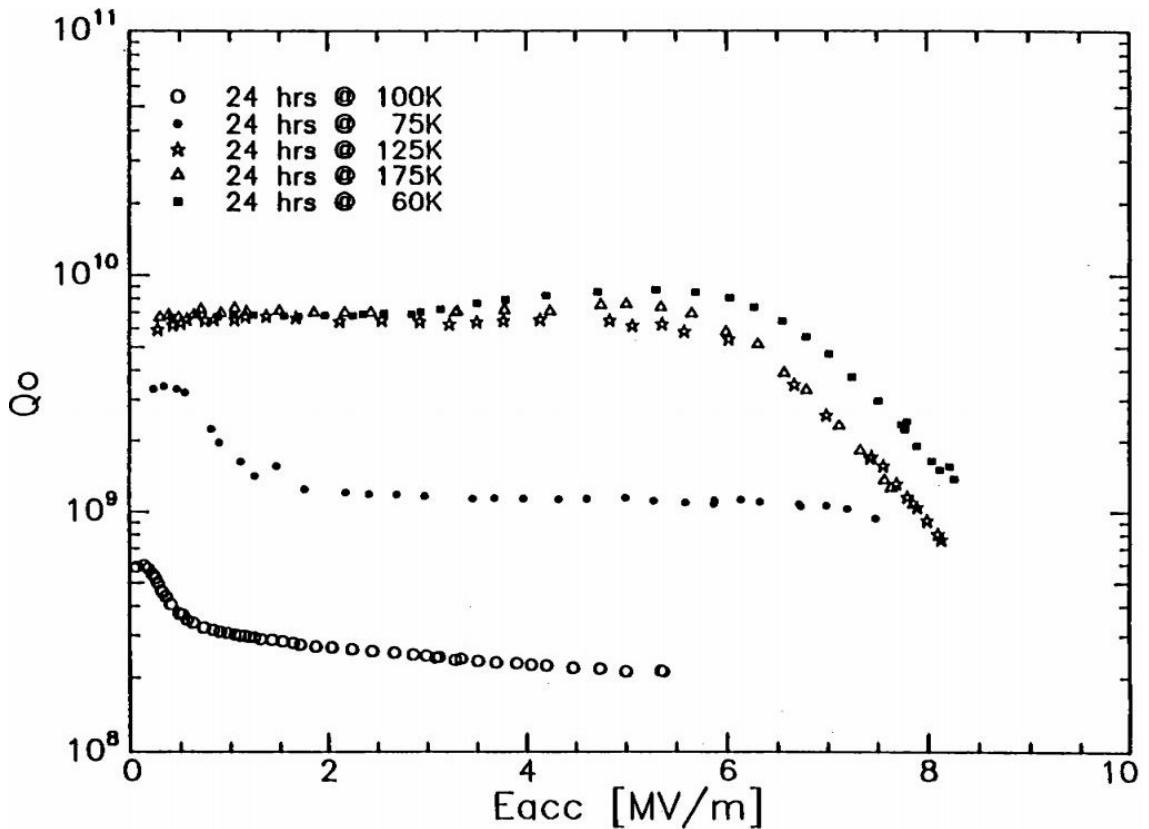


Fig. 2.4 The quality factor as a function of accelerating gradient for a cavity which is held at  $T = 60K$ ,  $T = 75K$ ,  $T = 100K$ ,  $T = 125K$  and  $T = 175K$  for 24 hours and then cooled down for testing. The quality factor of the cavity has severely degraded after being held at  $T = 75K$  or  $T = 100K$ , while holding the cavity at  $T = 60K$ ,  $T = 125K$  or  $T = 175K$  seems to have no effect on the cavity performance. This figure is reproduced from [67].



to form. These vortices can later be pinned due to the impurities within the bulk of the cavity [69, 70] and can cause dissipation when subjected to rf magnetic field [71, 72].

Recent studies have shown that the amount of trapped magnetic flux depends on the rate at which the cavity is cooled down through the critical temperature and the level of the ambient magnetic field [73]. Decreasing the trapped magnetic flux leads to better cavity performance.

## 2.8 Surface Defects and Vortices

Finally, the high-accelerating gradient performance of Nb SRF cavities is often limited by breakdown events below the intrinsic limiting surface fields of Nb. These breakdowns are often caused by point-like surface defects at discrete locations inside the cavity [74, 75]. One limiting scenario is that a surface defect can facilitate the entrance of vortex-semiloops which can lead to dissipation. The same defects can also act as a pinning site for a trapped vortex.

Lately, various optical and other inspection techniques for cavities have been developed. For example, a temperature map of the cavity exterior is taken and hot spots are identified [76, 77]. Then a high-resolution optical image of the cavity interior is taken and pits and other defects are identified [75, 78]. Later, the correlation between defects and hot spots is studied. As an example, a theory that describes the relation between the breakdown field and the geometry of surface pits has been developed

[79].

Currently, studies that focus on elemental composition and purity of the material [80], dc critical magnetic field or superheating field [81], postmortem microanalysis of hot and cold spots [82],[83] or various sophisticated optical inspection tools [75, 78] make up the backbone of SRF material science.

These efforts have resulted in advancements in cavity treatment recipes that have led to SRF cavities with high gradients and high-quality factors  $> 3 \times 10^{10}$  at 1.3 GHz and 2K. Sadly, there is a lack of detailed understanding of the causal links among surface treatments, defects, and ultimate rf performance at low temperatures, and there are many theoretical models being proposed to address the issue [56, 62, 69, 84]. Cavity uniformity will be one of the key requirements of the ILC; thus, the ability to mass produce high-quality SRF cavities and diagnose them rapidly is very important.

Currently, it is not possible to locally and directly probe rf performance of the active interior surface of a cavity at low temperatures. That is why we built a near-field magnetic microwave microscope that can be used to locally characterize the surface in the cryogenic rf regime. The same microscope can also be used to find and classify defects based on their nonlinear response signature. The microscope and the data will be presented in [Chapters 4 and 5](#).

## 2.9 Beyond Nb

There is also interest in looking beyond Nb to superconductors like  $MgB_2$ ,  $Nb_3Sn$  [85] and other superconductor coatings, or the possibility of reducing the cost by using Nb-coated copper cavities. For instance  $Nb_3Sn$  has higher critical temperature than Nb  $T_c(Nb_3Sn) = 18K$ , making it possible to operate accelerators at  $T = 4.2K$  inside ordinary liquid Helium, rather than spending money and effort to get to  $T = 2K$ . While  $Nb_3Sn$  is one of the best candidates to replace Nb in future particle accelerators, currently the progress is limited by surface defects and challenges in cavity fabrication [85].

There is also a proposal to create superconductor/insulator multilayer thin-film coatings with enhanced rf critical fields [86]. However, often it is very costly and/or difficult to build full-size SRF cavities with high-quality versions of these new materials to see if they really are superior. Hence there is a need to quantitatively examine these materials at high frequencies and low temperatures using simpler methods that effectively reproduce the demanding conditions found in operating SRF cavities, yet again demonstrating the need for novel characterization techniques. Both the magnetic microwave microscope that I will introduce in [Chapter 4](#), and the parallel plate resonator that I will introduce in [Chapter 11](#), can be very useful tools for rf characterization of superconductors, without the need to build a fully-functioning cavity.

# 3

---

## SRF Cavity Measurements at mK Temperatures

---

### 3.1 Motivation

There are several hypotheses regarding the origins of residual resistance in Nb SRF Cavities. For example, in a recent article [64] Gurevich and Kubo showed that subgap states in Nb could be responsible for the saturation of the surface resistance at low temperatures.

The superconducting density of states (DOS)  $\nu_s(E)$  for a BCS superconductor is given by [36, p.70]

$$\nu_s(E) = \begin{cases} \nu(0) \frac{E}{\sqrt{E^2 - \Delta^2}} & \text{if } E > \Delta \\ 0 & \text{if } E < \Delta \end{cases}, \quad (3.1)$$

where  $\nu(0)$  is the the DOS at the Fermi energy in the normal state and  $\Delta_{BCS}$  is the BCS energy gap. Eq. (3.1) predicts that there is a singularity at  $E = \Delta_{BCS}$ , and there are no available states to occupy at energies below the superconducting gap. However

I-V curves measured through tunneling experiments into superconductors showed no such singularity. This is because the simple BCS picture does not account for the retarded nature of the electron-electron attractive interaction. The quasiparticles have a finite recombination time, which can be approximately accounted for by adding an imaginary part to the energy  $E \rightarrow E - i\Gamma_{Dynes}$  [65], where  $\Gamma_{Dynes}$  is the phenomenological parameter used as a fitting parameter. The modified equation for  $\nu_s(E)$  is given by the phenomenological Dynes formula

$$\nu_s(E) = \text{Re} \left\{ \nu(0) \frac{(E - i\Gamma_{Dynes})}{\sqrt{(E - i\Gamma_{Dynes})^2 - \Delta_{BCS}^2}} \right\} . \quad (3.2)$$

Eq. (3.2) shows that the singularity in the DOS is now smeared out, and now there are some states available even for  $E < \Delta_{BCS}$ , and these are called the subgap states.

Gurevich and Kubo showed that a finite  $\Gamma_{Dynes}$  value would lead to a nonzero surface resistance even as  $T \rightarrow 0$ . The low temperature surface resistance as a function of temperature calculated for several values of  $\Gamma_{Dynes}/\Delta_{BCS}$  is shown in Fig. 3.1. Note that for  $T > \Delta_{BCS}/8k_B$  the three curves converge, thus one cannot use the experimental data in that range to get a sense of the value of the  $\Gamma_{Dynes}$  parameter. For example, It would be very helpful to know how various surface treatment recipes affect  $\Gamma_{Dynes}$ . Currently SRF cavities are usually tested inside cryomodules filled with superfluid helium. The lowest temperature one can reach there is about  $T \simeq 1.8K$ , which is equivalent to  $\Delta_{BCS}/k_B T \approx 10$ . This is the main motivation for this project, namely to measure the surface resistance of an SRF cavity in the temperature range

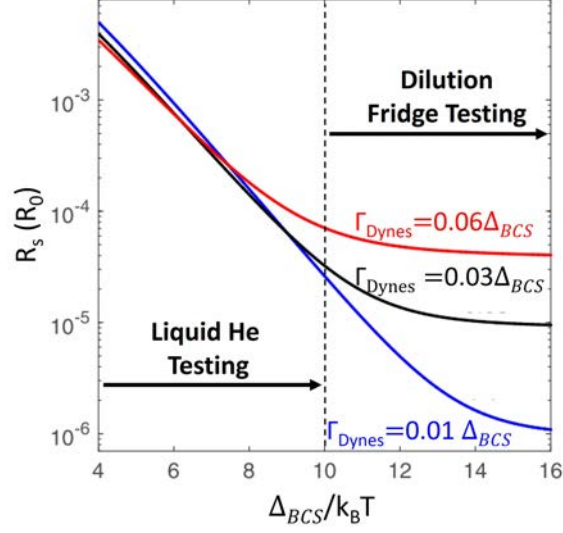


Fig. 3.1 Surface resistance (in units of  $R_0 = \frac{\mu_0^2 \sigma_n \omega \lambda^3 \Delta}{2\hbar}$ ) as a function of temperature calculated for several values of  $\Gamma_{Dynes} = 0.06\Delta_{BCS}$  (red),  $\Gamma_{Dynes} = 0.03\Delta_{BCS}$  (black) and  $\Gamma_{Dynes} = 0.01\Delta_{BCS}$  (blue). The vertical dashed line indicates the lowest temperature accessible in a conventional liquid helium testing. This figure is reproduced from Ref. [64].

that was never probed before.

While our initial motivation for cooling an SRF cavity to mK temperatures was to test the Gurevich-Kubo model, such an investigation is well suited to study a wide range of issues, from the severity of TLS losses in SRF cavities to the nature of residual resistance of Nb<sub>3</sub>Sn cavities. Many theories describing the physical processes in a superconductor are simplified as  $T \rightarrow T_c$  or as  $T \rightarrow 0$ . Having access to both regimes can properly inform theoretical research in the SRF community.

## 3.2 Mounting an SRF cavity in a dilution refrigerator

In a collaboration with Dr. Gianluigi Ciovati (DOE Jefferson Labs) a full scale 2.2 GHz single-cell SRF cavity was installed inside our dilution refrigerator system. The SRF cavity was suspended below the mixing chamber plate of the dilution refrigerator. The base temperature of the mixing chamber plate without heat load is about  $7mK$ .

A  $6'' \times 6'' \times 3''$  rectangular OFHC copper plate was attached to the mixing chamber of the dilution fridge via four  $8''$  long OFHC copper cylinders with  $1/2''$  diameter (see [Fig. 3.2](#)). The thermal conductance of those copper cylinders was supplemented with thermal braids connecting the copper plate to the mixing chamber plates. The plate was cut in two and a  $1.75''$  hole was cut in the center to accommodate the tube of the SRF cavity. The cavity was clamped by this plate, and the two parts of the plates were tightened together to provide maximum thermal connection, see [Fig. 3.2](#). A temperature sensor (Lakeshore Cernox CX-1010) was attached to the equator of the cavity as shown in [Fig. 3.3\(a\)](#).

During the first cool down, it took the cavity 160 hours to reach the base temperature of  $T \approx 700mK$ . This is due to the large heat capacity of the stainless steel (SS) flanges on the ends of the cavity [Fig. 3.3\(a\)](#). With a mass of  $2.18kg$  and heat capacity of approximately  $1J/kgK$  at  $T = 1K$  [87], the SS flanges were responsible for 95% of the total heat capacity of the structure. Additionally, SS has very low thermal conductivity at sub-K temperatures, and this adds to the cooling time. Replacing the original SS flanges with OFHC copper flanges (see [Fig. 3.3\(b\)](#)) reduced the cooling

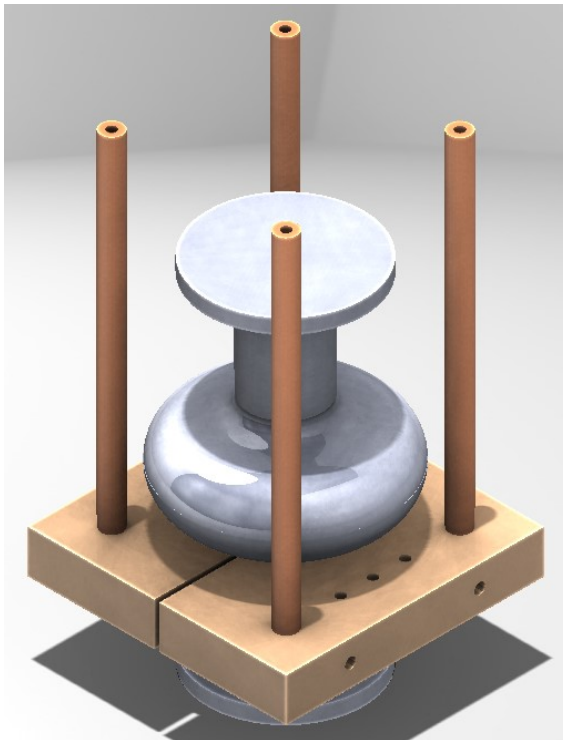


Fig. 3.2 3-dimensional drawing of the 2.2 GHz Nb cavity (silver) and the copper support structure (orange).

time to about 40 hours and the new base temperature at the equator of the cavity was

$$T = 70mK.$$

### 3.3 Liquid Nitrogen Precooling

As was discussed in [Sec. 2.6](#), it is important to cool down the Nb SRF cavity at a rate  $> 1K/min$  through the danger zone ( $75K < T < 150K$ ) to avoid the Q-disease. The rule of thumb is that the amount of time that the cavity temperature spends between 75 K and 150 K should not exceed 1 hour. Even with copper flanges



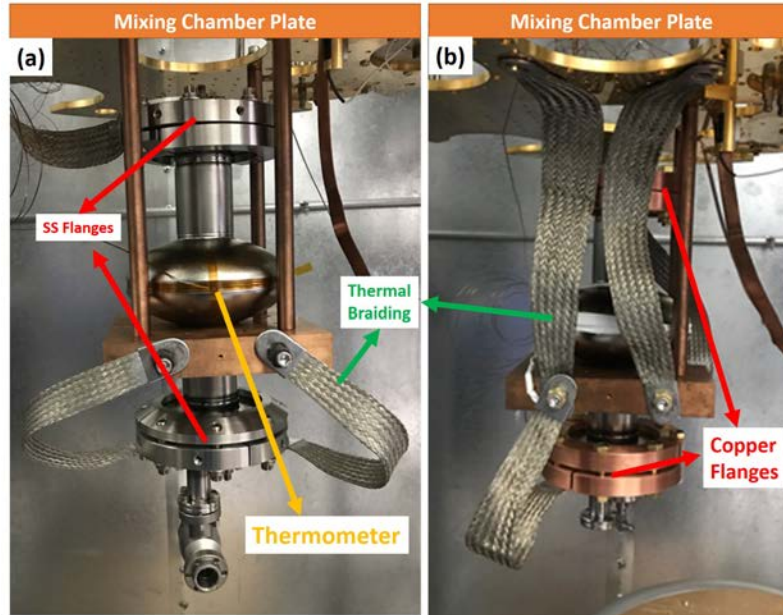


Fig. 3.3 (a) Nb SRF Cavity mounted below the mixing chamber plate of the dilution Fridge. Note the stainless steel flanges on the Nb cavity. (b) Steel clamps replaced by OFHC Copper equivalents.

and plenty of thermal braiding, the cooling rate observed in our cryostat does not meet this requirement.

A novel liquid nitrogen (LN) system was designed and built to assist with the cooling of the cavity (see Fig. 3.4). LN is supplied to a heat bath via a thin walled SS tube running between the room temperature environment and the mixing chamber plate. The heat bath is manufactured by making a pathway for LN inside a flat OFHC copper disk (Fig. 3.4(d)). The exhaust nitrogen vapor is returned through a second thin walled SS tube. The whole system is installed in an existing DN40 line-of-sight feedthrough inside the dilution fridge.

It is important to make sure that the extra thermal link provided by the LN precooling system does not raise the base temperature of the fridge. For this rea-

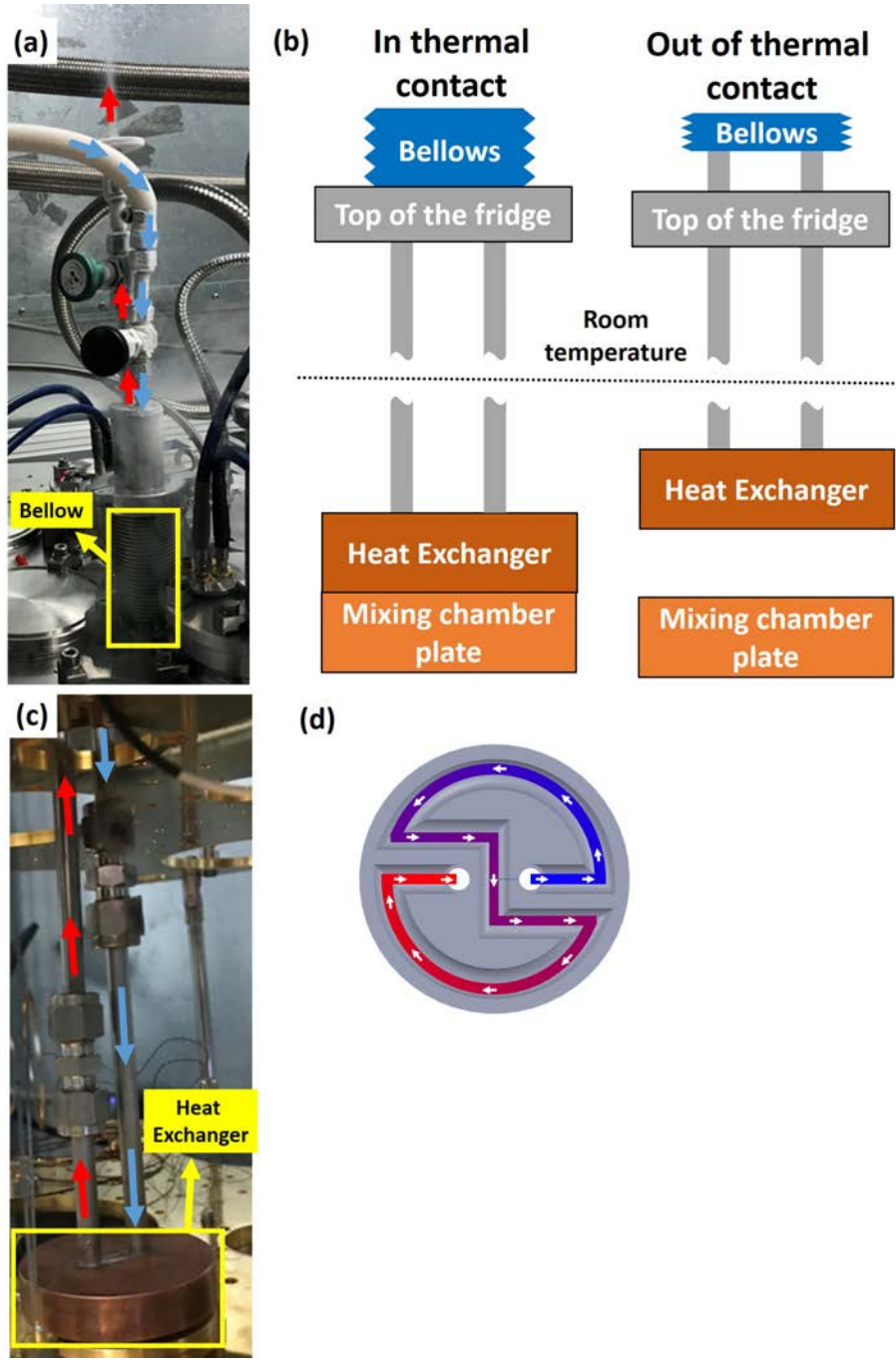


Fig. 3.4 The first generation version of the LN precooling system. (a) The top part of the LN precooling system is supported by a bellows mounted on the top of the cryostat. Blue arrows indicate the path of the cold LN and the red arrows indicate the path of the warmer nitrogen vapour returning from the heat bath. (b) The heat link between the mixing chamber plate and room temperature can be disabled by slightly raising the whole structure. (c) The heat bath rests on the mixing chamber plate and the thermal connection can be broken using the bellows on the top of the cryostat. (d) The cross section longitudinal view of the heat exchanger. The color gradient represent the relative temperature of LN, with blue being cold and red being warm. White arrows indicate the direction of the flow.

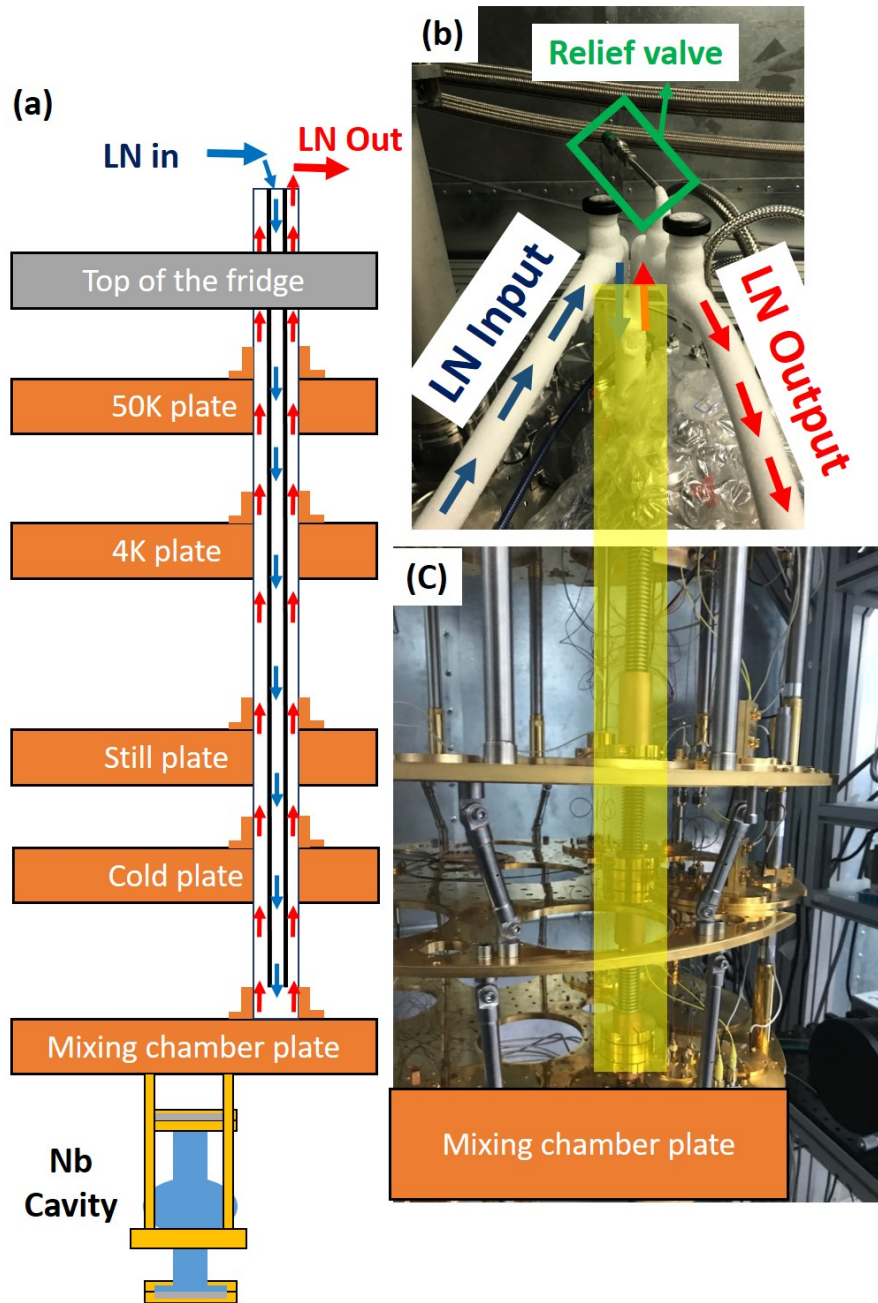


Fig. 3.5 a) Schematic of the LN precooling system (2<sup>nd</sup> generation). LN (blue arrows →) is supplied through the inner tube of 2 coaxial SS tubes and the nitrogen vapour (red arrows →) is extracted via the outer tube. b) Picture of the input and output lines on the top of the cryostat. A safety pressure relief valve is installed in the return path. c) Picture of the LN precooling system (highlighted by a yellow box) inside the dilution fridge.

son, the whole system was mounted on a bellows, and once the cavity temperature reaches  $T = 80K$ , the thermal link between the heat bath and the mixing chamber plate was terminated by slightly lifting the whole structure out of contact with the mixing chamber (MXC) plate using the bellows installed on the top of the refrigerator (see Fig. 3.4(a) and (b)). With this modification the cooling rate was increased by an additional  $5K/hour$ , from  $8K/hour$  to  $13K/hour$  above  $T > 80K$ .

While the extra  $5K/hour$  cooling rate is good progress, it is still below the needed specification of  $1K/min$ . In collaboration with BLUEFORS (the dilution fridge manufacturer) a more advanced version (2<sup>nd</sup> generation) of this system was designed and installed as shown in Fig. 3.5. In the 2<sup>nd</sup> generation of the LN precooling system, the liquid nitrogen is supplied via 2 thin walled coaxial SS tubes. Cold LN is fed from the inner tube, and the warmer nitrogen vapour returns via the outer tube. The outer tube is thermally attached to each stage of the cryostat providing additional cooling power without raising the temperature on the LN on the input line.

Instead of detaching the system from the mixing chamber as was done in 1<sup>st</sup> generation system, two valves are installed on both input and output lines on the top of the cryostat to seal off the system once  $T < 80K$  is reached. Once the base temperature is reached, the residual nitrogen gas inside the system freezes out, hence does not affect the base temperature of the cryostat. The coaxial SS tubes have very low thermal conductance, especially at cryogenic temperatures and do not raise the base temperature. For safety reasons, a pressure relief valve is installed on the output line. The liquid nitrogen was fed to the system at  $30psi$  by pressurizing an LN dewar with nitrogen gas. Also, previously the nitrogen vapour coming out of system was fed

into the room. To avoid the danger of asphyxiation of the people in the lab due to oxygen displacement by nitrogen gas, the outgoing nitrogen gas is now connected to the gas exhaust system available in the lab. Additionally, the room was equipped with oxygen sensors that would set off an alarm if the oxygen content of the air drops too much.

With the 2<sup>nd</sup> generation LN precooling system in the cryostat the cooling rate of the empty cryostat was  $\partial T/\partial t \approx -1K/min$  at the start of the cool down near 200K, see Fig. 3.6(a). When the SRF cavity was mounted on the mixing chamber plate the cooling rate decreased to  $\partial T/\partial t \approx -0.5K/min$ . The overall time required to reach the base temperature was decreased by about 15 hours, from 40 hours to 25 hours. However, as the temperature approached 120K, the extra cooling power from LN diminished and the cooling rate at  $T = 160K$  with the cavity attached was  $\partial T/\partial t \approx -16K/hour$ , see Fig. 3.6(b). As a result the cavity remains in the danger zone for about 4 hours, which is still longer than the requirement imposed by the Q-disease. Perhaps this time can be reduced further by using liquid helium rather than liquid nitrogen as the coolant.

The LN precooling system was able to partially mitigate the risk of having Q-disease in the Nb SRF cavity, however its biggest benefit seems to be the reduction of the required time to reach the base temperature of the cryostat. Especially in labs where rapid cycling between mK temperatures and room temperature is needed, the LN precooling system may be quite useful. The benefit of the LN system becomes clearer when the thermal mass of magnetic shielding and perhaps a superconducting magnet is considered. Also, warm nitrogen gas can be pumped through the LN system

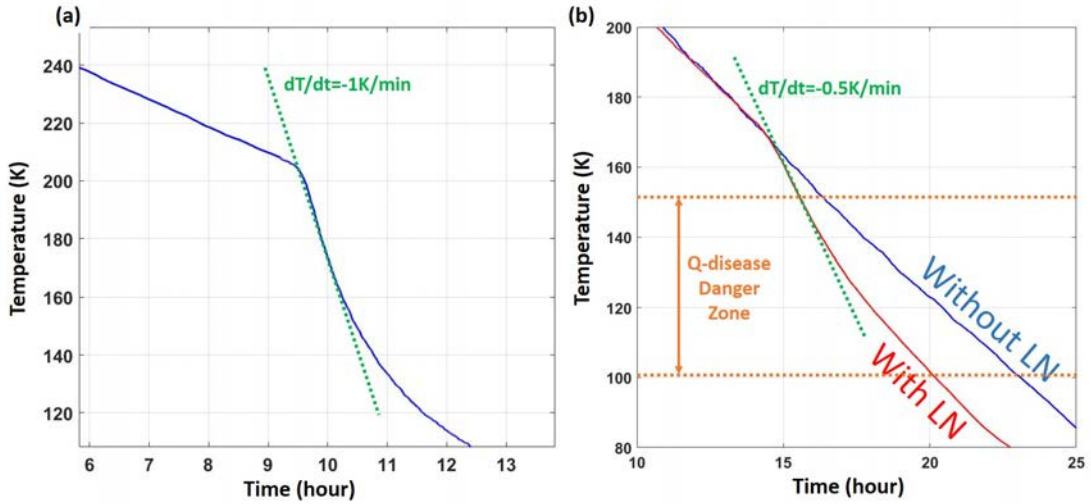


Fig. 3.6 a) The temperature measured at the mixing chamber of an empty cryostat. LN precooling started at  $T = 205\text{K}$  b) The temperature measured at the equator of the cavity vs time when no LN precooling is used (blue) and with LN precooling started at  $T = 160\text{K}$  (red). Time is measured from the moment the cooldown is started.

to speed up the warmup process without contaminating the interior of the cryostat.

### 3.4 Magnetic Shielding

As was discussed in [Sec. 2.7](#), trapped magnetic flux in the SRF cavity can lead to dissipation and increase the total resistance. Therefore it is very important to shield ambient magnetic field from the cavity when it is cooled through  $T_c$ . The ambient magnetic field at the location of the cavity was measured by a Bartington single axis cryogenic magnetometer and found to be  $|\vec{B}| = 200\mu\text{T}$  at room temperature, with the component along the axis of the cavity being the largest ( $B_z = 126\mu\text{T}$ ). This is consistent with the measurements done using the internal magnetic sensors of a cell



phone (Apple, iPhone 7).

Ideally, one should design a small magnetic shield around the experimental setup, and cryoperm is the best candidate for cryogenic applications. However, given the scale of our cavity, the estimated cost ranged between \$10,000–\$20,000 depending on the vendor. Hence we opted for a combination of cheaper solutions.

Three levels of magnetic shielding were used. Firstly a 0.004" thick rectangular Nickel–Iron–Cobalt Alloy foil which has relatively high magnetic permeability was wrapped around the cavity and the support structure (see Fig. 3.7(a)). Secondly, 3 cylindrical  $\mu$ -metal cans were demagnetized and were placed inside the still can (see Fig. 3.7(e)), which is the smallest can of the cryostat. The 3  $\mu$ -metal cylinders are coaxial, open on both ends and are supported by the bottom of the still can. To maximize the attenuation of the magnetic field, the  $\mu$ -metal cans are separated from each other. To avoid the creation of a thermal link between the still plate and the mixing chamber plate, the height of the  $\mu$ -metal is adjusted such that there is a 1cm gap between the top of the can and the bottom of the mixing chamber plate. Lastly, 40 layers of METGLAS 2605SA–1 foil was wrapped around the still can and 20 layers were wrapped around the 4K can of the dilution fridge (Fig. 3.7(b) and (c)). METGLAS [88] is an amorphous metal (glassy metal) that retains high relative magnetic permeability even at cryogenic temperatures [89]. The amount of METGLAS foil need for the whole shielding cost only \$250. Additionally, electric wires were wound around the outermost can of the cryostat (at room temperature) in a Helmholtz-coil fashion (Fig. 3.7(d)) to provide a cancellation field in the vertical direction at the location of the SRF cavity.

The magnetic field was measured *in-situ* using a Bartington single axis cryogenic magnetometer (borrowed from Dr. G. Ciovati at Jefferson Lab) and a custom built Superconducting Quantum Interference Filter (SQIF) Magnetometer [90]. Before the start of the cool down, a dc current was applied to the Helmholtz-coil wires to actively cancel any remnant magnetic field in the vertical direction at room temperature. As the temperature is decreased the value of the magnetic permeability of  $\mu$ -metal and METGLAS foil goes down, reducing their magnetic attenuation factor. Nevertheless, with the combination of passive shielding and active cancellation, the magnetic field at the location of the cavity never went above  $B = 50nT$  level as measured by the cryogenic magnetometer *in-situ*.

However the METGLAS foil introduced a new challenge. With the METGLAS foil mounted on the still can of the dilution refrigerator, the base temperature of the SRF cavity was raised to about  $T = 1.3K$ . The problem was remedied by removing the METGLAS foil from the still can. The METGLAS foil on the 4K can has less effect on the base temperature of the SRF cavity, raising it to about  $T = 250mK$ . In conclusion I can say that the METGLAS foil is an effective yet cheap alternative method to shield ambient magnetic field, but it must be used at higher temperature stages of the dilution fridge.



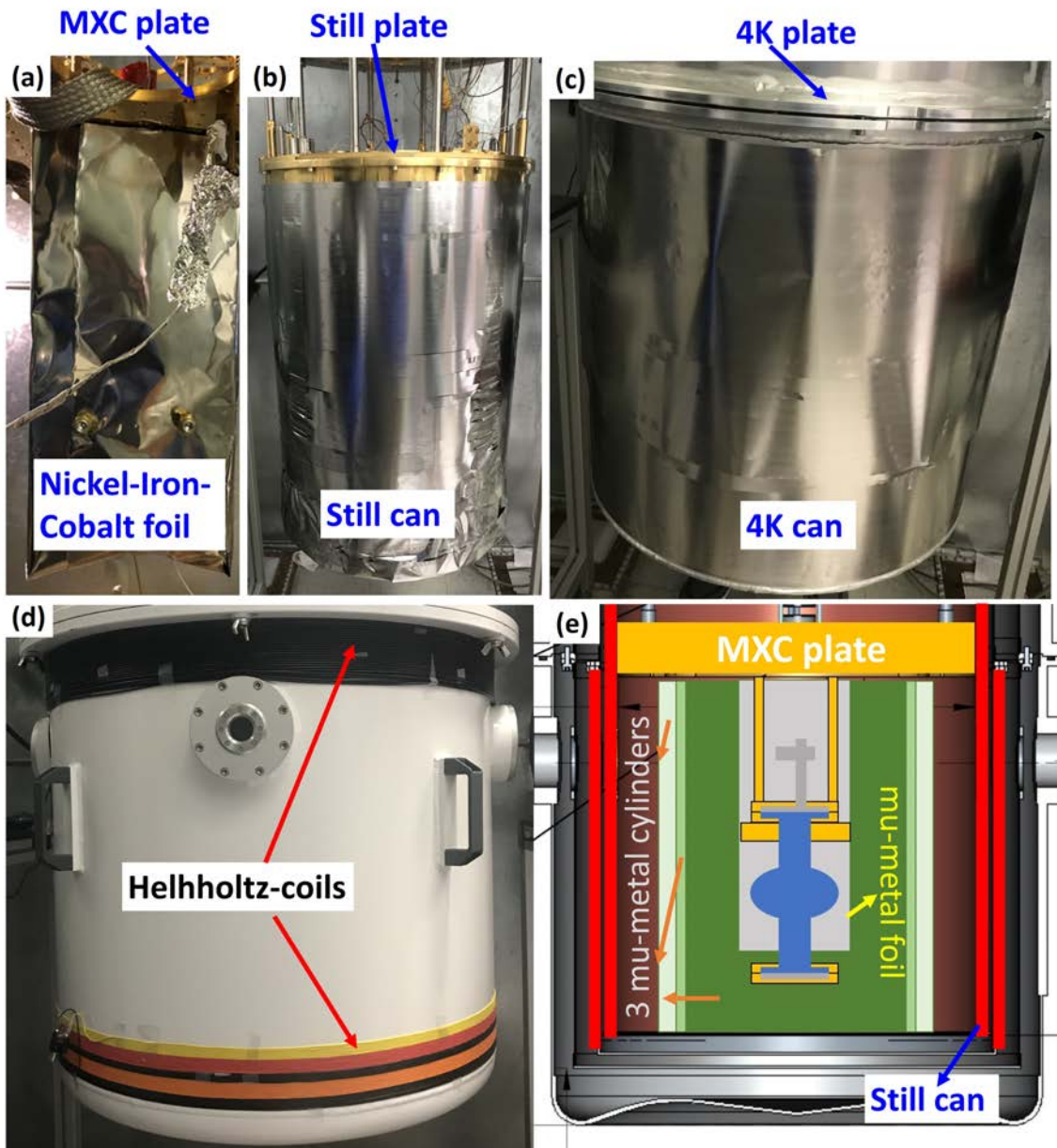


Fig. 3.7 (a) High- $\mu$  alloy metal foil wrapped around the cavity. (b) METGLAS foil wrapped around the Still Can. (c) METGLAS foil wrapped around the 4K Can. (d) Helmholtz-coils for active magnetic field cancellation with the cavity equator positioned at the center of the two coils. (e) Summary of the magnetic shielding shown in a cross-section view of the lower part of the cryostat. Three  $2\text{mm}$ -thick cylindrical  $\mu$  metal shields that are sitting inside the Still can are shown here. Red lines correspond to the location of METGLAS foil.

## 3.5 Phase Locked Loop

At mK temperatures, the expected quality factor of an SRF cavity is  $Q > 2 \times 10^{10}$ , corresponding to a resonance half width full maximum (HWFHM) of about  $\delta f \approx 100\text{mHz}$  given the  $f = 2.2\text{GHz}$  resonant frequency. Conventional network or spectrum analyzers can't accurately detect such sharp resonance. Moreover, cavities are prone to "Lorentz-force detuning". RF fields inside the cavity apply a Lorentz force on surface currents inside the cavity leading to an outward force and a small distortion in the cavity size and shape. Consequently, the resonant frequency of the cavity changes as a function of circulating power. The change in the resonance frequency can be as much as  $\Delta f = 600\text{Hz}$ , much larger than the resonance bandwidth [51]. A resonance locking system is required to accurately measure the quality factor of such a cavity.

The phase locked loop (PLL) is a circuit that is capable of locking a stable microwave (MW) source to the phase of the cavity resonance (see Fig. 3.8 and Fig. 3.9). The basic operation of this circuit is as follows. The MW signal fed into the cavity. The transmitted signal is first amplified by a low-noise amplifier (Low Noise Factory, LNF-LNC2\_6A), then sent through the line stretcher and phase shifter to control the phase, amplified again with a limiting amplifier (MITEQ, AFD4-020040-LM) and mixed with the MW signal coming directly from the source to produce a dc signal that depends on the phase difference between the two MW signals. This dc signal is then low-pass filtered, amplified and connected to the frequency modulation analog input port of the source. To lock to the cavity resonance, frequency modulation is

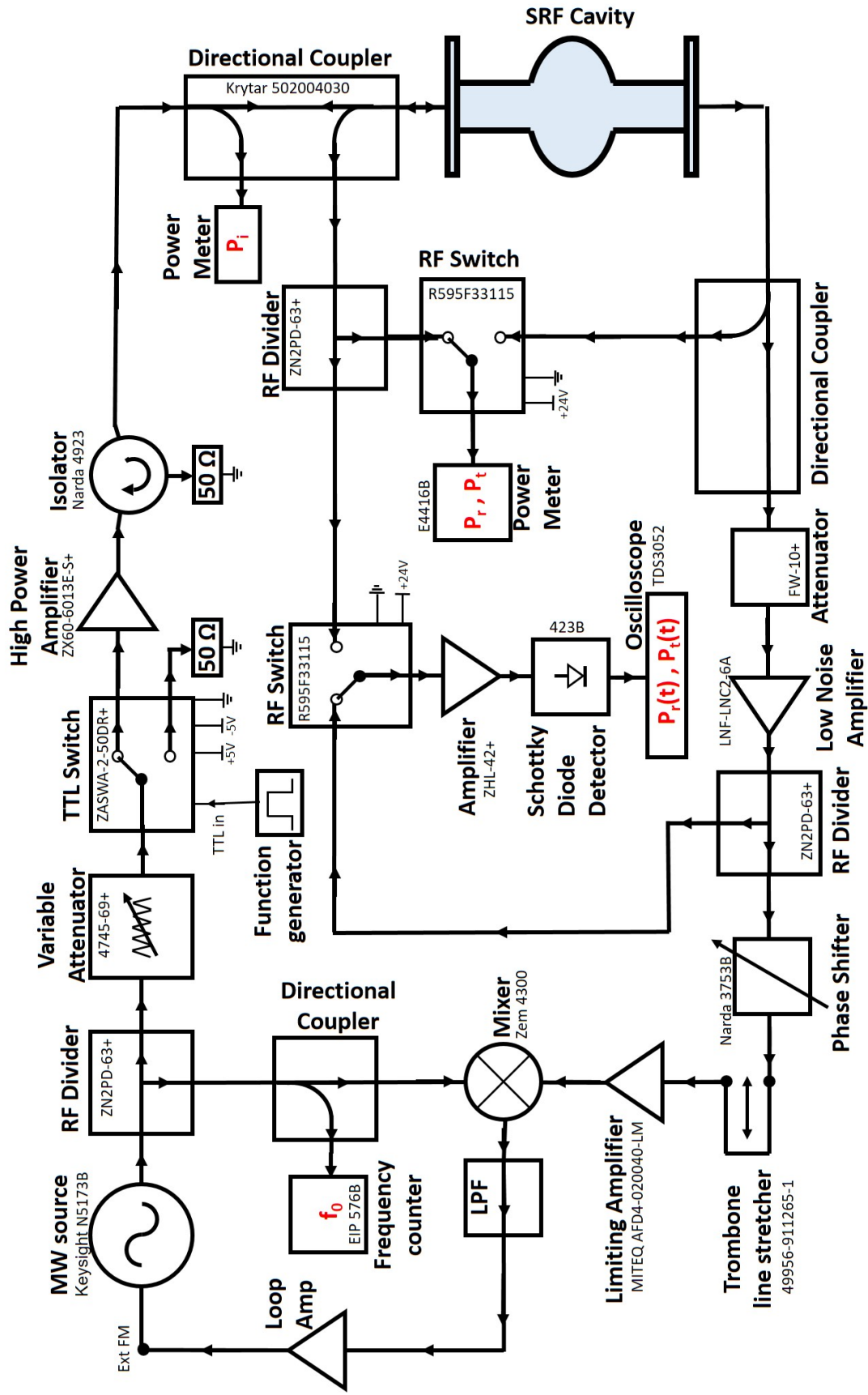


Fig. 3.8 Schematic of the PLL setup. The MW signal from the source and that from the cavity are mixed to produce a dc signal that depends on the phase difference between the two. The signal is amplified and sent to the frequency modulation input of the MW source, providing the feedback needed to keep the frequency of the MW source locked to the resonant frequency of the cavity. Measured quantities are shown in red.

temporarily turned off and the phase shifter is used to adjust the phase such that the feedback voltage is equal to zero. Once the frequency modulation is turned on, the PLL is locked to the resonance. [Table 3.1](#) lists the devices used in the PLL circuit. For a comprehensive discussion on SRF cavity measurements see Refs.[[91](#), [92](#)].

Device	Manufacturer	Model
Microwave Source	Keysight	N5173B
RF divider	Mini-circuits	ZN2PD-63+
Variable attenuator	Narda	4745-69
High Isolation (TTL) Switch	Mini-circuits	ZASWA-2-50DR+
High power amplifier	Mini-circuits	ZX60-6013E-S+
Isolator	Narda	4923
Bi-directional coupler	Krytar	502004030
directional coupler	Narda	
Low noise amplifier	Low Noise Factory	LNF-LNC2-6A
RF divider	Mini-circuits	ZNPD-63-S+
Attenuator	Mini-circuits	FW-10+
Delay line Variable	Dielectric Communications	49956-911265-1
Phase shifter	Narda	3753B
Limiting Amplifier	Miteq	AFD4-020040-LM
Mixer	Mini-circuits	Zem 4300
RF switch	Radial	R595F33115
High gain amplifier	Mini-circuits	ZHL-42+
Schottky diode	Keysight	423B
Function generator	HP	33120A
Power meter	Agilent	E4416B
Frequency counter	EIP	576B
Oscilloscope	Tektronix	TDS3052

Table 3.1 The list of components used in the PLL shown in [Fig. 3.8](#).

The power of the MW source is kept at the same level as the output of the limiting amplifier. The combination of a variable attenuator and a high power amplifier are

used in the input line to adjust the power of the MW signal that goes to the cavity ( $P_i$ ). In my measurements the high power amplifier was never used, because we never achieved the high quality factors that we anticipated. With a lossy cavity, too much MW power applied to the cavity will lead to excessive heating of the cavity.

The PLL circuit is used in two different modes. First, in continuous wave (CW) mode, the steady state value of incident ( $P_i$ ), reflected ( $P_r$ ) and transmitted ( $P_t$ ) powers are measured with a power meter. At the same time the resonant frequency of the cavity  $f_0$  is measured by a frequency counter. In the second mode, a transistor–transistor logic (TTL) signal is generated by a function generator which is connected to the TTL switch. This results in the pulsing of the power applied to the cavity and is referred to as the pulsed mode measurement. Both the reflected power and the transmitted power are amplified and converted to a voltage by using a Schottky diode. These voltages are measured by an oscilloscope that displays the time variation of  $P_r(t)$  and  $P_t(t)$ .

### 3.6 Operating Procedure

Once the cavity is cooled down to the base temperature, the transmission  $S_{21}(f)$  through the cavity is measured with a Keysight (model N5242A) Vector Network Analyzer (VNA). First, the measurements are performed at  $P_i = 0\text{dBm}$  MW power and an IF bandwidth of 500Hz, to detect the resonance peak. Then the 500Hz window around the peak is remeasured with an IF bandwidth of 10Hz. This measurement



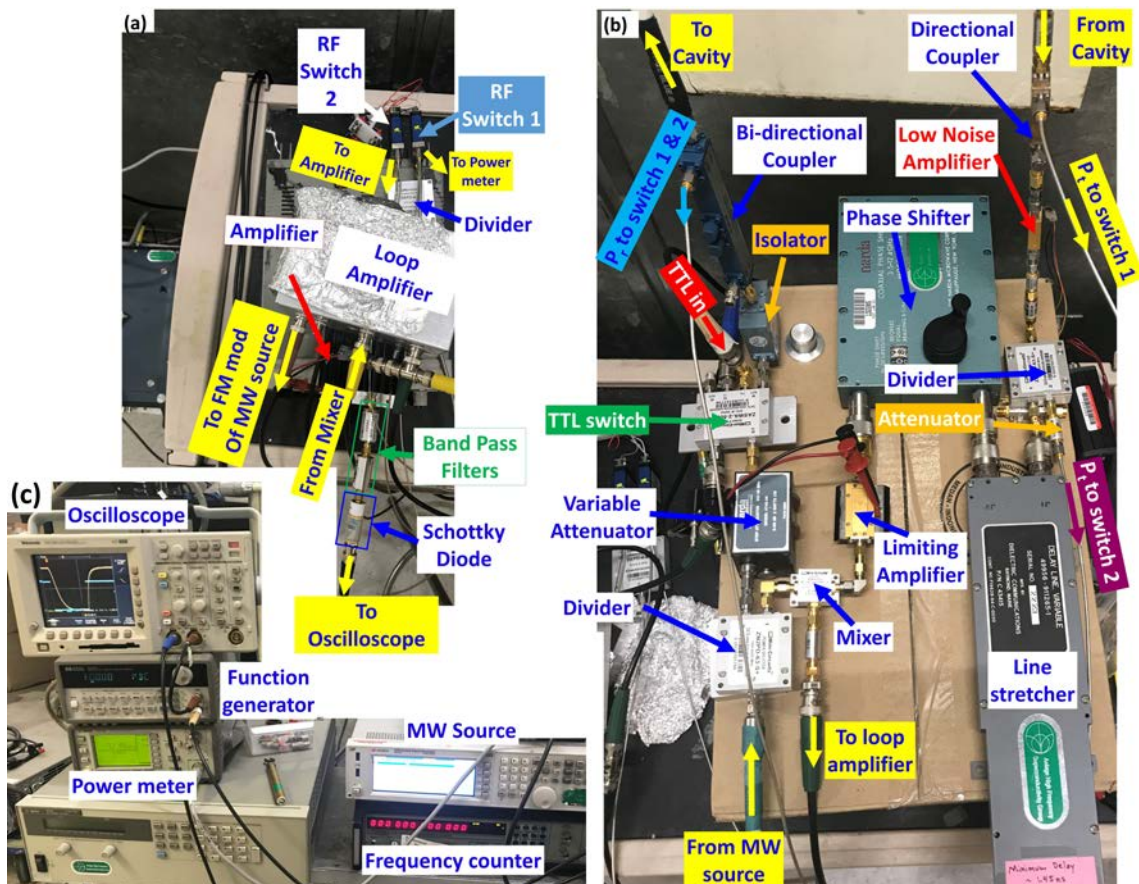


Fig. 3.9 Pictures of the PLL setup. (a) The reflected signal is divided into two and sent to RF Switches 1 and 2. Similarly the unamplified part of the transmitted power coming from the directional couplers is sent to switch 1 and the part of the transmitted power that is amplified by the low noise amplifier is sent to switch 2. The output of switch 1 goes to the power meter, enabling measurement of either transmitted and or reflected power depending on the switch setting. The output of switch 2 goes to the high gain amplifier followed by a Schottky diode. This signal is sent to the oscilloscope to measure the decay time of  $P_t(t)$  and  $P_r(t)$ . The loop amplifier amplifies the output of the mixer and feeds it into the FM modulation port of the MW source. (b) The main circuit of the PLL. The operation is described in the text. (c) Picture of the MW equipment used in the PLL circuit.

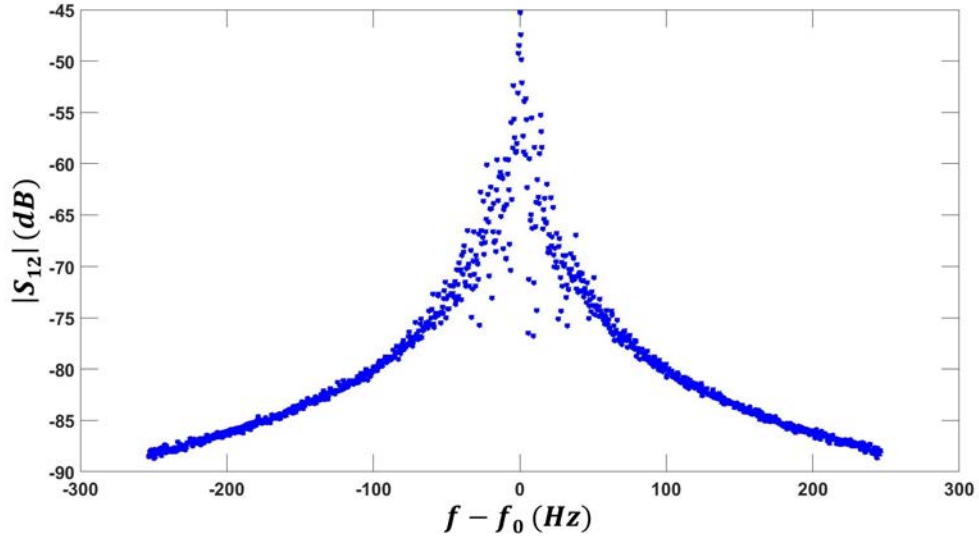


Fig. 3.10 Transmission through the cavity  $|S_{12}|$  as a function of frequency measured by the VNA. The data was taken with an IF bandwidth of 10Hz and 0 dBm applied power. The resonant frequency is  $f_0 = 2,266,858,113\text{Hz}$ .

takes 3 minutes to complete. No averaging was used, as it can increase the noise due to instability of the resonant frequency associated with Lorentz force detuning. Fig. 3.10 shows the  $|S_{21}(f)|$  at  $T = 200\text{mK}$ . Clearly, the expected HWFM is not measurable with the VNA because it is smaller than the 1Hz resolution of the VNA. The peak in  $|S_{21}(f)|$  is used to get an estimate for the resonance frequency  $f_0$ . Afterwards, the PLL circuit is connected to the cavity and locked to the cavity resonance (the locking procedure is described in Sec. 3.5).

The same antennas that are used to drive the cavity can also contribute to the loss. It is important to be able to differentiate between the measured total loss and the losses due to the resistance of the inner surface of the cavity. These losses can be

related through the quality factors

$$\frac{1}{Q_L} = \frac{1}{Q_0} + \frac{1}{Q_{in}} + \frac{1}{Q_{out}} \quad , \quad (3.3)$$

where  $Q_L$  is the loaded quality factor defined as the total energy stored in the cavity  $U$  divided by energy dissipated per cycle and  $Q_0$  is the intrinsic quality factor defined as  $U$  divided by energy dissipated per cycle in the cavity walls only. Here  $Q_{in}$  and  $Q_{out}$  are the quality factors associated with the input and output antennas. It is useful to define a coupling strength of an antenna  $\beta_{in} = Q_0/Q_{in}$  and  $\beta_{out} = Q_0/Q_{out}$ . In an SRF cavity the pickup antenna is weakly coupled, hence  $\beta_{out} \ll 1$ . To measure the intrinsic quality factor  $Q_0$  of the cavity, one first needs to measure the loaded quality factor  $Q_L$ , then one must measure the coupling strength  $\beta_{in}$ .

When the cavity is driven by some CW incident power  $P_i$ , it eventually reaches the steady state where  $U$  and the reflected power  $P_r$  are given by [58]

$$U = \frac{4\beta_{in}P_iQ_0}{(1 + \beta_{in})^2 \omega} \quad \text{and} \quad (3.4)$$

$$P_r = \left( \frac{\beta_{in} - 1}{\beta_{in} + 1} \right)^2 P_i \quad . \quad (3.5)$$

One could simply measure the  $P_r$  and  $P_i$  in the steady state using the PLL (Fig. 3.8), but this would give two different values for  $\beta_{in}$  that satisfy Eq. (3.5), namely  $\beta_{in} =$



$\frac{1 - \sqrt{P_r/P_i}}{1 + \sqrt{P_r/P_i}}$  when the antenna is undercoupled, or  $\beta_{in} = \frac{1 + \sqrt{P_r/P_i}}{1 - \sqrt{P_r/P_i}}$  when the antenna is overcoupled.

If the rf power is suddenly turned off after the cavity reaches its steady state, the transmitted power  $P_t$  should decay exponentially with a decay time proportional to the loaded quality factor  $\tau_d = Q_L/\omega$ ,

$$P_t(t) = P_t(0) \exp\left(-\frac{t}{\tau_d}\right). \quad (3.6)$$

Hence,  $P_t(t)$  can be measured to extract  $Q_L$ . In the PLL circuit this is achieved by installing a fast TTL-driven rf switch (Minicircuits, ZASWA-2-50DR+) on the path of the MW signal going to the cavity (see Fig. 3.8). A function generator is used to drive the switch and pulse the rf power incident on the SRF cavity. The transmitted signal is amplified and fed to a low-barrier Schottky diode detector which converts it to a voltage signal, which is monitored on an oscilloscope. Fig. 3.11(a) shows the transmitted power  $P_t$  as a function of time, as measured by the PLL. The RF power is turned off at  $t_{off} = 0.4s$  and the data is the average over 10 cycles. The decay time  $\tau_d = 197.1ms$  was extracted from the exponential fit to  $P_t(t)$  on a log-log plot. The resonance frequency is measured by a frequency counter to be  $f_0 = 2,266,888,357Hz$ . Given this, the loaded quality factor can be estimated as  $Q_L = 2.8 \times 10^9$ .

Similarly, the time dependence of reflected power  $P_r(t)$  can be used to determine the value of coupling strength  $\beta_{in}$ . In this case one should use data both when the rf power is suddenly turned off after the cavity reached its steady state, and when the rf

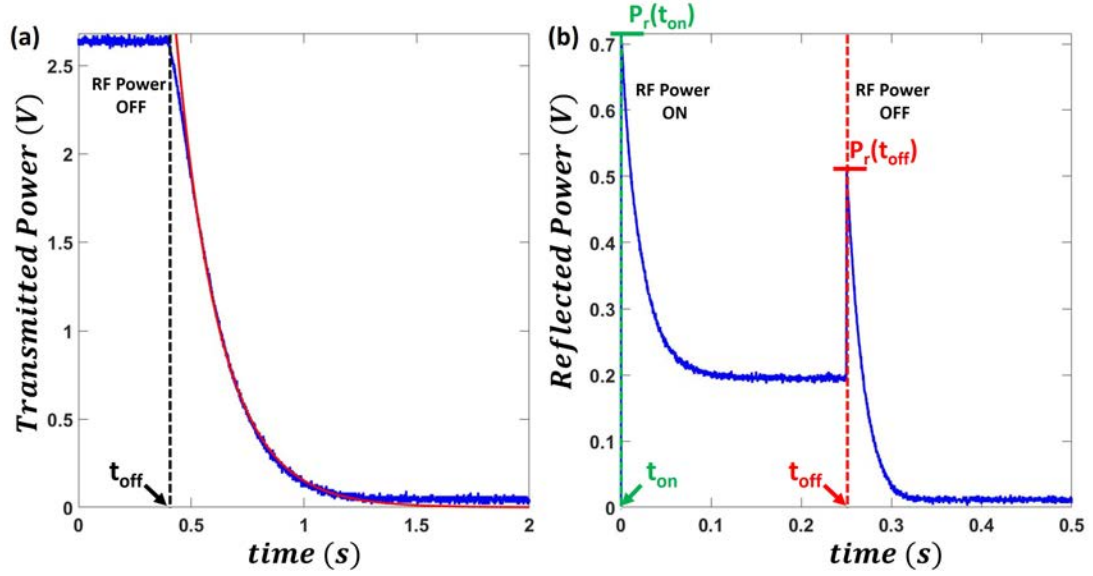


Fig. 3.11 (a) (blue) Transmitted power as a function of time after the input power is turned off. (red) Exponential fit according to Eq. (3.6) with  $\tau_d = 197.1ms$ . The measurement is averaged over 10 cycles. (b) (blue) Reflected power as a function of time. The input power is off for  $t < 0$ . The peak at  $t_{off} = 0.25s$  is smaller than the peak at  $t_{on} = 0$  indicating and that the input antenna is undercoupled ( $\beta_{in} < 1$ ). Dashed lines indicate the moments RF power is turned ON (green dashed line) or turned OFF (red dashed line). Note that a) and b) do not correspond to the same measurement.

power is turned on to a quiet cavity. The time dependence of  $P_r(t)$  is given as follows:

$$P_r(t) = \begin{cases} \left\{ 1 - \frac{2\beta_{in}}{1 + \beta_{in}} \left[ 1 - \exp\left(-\frac{t - t_{on}}{2\tau_d}\right) \right] \right\}^2 P_i & \text{after RF is turned ON } (t > t_{on}) \\ \frac{4\beta_{in}^2 P_i}{(1 + \beta_{in})^2} \exp\left(-\frac{t - t_{off}}{\tau_d}\right) & \text{after RF is turned OFF } (t > t_{off}), \end{cases} \quad (3.7)$$

where we assume that the cavity was in steady state before the MW power was turned

on or off. At  $t = t_{on}$  and  $t = t_{off}$  Eq. (3.7) yields

$$P_r(t_{on}) = P_i$$

$$P_r(t_{off}) = \frac{4\beta_{in}^2 P_i}{(1 + \beta_{in})^2} \quad (3.8)$$

resulting in a simple equation for  $\beta_{in}$

$$\beta_{in} = \frac{1}{2\sqrt{\frac{P_r(t_{on})}{P_r(t_{off})} - 1}} \quad (3.9)$$

So-called perfect coupling is achieved when  $P_r(t_{on}) = P_r(t_{off})$ , which corresponds to  $\beta_{in} = 1$ . According to Eq. (3.5) this corresponds to zero reflected power  $P_r = 0$  in steady state. Fig. 3.11(b) shows the measured  $P_r$  as a function of time, as measured by the PLL. The RF power is turned on at  $t_{on} = 0$  and turned back off at

$t_{off} = 0.25s$ . Here  $\frac{P_r(t_{on})}{P_r(t_{off})} = 1.41$  resulting in  $\beta_{in} = 0.73$ .

In summary, the PLL can measure 6 parameters: the resonant frequency  $f_0$ , the incident power  $P_i$ , the steady state transmitted power  $P_t$ , the steady state reflected power  $P_r$  and the pulsed transmitted and reflected powers  $P_t(t)$ ,  $P_r(t)$  after switching events. The transmitted power  $P_t(t)$  and the resonant frequency  $f_0$  are used to calculate the loaded quality factor  $Q_L$ . Usually the pulsed reflected power  $P_r(t)$  is used to evaluate whether the antenna is undercoupled or overcoupled and the steady state reflected power  $P_r$  is used to calculate  $\beta_{in}$ , the  $P_r(t)$  data measured using a Schottky

diode is noisier than the steady state  $P_r$  which is measured using a power meter. Once  $Q_L$  and  $\beta_{in}$  are known, the intrinsic (sometimes called the unloaded) quality factor of the cavity is given as  $Q_0 = Q_L(1 + \beta_{in})$  (assuming  $\beta_{out} \ll 1$ ). Finally, the accelerating gradient  $E_{acc}$  that electrons would experience in an SRF accelerator is calculated using

$$E_{acc} = k_e \sqrt{4\beta_{in}Q_L P_i / (1 + \beta_{in})} \quad , \quad (3.10)$$

where  $k_e$  depends on the resonant mode, the shape of the cavity, and number of cells.  $k_e$  is numerically calculated using computer simulations.

### 3.7 Summary of the measurements

The result of all SRF cavity measurements with the PLL circuit is summarized in [Table 3.2](#). First, an untreated 2.2GHz SRF cavity was sent to us from Jefferson Lab. It was used to test the support structure, test the liquid nitrogen precooling system and the PLL. It was characterized on Aug 14, 2018 and then sent back to Jefferson Lab (JLab) for surface treatment. Dr. G. Giovati cleaned the cavity and measured it in a liquid helium dewar (on Oct 10, 2018) before sending it back to us. A subsequent measurement (Oct 23, 2018) at UMD showed that the quality factor is drastically lower than the reference value obtained at JLab.

Date	Location	Magnetic Shielding	Active field cancellation	$T(K)$	$f_0(Hz)$	$\tau_d$ (ms)	$\beta_{in}$	$Q_0$
Aug 14, 2018	UMD	High $\mu$ alloy	OFF	0.2	2,267,283,812	21.35	0.73	$5.26 \times 10^8$
Oct 10, 2018	JLab	$\mu$ -metal can	ON	1.37	2,266,975,938	1222	3.596	$8 \times 10^{10}$
Oct 23, 2018	UMD	High $\mu$ alloy	OFF	0.8	2,266,858,114	193.25	< 0.034	$< 2.84 \times 10^9$
Nov 20, 2018	JLab	$\mu$ -metal can	ON	1.76	2,266,907,984	647	1.095	$1.93 \times 10^{10}$
Jun 25, 2019	UMD	High $\mu$ alloy +3 $\mu$ -metal cans	partially ON	0.35	2,266,888,357	197.1	too small to measure	$\approx 2.74 \times 10^9$
Sep 9, 2019	UMD	2 $\mu$ -metal cans +Metglas	ON	1.3	2,266,852,632	5.86	too small to measure	$\approx 8.35 \times 10^7$
Sep 16, 2019	UMD	2 $\mu$ -metal cans +Metglas	ON	0.8	2,266,848,408	10.57	too small to measure	$\approx 1.51 \times 10^8$
Sep 17, 2019	UMD	2 $\mu$ -metal cans +Metglas	OFF	0.8	2,266,848,412	9.96	too small to measure	$\approx 1.42 \times 10^8$
Nov 18, 2019	UMD	3 $\mu$ -metal cans	On	0.07	2,266,826,434	15.3	too small to measure	$\approx 2.18 \times 10^8$

Table 3.2 Summary of the 2.2GHz elliptical Nb SRF cavity measurements at UMD and JLab.

During the test at JLab, the input antenna was tuned to match the anticipated quality factors of  $Q > 8 \times 10^{10}$ . By definition  $\beta_{in} = Q_0/Q_{in}$  and a lossy cavity like ours will lead to a very small value of  $\beta_{in}$ . Eq. (3.7) suggests that  $\lim_{\beta_{in} \rightarrow 0} P_r(t_{off}) = 0$ . This makes any measurement of  $\beta_{in}$  from time decay of reflected power  $P_r(t)$  impossible.

Two possible explanations for the low Q-value that I measured were identified, the Q-disease, or a large ambient magnetic field in the UMD lab. The cavity was sent back to JLab where it was remeasured (Nov 20, 2018). In this measurement, the cavity was kept in the danger zone for Q-disease, 80-100 K for 16 h prior to final cool-down and rf test, and it was shown that the quality factor is close to the reference value, measured on Oct 10, 2018. Meanwhile, at UMD, we continued improving the magnetic shielding, as discussed in Sec. 3.4.

On Jun 25, 2019, the cavity was tested with additional  $\mu$ -metal cans used for shielding, however at the time we did not have a reliable *in-situ* magnetometer to precisely measure the magnetic field at the cavity under cryogenic conditions. A cryogenic fluxgate magnetometer was later borrowed from JLab and the METGLAS shielding was characterized, as was discussed in Sec. 3.4.

Several measurements performed in September, 2019 showed that the cavity had degraded to pre-treatment conditions (similar to the August, 2018 results). A possible breach of the cavity vacuum was suspected. The cavity was next pumped down using a standard turbo-molecular pump (Agilent V301). A measurement on November 18, 2019 showed that the evacuation slightly increased the Q.

Lastly, the cavity was taken to the Laboratory for Physical Sciences at UMD to check for leaks using an ion pump. With the help of Dr. Christopher J. Richardson and

Dr. Alan Kramer, the cavity was pumped down and then left with its pumping valve sealed for several days. When the valve was reopened enough pressure had built up inside the cavity to saturate the ion-pump, confirming the vacuum leak hypothesis.

Overall, a LN precooling system was successfully built and tested. An effective, yet inexpensive magnetic shielding solution was implemented. A PLL circuit was utilized to measure a quality factor of  $Q_0 = 2.74 \times 10^9$ . The setup is ready for a full scale cavity testing at mK temperatures, but repairs to the cavity are needed before proceeding with further measurements.

# 4

---

## Magnetic Microwave Microscopy

---

### 4.1 Overview of Scanning Probe Microscopy

*-what is the Universe made of?*

For thousands of years philosophers and naturalists alike tried to find the answer to this question. In fact, approximately 2500 years ago, the Greek philosopher Democritus postulated the existence of small indivisible building blocks of matter that he called "*atomos*"-uncuttable/indivisible. About 2000 years later, the microscope was invented in Europe and was used to study biological matter. At first, the resolution of a microscope was limited by its design and the quality of the lens used, before a fundamental limit was reached, namely the diffraction limit. The light from two points which are separated by the distance smaller than half the wavelength of the light cannot be distinguished, introducing a  $\approx 200nm$  resolution limit for an optical microscope. Electron Microscopes exploit this limit by using electrons instead of visible light, since their De Broglie wavelength can be in the picometer range.

In 1982, Binnig *et al.* introduced a new approach to microscopy, the scanning



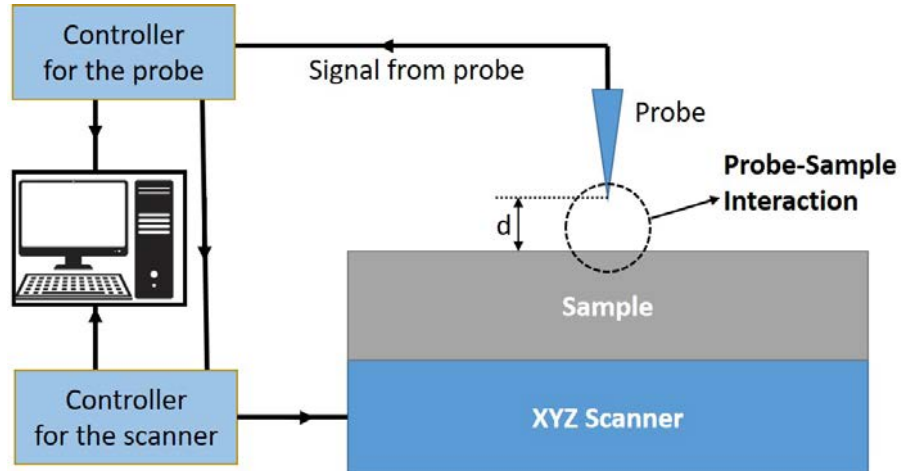


Fig. 4.1 Schematic of a scanning probe microscope (SPM). A probe is scanned over the sample, by either moving the probe or the sample itself. The probe-sample interaction, which is different depending on the type of microscope, produces a feedback signal which is used to adjust the probe-sample separation distance  $d$ . Both the interaction signal and the position are recorded and analyzed.

tunneling microscope (STM) [93]. In an STM a sharp conducting tip is used as a probe and scanned over the sample at a constant distance  $d$  by using the quantum tunneling current between the sample and the tip as a feedback signal (see Fig. 4.1). The value of the tunneling current has exponential dependence on the tip-sample separation  $d$  resulting in a  $\sim 10\text{pm}$  ( $10^{-11}\text{m}$ ) resolution. Many other alternatives to STM were later created, where a different probe and probe-sample interaction is used, together forming the family of scanning probe microscopy (SPM) techniques. A comprehensive list of SPM techniques is given in Ref. [94].

## 4.2 Near-Field Microwave Microscopy

Near-field microwave microscopy (NFMM) is a technique that combines the strength of SPM with the advantages of radio frequency (rf) surface characterization. It is an SPM based technique where a cavity resonator with a small hole, transmission line resonator, or a SQUID (described in [Chapter 1](#)) is used as a probe. The "near-field" refers to the regime where the size of the probe is much smaller than the wavelength of the rf signal used to examine the sample. In this regime the field has the characteristics of the static field. While the instantaneous value of the electromagnetic field oscillates with rf frequency, its amplitude is static with a spatial variation that depends on the geometry of the probe and the surroundings environment [[95](#), p.408]. The resolution of a NFMM strongly depends on probe-sample separation and the shape of the probe, since these two govern the volume to which the electromagnetic fields will be confined. Several generations of NFMMs were created in our group at UMD over the years. For a detailed description of this technique please see Refs.[[96](#), [97](#)].

A NFMM can locally image the surface impedance of the sample. Depending on the sample type one can extract the local value of surface conductance  $\sigma$  (or resistance  $\rho$ ), dielectric permittivity  $\epsilon$  or magnetic permeability  $\mu$ . Depending on the probe, a near-field microwave microscope coupling to the sample can be either capacitive (through  $\vec{E}$ ) or inductive (through  $\vec{B}$ ). [Fig. 4.2](#) shows the two probes that were previously used in our Lab. To study the surface electrodynamics of a superconductor, inductively coupled probes are often better suited because they induce screening cur-

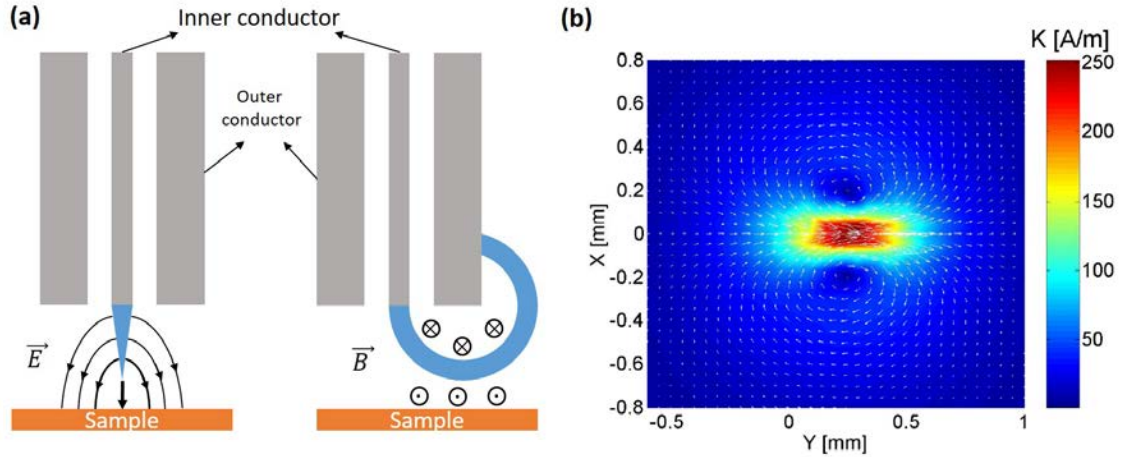


Fig. 4.2 (a) Schematic representation of a capacitively coupled probe and an inductively coupled probe. A capacitively coupled probe can be formed by connecting an STM tip to the inner conductor of a coaxial cable. An inductively coupled probe can be created by forming a loop using the inner conductor of a coaxial cable and shorting it with the outer conductor. (b) Top view of surface current distribution ( $K$ ) induced on the surface of a superconductor by a coaxial loop probe placed  $12\mu\text{m}$  above the sample. The computations have been performed with CST-Microwave Studio for an input power of  $1W$ . This figure is reproduced from [98].

rents in the superconductor. An example current distribution induced on the sample surface by an earlier generation probe is shown in Fig. 4.2(b).

### 4.3 Nonlinear response

The resolution of a NFMM can be further improved by using the nonlinear response of the sample. The nonlinear response can be measured through either intermodulation or higher harmonic response. Both in dielectrics and superconductors the  $n$ -th order nonlinear response  $P_{nf}$  of the sample depends on the applied power  $P_f$  as  $P_{nf} \propto (P_f)^n$ . This implies that most of the response will be coming from a small area

just below the probe where the input fields impinging on the sample are largest. This is illustrated by the work of Yasuo Cho [99], who showed that the higher the order of the harmonic response, the finer the resolution. However, harmonic response is weaker at higher orders and the even harmonics are only created when there is a mechanism to break the time reversal symmetry (such as superconducting vortices), hence the lowest odd harmonic, the third harmonic response (THR), is usually measured.

The contributions to the nonlinear response of a superconductor can be classified in terms of intrinsic nonlinear response and extrinsic response. Intrinsic nonlinear response refers to the nonlinear response that is expected from a pure homogeneous superconductor with no surface defects or edges. The superconducting current  $\vec{J}_s$  is given as  $\vec{J}_s = n_s e \vec{v}_s$ , where  $\vec{v}_s$  is the superfluid velocity and  $n_s$  is the superfluid density. Externally applied currents and magnetic fields can deplete the superfluid density  $n_s = n_s(|\vec{v}_s|)$  through the nonlinear Meissener effect, and it's functional form for  $J \ll J_c$  is given as follows:

$$\frac{n_s(T, J = 0)}{n_s(T, J)} = \frac{\lambda^2(T, J)}{\lambda^2(T, J = 0)} \cong 1 + \left( \frac{J}{J_{NL}} \right)^2, \quad (4.1)$$

where  $J_{NL}$  is the nonlinear scaling current density [100, 101]. The value for  $J_{NL}$  and it's temperature dependence can be used to identify the mechanism responsible for the generation of nonlinear response, be it an intrinsic response or nonlinearity due to a surface defect. It can be shown that the inductive nonlinear response of a superconductor is proportional to the change in penetration depth with current  $\Delta\lambda =$

$\lambda(T, J) - \lambda(T, J = 0)$  [102]. Lee calculated the third-harmonic response  $P_{3f}$  to be [103]:

$$P_{3f}(T, P_f) = \frac{\mu_0^2 \omega^2 \lambda^4(T)}{32 Z_0 J_{NL}^4(T)} P_f^3 G_{dist}(P_f) \quad , \quad (4.2)$$

where  $P_f$  is the fundamental power used to drive the probe,  $Z_0$  is the characteristic impedance of the transmission line and  $G_{dist}(P_f)$  is the geometry factor that depends on the spatial distribution of currents that are induced on the surface due to the MW field generated by the probe. In the low power limit  $G_{dist}(P_f)$  will be independent of the power applied to the probe or the temperature of the sample.

For an s-wave superconductor the temperature dependence of  $J_{NL}$  is given by [100, 104]

$$J_{NL}(T) = J_c(0) \left[ 1 - \left( \frac{T}{T_c} \right)^2 \right] \sqrt{1 - \left( \frac{T}{T_c} \right)^4} \quad . \quad (4.3)$$

The inhomogeneities and surface defects on the surface of a superconductor can serve to locally suppress  $J_c$  and  $J_{NL}$ , becoming extrinsic sources of nonlinear response. Eq. (4.2) shows that if the nonlinear response of a sample is mapped, the locations with low  $J_{NL}$  will generate stronger harmonic response [105, 106]. This provides an opportunity to create a magnetic microwave microscope that can detect the defects on the inner surface of an SRF cavity as described in Sec. 2.8. The temperature and field-dependence of the nonlinear response can provide enough information to deduce the type of defect. In this thesis two separate sources of measured nonlinear response will be presented in Chapters 6 and 8.

There are further benefits of measuring the nonlinear response rather than linear response. As was demonstrated by Oates [107], the nonlinear response is far more sensitive to applied rf power than the linear response. Fig. 4.3 shows the data that Oates obtained from a MgB<sub>2</sub> thin film stripline resonator. When measured over the same circulating power range, the intermodulation distortion (IMD) response spans 10 orders of magnitude while the surface resistance has changed only by a factor of  $\sim 10$ , and only in a narrow range in the high power limit. This indicates that more information can be extracted regarding the dynamics of a superconductor by using non-linear response, rather than simply focusing on linear response. In addition to that, Oates showed that the nonlinear response can be linked to the nonlinear surface impedance of the sample [108], which is an important parameter for a SRF cavity driven by high rf magnetic field. Finally, since the nonlinear response is generated only by the superconductor, there is no background signal from reflected waves etc., thus very high signal-to-noise ratio is achieved.

## 4.4 Previous generations of Magnetic Microwave Microscopes

Members of Anlage lab have been studying the nonlinear response of superconductors for 2 decades now. Over the years the resolution of the magnetic probe was constantly refined and the experimental setup was upgraded multiple times. The first

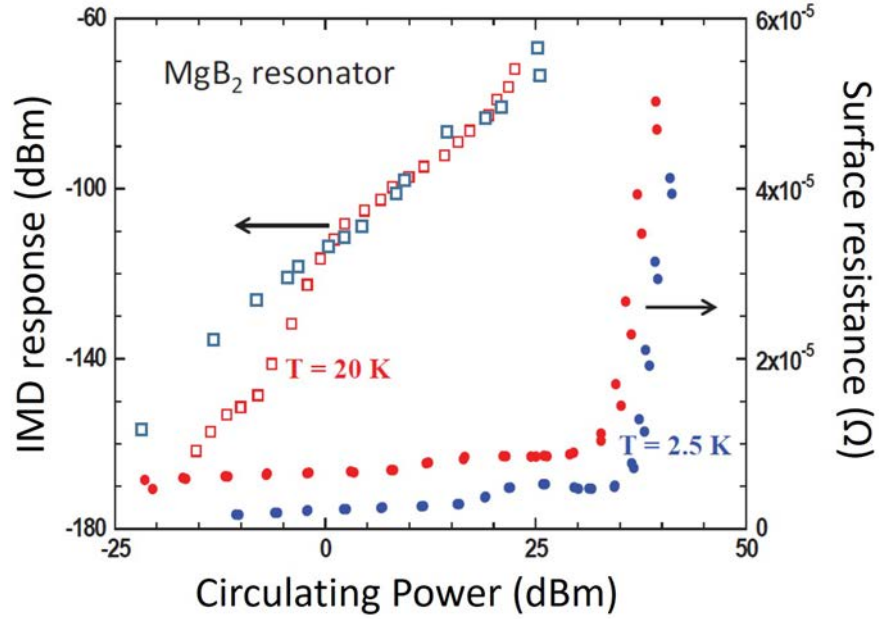


Fig. 4.3 Intermodulation distortion (IMD) response ( $\square$ ) and surface resistance ( $\circ$ ) vs the circulating power inside the resonator. The data is measured on a  $\text{MgB}_2$  stripline resonator at  $T = 2.5\text{K}$  (Blue) and  $T = 20\text{K}$  (Red). Note that the IMD is presented in a log scale while the surface resistance is presented on a linear scale. This figure is reproduced from Ref. [107].

magnetic microscope in our group was built by Sheng-Chiang Lee [102]. Lee used a probe made by shorting the inner conductor of the coaxial cable with the outer conductor (see Fig. 4.2(b)) to measure the second and third order harmonic response of a high-temperature superconductor, mainly YBCO. He imaged the harmonic response over the YBCO grain boundary (GB) at mm scale, and showed enhanced nonlinear signal at the location of the GB. He also extracted the geometry-free scaling current density  $J_{NL}$  from third-harmonic response.

Dragos Mircea improved on Sheng-Chiang Lee's design and mechanically polished the outer radius of the loop probe to create a micro-loop that further refined the resolution of the microscope. He also measured the phase of the harmonic response

in addition to its amplitude, and found that there are both resistive and inductive components to the harmonic response with the resistive component extending to temperatures above  $T_c$  in under-doped YBCO [109].

Finally, Tamin Tai and Dragos Mircea were the first to use the conventional magnetic recording hard disk drive magnetic writer head as a magnetic probe, similar to the ones I used. Using this new probe, Tai measured the linear response (reflected signal  $S_{11}(f)$ ) of Nb as it transitioned from the normal to the superconducting states and was able to fully interpret the data using a magnetic circuit model [110]. He also measured nanoscale harmonic response of Nb and  $MgB_2$ .

All my predecessors [98, 103, 104] greatly contributed to the collective knowledge that our lab has about the nonlinear electrodynamics of superconductors. However, their measurements were performed on a cryogenic wafer-probe station (see [104, p.35]) which relied on liquid helium or liquid nitrogen for continuous operation. The base temperature was about 4.5K, and the time available for measurement was limited due to the finite volume of the helium or nitrogen storage Dewar. Similarly, both the magnetic loop probe and the earlier generations of magnetic writer probe are inferior to the probes available to us today. This led to several improvements that I will be discussing next.



## 4.5 Magnetic Probe from Hard Disk Drive

Over the course of history, from the invention of steam engines and the industrial revolution to the digital revolution, humanity has witnessed several game changing moments. Today we are living at the dawn of another revolution. Artificial intelligence (AI), machine learning (ML) and the internet of things (IOT) are completely changing how humans interact with the surrounding world. The success of AI depends on the amount of data available for training. Nowadays everything around us is being recorded, surveillance cameras on the streets, your browser history, health records, geolocation, financial transactions, voice recordings... simply everything. This digital data is the new currency for many businesses where you can get free service if you willingly share your data. This is the age of "Big Data", but how is all of this data stored?

Magnetic recording technology has enabled this data revolution, and as of now continues to be the optimal method for data storage over prolonged periods of time. In 1898, Valdemar Poulsen became the first person to successfully demonstrate the possibility of magnetic recording by recording his own voice on a steel wire. Before the development of computers, magnetic recording was mainly used in sound recording for motion pictures and VHS home video recorders.

The need for magnetic recording surged with the widespread usage of computers. A magnetic recorder consists of a magnetic medium and a magnetic head, which encodes the information by locally magnetizing the medium. Many designs for the

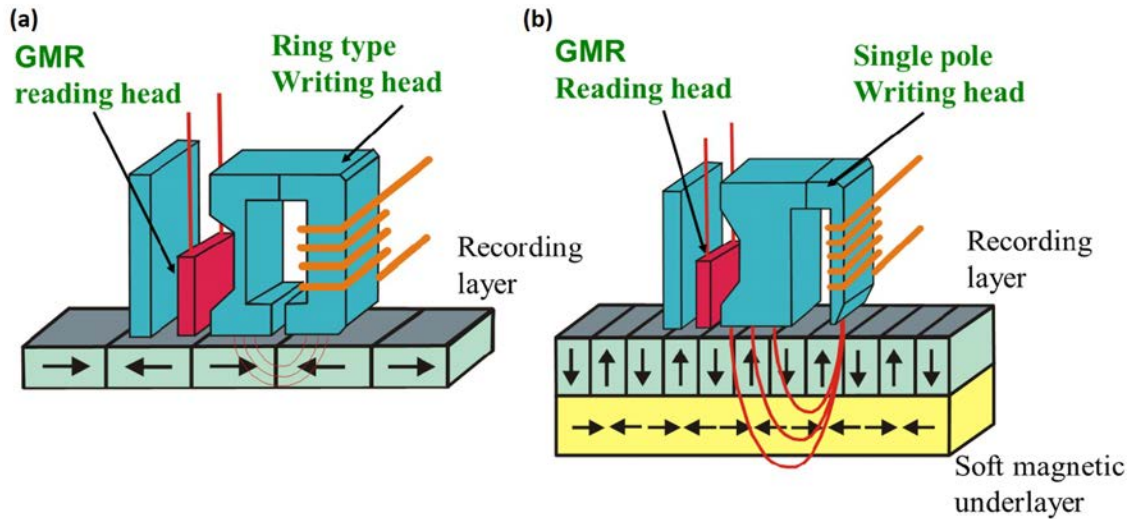


Fig. 4.4 (a) Gapped-ring core writer head and recording medium structure for longitudinal magnetic recording. (b) Single pole writer head and recording medium structure with a magnetic underlayer for perpendicular magnetic recording. A reading head that utilizes the giant magneto-resistance (GMR) effect to measure the magnetization of the recording layer is used in both cases. This figure is reproduced from Ref. [111].

magnetic writer heads had been tested, with the gapped-ring core writer heads dominating the market in the early years. In this design, the electrical coils were wound around a ring-shaped magnetic core with a small gap parallel to the surface of magnetic medium beneath it (see Fig. 4.4(a)). The time-dependent fringing magnetic field, emerging from the gap, magnetizes the magnetic medium longitudinally. Initially, the same head was used as writer and reader, however with the development of multilayer magnetic thin film technology, a separate reader head that uses the giant magneto-resistance (GMR) effect became prevalent. The GMR head is much more sensitive to magnetic fields, hence it can read the data at a faster speed.

To increase the storage density, perpendicular magnetic recording was proposed in 1977, although the challenges in the design delayed practical implementation until

2005. In this design a single pole writer head is used together with a soft magnetic underlayer which provides the return path for the magnetic flux ((see Fig. 4.4(b)).

After 120 years of progress, currently available magnetic writer heads are truly an engineering marvel. Nearly 1000 processing steps are needed to fabricate one [112]. Once ready, the resulting product has sub- $\mu m$  resolution and can operate at GHz bandwidths as was independently verified by Koblischka *et al.*[113]. These properties make a magnetic writer head an appealing candidate to be used as a magnetic microwave microscopy probe. Other researchers are already using magnetic writer heads to drive nitrogen vacancy centers in diamond [114, 115] and for characterization of superconducting microwave circuits [116]. For a "head to head" comparison of magnetic writer heads with other magnetic probes reported in the literature, see Section 1.2 of Ref. [104].

We obtained several batches of these near state-of-the-art heads from Dr. Mike A. Seigler of Seagate Technology and Dr. Dragos I. Mircea of Western Digital Corporation. A picture of a Seagate magnetic writer probe is shown in Fig. 4.5(a). This probe consists of a glider, a transmission line and an aluminum assembly that holds the glider and the transmission line together. The glider shown in Fig. 4.5(e) is the main part of the probe and it houses the magnetic writer head that is shown in Fig. 4.4. The bottom surface of the glider, the air bearing surface, is textured to provide a gliding motion using the air-flow produced by the high revolution speed of the disk during the operation of the hard-disk drive (HDD). Fig. 4.5(d) shows the top-view of the glider where connections to the transmission line are highlighted. The red box indicates the location of the actual magnetic writer pole (or yoke), and a magnified view is shown

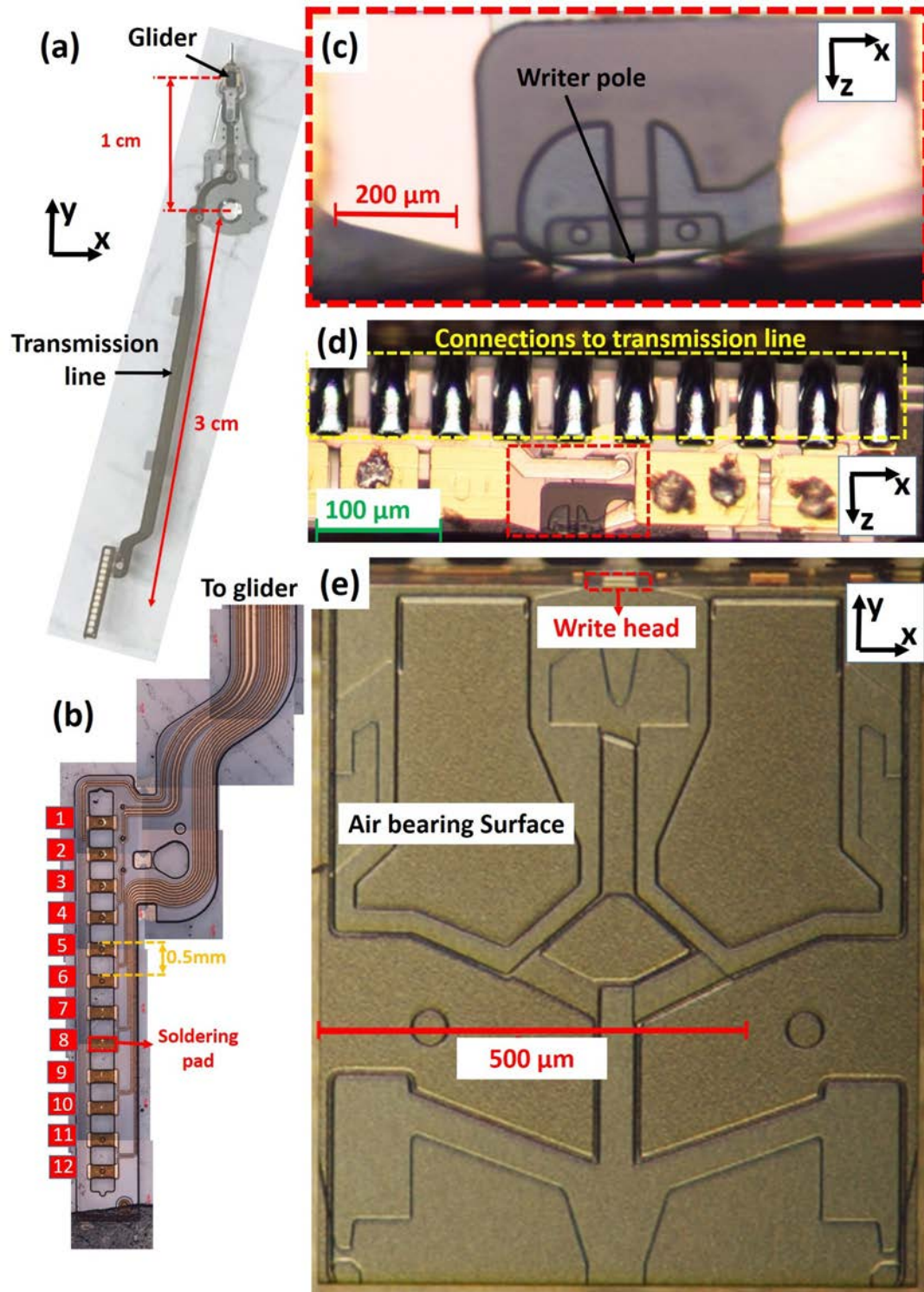


Fig. 4.5 (a) A picture of a Seagate magnetic writer probe, with glider and transmission line. (b) The close-up view of the pads at the end of transmission line that are used to make electrical connection to the writer head. Pads 3 – 4 are connected to the writer head. (c) A close up view of the writer head, the red area highlighted in (d). (d) the top view of the glider where the magnetic writer head is deposited. (e) A close-up view of the glider.

in Fig. 4.5(c). Note that the size of the magnetic pole itself is around  $\sim 100\text{nm}$  and cannot be seen here, but can be seen in SEM image shown in Fig. 4.6.

Fig. 4.5(b) shows the pads in the end of the transmission line that is used to make electrical connections to the probe. Pads 3 – 4 are connected to the writer head. The connection can be checked by measuring the resistance between pad 3 and 4 which is  $R_{\text{writer}} = 6\Omega$  at room temperature. Note that the lines connected to the writer-head are wider than the rest, because they are designed to support larger currents. Pads 7 – 8 and 9 – 10 are connected to 2 independent Tunnel-Magnetoresistance (TMR) sensors which are used for the readout circuit. The purpose of the rest of the pads is unknown to us as it is proprietary information. The width of the pads is about  $250\mu\text{m}$  which makes soldering a challenging task.

Fig. 4.6 shows the SEM image of the Western Digital Dragonfly probe's glider. The location of both the reader head and the writer head can be clearly seen in Fig. 4.6(b). Note the amount of magnetic shielding around the write head and the read head. These shields help to focus the writing and reading process to the small area below the probe, greatly improving the resolution.

#### 4.5.1 HFSS Simulations

Before using the magnetic writer probe in our microscope, we need to have a qualitative understanding of its magnetic field distribution and the resulting screening currents on the sample surface. The ANSYS High Frequency Structure Simulator (HFSS) software was used to simulate and visualize the surface currents induced on



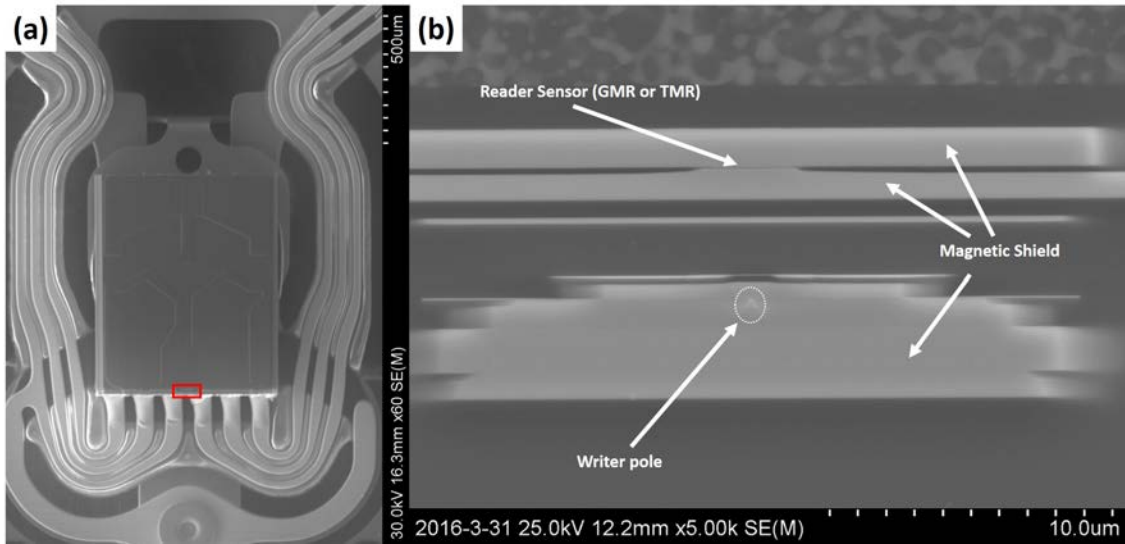


Fig. 4.6 (a) SEM image of the Western Digital Dragonfly probe's glider. (b) Magnified view of the read and write heads shown with a red box in (a). The reader and writer heads are separated by several layers of magnetic shielding.

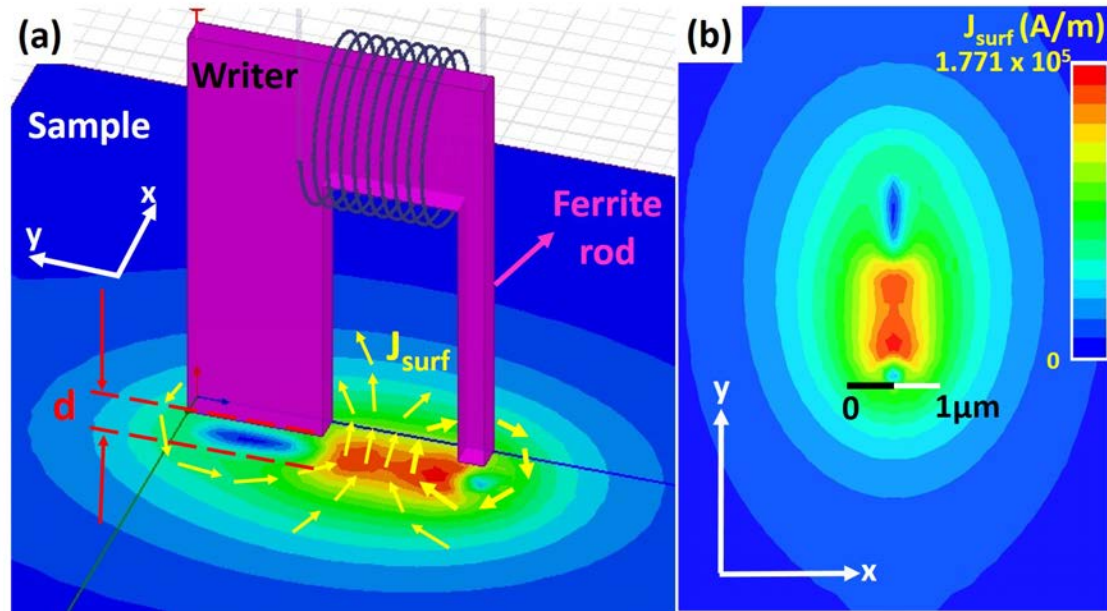


Fig. 4.7 (a) HFSS simulation of a magnetic writer a height  $d$  above a perfectly conducting sample. We model the probe as a  $200\text{nm} \times 200\text{nm} \times 3\mu\text{m}$  ferrite rod perpendicular to the surface, driven by a 10 turn gold wire. This rod is part of a bigger magnetic yoke structure. The diameter of the coil is  $1.2\mu\text{m}$  and the probe is  $d = 200\text{nm}$  away from the surface of the sample. Yellow arrows indicate the direction of current flow. (b) Distribution of the magnitude of surface current density  $|\vec{J}_{surf}|$  on the sample surface. The colorbar indicates the magnitude of surface current density in a linear scale. The loop is excited by a  $I = 50\text{mA}$  RF current at  $f = 1.5\text{GHz}$  frequency. The  $x$  and  $y$  axes are the same as the ones defined in Fig. 4.5.

the sample by the magnetic probe. When a magnetic writer probe is used with superconducting samples, the magnetic field will not be able to penetrate through the sample, in contrast to the situation shown in Fig. 4.4. Fig. 4.7(a) shows the configuration used for HFSS simulation. The superconducting sample is modeled as a perfect conductor. Arrows indicate the direction of current flow. Fig. 4.7(b) shows the distribution of the magnitude of surface current density  $\vec{J}_{surf}$  on the sample surface. From our simulation we see that largest current is localized to a 500 nm diameter circle.

Later, a more rigorous study of the probe structure was performed by Eddie Chang, an undergraduate researcher in our lab who worked under my supervision. Unfortunately, many of the magnetic recording companies are not willing to share information about the details of the writer head designs. To create the full picture we had to rely on US patents, such as [117] and [118]. In this simulation, the main pole of the writer head was designed as a  $250\text{nm} \times 250\text{nm} \times 1\mu\text{m}$  long rod, whose final 250nm was tapered down to a  $60\text{nm} \times 40\text{nm}$  rectangle, to enhance the magnetic field (see Fig. 4.8(a)). Ten gold coil turns with 500nm diameter that are wound around the main pole were used as excitation coils (see Fig. 4.8(b)). The return pole was designed as a C shaped core that surrounds the main pole (see Fig. 4.8(c)), which is very similar to a simulation performed by researchers from Seagate in Ref. [114, 115]. The superconducting sample is again modeled as a perfect conductor. The probe is kept 50nm above the sample. Alumina is an electric insulator with a relatively high value of thermal conductance. It is generally used to provide structural support and aid with heat removal. Fig. 4.9 shows the simulated spatial distribution of MW magnetic field as experienced by the superconductor.

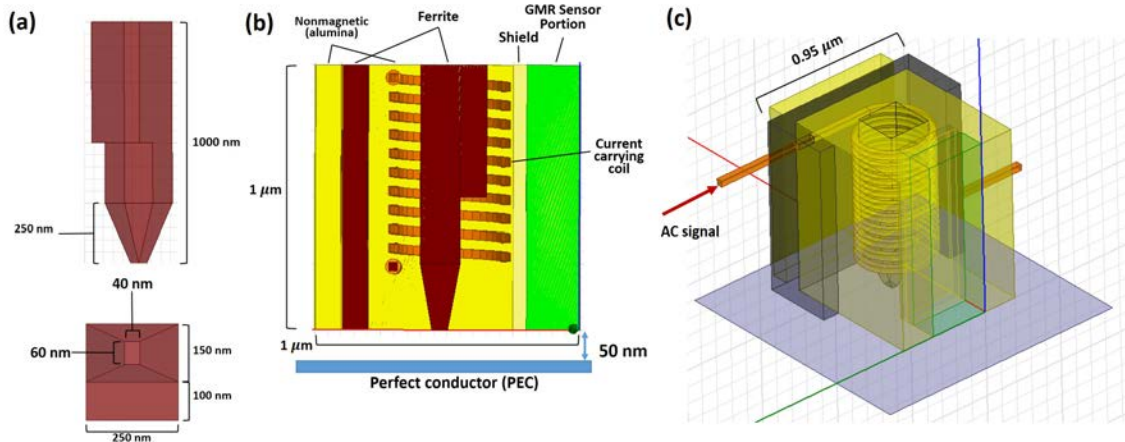


Fig. 4.8 (a) The shape of the main pole of the writer head as deduced from [117] and [118]. (b) Schematic of the HFSS simulation. The main pole and the return pole, both of which are simulated as ferrites, are located 50nm above the superconductor, which is modeled as a perfect conductor. (c) The full design of the writer head as done in our HFSS simulation. The  $x$  and  $y$  axes are same as those defined in Fig. 4.5.

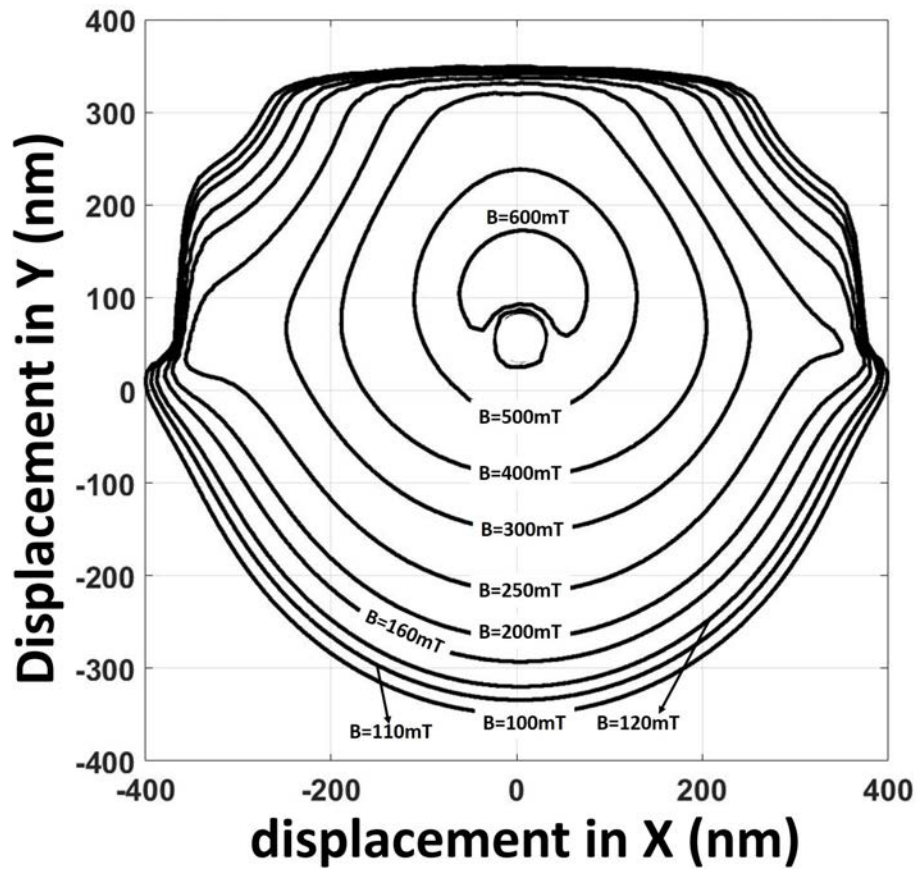


Fig. 4.9 The spatial distribution on the surface of the superconductor simulated by the HFSS model shown in Fig. 4.8. The contour plot of magnitude of the magnetic fields component normal to the surface. The  $x$  and  $y$  axes are same with the ones defined in Fig. 4.5.



## 4.5.2 Numerical simulation by Seagate

Finally, the result of numerical simulation based on the Stoner–Wohlfarth model [119] was provided by Mike Seigler of Seagate Technology for our type of write head. The simulation was performed for 17 nm probe-sample separation and 60 mA excitation current. The simulation was performed over the magnetic medium with no soft underlayer present. Fig. 4.10 shows the result of this simulation: The peak rf field amplitude is greater than  $600mT$  and the fields are localized to  $< 100nm$  length scales. Note that when the probe is used with a superconducting sample the resolution will likely be less impressive.

In summary, all models presented above agree in two key aspects: Magnetic writer probe can produce rf strong magnetic fields ( $B_{rf} > 600mT$ ) localized to sub- $\mu m$  length scale. A near field magnetic microscope that utilizes these writer probes can achieve sub- $\mu m$  resolution. Furthermore, this microscope can be used to study Nb and other materials at the regime most relevant to the SRF applications, the one where rf field amplitude approaches the superheating field of the material  $B_{rf} \rightarrow B_{sh}$ . In case of Nb which has the upper critical field of  $B_{c2} = 200mT$ , this microscope can locally drive the sample into the normal state, creating artificial hot spots.

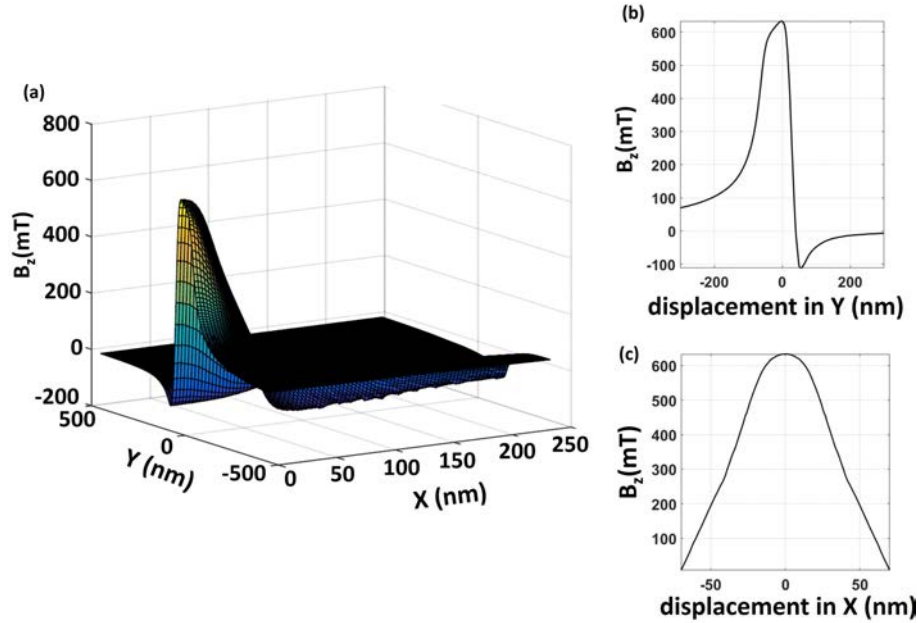


Fig. 4.10 (a) The spatial distribution of the magnetic field normal to the surface under the writer probe, calculated using the Stoner–Wohlfarth model for our type of write head. The probe is positioned 17nm above the magnetic medium with no soft magnetic underlayer. (b) The  $y$ -line cut at  $x = 0$ . (c) The  $x$ -line cut at  $y = 0$ . The  $x$  and  $y$  axes are same with the ones defined in Fig. 4.5.

## 4.6 Experimental setup

A new, completely dry cryogenic cryostat for cooling experiments to temperatures below 2.7 K in a vacuum environment was installed in our lab. The cooldown process for this new setup is fully automated in the sense that the user evacuates the system and starts the helium compressor and everything else is automatic (requiring no user intervention or control) down to the base temperature of the cryostat. The cryostat can operate in a continuous manner at base temperature for weeks or months at a time with minimal attention from the user and without consuming any cryogenics or gases. This new setup significantly improves our efficiency to perform measure-

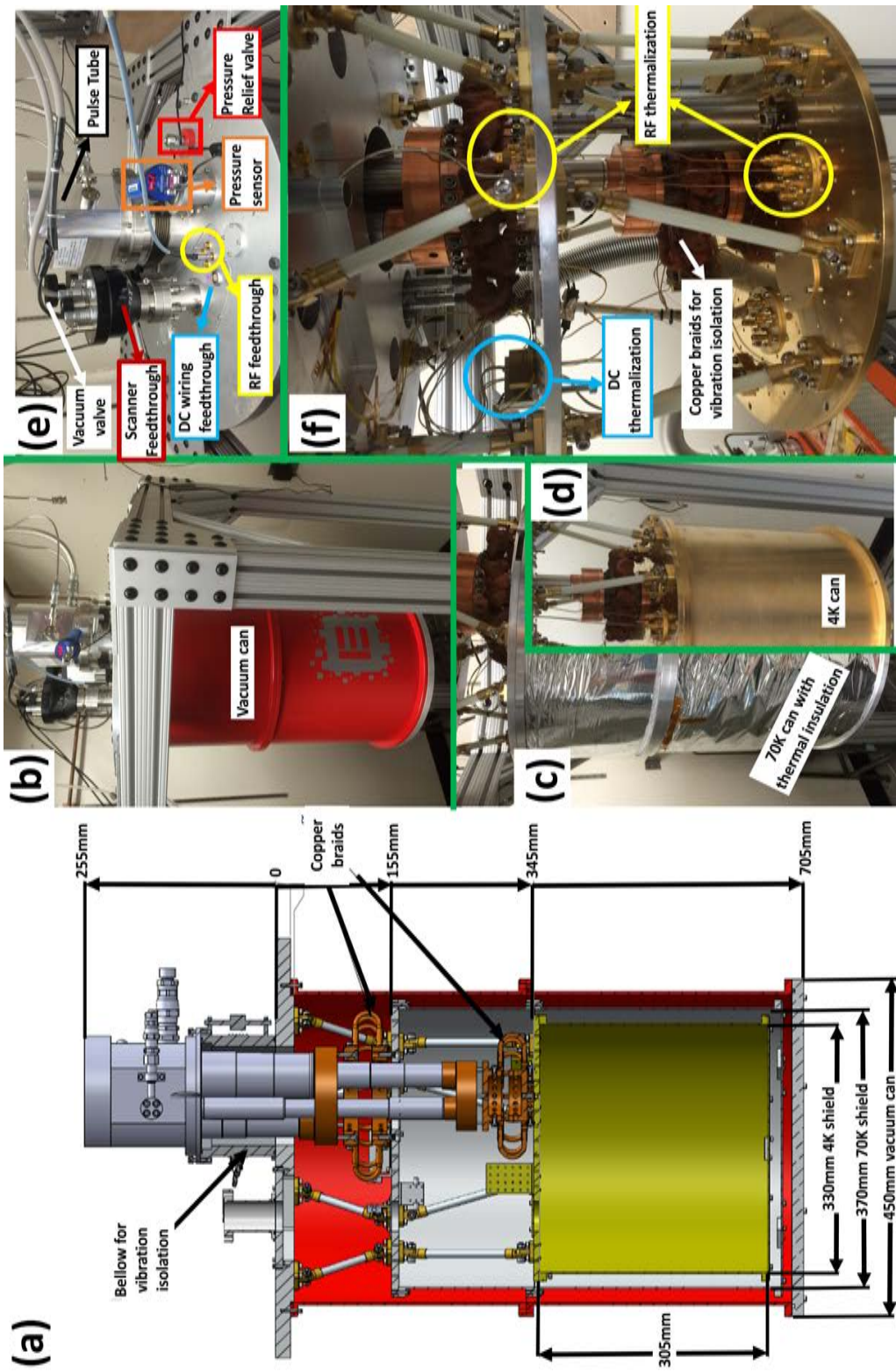


Fig. 4.11 (a) Schematic of the dry pulsed-tube cryostat manufactured by Entropy Cryogenics. (b) Picture of the fully closed cryostat. (c) Picture of the cryostat when vacuum can is taken off (d) Picture of the cryostat with only 4K can. (e) Picture of the top plate of the cryostat which houses the pulsed-tube, rf feed-through, dc wiring feed-through and the pressure sensor. (f) Inside of the cryostat, both rf connections and dc wiring are thermalized at each stage.

ments and gives us ability to collect vast amounts of measurement data with great reproducibility.

[Fig. 4.11](#)(a) shows the schematics of the cryostat. The cryostat has three plates: a room temperature top plate, a 70K plate and a cold plate; and three shielding cans: outer vacuum can, 70K can and the 4K can. The diameter of the 4K can is 330mm and it's height is 305mm, this dictates the volume of the usable experimental space. 70 layers of super-insulation is wrapped around the 70K can (see [Fig. 4.11](#)(c)). The pulse tube is connected to the 70K plate and cold plate via copper braids to minimize the vibration at the cold plate (see [Fig. 4.11](#)(f)). For the same purposes, the pulse tube is supported by a bellows that is mounted on the top plate. The top plate also houses the feedthroughs for both rf and dc connections and a pressure sensor (see [Fig. 4.11](#)(e)). The base pressure of the cryostat at the cryogenic temperatures is  $8 \times 10^{-8} Torr$ . RF connection between the experiment and room temperature electronics is made via Beryllium Copper semi-rigid coaxial cables, which are thermally anchored at each stage (see [Fig. 4.11](#)(f)). The dc wiring for thermometers and a heater is also thermalized at each stage.

[Fig. 4.12](#) shows an example of a fixed-point measurement setup. In this case a custom made copper holder is used to firmly hold the bulk sample, and the gap between the sample and the copper holder is filled with indium foil. The copper holder is thermally anchored to the cold plate of the cryostat. Another copper plate, not seen in this picture is used to firmly press the probe against the sample, providing both good probe-sample contact and thermalization for the probe. Slight modifications to the setup are made each time depending on the shape of the sample. The raster

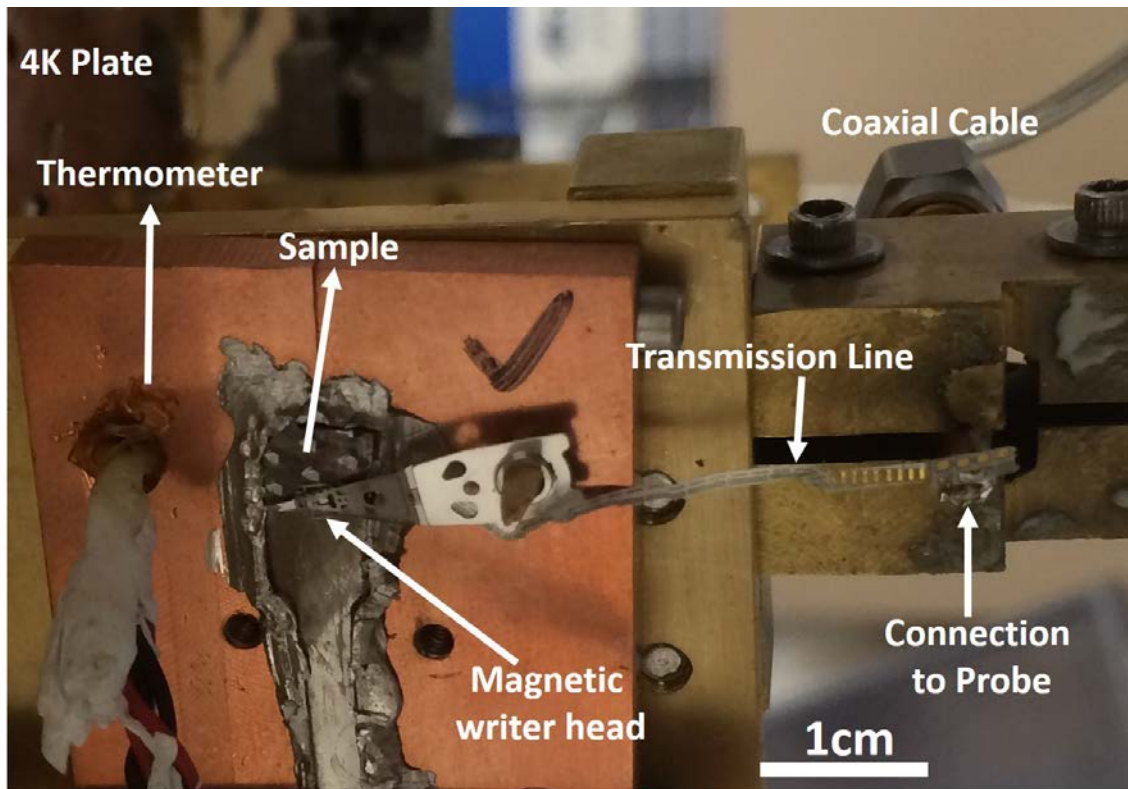


Fig. 4.12 Photograph of the Experimental setup. The magnetic writer head is connected to an SMA coaxial connector by directly soldering it to the pads on the end of writer probe's transmission line. The Nb sample is attached to the cold plate of the cryostat. The probe is in direct contact with the sample in this fixed-point measurement case.

scanning efforts will be discussed separately in [Chapter 10](#).

A Cernox thermometer is installed in close proximity to the sample. A Lakeshore model 340 temperature controller is used to control the sample temperature by utilizing a PID loop. The heater, which is not shown in the picture, is mounted on the cold plate just below the pulse tube. This arrangement minimizes possible temperature gradients on the cold plate.

To measure the electrodynamic response of the superconductor, a microwave signal is produced by a microwave source (HP 83620B) and sent to the magnetic



writer probe inside the cryostat. Electrical contacts are made by directly soldering SMA coaxial connectors to the pads on the end of the writer probe transmission line (see [Fig. 4.5](#) and [Fig. 4.12](#)). The probe produces an rf magnetic field which is mostly perpendicular to the sample surface. The sample is in the superconducting state, so to maintain the Meissner state, a screening current is induced on the surface (see [Fig. 4.13\(b\)](#)). This current generates a response magnetic field that is coupled back to the same probe, creates a propagating signal on the attached transmission line structure. This signal is branched out using a directional coupler and is measured with a spectrum analyzer (Agilent E4407B) at room temperature. Both linear and nonlinear responses to an applied rf magnetic field are expected. To improve the signal-to-noise ratio, stray nonlinear signals produced by the amplifiers and the spectrum analyzer itself have to be suppressed. For this reason, high-pass filters are installed between the probe and spectrum analyzer in order to block the fundamental input frequency signal from reaching the spectrum analyzer and producing nonlinear signals (see [Fig. 4.13\(a\)](#) and [\(b\)](#)). Also, due to device imperfections, the microwave source can also produce some nonlinear signal which are suppressed by means of a low pass filter. The detailed description of the microscope operation is given in [Appendix A](#).

No external dc magnetic field is applied to the sample. The entire setup is shielded from external magnetic field by a cylindrical superconducting shield installed around the coldest enclosure of the cryostat.

The nonlinear response of the sample is measured as a function of frequency, input microwave power and temperature. The data and the model fits are presented in the next two chapters, [Chapters 5](#) and [6](#).

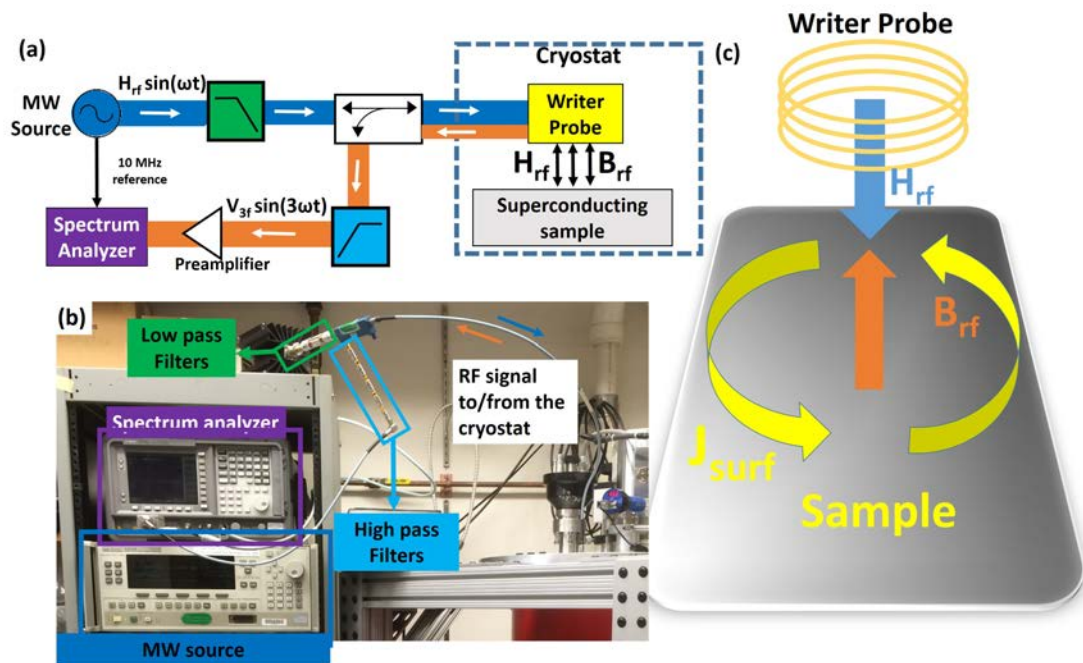


Fig. 4.13 (a) Schematic of experimental setup. A microwave (MW) source is used to generate an rf signal and feed it to the magnetic writer probe. The sample response magnetic field is coupled back to the probe and measured with a spectrum analyzer. (b) The picture of the measurement setup on the rack. (c) Sketch of the probe-sample interaction. The magnetic probe is approximated as a current loop producing perpendicular magnetic field inducing screening currents on the surface of the sample. This current generates a response magnetic field that is coupled back to the same probe.

### 4.6.1 Advantages of this method

Traditional microwave characterization techniques of samples usually provide the response averaged over the entire surface of the sample. In superconductors, local inhomogeneities like surface defects, grain boundaries, dislocations and the edges of the sample generate strongest response, since the surface currents are enhanced there. For example, the surface resistance measured from the SRF cavity that was presented in [Chapter 3](#), is an averaged response of the entire cavity with no information about the source of the loss or its location.

The magnetic microwave microscope that we built can probe the electrodynamic response of the superconductor at a local scale and is immune to edge effects. It can be used to study the intrinsic response of the sample or to characterize the surface defects one at a time. The amplitude of the magnetic field produced by the magnetic writer probe is higher than the upper critical field of Nb, thus one can locally drive the Nb into the normal state. This advantage can be utilized to study the SRF-grade samples at the limits of their superconducting response and this is precisely where they will be utilized.

By now it is clear that dc characterization methods (RRR, DC critical field measurements etc.) are not sufficient and cannot be directly linked to RF performance of the cavity at low temperatures. As I will describe in [Chapter 7](#), there exists a finite time-scale for the nucleation of vortices, hence a static characterization of the material will completely miss this feature.



# 5

---

## Data from the Magnetic Microscope

---

The measured nonlinear response will be presented and discussed in this chapter. Numerical fits to the data will be done in [Chapter 6](#) and [Chapter 7](#). Five SRF grade bulk Nb and Nb thin film samples from 4 different labs around the world were examined. [Table 5.1](#) contains the list of samples with their type, origin and references where further details can be found.

Sample ID	Sample Type	Source	Reference for sample preparation
Sample 1	Nb film on Cu	CERN	[ <a href="#">120</a> , <a href="#">121</a> ]
Sample 2	Bulk Nb	Bieler group at Michigan State university (MSU)	[ <a href="#">122</a> , <a href="#">123</a> ]
Sample 3	Bulk Nb	Gianluigi Ciovati's group at Jefferson Lab	[ <a href="#">124</a> ]
Sample 4	Nb film on Cu	Malyshev group at the Accelerator Science and Technology Centre (ASTeC)	[ <a href="#">125</a> ]
Sample 5	Nb film on Sapphire	Valente-Feliciano group at Jefferson Lab	[ <a href="#">126</a> ]

Table 5.1 The list of samples measured for this thesis with their type, origin and references where further details can be found.

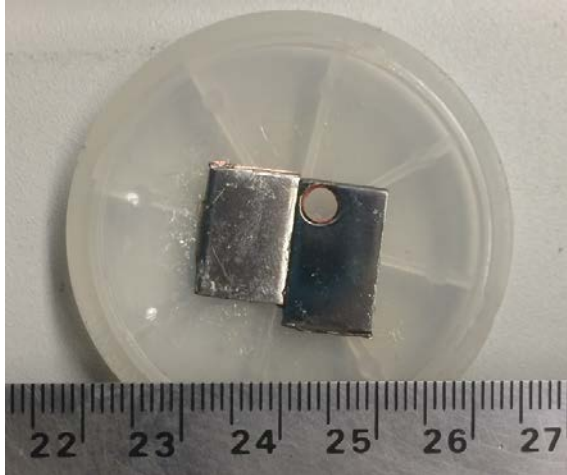


Fig. 5.1 Picture of Sample 1, Nb film on copper from CERN.

## 5.1 Sample 1 – Nb film on copper from CERN

First, a thin-film sample that was prepared at CERN by depositing Nb on a copper substrate was measured. This Nb film was deposited using the high-power impulse magnetron sputtering (HIPIMS) technique [127]. The HIPIMS plasma (containing both Nb atoms and Nb ions, with a high fraction of Nb ions) was driven with rectangular voltage pulses in a frequency range of  $50 - 500\text{Hz}$  and pulse duration range of  $50 - 200\mu\text{s}$ . The peak discharge current density was kept in the range of  $0.2 - 1\text{A}/\text{cm}^2$ . This sample is well characterized by point-contact tunneling spectroscopy, low-energy muon spin rotation, and SEM. The point-contact tunneling measurements revealed that the sample has a distribution of surface superconducting gap values with a peak at  $\Delta = 1.48\text{meV}$  [121]. However, the tunneling data also shows a few locations with large zero-bias conductance peaks. The sample has a fine-grain structure with 50-100-nm average grain size [120].

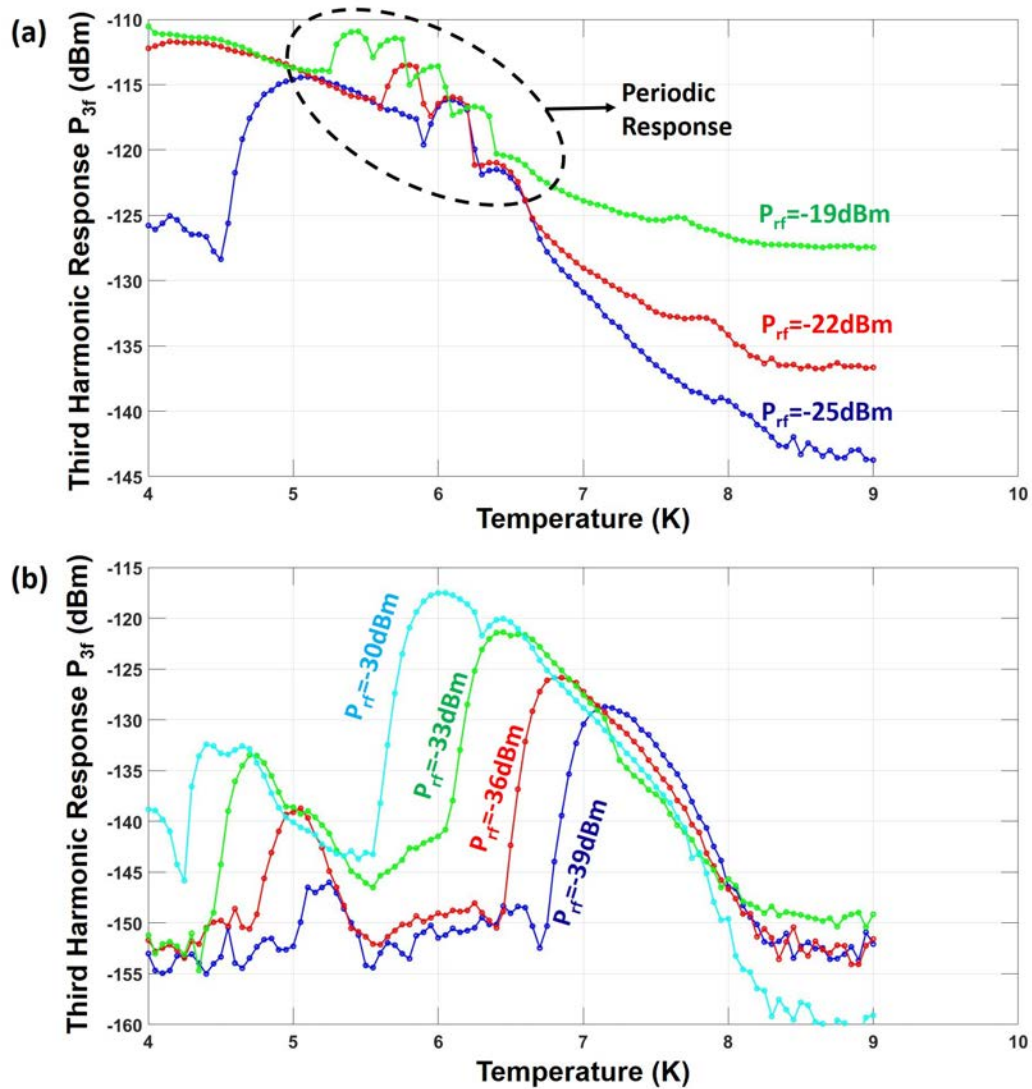


Fig. 5.2 Temperature dependence of third-harmonic response  $P_{3f}$  from Sample 1 for  $f = 2.2$  GHz input frequency. (a) High input power limit with input powers  $P_{rf} = -25$  dBm (blue),  $P_{rf} = -22$  dBm (red),  $P_{rf} = -19$  dBm (green). (b) Low input power limit with input powers  $P_{rf} = -39$  dBm (blue),  $P_{rf} = -36$  dBm (red),  $P_{rf} = -33$  dBm (green),  $P_{rf} = -30$  dBm (cyan). A peak in  $P_{3f}(T)$  around  $T_c$  is expected from the Ginzburg-Landau (GL) model. Note the periodicity as a function of temperature between  $5K < T < 7K$ .

Fig. 5.2 shows the temperature dependence of the third-harmonic response power  $P_{3f}$  for different values of rf input power  $P_{rf}$ . For a given  $P_{rf}$ , the sample is warmed up to  $T = 10K$  (above  $T_c$ ) to release any trapped flux, and then cooled down again. The measurement is taken at 0.05K temperature steps. A PID loop is used to reach 0.02K stability in the temperature. The measurement is taken with video bandwidth and resolution bandwidth of 1Hz with 5 times averaging. The noise floor of the spectrum analyzer with these settings is -160 dBm which at 5 GHz corresponds to 30,000 photons/s.

The peak in  $P_{3f}(T)$  around  $T_c$  is expected from, for example, the Ginzburg–Landau (GL) model [105]. This peak is the signature of the intrinsic nonlinearity arising from the suppression of superfluid density by the surface current. The effect of this modulation of the superconducting order parameter is particularly large near  $T_c$ , where the equilibrium order parameter is small in magnitude. From the low input power response shown in Fig. 5.2(b) the  $T_c$  for this sample can be estimated as  $T \approx 8.2K$ , above which the nonlinear response appears to be temperature independent.

The reproducibility of the third-harmonic response power was checked by repeating the same measurement after one week. Fig. 5.3 shows the dependence of the third-harmonic response on the direction of the temperature sweep. A small hysteresis in temperature can be seen around  $T_c$ . The data shown in red is acquired under identical conditions as the data shown in green, but was measured at the same location with one week difference.

The nonlinear response above  $T_c$  comes from the magnetic writer probe itself. One of the mechanisms responsible for the nonlinear response of the writer probe is

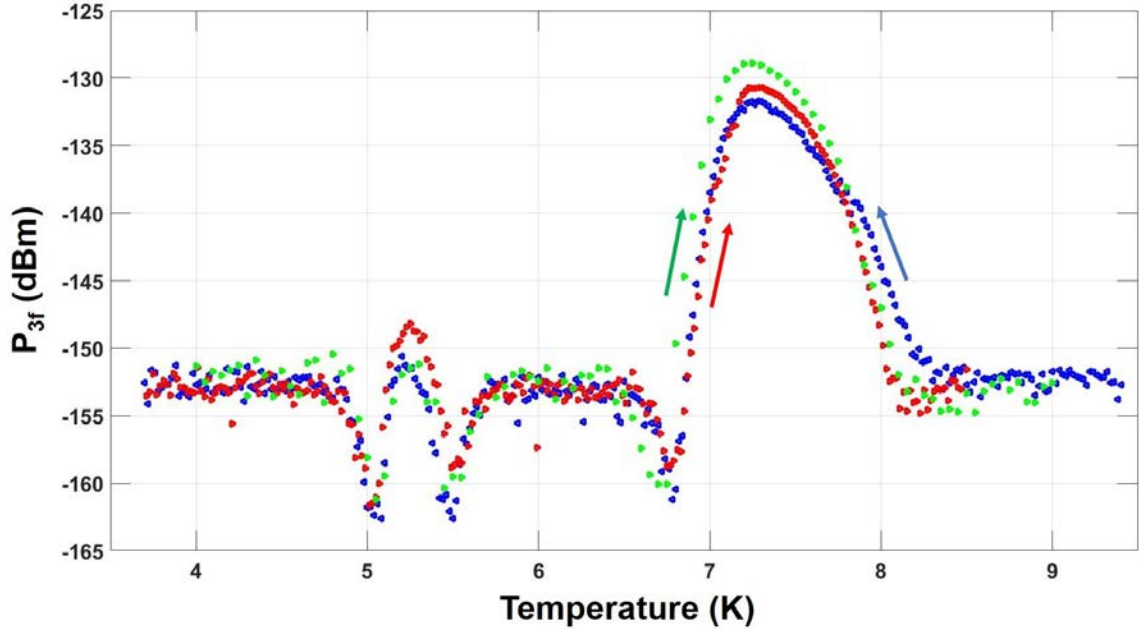


Fig. 5.3 Third-harmonic response  $P_{3f}$  from Sample 1 as a function of temperature while cooling down (blue) and warming up (green and red). The data is taken at input frequency  $f = 2.2$  GHz and input power  $P_{rf} = -40$  dBm. The data shown in green color is acquired 1 week before the other two.

the hysteresis loop of the ferrite material that is used in the yoke of the writer head (see Figs. 4.4 and 4.8). Also, high driving currents can saturate the magnetic parts of the writer head which will stagnate the magnetic field generated by the probe. This could be another mechanism responsible for the nonlinear response of the writer probe.

Fortunately, the nonlinear response of the probe is temperature independent in the 3K-10K range used in my measurements and shows up as baseline nonlinear response around  $-152$  dBm in Fig. 5.3. Dips below the baseline at  $T = 5$  K;  $T = 5.5$  K and  $T = 6.8$  K show the destructive interference between the superconductor nonlinearity and the probe nonlinearity. It was previously observed that the third harmonic nonlinear response has a phase that evolves rapidly with temperature below

$T_c$  [109], giving rise to this partial cancellation.

At higher input powers, nearly periodic peaks and dips in  $P_{3f}(T)$  are observed as a function of temperature (see Fig. 5.2(a)). As input power is increased the number of peaks also increases. The periodicity of the nonlinear response is clearer in a linear scale (third-harmonic voltage  $V_{3f}$ ) than the logarithmic scale (third-harmonic power  $P_{3f}$  in dBm). Assuming that the spectrum analyzer and coaxial lines have the standard  $Z_0 = 50\Omega$  characteristic impedance, the third-harmonic voltage measured by the spectrum analyzer can be related to the third-harmonic voltage as follows:

$$P_{3f}(\text{Watts}) = \frac{V_{3f}(\text{V})^2}{2Z_0} \quad . \quad (5.1)$$

Similarly we can calculate the voltage applied to the magnetic writer probe assuming it also has  $Z_0 = 50\Omega$  impedance [128]. Since the exact magnitude of applied magnetic field at the surface of the sample is not known, the input RF magnetic field amplitude is presented in arbitrary units. The relation between applied RF power and RF magnetic field in a.u. is written as:

$$H_{rf}(\text{a.u.}) = 1000\sqrt{2Z_0P_{rf}(\text{Watts})} \quad . \quad (5.2)$$

Fig. 5.4 shows a plot of measured third-harmonic response vs temperature ( $T$ ) and applied rf field amplitude ( $H_{rf}$ ) at an  $f = 2.2\text{GHz}$  input frequency. In Fig. 5.4(a) the third-harmonic response power is plotted on a logarithmic scale, whereas Fig. 5.4(b) shows the equivalent third-harmonic voltage, calculated using Eq. (5.1). Fig. 5.5(a)

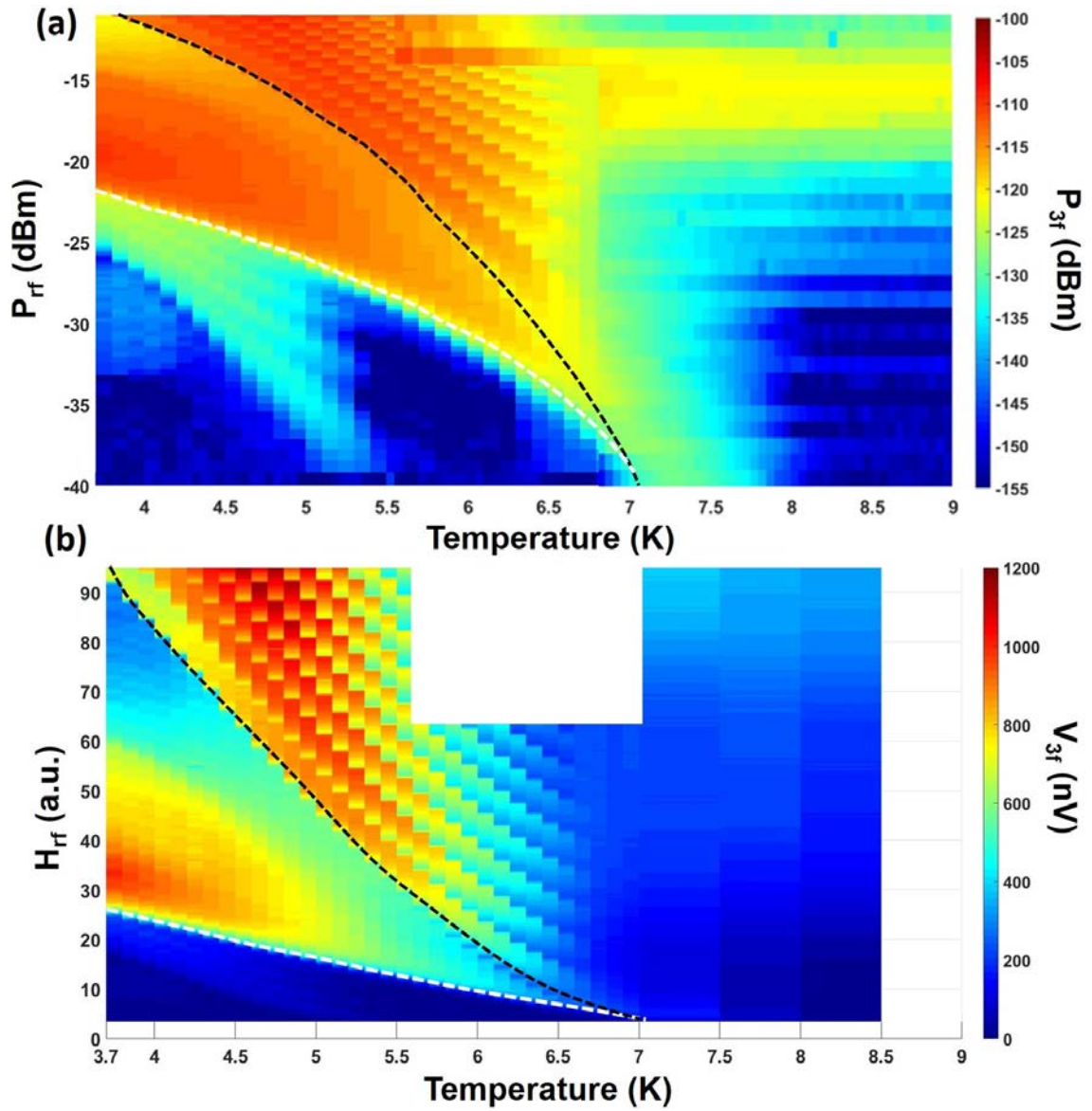


Fig. 5.4 (a) Third-harmonic response power  $P_{3f}$  data (logarithmic scale) from Sample 1 as a function of temperature  $T$  and applied rf power  $P_{rf}$ . (b) Third-harmonic voltage response  $V_{3f}$  data (on a linear scale) vs temperature and applied rf field amplitude  $H_{rf}$  from Sample 1. The white dashed line shows the onset of nonlinear response that we attribute to vortex nucleation as will be discussed in [Chapter 8](#). The black dashed line shows the onset of periodic response. The response is measured at input frequency of  $f = 2.2GHz$ .

shows a vertical line cut through this image ( $V_{3f}$  vs  $H_{rf}$ ) at a constant temperature of  $T = 5.1K$ . To analyze the temperature dependence of the periodic response, the RF field amplitudes corresponding to the dips in  $V_{3f}(H_{rf})$  were identified and defined as  $H_{pn}(T)$  where  $n$  stands for  $n$ 'th dip and  $T$  is the temperature of the measurement. As shown in the figure,  $H_{p1}$ ,  $H_{p2}$  and  $H_{p3}$  are the rf field amplitudes corresponding to the first three dips in  $V_{3f}(H_{rf})$ . At all temperatures, the third-harmonic response has a sharp jump at an onset field  $H_v(T)$  (see the white dashed line in Fig. 5.4). As the rf field amplitude  $H_{rf}$  is further increased, above a temperature-dependent onset amplitude  $H_{p0}(T)$ ,  $V_{3f}$  becomes periodic as a function of  $H_{rf}$  (see the black dashed line in Fig. 5.4). Fig. 5.5(b) shows the temperature dependence of  $H_{p1}(T)$ ,  $H_{p2}(T)$ ,  $H_{p3}(T)$ ,  $H_{p4}(T)$ ,  $H_{p5}(T)$ ,  $H_{p6}(T)$  and  $H_v(T)$ . Clearly, the  $H_p$  have the same temperature dependence while  $H_v$  has a different temperature dependence, indicating that they most likely have different origins.

## 5.2 Sample 2 – Bulk Nb from MSU

Also, a bulk Nb sample provided by the Bieler group (MSU) originating from a Tokyo-Denkai large-grain Nb single crystal was examined. The surface of the sample was mechanically polished and then electropolished. Later, the sample was strained to 40% elongation, cut in half, and two differently oriented halves (F and C) are welded back together [122, 129]. The sample is then measured for a third-harmonic response at several fixed positions on side C of the sample about 4 mm away from the weld.



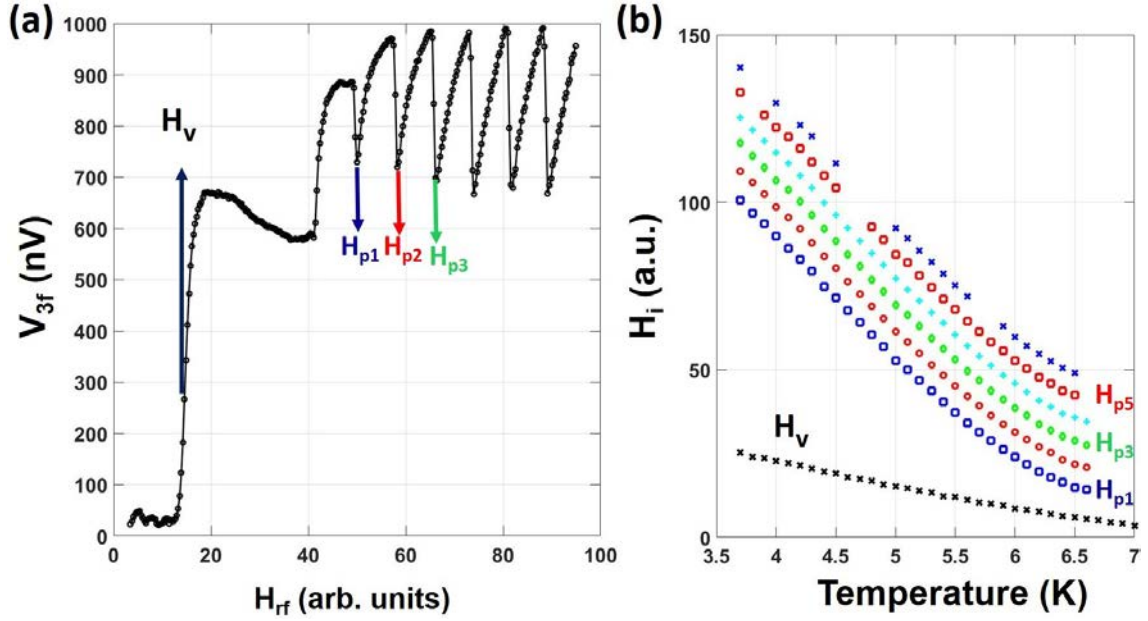


Fig. 5.5 (a) Third-harmonic response  $V_{3f}$  data at  $T = 5.1K$  and  $f = 2.2GHz$  measured on Sample 1. (b)  $H_{p1}$  (blue  $\square$ ),  $H_{p2}$  (red  $\circ$ ),  $H_{p3}$  (green  $\diamond$ ),  $H_{p4}$  (cyan  $+$ ),  $H_{p5}$  (red  $\square$ ),  $H_{p6}$  (blue  $\times$ ) and onset of nonlinearity  $H_v$  (black  $\times$  markers) vs temperature.

This location experiences a brief thermal excursion that retains much of the deformed dislocation defect structure as described in more detail in Fig. 16 of Ref. [122] and Ref. [123]. This sample was shown in Fig. 4.12.

Fig. 5.6 shows the temperature dependence of the third-harmonic response power  $P_{3f}$  for different values of rf input power  $P_{rf}$ . The measurement was performed both during the cool down and warmup of the sample. No hysteresis in temperature was observed. The nonlinear response of the sample goes to the noise floor of the spectrum analyzer exactly at  $T = 9.2K$ . In this particular location no periodic response was observed even at very high input powers  $P_{rf}$ . As was discussed before, the nonlinear response above  $T > 9.2K$  comes from the probe itself and the dip at  $T = 7.5K$  when measured with  $P_{rf} = -10dBm$  is the result of the destructive interference between

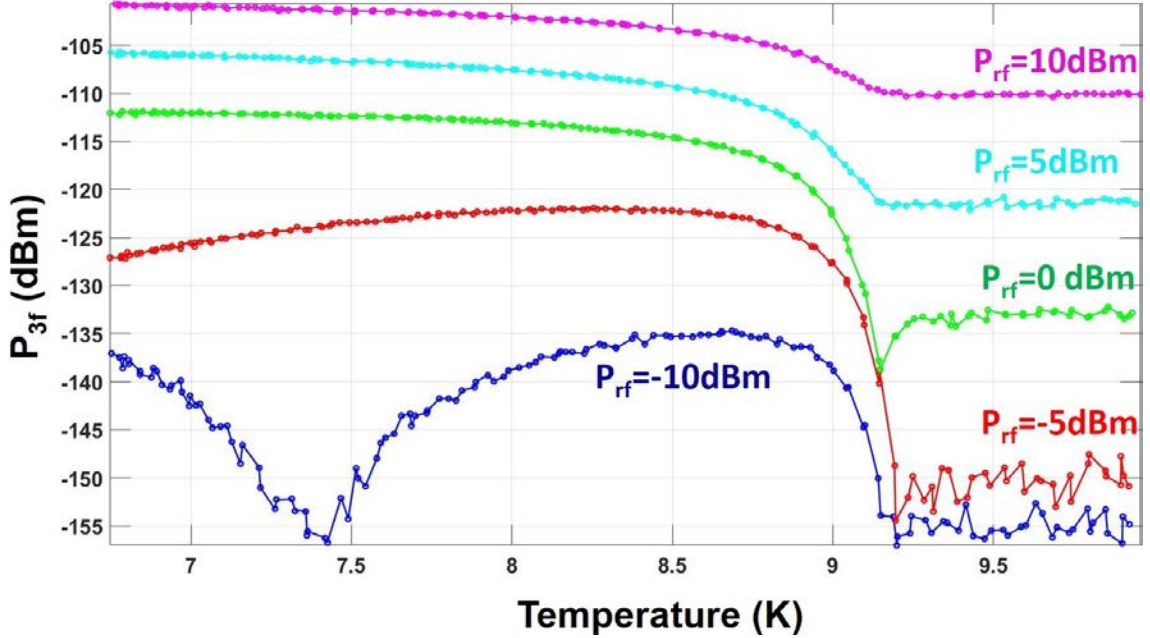


Fig. 5.6 Temperature dependence of third-harmonic response  $P_{3f}$  from Sample 2 for  $f = 1.49\text{GHz}$  input frequency with input powers  $P_{rf} = -10\text{dBm}$  (blue),  $P_{rf} = -5\text{dBm}$  (red),  $P_{rf} = 0\text{dBm}$  (green),  $P_{rf} = 5\text{dBm}$  (cyan) and  $P_{rf} = 10\text{dBm}$  (magenta). The measurement is taken with video bandwidth and resolution bandwidth of  $3\text{Hz}$  with 5 times averaging. The noise floor of the spectrum analyzer with these settings is  $-155\text{dBm}$ .

different sources of nonlinear response.

Fig. 5.7 shows a plot of measured third-harmonic response ( $V_{3f}$ ) vs temperature ( $T$ ) and applied rf field amplitude ( $H_{rf}$ ) at an  $f = 4.38\text{GHz}$  input frequency. The measurement is performed on a different location than the one shown in Fig. 5.6. A temperature-independent probe background calculated using Eq. (5.3) below is subtracted from the data for clarity. One notes several families of nonlinear response (separated by white and black dashed lines) that are roughly periodic as a function of applied rf amplitude (see Fig. 5.9). Fig. 5.8 shows a vertical line cut through this image ( $V_{3f}$  vs  $H_{rf}$ ) at a constant temperature of  $T = 9.0\text{K}$ . Similar to Fig. 5.4,  $H_{p1}$ ,  $H_{p2}$  and  $H_{p3}$  are the rf field amplitudes corresponding to the first three dips in  $V_{3f}(H_{rf})$ .

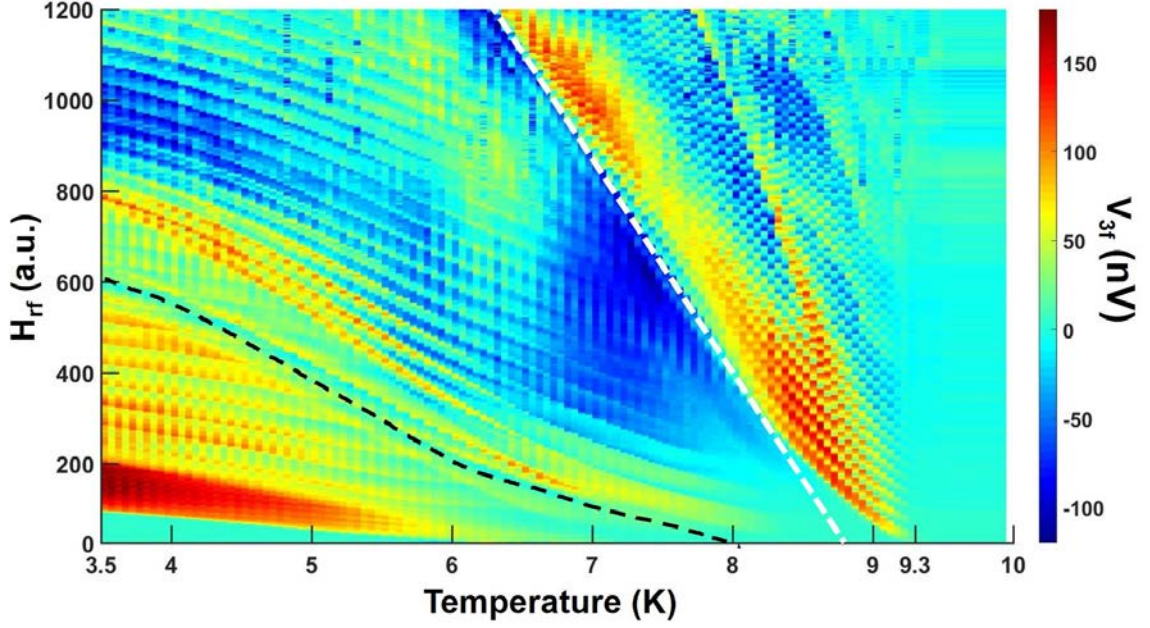


Fig. 5.7 Third-harmonic voltage  $V_{3f}$  data vs temperature and applied rf field amplitude from sample 2 measured at a  $4.38\text{GHz}$  rf input frequency. A temperature-independent probe background nonlinearity (Eq. (5.3)) has been subtracted, resulting in some negative values of  $V_{3f}$ .

Interestingly, the onset of nonlinearity here is the same as the onset of periodic response.

The probe background response was measured at  $0.5\text{K}$  temperature intervals between  $T = 9.4\text{K}$  and  $T = 10.0\text{K}$ . There is no temperature-dependent  $V_{3f}$  signal above  $9.3\text{K}$ , indicating that the superconducting sample is indeed the source of the signal. The green dashed line in Fig. 5.8 shows the probe background averaged over the temperatures between  $T = 9.4\text{K}$  and  $T = 10.0\text{K}$ . It was found that the probe background can be fit to a polynomial

$$V_{bg} = c_1 H_{rf}^3 + c_2 H_{rf}^6 + c_3 H_{rf}^9 \quad , \quad (5.3)$$

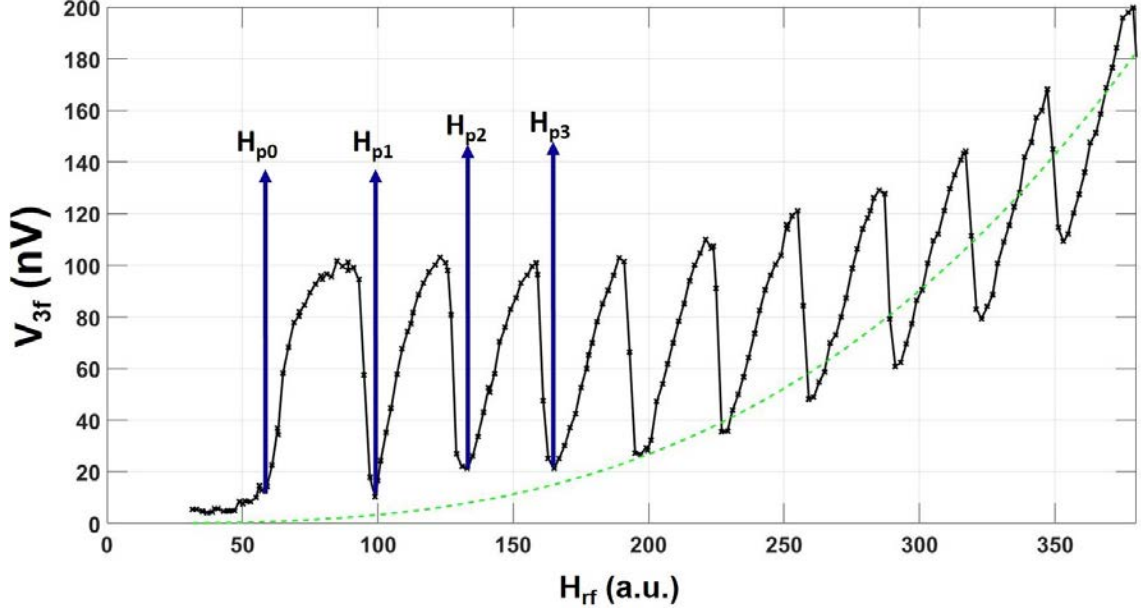


Fig. 5.8 Third-harmonic response  $V_{3f}$  data at  $T = 9.0K$  and  $f = 4.38GHz$  measured on Sample 2. The probe background measured above  $T_c$  is shown as the green dashed line.

where the parameters  $c_1, c_2, c_3$  are unique to each magnetic writer probe and depend on frequency. For the data shown in Figs. 5.7 and 5.8  $c_1 = 3.274 \times 10^{-6} nV / (a.u.)^3, c_2 = 5.943 \times 10^{-16} nV / (a.u.)^6$  and  $c_3 = 6.880 \times 10^{-26} nV / (a.u.)^9$ . Fig. 5.9 shows the temperature dependence of the the dips  $H_{pn}(T)$  extracted from the data shown in Fig. 5.7. We find that  $H_{pn}$  decreases linearly with increasing temperature and reaches a finite saturation value at  $T_c$ . To link the experimental data with the outcome of the current-biased RSJ model that will be presented in Chapter 6, all dips  $H_{pn}(T)$  are fit to a straight line, then the slope of the line is defined as the "period" and the y-intercept is defined as the onset of periodicity  $H_{p0}(T)$  (see Fig. 5.10).

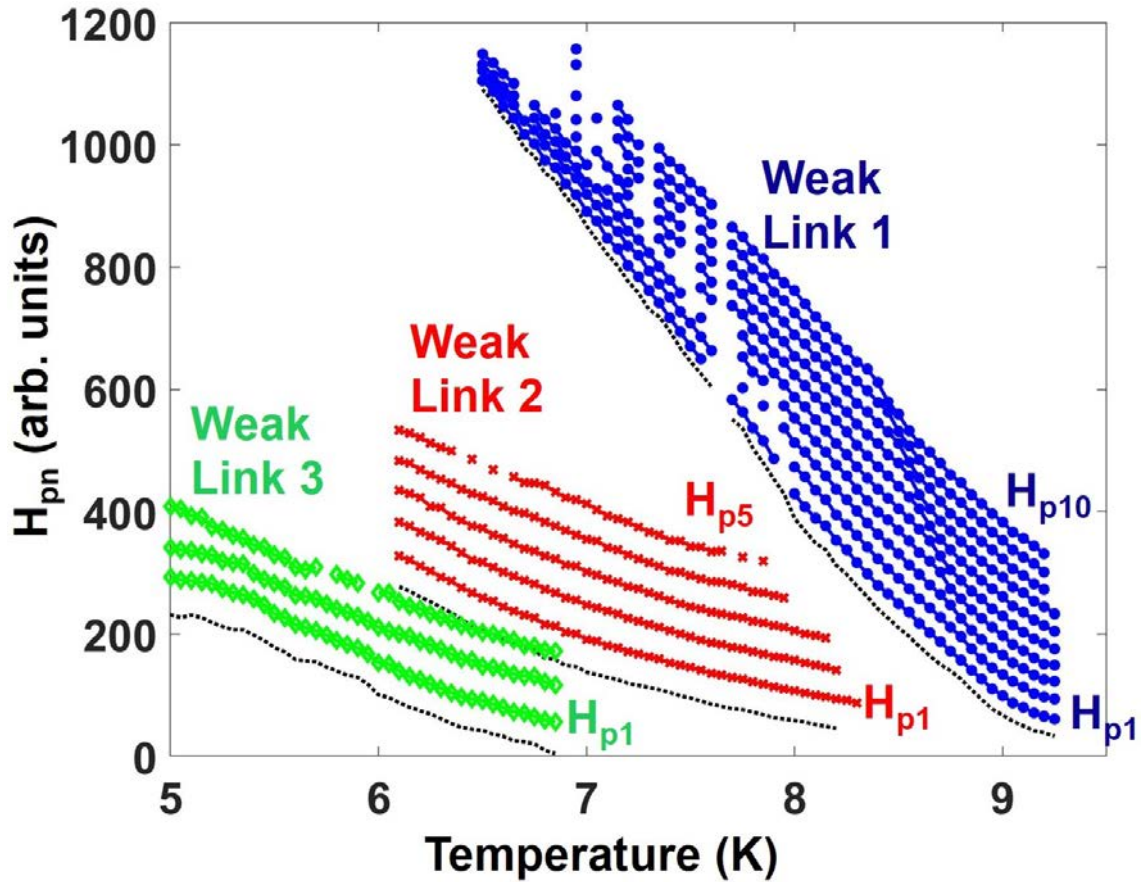


Fig. 5.9 The first few  $H_{pn}$  and the onset of periodicity  $H_{p0}$  (black dashed line) vs temperature for sample 2. Three separate families of dips (blue, red, green) can be attributed to 3 separate weak-links.

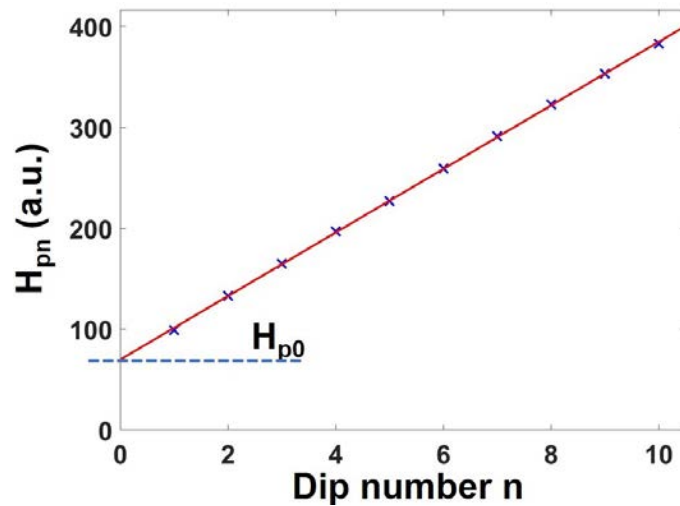


Fig. 5.10  $H_{pn}$  vs  $n$  for the sample 2 at  $T = 9.0\text{K}$ . The solid line is a linear fit to the data.  $H_{p0}$  is defined as the y-intercept of this fit. The "period" is defined as the slope of the fit line. In this particular example,  $H_{p0} = 70.1\text{ a.u.}$  and the period is  $31.54\text{ a.u.}$

### 5.3 Sample 3 – Bulk Nb from Jefferson Lab

Another set of bulk Nb samples is provided by the Ciovati group at Jefferson Lab. A high-purity fine-grain niobium sheet is cut into small samples by wire electrodischarge machining. Later, these samples are etched using buffered chemical polishing, heat treated at 600°C, and etched again. Afterward, the samples are nanopolished to obtain a surface with mirror-quality smoothness. Further details of sample preparation and characterization are available in ref. [124]. The data from this sample are very similar to the data obtained from large-grain bulk Nb sample. Fig. 5.11 shows representative nonlinear response data from sample F9 mentioned in Ref. [124].

### 5.4 Sample 4 – Nb film on copper from ASTeC

A set of Nb on copper thin-film samples was provided by the Malyshev group at the Accelerator Science and Technology Centre (ASTeC) in Warrington, UK. Four samples are deposited by high-power impulse magnetron sputtering at 700°C and various bias voltages on the Cu substrate [125]. The HIPIMS plasma is driven with rectangular voltage pulses at a 200Hz frequency and 100μs pulse duration. The peak discharge current for each pulse is approximately 40A. All Nb film depositions are continued for 4 hours and the resulting films have a thickness of 1.4μm. The residual resistivity ratio (RRR) is measured to be in the 42 – 54 range, peaking for the film prepared at 0 bias voltage. Fig. 5.12 shows representative nonlinear response data from one of



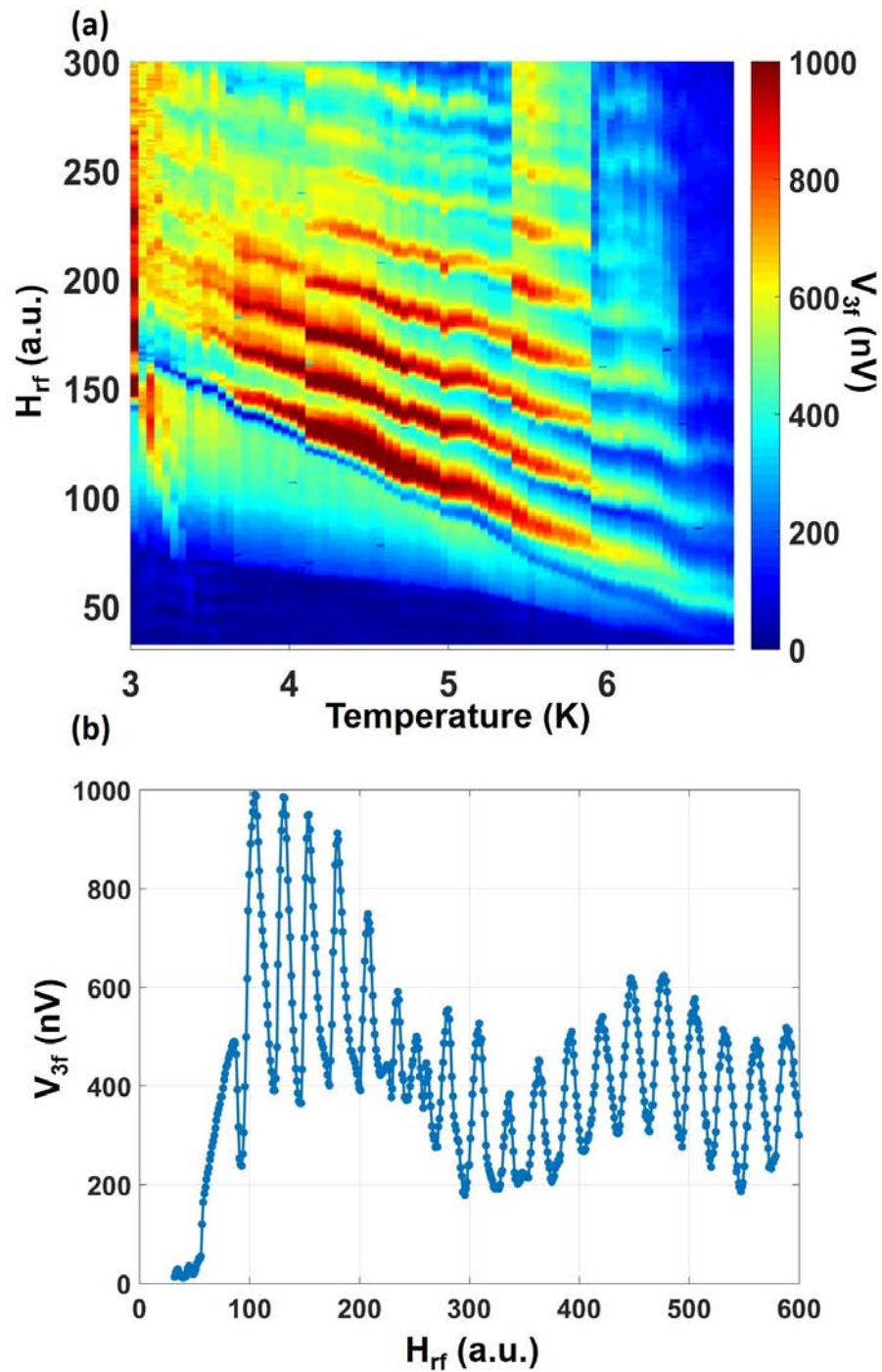


Fig. 5.11 (a) Third-harmonic data  $V_{3f}$  vs temperature and applied rf field amplitude  $H_{rf}$  measured on Sample 3 at  $f = 5.07GHz$  rf input frequency. (b) Vertical line cut through this image ( $V_{3f}$  vs  $H_{rf}$ ) at a constant temperature of  $T = 5.0K$ .

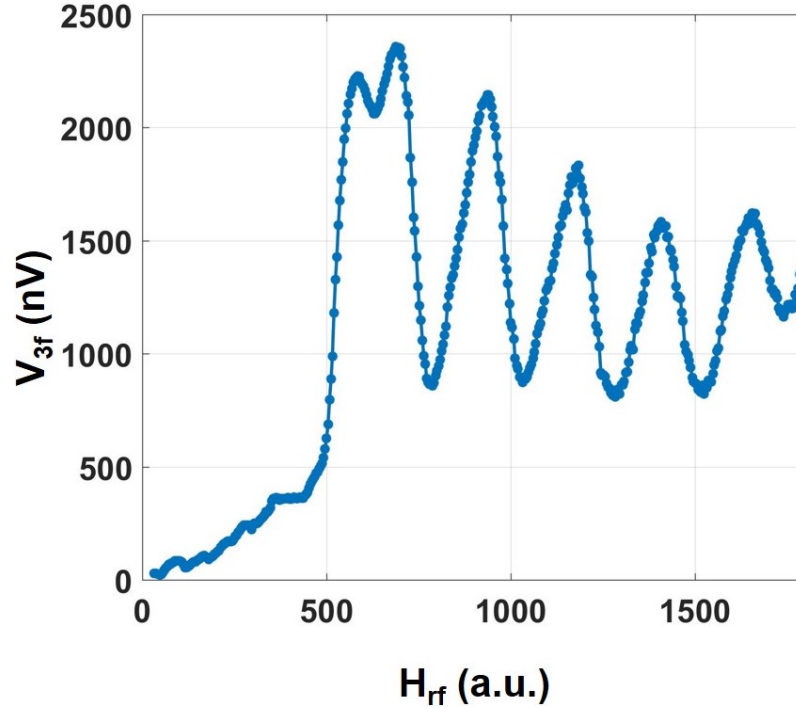


Fig. 5.12 Third-harmonic response  $V_{3f}$  vs input rf field amplitude  $H_{rf}$  data measured on Sample 4 at  $T = 7.5K$  and  $f = 4.855GHz$  rf input frequency.

those samples.

## 5.5 Sample 5 – Nb film on sapphire from Jefferson lab

A set of Nb thin-films were provided by the Valente-Feliciano group at Jefferson Lab. The sample is coated using energetic condensation deposition in UHV via an electron cyclotron resonance (ECR) Nb ion source with a continuous ion energy of 184 eV [126]. The sample has a thickness of 570 nm and is deposited on an  $Al_2O_3$  substrate. The critical temperature is measured to be  $T_c = 9.18K$  and the  $RRR$  is 31. Fig. 5.13 shows representative nonlinear response data from this sample. In this case,



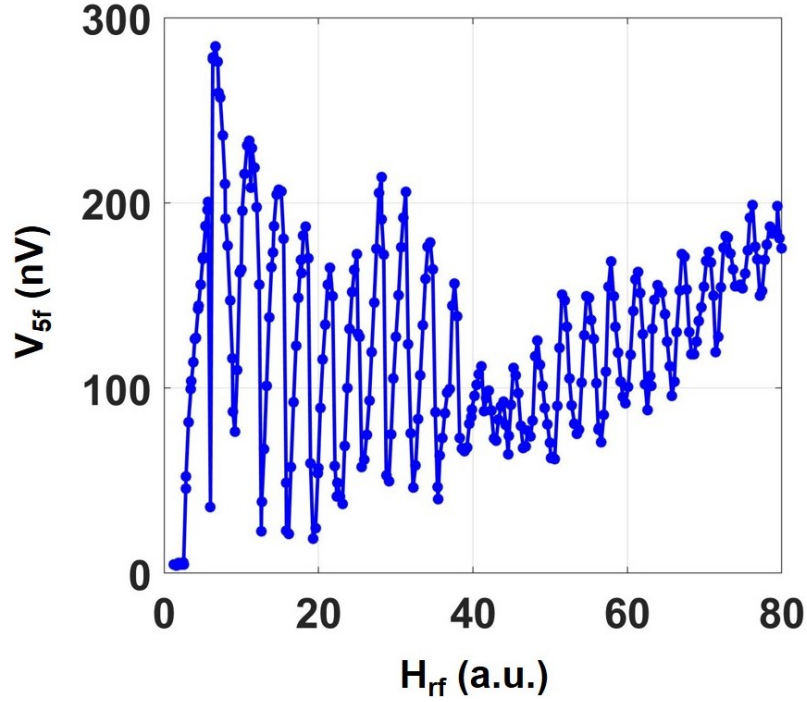


Fig. 5.13 Fifth-harmonic response  $V_{5f}$  vs input rf field amplitude  $H_{rf}$  data measured on Sample 5 at  $T = 4.2K$  and  $f = 1.361GHz$  rf input frequency on Nb thin-film.

the fifth-harmonic response  $V_{5f}$  is measured and a periodic response of  $V_{5f}$  vs  $H_{rf}$  is observed. A similar behavior of  $V_{5f}(H_{rf})$  is observed in the CERN film, Sample 1. We find that the driven RSJ model shows dips in  $V_{5f}$  and  $V_{7f}$  at the same  $H_{rf}$  as  $V_{3f}$  which was confirmed by our measurements up to the 7<sup>th</sup> harmonic response.

## 5.6 Discussion

The first thing to note is that all superconducting samples that I have measured show an abundance of nonlinear response at virtually all excitation field amplitudes and all temperatures below  $T_c$ . For all the samples, a very similar periodic response

of  $V_{3f}$  vs  $H_{rf}$  is observed, showing that this is a generic response of this material. Overall, two types of nonlinear response are observed: a low-field nonperiodic and a higher-field periodic response. All Nb samples show either periodic or low-field response, or both, depending on the spatial location of the magnetic writer probe on the surface of the sample. The intrinsic low-field nonlinear response calculated based on the Ginzburg-Landau (GL) model near  $T_c$  has a strong dependence on the sample thickness [105, 130]. Therefore, bulk Nb samples tend to have a weaker intrinsic nonlinear response compared to thin-film Nb samples. In Chapter 6, I will present the current-biased Resistively Shunted Junction (RSJ) model which can fully explain the periodic nonlinear response. Some parts of the non-periodic response, particularly the response shown in Fig. 5.5(a) can be well described using the nonlinear response produced by vortex semiloops, and this mechanism will be discussed in Chapter 8.

Our understanding of the nonlinear response is limited by the knowledge of the exact field distribution produced by the magnetic writer head on the sample surface. Nonetheless, the magnetic probe is still a very useful tool that can be utilized to compare rf responses across a variety of samples and to identify the source of the nonlinearity. For instance, an important parameter in SRF cavities is the vortex nucleation field, an estimate for which can be obtained by using the measured nonlinear response. This can be achieved by comparing the temperature dependence and absolute value of the onset of nonlinearity  $H_\nu(T)$ , where  $\nu$  stands for vortex, as we believe that vortex nucleation is the reason for the sharp onset of nonlinear response at low rf driving amplitude. This belief is supported by the measured temperature dependence of  $H_\nu(T)$  shown in Fig. 5.5(b) which is similar to the temperature dependence

of the lower critical field  $H_{c1}$ . Furthermore, the Time-Dependent Ginzburg Landau simulations presented in [Chapter 8](#) show that the magnetic writer probe used in my experiment can drive vortex semiloops into the bulk of the superconducting sample. The third-harmonic response generated by these vortex semiloops has a sharp onset as a function of driving rf field amplitude, with the onset field corresponding to first vortex nucleation. Of course, the distribution of rf magnetic field that the sample experiences under the magnetic writer head is categorically different from the one it experiences in an SRF cavity. The magnetic field created by the magnetic writer probe is very "aggressive" and introduces a significant perpendicular component; hence, it does not precisely replicate the parallel rf magnetic fields experienced inside a SRF cavity. Also, the  $H_v$  is measured in arbitrary units and can not be used to get the absolute value of the vortex nucleation field. However, one can use  $H_v$  to compare the value of vortex nucleation field between 2 samples, with lower  $H_v$  indicating lower vortex nucleation field, hence poorer performance in an SRF application.

The third-harmonic onset approach has been used to measure the lower critical field of multilayer structures [[131](#), [132](#)], but the measurements are performed in the  $kHz$  frequency range where the time dynamics of the superconductor can be substantially different from the measurements performed in the  $GHz$  range. The relevant time scales in superconductor response to electromagnetic stimulus will be discussed in [Chapter 9](#).

# 6

---

## Modeling of Harmonic Response

---

In this chapter I will model the periodic nonlinear response described in [Chapter 5](#). The Resistively Shunted Junction (RSJ) Model described here can accurately describe the periodic response and extract some intrinsic parameters associated with the source of this response, such as the BCS superconducting gap and critical temperature. I will also show how two independent models, RSJ and the Vortex-semiloops simulations discussed in [Sec. 8.7](#), can be combined to fit the harmonic response measured at a single location.

### 6.1 Resistively Shunted Junction (RSJ) Model

#### 6.1.1 Weak-links on the surface of Nb

The oxidation of Nb when exposed to air is a well-known and complex phenomenon [[133–136](#)]. Oxygen forms a solid solution in Nb and produces materials with a continuous range of transition temperatures below the bulk  $T_c$  of pure Nb (see

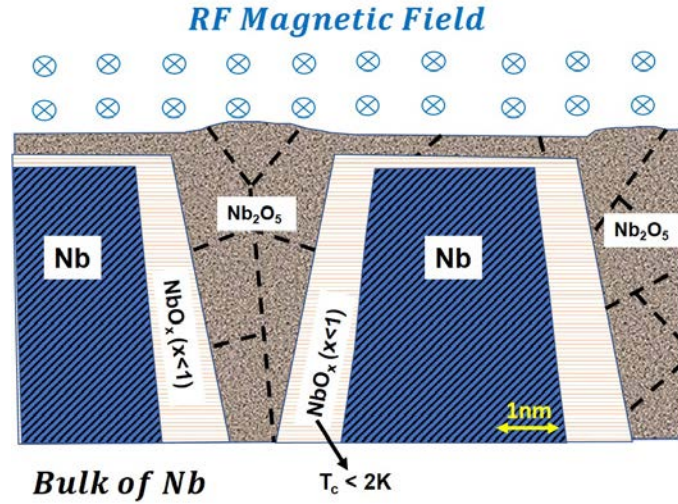


Fig. 6.1 Illustration of oxidation in air of a smooth, single crystal Nb. Metallic NbO<sub>x</sub> and Nb<sub>2</sub>O<sub>5</sub>, which is an insulator, form at the surface when Nb is exposed to air for 30 minutes. RF magnetic field applied to such a surface will drive rf currents through this junction. Parts of this figure are reproduced from [133].

Fig. 6.1). A thin Nb-oxide layer on the surface of Nb sandwiched with a Nb superconductor on both sides can create a superconductor-insulator-superconductor (SIS) or superconductor-normal-metal-superconductor (SNS) Josephson junction [129]. The linear and nonlinear rf impedance of weak-link Josephson junctions can be theoretically modeled in various ways [137–142]. Experimental data showing the rf response of a weak-link Josephson junction in a high-temperature superconductor have been presented in Ref. [137, 143, 144].

### 6.1.2 The response of a weak-link to RF stimulus

To model the periodic part of third-harmonic response as a function of applied rf magnetic field shown in Figs. 5.4, 5.5, 5.7 and 5.8 we utilized the rf current-driven

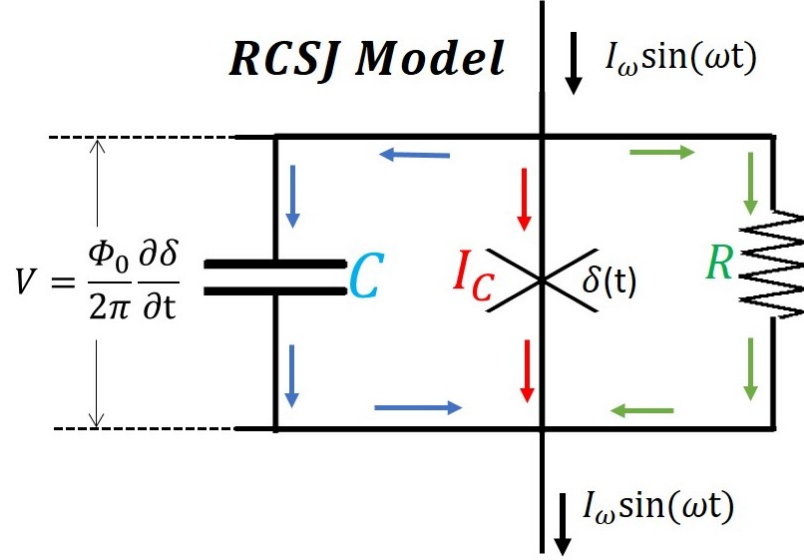


Fig. 6.2 The simplest circuit model for a Josephson Junction. The driving current flows through 3 parallel branches: a capacitive branch due to an Insulating layer, an idealized Junction, and a resistive branch.

RCSJ Model by McDonald and Clem [139]. In this model the Josephson junction (*JJ*) is modeled as an ideal short junction shunted by a resistance (*R*) and a capacitance (*C*) to form a parallel circuit (see Fig. 6.2). In our experiment, the surface currents bias a junction at or near the surface. For a small driving frequency compared to the plasma frequency  $\omega_p = \sqrt{\frac{2\pi I_c}{\Phi_0 C}}$  of the junction, the model can be simplified and the capacitive branch can be ignored. Here  $I_c$  is the critical current of the junction and

$\Phi_0 = \frac{h}{2e}$  is the magnetic flux quantum. The simplified circuit equations become:

$$I_c \sin \delta + \frac{V}{R} + \frac{\Phi_0 C}{2\pi} \frac{\partial^2 \delta}{\partial t^2} = I_\omega \sin(\omega t) \quad \text{and} \quad (6.1)$$

$$V = \frac{\Phi_0}{2\pi} \frac{\partial \delta}{\partial t} \quad ,$$

where  $\delta$  is the gauge-invariant phase difference on the JJ,  $V$  is the potential difference across the junction and  $I_\omega \sin(\omega t)$  is the rf current bias. Eq. (6.1) can be rearranged as

$$\frac{I_c R}{\omega} \sin \delta + \frac{\Phi_0}{2\pi} \frac{\partial \delta}{\partial(\omega t)} = \frac{I_\omega R}{\omega} \sin(\omega t) \quad . \quad (6.2)$$

Eq. (6.2) has 2 key parameters:  $I_c R/\omega$  and  $I_\omega R/\omega$ . Eq. (6.2) is solved for a known  $I_c R$  and  $I_\omega R$  using the classic Runge-Kutta method to obtain  $\delta(\omega t)$  and  $V(\omega t)$ . The gauge-invariant phase  $\delta(t)$  was solved with  $\omega \Delta t/2\pi = 10^{-5}$  time steps until the steady state solution is reached, which was defined as the time when the condition  $|\delta(t) - \delta(t - 16\pi/\omega)| < 10^{-4} \delta(t - 16\pi/\omega)$  is satisfied at all times in the range of  $(t - 16\pi/\omega, t)$ . Fig. 6.3 shows the gauge-invariant phase difference  $\delta$  and voltage across an RSJ for one RF period. The curves are the solutions to Eq. (6.2) for  $\omega/2\pi = 1\text{GHz}$ ,  $I_c R = 20\mu\text{V}$  and  $I_\omega R = 20\mu\text{V}$  (red),  $I_\omega R = 25\mu\text{V}$  (green) and  $I_\omega R = 30\mu\text{V}$  (blue). For the driving current less than the critical current of the junction  $I_\omega < I_c$ , most of the current passes through the ideal junction branch (see Eq. (6.1)). For  $I_\omega > I_c$ , parts of the current will be diverted to the resistive branch and generate a

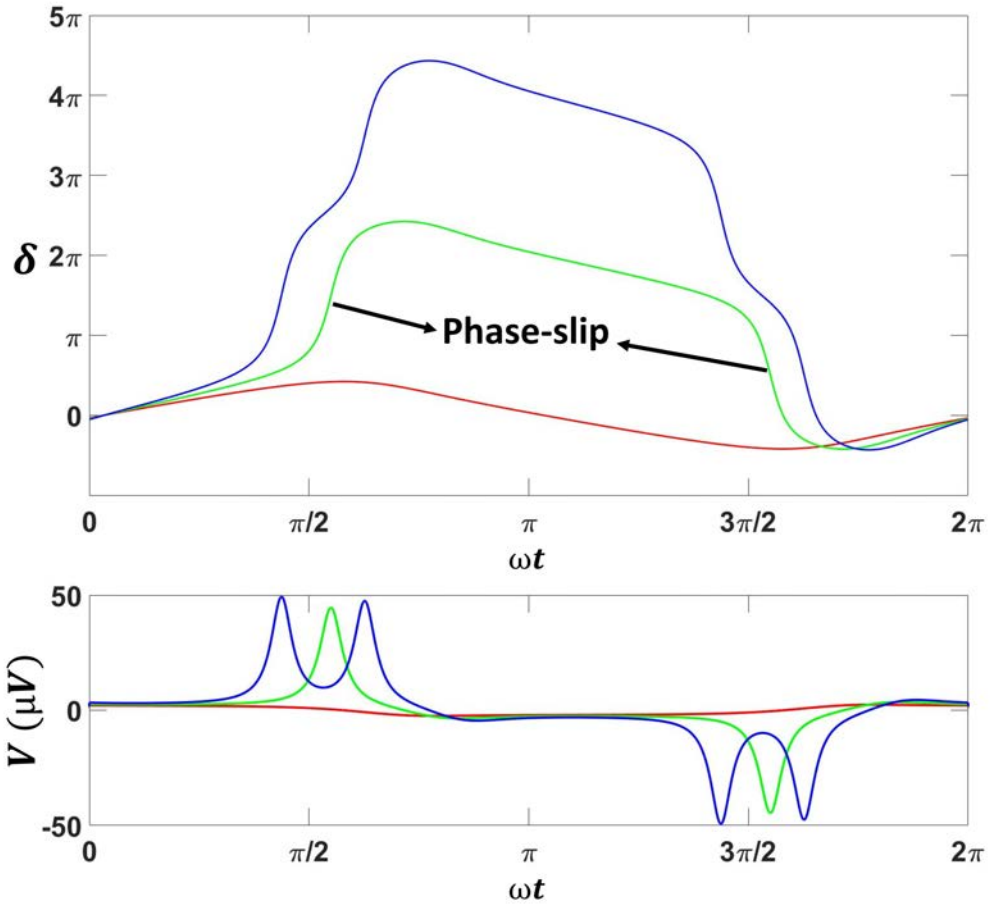


Fig. 6.3 Calculated gauge-invariant phase difference  $\delta$  (top) and voltage (bottom) across an RSJ as a function of normalized time  $\omega t$  for one RF period in steady state. The calculation is done using Eq. (6.2) with frequency of  $\omega/2\pi = 1\text{GHz}$ ,  $I_c R = 20\mu\text{V}$  and  $I_\omega R = 20\mu\text{V}$  (red),  $I_\omega R = 25\mu\text{V}$  (green) and  $I_\omega R = 30\mu\text{V}$  (blue). Note that the  $2\pi$  phase slips in  $\delta(\omega t)$  produce voltage spikes across the junction, leading to harmonic response.

finite voltage across the junction, leading to a  $2\pi$  phase-slip across the junction (see Fig. 6.3). The total number of these phase-slips events within one rf cycle increases with  $I_\omega$ .



### 6.1.3 Weak-link harmonic response

In general, the voltage drop on the junction is nonsinusoidal in time and contains harmonics and subharmonics of the driving frequency  $\omega$ . After the solution for  $\delta(t)$  comes to steady state the Fourier transform of  $V(t)$  is taken to calculate the third-harmonic voltage  $V_{3\omega}$  and phase  $\Theta_{3\omega}$  across the junction,

$$V_{3\omega}e^{i\Theta_{3\omega}} = 2 \int_0^{2\pi/\omega} V(t)e^{3i\omega t} dt \quad (6.3)$$

where  $i = \sqrt{-1}$ . One can calculate the third-harmonic voltage  $V_{3\omega}$  across the junction as a function of driving current amplitude  $I_\omega$  for a given critical voltage of the junction  $I_c R$ . Fig. 6.4 show an example for such a calculation done at  $\omega/2\pi = 1\text{GHz}$  and  $I_c R = 20\mu\text{V}$ . The result closely resembles the experimental data shown in Figs. 5.4, 5.5, 5.7 and 5.8. The markers correspond to the three curves shown in Fig. 6.3. Each peak in  $V_{3\omega}$  vs  $I_\omega R$  corresponds to creating an additional  $2\pi$  phase-slip across the junction in the driving RF cycle.

Note that the separation between the dips as a function of  $I_\omega R$  is constant. This calculation was repeated for a very large range of  $I_c R$  values. Using a procedure similar to that outlined on page 93, the  $I_\omega R$  amplitudes corresponding to the dips in  $V_{3\omega}(I_\omega R)$  were identified and defined as  $H_{pn}(I_c R)$ , where  $n$  stands for  $n$ 'th dip. To uniquely relate experimental data at a temperature  $T$  to the RSJ calculation at a constant  $I_c R$ , all dips  $H_{pn}(I_c R)$  are fit to a straight line, then the slope of the line is defined as the "period" and the y-intercept is defined as the onset of periodicity  $H_{p0}(I_c R)$  (similar to Fig. 5.10).

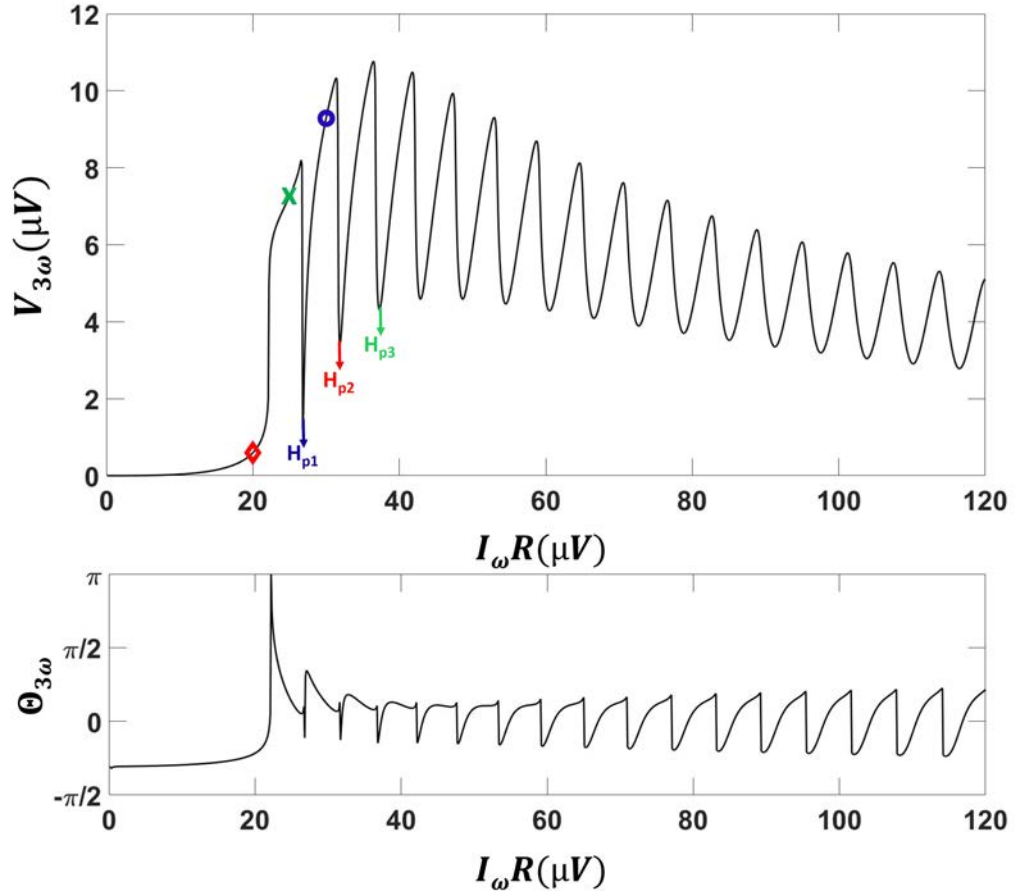


Fig. 6.4 Calculated magnitude (top) and phase (bottom) of third harmonic voltage across an RSJ junction vs  $I_\omega R$  for  $I_c R = 20 \mu V$ . The markers correspond to three curves shown in Fig. 6.3:  $\diamond$ -red line,  $\times$ -green line, and  $\circ$ -blue line. Each periodic feature in  $V_{3\omega}$  and  $\Theta_{3\omega}$  correspond to an additional  $2\pi$  phase slip in the junction during each rf period.

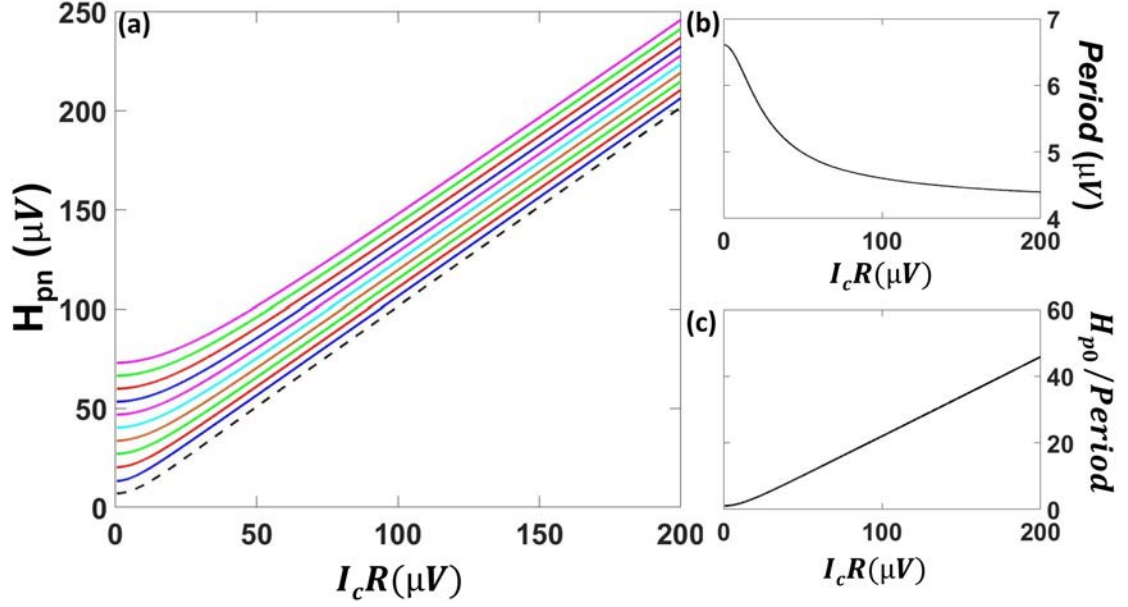


Fig. 6.5 (a) Solid lines:  $H_{p1}$ ,  $H_{p2}$ ,  $H_{p3}$ ,  $H_{p4}$ ,  $H_{p5}$ ,  $H_{p6}$ ,  $H_{p7}$ ,  $H_{p8}$ ,  $H_{p9}$ ,  $H_{p10}$  and  $H_{p0}$  (dashed line) vs  $I_cR$  calculated from the RSJ model. (b) Period of the dips  $H_{pn}$  vs  $I_cR$ . (c) Onset-to-period ratio  $\frac{H_{p0}}{\text{Period}}$  vs  $I_cR$ .

Fig. 6.5(a) shows  $H_{p0}$  to  $H_{p10}$  vs  $I_cR$  calculated from the RSJ model. The period is found to be nearly constant as a function of  $I_cR$  (see Fig. 6.5(b)).  $H_{p0}$  linearly decreases with  $I_cR$  and saturates at low  $I_cR$  values. This is consistent with the experimental data shown in Fig. 5.9, where  $H_{p0}$  saturates as  $T \rightarrow T_c$ .

The results shown in Figs. 6.3 to 6.5 are calculated for  $f = 1\text{GHz}$ . However, as evident from Eq. (6.2), these results can be generalized to other frequencies, by means of the following scaling:  $I_cR \rightarrow I_cR \times f/1\text{GHz}$ ,  $I_\omega R \rightarrow I_\omega R \times f/1\text{GHz}$  and  $V \rightarrow V \times f/1\text{GHz}$ . For example the solutions of Eq. (6.2) for  $I_cR = I_\omega R = 10\mu V$  at  $\omega/2\pi = 1\text{GHz}$  and the solution for  $I_cR = I_\omega R = 20\mu V$  at  $\omega/2\pi = 2\text{GHz}$  should be identical.

### 6.1.4 Fitting the measured third harmonic data

The challenging part of this model is to relate simulation results to experimental data. From measurements we have  $H_{rf}$  in arbitrary units, while in the RSJ calculation

we have the biasing current  $I_\omega R$  in  $\mu V$ . A scaling factor  $X_{scale} = \frac{I_\omega R}{H_{rf}}$  has to be found.

Also,  $V_{3\omega}$  is calculated across the junction, while the third harmonic response  $V_{3f}$  is measured at the probe through a transmission line, which is lossy. Thus, a scaling

factor for harmonic signal  $Y_{scale} = \frac{V_{3\omega}}{V_{3f}}$  is also required.

For the current-biased resistively shunted junction (RSJ) model, I realized that the onset-to-period ratio uniquely and monotonically depends on  $I_c R$  (see Fig. 6.5(c)) and does not depend on the choice of  $X_{scale}$ . Thus the measured onset-to-period ratio from the data taken at a constant temperature allows direct extraction of  $I_c R(T)$  for the junction.

To calculate  $I_c R(T)$  of the junction, for every temperature the onset-to-period ratio  $\frac{H_{p0}}{Period}$  was calculated from the data. Then the unique value of  $I_c R$  corresponding to that onset-to-period ratio was identified. This procedure was then repeated for each measurement temperature to find  $I_c R(T)$ . Once  $I_c R(T)$  is known,  $X_{scale}(T)$  is calculated as the ratio of  $H_{p0}$  calculated from the RSJ model to  $H_{p0}$  calculated from the experimental data, while  $Y_{scale}(T)$  is left as a free fitting parameter.

Fig. 6.6 show the RSJ fit to the third-harmonic response measured on Sample 2 and shown in Fig. 5.8. The onset-to-period ratio for this dataset was found to be

$\frac{H_{p0}}{Period} = 2.22$  (see Fig. 5.10), which at  $f = 4.38GHz$  correspond to  $I_c R = 49.4\mu V$ .

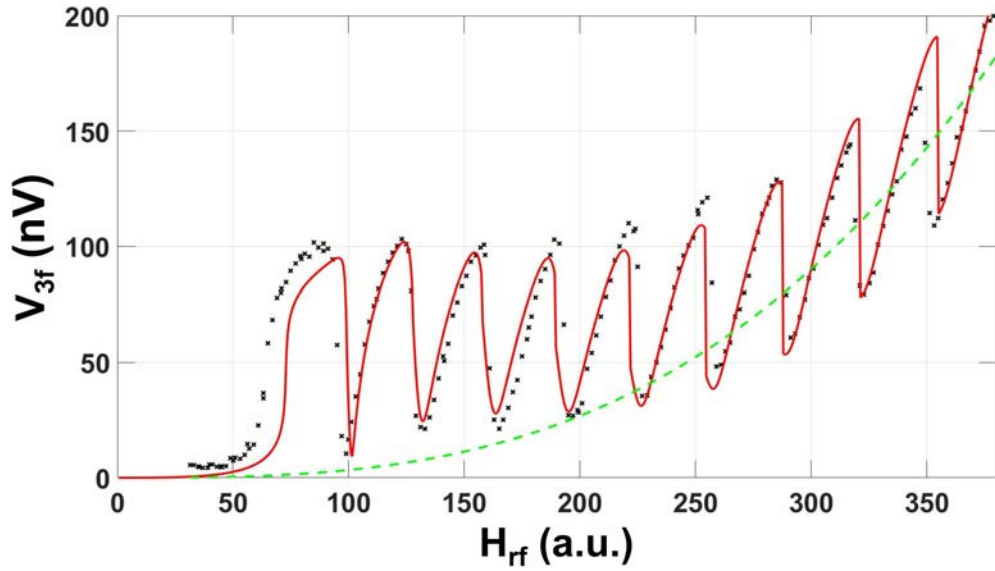


Fig. 6.6 Third-harmonic response  $V_{3f}$  data at  $T = 9.0K$  and  $f = 4.38GHz$  measured on Sample 2 (black  $\times$  markers). The probe background measured above  $T_c$  is shown as the green dashed line. The RSJ fit with  $I_c R = 49.4\mu V$  is shown as the red solid line.

The RSJ fit, which is shown as the red solid line in Fig. 6.6, is the result of complex addition of the probe background and solution to the RSJ circuit equation (Eq. (6.2)) for  $I_c R = 49.4\mu V$  and  $f = 4.38GHz$ . Eq. (5.3) is used to calculate the probe background shown as the green dashed line in Fig. 6.6. The probe background is assumed to be constant as a function of temperature and in-phase with the  $H_{rf}$ . As a result of the complex addition, some dips in  $V_{3f}(H_{rf})$  above  $H_{rf} > 200a.u.$  are lower than the probe background.

This fitting procedure is repeated for each temperature. Note that three families of periodic features are visible in Fig. 5.7, with different periods and onsets  $H_{p0}$  (see Fig. 5.9). Each of these families can be attributed to a separate weak-link and fit independently. The summary of the fit parameters used is given in Table 6.1.

An estimate of the applied rf field strength created by the probe on the surface of the sample can be made as follows. At higher temperatures as  $T \rightarrow T_c$ , the upper critical magnetic field is given by  $B_{c2}(T) \approx 2B_{c2}(0)(1 - T/T_c)$ . By determining the  $H_{rf}$  value at which the periodic nonlinear response is suppressed, and assuming  $B_{c2}(0) = 240mT$  [51, 126] and  $T_c = 9.3K$ , we can estimate the rf field experienced by the defect to be  $11.4\mu T/(arb.unit)$ . This approximately calibrates the vertical axis in Fig. 5.7 and the horizontal axis in Fig. 6.6. Similarly, using the horizontal scaling factor of  $\langle X_{scale} \rangle = 0.22\mu V/(arb.units)$  obtained from the RSJ fit and an estimated weak-link normal state resistance of  $R_n = 100\Omega$  [129], we can estimate the driving current flowing through the weak-link to be  $2.2nA/(a.u.)$ . Thus, for weak-link 1 in Fig. 5.7, this would correspond to a maximum rf magnetic field amplitude of  $13.7mT$  and maximum driving current of  $I_\omega = 2.6\mu A$  with a zero-temperature critical current of  $I_c(0) = 12.6\mu A$ .

Fig. 6.7 show the combined fit to the third-harmonic response measured on Sample 1 and shown in Fig. 5.5(a). The onset-to-period ratio for this dataset was found to be  $\frac{H_{p0}}{Period} = 4.8$ , which at  $f = 2.2GHz$  correspond to  $I_c R = 58.3\mu V$ . Next, the horizontal axis scaling factor for the RSJ model is fixed to match the  $H_{p0}$  from the RSJ model to the  $H_{p0}$  from the data.

The RSJ fit with this parameters does not account for the  $H_{rf} < H_{p0}$  part of the data. This "pedestal" low-field non-periodic part of the third harmonic data can be attributed to intrinsic response due to vortex semiloops created by our magnetic writer probe. This response is calculated by solving Time-Dependent Ginzburg Landau

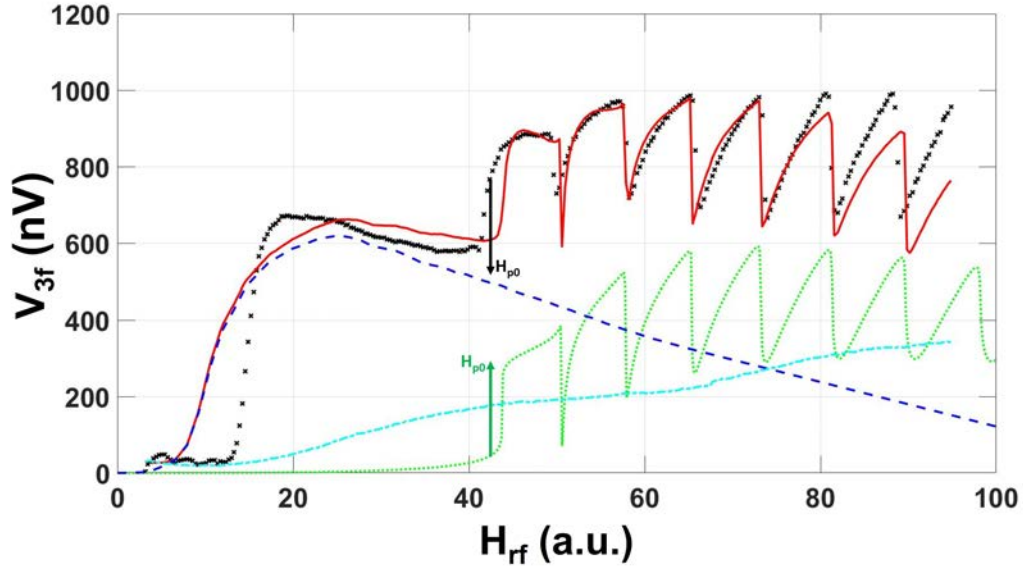


Fig. 6.7 Third-harmonic response  $V_{3f}$  data from Sample 1 at  $T = 5.1K$  and  $f = 2.2GHz$  (black  $\times$  markers). Also shown are the RSJ fit with  $I_c R = 58.3\mu V$  (green dashed-dotted line), time-dependent Ginzburg-Landau fit with  $H_{dp} = 12$  (blue dashed line) (see Sec. 8.7), probe background (cyan dotted line) and complete fit obtained by vector complex addition (red solid line).

(TDGL) equations for a magnetic writer probe above the superconducting sample. The magnetic writer probe was approximated to be a pointlike magnetic dipole with a sinusoidal time-dependent magnetic moment  $\vec{M}_{dp}(t)$ , located at a height  $h_{dp}$  above the origin and parallel to the surface. This model is presented in great detail in Sec. 7.4.2.

In total the data shown in Fig. 6.7 have contributions from a nonlinear response generated by the current-biased junction, intrinsic low-field nonlinearity modeled by TDGL, and a temperature-independent probe background. A complex vector addition of all three contributions is performed for a full fit. The probe background was measured at 10K and the phase of the probe background was assumed to be constant and is set to zero, while the complex values of the model responses are included in

the sum. The horizontal and vertical axis scaling factors for the TDGL model and the vertical axis scaling factor for the RSJ model are the three fitting parameters.

### 6.1.5 Extracting BCS superconducting gap value

Fig. 6.8(a) shows the values of the  $I_c R(T)$  extracted from the fits to data measured on sample 1 (see Fig. 5.5) and Sample 2 (see Fig. 5.9). As a next step, the Ambegaokar-Baratoff relations were used to estimate the superconducting gap  $\Delta(T)$  from  $I_c R(T)$  [145, 146]:

$$I_c R(T) = \frac{\pi \Delta(T)}{2e} \tanh\left(\frac{\Delta(T)}{2k_B T}\right) . \quad (6.4)$$

Here we assume that the junction formed by the weak-link is an Superconductor-Insulator-Superconductor (SIS) junction. Finally, the temperature dependence of the superconducting gap  $\Delta(T)$  was fit to the temperature dependence of the gap predicted by BCS theory (see Eq. (1.13) and Fig. 1.6) [36] and  $\Delta(0)$  was extracted (see Fig. 6.8(b)). The resulting fitting parameters are summarized in Table 6.1.

Superconducting gap values obtained from fits shown in Table 6.1 are lower than the bulk value  $\Delta(0) = 1.55 \text{ meV}$  reported elsewhere [147]. Nb samples with higher oxygen content tend to have lower superconducting gap values [133, 148]. Thus the superconducting gap value at a Nb/NbO<sub>x</sub>/Nb weak-link can be lower due to a gradient in oxygen content. The fact that the responses from the three weak-links on Sample 2 have different superconducting gap  $\Delta(0)$  values and  $T_c$ 's shows that they



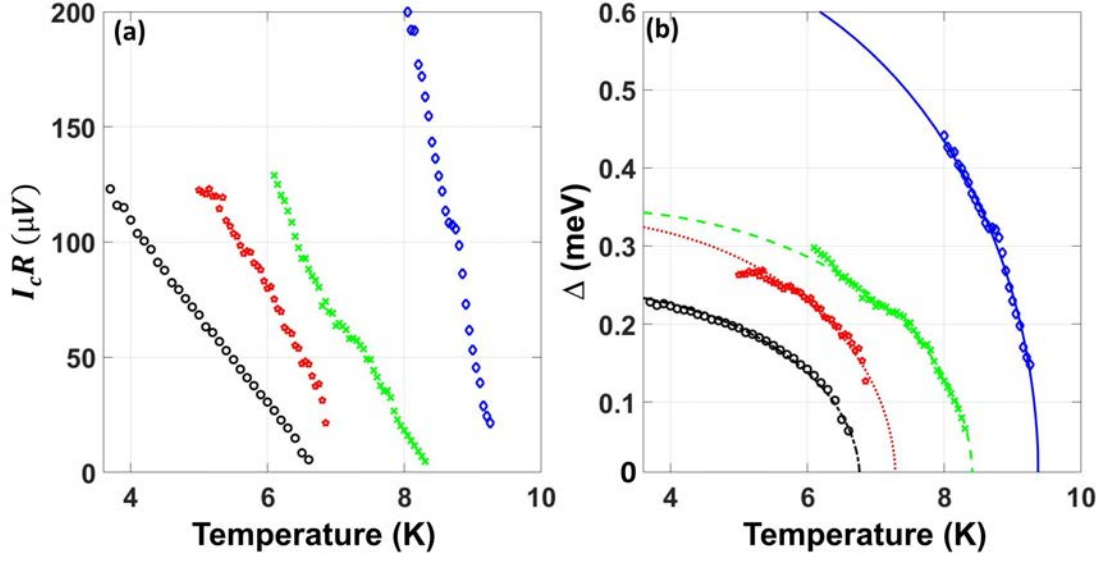


Fig. 6.8 (a)  $I_c R(T)$  values extracted from the RSJ fit to the sample 1 data (black  $\circ$  markers) and weak-link 1 (blue  $\diamond$  markers), weak-link 2 (green  $\times$  markers) and weak-link 3 (red  $\star$  markers) of sample 2. (b) Calculated superconducting gap from sample 1 data (black  $\circ$  markers-dash-dotted line) and weak-link 1 (blue  $\diamond$  markers-solid line), weak-link 2 (green  $\times$  markers-dashed line) and weak-link 3 (red  $\star$  markers-dotted line) of sample 2.

likely have different oxygen content.

### 6.1.6 Discussion

In summary, the RSJ model can explain the periodicity in  $V_{3f}(H_{rf})$  that have been observed in many samples that we have measured. This confirms the existence of active weak-links on air-exposed SRF grade Nb samples.

The fact that we can distinguish the nonlinear response coming from three separate weak-links on Sample 2 demonstrates the strength of the nonlinear response approach to surface characterization. A single point measurement was sensitive enough to study three surface defects simultaneously. The values for the  $\langle X_{scale} \rangle$  listed in

Sample	Weak-Link Family	$\Delta(0)$ (meV)	$T_c$ (K)	$\langle X_{scale} \rangle$ ( $\mu V/a.u.$ )	$\langle Y_{scale} \rangle$ (nV/nV)
Sample 1	-	0.25	6.76	1.61	22.85
Sample 2	1	0.80	9.28	0.22	68.56
	2	0.35	8.41	0.12	120
	3	0.33	7.28	0.11	125

Table 6.1 Summary of RSJ model fit parameters extracted from third-harmonic data on two Nb samples. Weak-link number indicates the family number in the data.

Table 6.1 show that perhaps weak-link 1 is located closest to the probe, hence experiences the highest driving current for the same applied rf field  $H_{rf}$ . Furthermore, the weak-link 1 has the smallest value of  $\langle Y_{scale} \rangle$  among the three, indicating lower attenuation of nonlinear response which reaffirms the hypothesis that weak-link 1 is located closest to the probe.

I also demonstrate the ability to successfully differentiate between the sources of local nonlinearity based on their dependence on rf field amplitude and temperature. For example, in Fig. 6.7, we can clearly distinguish between the nonlinear response generated by a weak-link and nucleation of vortex semiloops. The  $H_{rf}$  value at which the vortex nonlinearity is measured is lower than the onset of junction nonlinear response  $H_{p0}$ . We attribute this to the fact that vortex-semiloops are created just beneath the probe while the surface weak-link can be anywhere on the surface within the writer head field of view. As evident by the spatial distribution of the magnetic field generated by the magnetic writer probe (see Fig. 4.10), the rf field experienced by the weak-link in this scenario can be considerably lower than the rf field on the surface of the superconducting sample just below the probe.

# 7

---

## Ginzburg-Landau Simulations

---

### 7.1 Ginzburg-Landau Theory

#### 7.1.1 Ginzburg-Landau Free Energy Functional

In 1950, 7 years before the BCS Theory, Ginzburg and Landau postulated the complete fundamental equations for macroscopic superconductivity [18]. Their work is praised as a triumph of physical intuition. The London equations for superconductor electrodynamics [15–17, 19] (Sec. 1.2.2), the Abrikosov vortex lattice [26], and the Josephson relations [29, 149] (Sec. 1.2.7), all can be found as solutions to the GL equations. The GL theory is a generic macroscopic model appropriate for understanding the electrodynamic response of superconductors subjected to static magnetic fields and currents in the limit of weak superconductivity. GL theory is an example of a mean-field theory, where the attention is given to the collective properties instead of individual particles. Mean-field theories provide a good qualitative description of phase transition behavior.

Ginzburg and Landau started from the theory of second-order phase transitions, which they had previously developed. The GL model defines a superconductor as a charged Bose superfluid with particles of mass  $m_*$  and charge  $e_*$  and introduces a complex-valued "order parameter"  $\Psi(\vec{r})$ , where  $\vec{r}$  is position. The order parameter is a measure of the local strength of the superconducting state and is defined as  $|\Psi(\vec{r})|^2 = n_s(\vec{r})$  where  $n_s(\vec{r})$  is the superfluid density at position  $\vec{r}$ . In the ordered (superconducting) phase the order parameter is nonzero. If the superconducting state is fully destroyed in any domain within the sample, that domain is said to be in the non-ordered phase (normal state), and the order parameter has to go to zero there  $\Psi(\vec{r}) = 0$ , hence  $n_s(\vec{r}) = 0$ .

GL starts with an expression for the free energy of a superconductor in terms of position-dependent order parameter and vector potential. The total Ginzburg-Landau free energy has the form  $F_{tot}(\Psi(\vec{r}), \vec{A}(\vec{r})) = \int d^3\vec{r} \mathcal{F}_{GL}(\vec{r})$ , where  $\vec{A}$  is the magnetic vector potential and the Ginzburg-Landau free energy density as a function position  $\vec{r}$  is [150]:

$$\mathcal{F}_{GL}(\vec{r}) = \mathcal{F}_L(\Psi(\vec{r})) + \mathcal{F}_{grad}(\Psi(\vec{r}), \vec{A}(\vec{r})) + \mathcal{U}_{mag}(\vec{A}(\vec{r})) \quad . \quad (7.1)$$

Here,  $\mathcal{F}_L$  is Landau term which is the same free energy density as in the Landau mean field theory.  $\mathcal{F}_L$  does not include any direct effects of the externally applied magnetic field. It is the free energy density which depends only on  $\Psi(\vec{r}, T)$ , where  $T$

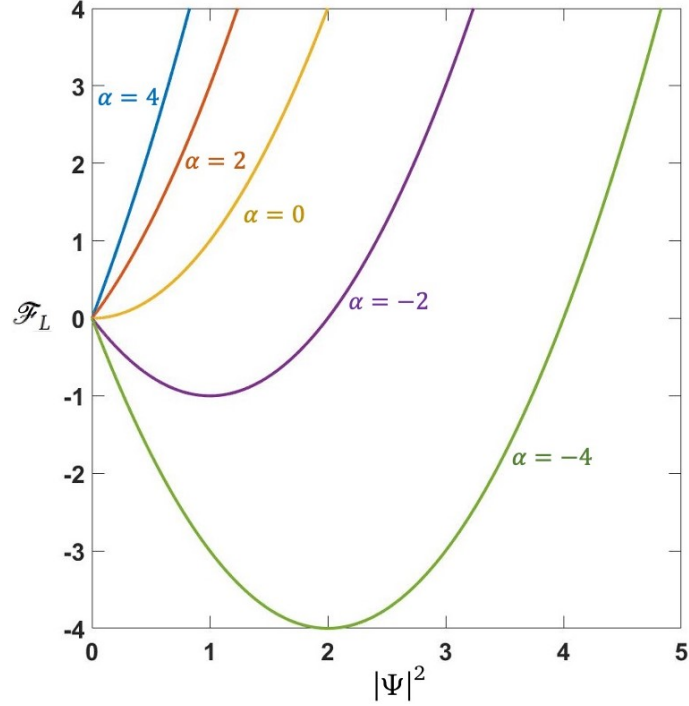


Fig. 7.1  $\mathcal{F}_L$  vs  $|\Psi|^2$  for several  $\alpha$  values ( $\beta = 1$ ). Note the existence of a minimum in  $\mathcal{F}_L$  at finite non-zero  $|\Psi|^2$  when  $\alpha < 0$ .

is temperature and the analytic function of that dependence has the following form:

$$\mathcal{F}_L(\Psi) = \alpha(\vec{r}, T)\Psi^2 + \frac{\beta(\vec{r}, T)}{2}\Psi^4 + \dots \quad (7.2)$$

where  $\alpha(\vec{r}, T)$  and  $\beta(\vec{r}, T)$  are the temperature and position-dependent phenomenological expansion parameters.  $\beta < 0$  corresponds to the ground state being at  $|\Psi(\vec{r}, T)|^2 = \infty$ , thus we set  $\beta > 0$ . For any  $\alpha > 0$  (given  $\beta > 0$ ) the ground state is the state with no superfluid density  $|\Psi(\vec{r}, T)|^2 = 0$ , representing the normal state.

Fig. 7.1 shows  $\mathcal{F}_L$  vs  $|\Psi|^2$  for several  $\alpha$  values. Here we see that for  $\alpha > 0$  the minima for  $\mathcal{F}_L$  occurs at  $\Psi = 0$ . This means that for any  $\alpha > 0$  the ground state is the state with no superfluid density, thus the normal state. For  $\alpha < 0$  the minima for  $\mathcal{F}_L$

occurs at  $\Psi = \Psi_\infty$ , where  $|\Psi_\infty(T)|^2$  is the bulk superfluid density in the absence of external magnetic field,

$$\Psi_\infty(T) = \sqrt{\frac{-\alpha(T)}{\beta(T)}} . \quad (7.3)$$

Since a transition from the superconducting state to the normal state is expected at the superconducting critical temperature  $T_c$ , one would expect  $\alpha$  to change sign at  $T_c$ . Furthermore,  $\alpha$  is expected to be an analytic function of temperature, thus one can postulate the following temperature dependence for  $\alpha$ ,

$$\alpha(T) = \alpha'(T - T_c) . \quad (7.4)$$

Substituting  $\Psi_\infty$  back into [Eq. \(7.2\)](#) we get the condensation energy

$$\mathcal{F}_{sc} - \mathcal{F}_n = \mathcal{F}_L(\Psi_\infty) = \alpha\Psi_\infty^2 + \frac{\beta}{2}\Psi_\infty^4 = \alpha\frac{-\alpha}{\beta} + \frac{\beta}{2}\frac{\alpha^2}{\beta^2} = -\frac{\alpha^2}{2\beta} , \quad (7.5)$$

with  $\mathcal{F}_n$  being the free energy density of the normal state.

$\mathcal{F}_{grad}$  is a kinetic energy term due to interaction of superconducting current and magnetic field and is given by

$$\mathcal{F}_{grad}(\Psi(\vec{r}), \vec{A}(\vec{r})) = \frac{\hbar^2}{2m_*} \left| \left( \vec{\nabla} - \frac{ie_*}{\hbar} \vec{A} \right) \Psi \right|^2 . \quad (7.6)$$

Finally,  $\mathcal{U}_{mag}(\vec{A})$  is the magnetic field energy density and given by

$$\mathcal{U}_{mag}(\vec{A}) = \frac{1}{2\mu_0} |\vec{\nabla} \times \vec{A} - \vec{B}_a|^2, \quad (7.7)$$

where  $m_* = 2m_e$  is the mass of the Cooper pair,  $e_* = 2e$  is the charge of the Cooper pair,

$\vec{B}_a = \vec{B}_a(\vec{r}, t)$  is the amplitude of the externally applied magnetic field, and  $i = \sqrt{-1}$ .

Substituting Eq. (7.2), Eq. (7.6) and Eq. (7.7):

$$\mathcal{F}_{GL}(\vec{r}) = \alpha(\vec{r}, T)\Psi^2 + \frac{\beta(\vec{r}, T)}{2}\Psi^4 + \frac{\hbar^2}{2m_*} \left| \left( \vec{\nabla} - \frac{ie_*}{\hbar}\vec{A} \right) \Psi \right|^2 + \frac{1}{2\mu_0} |\vec{\nabla} \times \vec{A} - \vec{B}_a|^2. \quad (7.8)$$

Taking variational derivatives and minimizing the free energy with respect to  $\Psi$  and  $\vec{A}$  leads to the coupled Ginzburg-Landau equations [21, 36, 151–153]:

$$\alpha\Psi + \beta|\Psi|^2\Psi + \frac{\hbar^2}{2m_*} \left( \vec{\nabla} - \frac{ie_*}{\hbar}\vec{A} \right)^2 \Psi = 0 \quad \text{and} \quad (7.9)$$

$$\frac{1}{\mu_0} \vec{\nabla} \times (\vec{\nabla} \times \vec{A} - \vec{B}_a) = \frac{e_*\hbar}{2m_*i} (\Psi^* \vec{\nabla} \Psi - \Psi \vec{\nabla} \Psi^*) - \frac{e_*^2}{m_*} |\Psi|^2 \vec{A}, \quad (7.10)$$

where  $\alpha = \alpha(\vec{r}, T)$  and  $\beta = \beta(\vec{r}, T)$ .

### 7.1.2 Gor'kov's validation of GL theory

Although the Ginzburg-Landau theory precedes the Bardeen-Cooper-Schrieffer (BCS) microscopic theory [154, 155], in 1959 Gor'kov was able to derive the same equation from BCS theory in the limit where the temperature is close to the superconducting critical temperature [21]. To derive a GL like equation, Gor'kov had used several assumptions, thus limiting the range of applicability of the GL model. Here are the assumptions made by Gor'kov:

1) The order parameter  $\Psi$  is small, or more accurately  $\Delta(T) \ll k_B T$ , where  $\Delta(T)$  is the BCS superconducting gap.

2) The length scale for the spatial variation of both the order parameter and the magnetic field is larger than the coherence length.

3) The electrodynamics is in the local, London Limit ( i.e. the penetration depth  $\lambda(T)$  is larger than the coherence length  $\xi(T)$  and mean free path  $l$ ).

4) The magnetic fields are weak  $H \ll H_c(0)$ , where  $H_c$  is the thermodynamic critical magnetic field.

Here, I will discuss the relationship between the GL parameters, BCS parameters and experimentally measured quantities. Later, in [Sec. 7.3.2](#), I will evaluate the GL parameters for real materials, mainly Nb.

Gor'kov showed that as temperature approaches  $T_c$ , the order parameter  $\Psi$  can



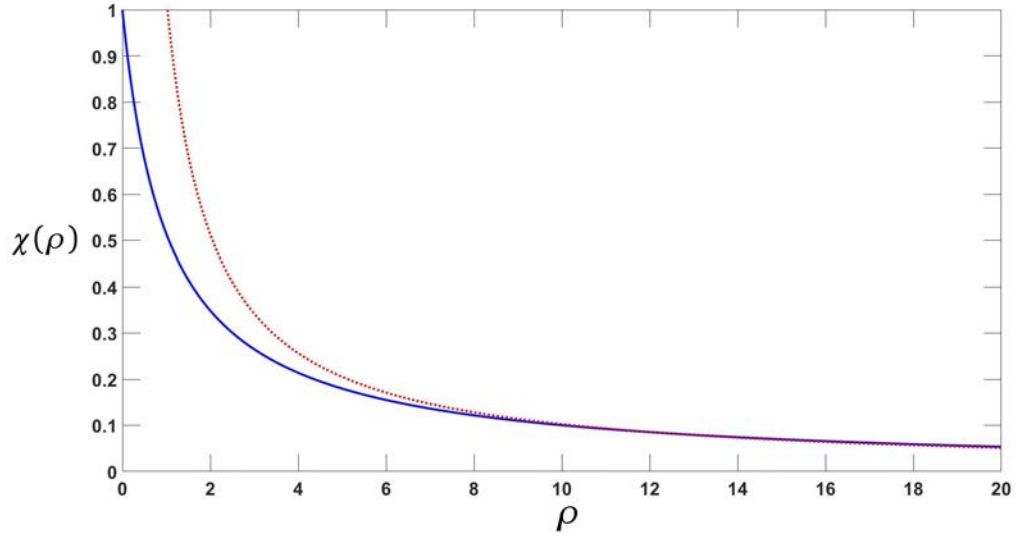


Fig. 7.2 Blue solid line: Gorkov function  $\chi(\rho)$  vs  $\rho$  using Eq. (7.12). Red dashed line: is the large- $\rho$  asymptotic behaviour  $\frac{\pi^2}{7\zeta(3)\rho}$ .

be related to BCS superconducting gap  $\Delta$  as [21, 151]:

$$\Psi = \frac{\sqrt{7\zeta(3)n_e\chi(\rho)}}{4\pi k_B T_c} \Delta, \quad (7.11)$$

where  $|\Psi|^2$  and  $n_e$  have units of inverse volume, whereas  $\Delta$  and  $k_B T_c$  have units of Energy. Here  $\zeta(x)$  is the Riemann zeta function,  $n_e$  is the number density of the electrons in the normal metal and  $\chi(\rho)$  is the function introduced by Gor'kov [151, 152]:

$$\chi(\rho) = \frac{8}{7\zeta(3)} \sum_{n=0}^{\infty} \frac{1}{(2n+1)^2(2n+1+\rho)}, \quad (7.12)$$

where  $\rho = \frac{\hbar v_F}{2\pi k_B T_c l}$  is a dimensionless parameter that is basically  $\rho = \frac{\xi_0}{0.36\pi l}$  where

$\xi_0 = \frac{0.18\hbar v_F}{k_B T_c}$  is the Pippard coherence length. The function  $\chi(\rho)$  is plotted in Fig. 7.2

and it shows that for a superconductor in the clean limit, as  $\rho \rightarrow 0$ ,  $\chi(\rho) \rightarrow 1$ , and

for a superconductor in the dirty limit  $\rho \gg 1$ ,  $\chi(\rho) \rightarrow \frac{\pi^2}{7\zeta(3)\rho}$ .

Now that we know the relation between  $\Psi$  and  $\Delta$ , Eq. (7.8), Eq. (7.9) and (Eq. (7.10)) can be rewritten with  $\Delta$  as the expansion variable:

$$\mathcal{F}_{GL}(\vec{r}) = \alpha_{\Delta} \Delta^2 + \frac{\beta_{\Delta}}{2} \Delta^4 + \gamma \hbar^2 \left| \left( \vec{\nabla} - \frac{ie_* \vec{A}}{\hbar} \right) \Delta \right|^2 + \frac{1}{2\mu_0} |\vec{\nabla} \times \vec{A} - \vec{B}_a|^2, \quad (7.13)$$

$$\alpha_{\Delta} \Delta + \beta_{\Delta} |\Delta|^2 \Delta + \gamma \hbar^2 \left( \vec{\nabla} - \frac{ie_* \vec{A}}{\hbar} \right)^2 \Delta = 0, \quad (7.14)$$

$$\frac{1}{\mu_0} \vec{\nabla} \times (\vec{\nabla} \times \vec{A} - \vec{B}_a) = -i\gamma e_* \hbar (\Delta^* \vec{\nabla} \Delta - \Delta \vec{\nabla} \Delta^*) - 2\gamma e_*^2 |\Delta|^2 \vec{A}. \quad (7.15)$$

The coefficients  $\alpha_{\Delta} = \alpha_{\Delta}(\vec{r}, T)$  and  $\beta_{\Delta} = \beta_{\Delta}(\vec{r}, T)$  are defined by means of the microscopic characteristics of superconductor [156, p.370]:

$$\alpha_{\Delta}(T) = \nu(T) \ln(T/T_c) \quad \text{and} \quad (7.16)$$

$$\beta_{\Delta}(T) = \frac{7\zeta(3)\nu(0)}{8\pi^2k_B^2T^2} . \quad (7.17)$$

Note that as  $T \rightarrow T_c$ ,  $\ln(T/T_c) \rightarrow -(1 - T/T_c)$  which is in agreement with [Eq. \(7.4\)](#).

By definition, in the absence of any field and as  $T \rightarrow T_c$  the superconducting energy gap is given as

$$\Delta_{\infty}(T) = \sqrt{-\frac{\alpha_{\Delta}(0)}{\beta_{\Delta}(0)}} = \sqrt{\frac{8\pi^2k_B^2T^2\ln(T_c/T)}{7\zeta(3)}} \approx \frac{4k_B T_c \sqrt{\eta_0}}{\pi} \sqrt{(1 - T/T_c)} . \quad (7.18)$$

Here,  $\Delta_{\infty}(T)$  is the value of the superconducting gap in the bulk of a sample in the absence of external magnetic field and  $\eta_0 \equiv \frac{\pi^4}{14\zeta(3)} = 5.79$ . Note that this result is consistent with the approximate temperature dependence of the BCS superconducting gap  $\Delta_{BCS}(T) \approx 1.74\Delta_{BCS}(0)(1 - T/T_c)^{1/2}$  near  $T_c$  that I discussed in the end of [Sec. 1.3](#). I shall introduce an effective parameter  $\Delta_{\infty}(0) \equiv \frac{4k_B T_c \sqrt{\eta_0}}{\pi} = 3.064k_B T_c$ , and emphasize that it has a different value than the zero-temperature BCS Gap  $\Delta_{BCS}(0) = 1.764k_B T_c$  because the assumptions used to derive this value are valid only near the critical temperature  $T_c$ .

The temperature of dependence of  $\alpha_{\Delta}$  and  $\beta_{\Delta}$  that is given in [Eq. \(7.16\)](#) and [Eq. \(7.17\)](#) comes from the microscopic theory. However, this temperature dependence can be modified to better fit the experimental evidence, as long as at  $T \rightarrow T_c$  the

theoretically predicted temperature dependence is preserved. For now, I will introduce the temperature kernels  $f_\alpha(T)$  and  $f_\beta(T)$  which show the temperature dependence for the  $\alpha_\Delta$  and  $\beta_\Delta$  parameters, and is given as follows [157]:

$$\alpha_\Delta(T) = -\nu(0)f_\alpha(T) \quad , \quad \text{where} \quad f_\alpha(T) = 1 - T/T_c \quad \text{and} \quad (7.19)$$

$$\beta_\Delta(T) = \frac{7\zeta(3)\nu(0)}{8\pi^2k_B^2T_c^2}f_\beta(T) \quad , \quad \text{where} \quad f_\beta(T) = \frac{T_c^2}{T^2} \quad . \quad (7.20)$$

The third coefficient in Eq. (7.13),  $\gamma = \gamma(\vec{r})$  is defined as follows [156, 158]:

$$\gamma = \frac{\pi^2n_e\chi(\rho)}{64m_e\eta_0k_B^2T_c^2} = \frac{\nu(0)\pi D}{8k_B T_c \hbar} \quad , \quad (7.21)$$

$$\text{with} \quad D = \frac{\pi\hbar v_F^2}{12\eta_0k_B T_c}\chi(\rho) = \begin{cases} \frac{v_F l}{3} & \text{if } l < \xi_0, \text{ i.e. Dirty limit} \\ \frac{v_F \xi_0 / 1.33}{3} & \text{if } l > \xi_0, \text{ i.e. Clean limit} \end{cases} \quad . \quad (7.22)$$

Here  $E_F$ ,  $p_F$ , and  $v_F$  is the Fermi energy, momentum and speed, in that order.  $\nu(0)$  is the DOS at the Fermi Energy  $E_F$  and  $D$  is the phenomenological electron diffusion coefficient with  $l$  being the quasi-particle mean free path [152, 159]. The equation

tions used for the Fermi Energy and density of states are given below [160, 161]:

$$E_F = \frac{m_e v_F^2}{2} = \frac{\hbar^2}{2m_e} (3\pi^2 n_e)^{2/3} \quad , \quad (7.23)$$

$$v(0) = \frac{m_e p_F}{2\pi^2 \hbar^2} = \frac{m_e}{2\pi^2 \hbar^2} (3\pi^2 n_e)^{1/3} \quad . \quad (7.24)$$

Note that all the masses  $m$  used in Gor'kov's paper [21], Schmid's paper [162] and Kopnin's book [158] correspond to free electron mass  $m_e$ . No effective Cooper pair mass  $m_* = 2m_e$  is considered in any of their equations. Hence the mass in Eq. (7.21) is an electron mass  $m_e$ .

We can define the characteristic length for variation of  $\Delta$  (a.k.a. the GL coherence length  $\xi$ ) by considering a simplified case with no magnetic field. With  $\vec{A} = 0$  Eq. (7.14) can be simplified as:

$$\frac{\Delta}{\Delta_\infty} + \left| \frac{\Delta}{\Delta_\infty} \right|^3 - \frac{\gamma \hbar^2}{\alpha_\Delta} \nabla^2 \frac{\Delta}{\Delta_\infty} = 0 \quad . \quad (7.25)$$

The GL coherence length  $\xi$  can be defined as follows [156, 158, 163, 164]:

$$\xi(T) = \sqrt{\frac{\gamma \hbar^2}{\alpha_\Delta(T)}} = \sqrt{\frac{\pi \hbar D}{8k_B T_c f_\alpha(T)}} = \frac{\hbar}{\sqrt{2m_* \alpha(T)}} \quad . \quad (7.26)$$

Similarly, the London penetration depth  $\lambda$  can be calculated from Eq. (7.15),

ignoring  $\vec{\nabla}\Delta$  and taking the curl of both sides:

$$\frac{1}{2\mu_0\gamma e_*^2 |\Delta|^2} \nabla^2 \vec{B} = \vec{B} \quad . \quad (7.27)$$

Eq. (7.27) is the same equation as Eq. (1.6) with a penetration depth that can be expressed as follows:

$$\lambda^2(T) = \frac{1}{2\mu_0\gamma e_*^2 |\Delta(T)|^2} \quad , \text{ or} \quad (7.28)$$

$$\lambda(T) = \sqrt{\frac{\beta_\Delta(T)}{2\mu_0\gamma e_*^2 \alpha_\Delta(T)}} = \sqrt{\frac{\pi\hbar f_\beta(T)}{4\eta_0 k_B T_c \mu_0 e_*^2 \nu(0) Df_\alpha(T)}} \quad . \quad (7.29)$$

Superconductors are classified into Type I and Type II based on their response to an applied magnetic field. The ratio of London penetration length to GL coherence length is an important parameter which determines the type of a superconductor. This ratio is defined as the GL parameter  $\kappa$ :

$$\kappa(T) = \lambda(T)/\xi(T) = \frac{1}{e_* D} \sqrt{\frac{2f_\beta(T)}{\eta_0 \mu_0 \nu(0)}} \quad . \quad (7.30)$$

A type I superconductor, where  $\kappa < 1/\sqrt{2}$ , has a positive surface energy, meaning that extra energy is needed to create a new Superconductor/Nonsuperconductor interface or boundary. Hence a type I superconductor completely expels magnetic field until a critical magnetic field  $H_c$  level is reached above which the superconduct-

ing state is lost. But a type II superconductor with  $\kappa > 1/\sqrt{2}$  has negative interface energy. That is why when a type II superconductor is subjected to an external magnetic field above its lower critical field  $H_{c1}$ , it enters into the mixed-state, and when the magnetic field amplitude reaches the upper critical field  $H_{c2}$ , the superconducting state is lost. The mixed-state is a state where a mixture of superconducting domains and Abrikosov vortices can coexist [26].

While the assumptions used in the derivation of the GL equations are valid only when  $T \rightarrow T_c$ , it is in good agreement with experimental results for temperatures down to  $0.7T_c$  [160]. GL generalizes the theory of superconductivity beyond BCS by explicitly considering inhomogeneous materials, including surfaces, interfaces, defects, vortices, etc. It is more flexible than BCS theory, which is only valid for homogeneous superconductors. Inhomogeneity in a superconductor can arise from the presence of surfaces, contact with a normal metal, defects, or due to layered or granular structure. Apart from the GL model, the Bogoliubov-de Gennes (BdG) equations [153, 165–167], Gorkov’s Green function method [158, 168, 169], the Matsubara formalism [170, 171] or Usadel’s equations [172] can be used to study inhomogeneous superconductors [173]. However, none of them can offer the relative simplicity of the GL model and the physical insights it offers compared to these other more microscopic approaches.

## 7.2 Time-dependent GL model

The GL model is a very successful, yet simple model. However the GL equations are static, thus cannot be used to study the temporal evolution of the order parameter and the screening currents. This has motivated several authors to seek a time-dependent generalization of the GL equations. In 1966, Schmid proposed a time-dependent generalization of the GL equations that could be utilized to study the dynamics of the order parameter [162]. He added a time dependence to the electron-electron interaction and followed Gor'kov's derivation [21] to derive the time-dependent Ginzburg-Landau (TDGL) equations. Gor'kov and Eliashberg derived a similar equation [174], but noted that for the case of a gapped superconductor, there exists a singularity in the density of states vs energy spectrum which prohibits expanding various quantities in powers of the gap  $\Delta$ .

Gor'kov limited the use of TDGL to gapless superconductors, or to materials with magnetic impurities or other pair-breaking mechanisms that would round off the singularity in the BCS density of states [36]. Proximity to a boundary with a normal metal, along with strong external magnetic fields and currents can also lead to gapless superconductivity before completely destroying it. Of relevance to the case of SRF cavities, numerous researchers have noted a substantial reduction in the singularity, and broadening of the density of states spectrum, under SRF operating conditions [61, 64] or with various types of impurities and imperfections in the near-surface region [65, 147, 175–177]. Recently, researchers at Jefferson lab performed tunneling



spectroscopy on Nb samples prepared for SRF applications and showed that at about 50% of locations on the surface the tunneling spectra showed a gapless spectra or zero-bias conductance peaks [178]. Such conditions would also justify the use and relevance of the TDGL equations to study the screening response of SRF cavities.

Once the GL free energy is known in its functional form (Eq. (7.13)), the relaxation dynamical equation can be written by considering how the order parameter evolves after being slightly disturbed from its equilibrium value [158, 179]:

$$-\Upsilon \left( \frac{\partial}{\partial t} + \frac{i}{\hbar} e_* \Phi \right) \Delta(\vec{r}, t) = \frac{\delta \mathcal{F}_{GL}(\vec{r}, t)}{\delta \Delta^*} , \quad (7.31)$$

where  $\Upsilon$  plays the role of a friction coefficient and is inspired by Landau and Khalatnikov's treatment of superfluid helium [180]. Here, the scalar electric potential  $\Phi$  is included to make the equation describing the dynamics of the superconducting order parameter gauge invariant. The TDGL equations are then derived through the variational derivatives of the GL free energy equation (Eq. (7.13)) with respect to  $\Delta^*$  and  $\vec{A}$  and are given as follows [162, 181]:

$$\frac{\gamma \hbar^2}{D} \left( \frac{\partial}{\partial t} + \frac{i}{\hbar} e_* \Phi \right) \Delta = -\gamma \hbar^2 \left( \vec{\nabla} - \frac{ie_*}{\hbar} \vec{A} \right)^2 \Delta - \alpha_{\Delta}(\vec{r}, T) \Delta - \beta_{\Delta}(\vec{r}, T) |\Delta|^2 \Delta , \quad (7.32)$$

$$\sigma \left( \frac{\partial \vec{A}}{\partial t} + \vec{\nabla} \Phi \right) = -i\gamma e_* \hbar (\Delta^* \vec{\nabla} \Delta - \Delta \vec{\nabla} \Delta^*) - 2\gamma e_*^2 |\Delta|^2 \vec{A} - \frac{1}{\mu_0} \vec{\nabla} \times (\vec{\nabla} \times \vec{A} - \vec{B}_a) \quad , \quad (7.33)$$

where  $\Delta = \Delta(\vec{r}, T, t)$  is the time-dependent SC gap,  $\vec{A} = \vec{A}(\vec{r}, t)$  is the magnetic vector potential,  $\vec{B}_a = \vec{B}_a(\vec{r}, t)$  is the externally applied magnetic field,  $\Phi = \Phi(\vec{r}, t)$  is the scalar electric potential,  $D$  is the phenomenological electron diffusion coefficient given by Eq. (7.22),  $\sigma$  is the electric conductivity of the normal (non-superconducting) state. For a gapless superconductor Gor'kov and Eliashberg were able to calculate the

characteristic relaxation rate for the order parameter to be  $\tau_{GL} = \frac{\pi \hbar}{8k_B(T_c - T)}$  which is equal to  $\tau_{GL-1K} \approx 3 \times 10^{-12}$  s for  $T_c - T = 1$  K. It is evident from Eq. (7.32) that

$$\Upsilon = \frac{\gamma \hbar^2}{D} \text{ and can also be written as } \Upsilon = |\alpha_\Delta(T)| \tau_\Delta(T), \text{ where } \tau_\Delta(T) = \frac{\xi(T)^2}{D}$$

is a characteristic time for the relaxation of the superconducting gap  $\Delta$  [158, 182]. From Eq. (7.33) one finds that the characteristic time for the relaxation of magnetic vector potential  $\vec{A}$  is  $\tau_j = \mu_0 \lambda^2 \sigma_n$  [158].

Eq. (7.32) was first proposed by Schmid [162], following the derivation of the GL equation from BCS [154, 155] by Gor'kov [174]. Eq. (7.33) is Ampere's law  $\vec{\nabla} \times \vec{B}(\vec{r}) =$

$$\mu_0 (\vec{J}_s(\vec{r}) + \vec{J}_n(\vec{r})), \text{ where } \vec{J}_n(\vec{r}) = -\sigma \frac{\partial \vec{A}(\vec{r})}{\partial t}$$

is the normal current and the supercurrent is defined in Eq. (7.34).

The superconducting current can be obtained from the expectation value of the

momentum operator for a charged particle of charge  $e_*$  in a magnetic field:

$$\vec{J}_s(\vec{r}, t) = -i\gamma e_* \hbar (\Delta^* \vec{\nabla} \Delta - \Delta \vec{\nabla} \Delta^*) - 2\gamma e_*^2 |\Delta|^2 \vec{A} \quad . \quad (7.34)$$

## 7.3 TDGL simulations

### 7.3.1 Gauge invariance, boundary conditions and normalization

The TDGL equations are invariant under the following change of gauge [183, 184]:

$$\Delta(\vec{r}, t) \rightarrow \Delta(\vec{r}, t) e^{i\chi(\vec{r}, t)} \quad , \quad (7.35)$$

$$\vec{A}(\vec{r}, t) \rightarrow \vec{A}(\vec{r}, t) + \frac{\hbar}{e_*} \vec{\nabla} \chi(\vec{r}, t) \quad , \quad (7.36)$$

$$\Phi(\vec{r}, t) \rightarrow \Phi(\vec{r}, t) - \frac{\hbar}{e_*} \frac{\partial \chi(\vec{r}, t)}{\partial t} \quad , \quad (7.37)$$

where  $\chi(\vec{r}, t)$  is any (sufficiently smooth) real-valued scalar function of position and

time. One can fix the gauge as  $\frac{\partial \chi(\vec{r}, t)}{\partial t} = \frac{e_*}{\hbar} \Phi(\vec{r}, t)$  in order to effectively eliminate the electric potential at all times [184, 185].

To numerically simulate the superconducting domain, one must specify the boundary conditions for the order parameter, current density, and vector potential. Accord-

ing to de Gennes, on the boundary  $\partial\Omega$  of the superconducting domain  $\Omega$  the following boundary condition should be enforced [153, 167]:

$$\left( \vec{\nabla} - \frac{ie_*}{\hbar} \vec{A} \right) \Delta \cdot \hat{n} = \frac{i}{b} \Delta \quad \text{on } \partial\Omega \quad , \quad (7.38)$$

where  $\hat{n}$  is unit vector normal to the surface and  $b$  is a real constant that has units of length and is known as the extrapolation length. In this work only the superconductor-insulator boundary is considered where  $b = \infty$ . Any current passing through the boundary between a superconducting domain and vacuum/insulator would be non-physical, thus:

$$\left( \vec{\nabla} - \frac{ie_*}{\hbar} \vec{A} \right) \Delta \cdot \hat{n} = 0 \quad \text{on } \partial\Omega \quad . \quad (7.39)$$

It is useful to introduce dimensionless variables (denoted by twiddles  $\tilde{\phantom{x}}$ ) to simplify the simulation and normalize Eq. (9.3) and Eq. (7.33): The superconducting gap is scaled according to  $\Delta_\infty(0)$ ,  $\Delta \rightarrow \Delta_\infty(0) \tilde{\Delta}$  where  $\Delta_\infty(0) = \frac{4k_B T_c \sqrt{\eta_0}}{\pi}$  is the bulk superconducting density at zero temperature in the absence of external magnetic field as defined in Eq. (7.18). The spatial coordinates are scaled according

to the zero temperature GL coherence length  $\xi(0) \equiv \sqrt{\frac{\pi \hbar D}{8k_B T_c}}$  (Eq. (7.26)), so that

$(x, y, z) \rightarrow (\xi(0) \tilde{x}, \xi(0) \tilde{y}, \xi(0) \tilde{z})$ , thus  $\vec{\nabla} \rightarrow \frac{1}{\xi(0)} \vec{\tilde{\nabla}}$ <sup>1</sup>. Time is scaled according to the

---

<sup>1</sup>Note that the zero temperature London penetration depth  $\lambda(0)$  can also be used as a normalization length scale (See Ref. [184])

characteristic time for the relaxation of the vector potential  $\tau_j(0)$ ,  $t \rightarrow \tau_j(0)\tilde{t}$  where  $\tau_j(0) \equiv \mu_0 \lambda_0^2 \sigma_n$ <sup>2</sup> and  $\sigma_n = 2e^2 \nu(0) \nu_F l / 3$  is the normal state conductivity at 0K [56, 181] (as opposed to the conductivity of non-superconducting current at any temperature denoted as  $\sigma(T)$ ). The temperature is scaled according to the critical temperature

of the superconductor  $T_c$ ,  $T \rightarrow T_c \tilde{T}$ . The magnetic vector potential  $\vec{A} \rightarrow \frac{\Phi_0}{2\pi\xi(0)} \vec{\tilde{A}}$  and

magnetic field  $\vec{B} \rightarrow B_{c2}(0) \vec{\tilde{B}}$ , where  $B_{c2} = \frac{\Phi_0}{2\pi\xi(0)^2}$  is the second critical field at zero

temperature and  $\Phi_0 = \frac{h}{e_*}$  is the magnetic flux quantum. The superconductor current

is scaled in terms of  $J_c$ ,  $\vec{J} \rightarrow \frac{J_c}{\kappa} \vec{\tilde{J}}$ , where  $J_c = \frac{\Phi_0}{2\pi\mu_0\lambda(0)\xi(0)^2} = \frac{B_{c2}}{\mu_0\lambda(0)}$  is the critical current density at  $T = 0$  and  $B = 0$ , and  $\kappa$  is the GL parameter and is defined as

the ratio of two characteristic length scales  $\kappa \equiv \frac{\lambda}{\xi}$  (see Eq. (7.30)). The normal state conductivity is scaled with its zero temperature value  $\sigma \rightarrow \sigma_n \tilde{\sigma}$  and since it is nearly

constant in the temperature range of interest for Nb, it is set to  $\tilde{\sigma} = 1$ . The "normalized friction coefficient" is defined as the ratio between the two characteristic time scales

$\tau_\Delta$  and  $\tau_j$ ,  $\eta \equiv \frac{\tau_\Delta}{\tau_j}$  [182, 188]. For cases when the source of externally applied magnetic field is outside of the superconducting domain, the  $\vec{B}_a$  term in Eq. (7.33) should

be dropped because  $\vec{\nabla} \times \vec{B}_a = 0$  everywhere within the superconducting domain.

Rewriting Eq. (9.3) and Eq. (7.33) using the newly introduced dimensionless

---

<sup>2</sup>This characteristic time scale is also used to normalize TDGL equations in Refs. [182, 184, 186–188]

quantities and dropping " $\sim$ " we have :

$$\eta \frac{\partial \Delta}{\partial t} = (\vec{\nabla} - i\vec{A})^2 \Delta + f_\alpha \Delta - f_\beta |\Delta|^2 \Delta \quad , \quad (7.40)$$

$$\sigma \frac{\partial \vec{A}}{\partial t} = \frac{1}{2i} (\Delta^* \vec{\nabla} \Delta - \Delta \vec{\nabla} \Delta^*) - |\Delta|^2 \vec{A} - \kappa^2 \vec{\nabla} \times \vec{\nabla} \times \vec{A} \quad , \quad (7.41)$$

$$\vec{J}_s = \frac{1}{2i} (\Delta^* \vec{\nabla} \Delta - \Delta \vec{\nabla} \Delta^*) - |\Delta|^2 \vec{A} \quad , \quad (7.42)$$

where the explicit parametric temperature dependence is contained in  $f_\alpha$  and  $f_\beta$ . It should be stressed that the quantities  $\sigma$ ,  $\Delta$ ,  $\vec{A}$ ,  $\vec{\nabla}$  and  $t$  appearing in these equations are all their dimensionless versions.

### 7.3.2 Material parameters

The main objective of this work is to simulate the response of SRF grade Nb, thus the parameter values must be chosen accordingly. Experimental values for relevant parameters in these materials are summarized in [Table 7.1](#).

Some of these parameters can be computed from purely theoretical considerations. However, it would not be wise to expect complete agreement between the quantities calculated using the phenomenological model and the quantities calculated using

Parameter Name	Symbol	Value	Reference
Effective penetration depth	$\lambda_{eff}(0)$	47 nm	[189]
London penetration depth	$\lambda_L(0)$	39 nm	[189]
Coherence length	$\xi(0)$	38 nm	[189]
Second critical field	$H_{c2}$	442 mT	[190]
Critical temperature	$T_c$	9.2 K	[189]
Fermi velocity	$v_F$	$1.37 \times 10^6$ m/s	[191]
Free electron density	$n_e$	$5.56 \times 10^{28}$ m <sup>-3</sup>	[191]
Ginzburg-Landau time	$\tau_{GL}$	$3.26 \times 10^{-13}$ s	$\pi\hbar/8k_B T_c$
electron phonon inelastic scattering time	$\tau_e$	$4.17 \times 10^{-12}$ s	[192]
Normal state conductivity	$\sigma_n$	$2 \times 10^8 - 2 \times 10^9$ S/m	[193, 194]

Table 7.1 Measured values of SRF quality bulk Nb parameters used for numerical simulations.

the microscopic model. The phenomenological model is derived for  $T \rightarrow T_c$ , hence this is the range where an agreement between GL and BCS is expected.

At temperatures near  $T_c$  all superconductors are considered to be in the local limit, because the penetration depth diverges. I should limit myself to dirty Nb since this is where both TDGL and gTDGL are valid. According to Tinkham [36, p.103], in the dirty local limit the temperature dependence of the penetration depth is given as follows:

$$\lambda_{eff}(T) = \lambda_{eff}(0) \left[ \frac{\Delta(T)}{\Delta(0)} \tanh\left(\frac{\Delta(T)}{2k_B T}\right) \right]^{-1/2}. \quad (7.43)$$

$$\text{Given that } \lim_{T \rightarrow T_c} \tanh\left(\frac{\Delta(T)}{2k_B T}\right) = \frac{\Delta(T)}{2k_B T} \text{ and } \lim_{T \rightarrow T_c} \frac{\Delta(T)}{\Delta(0)} = 1.74(1 - T/T_c)^{1/2}$$

we can get the limiting value of penetration depth as follows:

$$\lim_{T \rightarrow T_c} \lambda_{eff}(T) = \lambda_{eff}(0) \left[ \frac{\Delta^2(T) \Delta(0)}{\Delta^2(0) 2k_B T_c} \right]^{-1/2} = \frac{\lambda_{eff}(0)}{\sqrt{2.67}} \frac{1}{\sqrt{1-T/T_c}} = \frac{28.76 \text{ nm}}{\sqrt{1-T/T_c}}, \quad (7.44)$$

where I used  $\lambda_{eff}(0) = 47 \text{ nm}$  from [Table 7.1](#). Using [Eq. \(7.29\)](#) along with  $n_e$  listed on [Table 7.1](#) one finds:

$$\lambda(T) = \sqrt{\frac{\beta_\Delta(T)}{2\mu_0 \gamma e^2 \alpha_\Delta(T)}} = \frac{15.94 \text{ nm}}{\sqrt{1-T/T_c}}, \quad (7.45)$$

where I used [Eq. \(7.21\)](#), [Eq. \(7.16\)](#) and [Eq. \(7.17\)](#) to evaluate  $\gamma$ ,  $\alpha_\Delta(T)$  and  $\beta_\Delta(T)$ . Clearly the result of [Eq. \(7.45\)](#) is in disagreement with the real material value obtained in [Eq. \(7.44\)](#). I will address this issue later. For now let me perform the same comparison for  $\xi$ . Again, according to Tinkham [[36](#), p.119], the GL coherence length  $\xi$  can be related to the Pippard's coherence length  $\xi_0$  in the following fashion:

$$\frac{\xi(T)}{\xi_0} = \frac{\pi H_c(0) \lambda_L(0)}{2\sqrt{3} H_c(T) \lambda_{eff}(T)}, \quad (7.46)$$

where  $H_c$  is the superconducting critical field, which can be approximated near  $T_c$  as  $H_c(T) = 1.73 H_c(0)(1 - T/T_c)$ . Using this, and the London penetration depth  $\lambda_L$  from



Table 7.1 and effective penetration depth  $\lambda_{eff}$  from Eq. (7.44) we get:

$$\xi(T) = \frac{27 \text{ nm}}{\sqrt{1 - T/T_c}} \quad . \quad (7.47)$$

Using Eq. (7.26) along with  $n_e$  listed on Table 7.1 one finds:

$$\xi(T) = \sqrt{\frac{\gamma \hbar^2}{\alpha_\Delta(T)}} = \frac{149.6 \text{ nm}}{\sqrt{1 - T/T_c}} \quad . \quad (7.48)$$

Yet again, the result of Eq. (7.48) is way off from the material value obtained in Eq. (7.47). This is because until now I have neglected the fact that the effective mass of the Cooper pair can be higher than the expected  $2m_e$ . This can be caused by the band structure of a material and phonon "dressing" effects [36]. Defects and impurities can also change the penetration depth locally which one can attribute either to a change in effective mass  $m_*$  or local superfluid density  $n_s$ . It's effect is accounted for in the definition of  $\gamma$  in Eq. (7.21) which makes up for the neglect of this degree of freedom by Gor'kov and Kopnin (note that  $\gamma$  appears in both Eqs. (7.45) and (7.48)). While there are some proposed methods to measure the effective mass  $m_*$  [195–197], sadly as of today this value remains experimentally inaccessible. Note that the quantities  $n_s l / m_*$  appear together in the definition of  $\gamma$  ( $l$  does not explicitly appear in Eq. (7.21) and is accounted for in  $\chi(\rho)$ ;  $n_e = 2n_s$ ). Thus it is customary to set  $m_* = 2m_e$  and attribute all local variations of penetration depth to local variations in superfluid density or

mean-free path. The parameter  $\gamma$  itself will have to be corrected as  $\gamma^* = \frac{n_s^*}{n_s} \gamma$  where  $n_s^*$

represents an effective superfluid density. This zero temperature effective superfluid density  $n_s^*(0)$  will be set to match the theoretical and experimental values listed in [Table 7.1](#). For Nb we shall use:

$$n_s^*(0) = \frac{(15.94 \text{ nm})^2}{(28.76 \text{ nm})^2} n_e / 2 = 8.54 \times 10^{27} \text{ m}^{-3} < n_s \quad \text{and} \quad \frac{n_s^*}{n_s} = 0.31 \quad . \quad (7.49)$$

Using this value of  $n_s^*(0)$  will change  $\gamma$  to  $\gamma^* = 0.31\gamma$ , and therefore using [Eq. \(7.16\)](#) and [Eq. \(7.17\)](#) we find that  $\lambda(T) = 28.75 \text{ nm} / \sqrt{1 - T/T_c}$  and  $\xi(T) = 89.92 \text{ nm} / \sqrt{1 - T/T_c}$ , which are closer to the BCS values obtained using [Eq. \(7.44\)](#), [Eq. \(7.48\)](#) and experimental numbers listed in [Table 7.1](#). Note that  $\lambda(T)$  and  $\xi(T)$  also depend on the value of mean-free path  $l$  and this dependence is plotted in [Fig. 7.3](#).

[Fig. 7.3](#) shows that both  $\lambda$  and  $\xi$  depend on the value of mean-free-path  $l$ , through the diffusion coefficient  $D$  and parameter  $\gamma^*$ . The BCS surface resistance also has  $l$ -dependence with a shallow minimum around  $l \approx \xi(0)$  [[56](#), [198](#)]. Recently, it was revealed that the residual resistance caused by trapped vortices also depends on the mean-free-path value  $l$  [[72](#)] establishing  $l$  as one of the parameters that needs to be tuned for optimal SRF performance. With the modified  $\gamma^*$  one can compute the time-scales governing the relaxation of the order parameter and magnetic vector potential  $\vec{A}$  for Nb in the dirty limit:

$$\tau_{\Delta}(0) = \frac{\xi^2(0)}{D} = \frac{\gamma^* \hbar^2}{\alpha_{\Delta}(0) D} = \frac{n_s^*}{n_s} \tau_{GL}(0) = 9.91 \times 10^{-14} \text{ s} \quad , \quad (7.50)$$

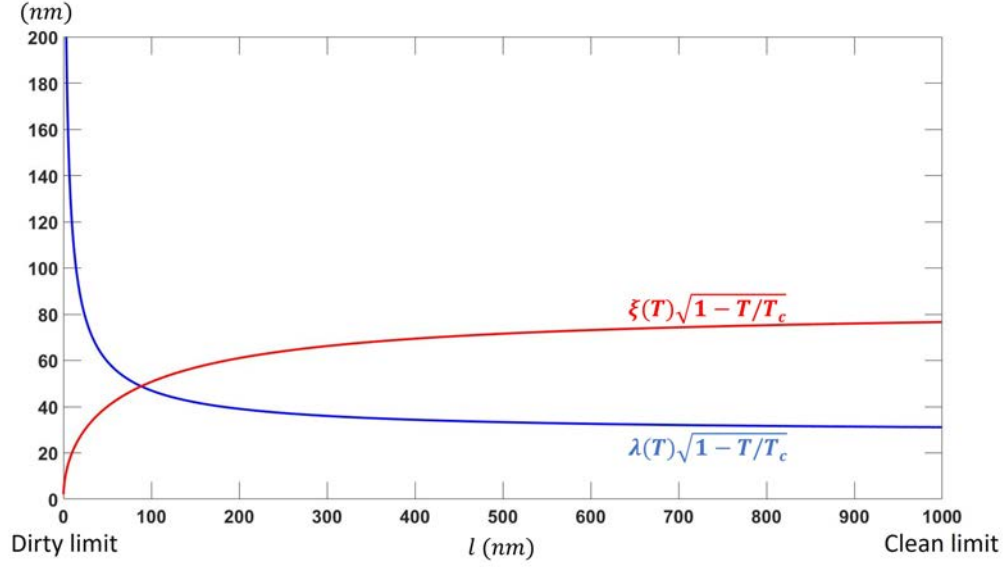


Fig. 7.3 Magnetic penetration depth  $\lambda(T)$  (blue) and coherence length  $\xi(T)$  (red) vs mean-free path  $l$ , calculated using Eq. (7.26) and Eq. (7.29) where  $\gamma$  is calculated using Eq. (7.21) with  $n_s^* = 8.54 \times 10^{27} \text{ m}^{-3}$  for Nb. Both quantities are multiplied by  $f_\alpha(T) = \sqrt{1 - T/T_c}$  to show the temperature independent dependence on the mean free path.

$$\tau_j(0) = \mu_0 \lambda(0)^2 \sigma_n = \frac{1}{\eta_0 n_s^*} \frac{n_s v_F l / 3}{D} \tau_{GL} = 1.81 \times 10^{-13} \text{ s} \quad . \quad (7.51)$$

As I discussed in Sec. 7.3.1, in the simulation time is expressed in units of  $\tau_j(0)$ , consequently a frequency range of 500 MHz-5 GHz and mean-free-path value range of 0 – 500 nm corresponds to a period of rf oscillation in the range of 200 – 6000  $\tau_j$ . Hence, the period of rf magnetic field used in the simulations is chosen to be in the

same range  $\frac{2\pi}{\omega} = 200 - 6000 \tau_j$ . Note that in the dirty limit  $\frac{v_F l / 3}{D} \rightarrow 1$ .

The "normalized" friction coefficient is defined as :

$$\eta = \frac{\tau_{\Delta}}{\tau_j} = \frac{\xi^2/D}{\mu_0\lambda(0)^2\sigma_n} = \begin{cases} \eta_0 \left( \frac{n_s^*}{n_s} \right)^2 = 1.78 & \text{for Nb in the dirty limit } (l < \xi_0) \\ \eta_0 \left( \frac{n_s^*}{n_s} \right)^2 \frac{\xi_0}{1.33l} = \frac{1.34}{l/\xi_0} & \text{for Nb in the clean limit } (l > \xi_0). \end{cases} \quad (7.52)$$

Many theoreticians argue that the value of the normalized friction coefficient  $\eta$

should be fixed at  $\eta = \eta_0 = \frac{\pi^4}{14\zeta(3)} = 5.79$  [158], but Eq. (7.52) clearly indicates that the value of  $\eta$  is tunable and it's value is simply limited to be  $\eta \leq \eta_0$  since  $n_s > n_c/2$  would be nonphysical. In a clean limit superconductor  $\eta$  would also be proportional to  $l^{-1}$  but that is where the applicability of the GL model is called into question, so can be ignored.

### 7.3.3 Introduction and Treatment of Defects

The way a superconducting vortex is created and its dynamics when subjected to alternating current has been, and will continue to be, the topic of many research publications [20, 28, 186, 199–203]. When a superconducting vortex system is subjected to an electric current, it experiences a Lorentz force perpendicular to the direction of the current and magnetic field. The Lorentz force causes the vortex to move, creating an effective friction force and dissipation due to flux motion [27]. The friction force

is associated with quasiparticle excitations in the vortex core due to their interaction with the lattice, and generally increases with vortex velocity [28]. The dissipation can be reduced by introducing pinning sites and creating a pinning force to counteract the Lorentz force [199, 200, 202]. Artificial pinning centers and careful nanostructuring can be used to optimize a superconducting material for a specific application. The material design process can be guided by numerical simulation techniques that identify the location and the external magnetic field value at which a vortex is expected to penetrate into the superconducting sample [204].

One of the strengths of the GL model is its ability to accurately describe the interaction between vortices and sample inhomogeneities, material defects like magnetic inclusions, grain boundaries etc. Some common SRF surface defects, such as lossy Nb-oxides and metallic Nb-hydrides near the surface of Nb [56] are either non-superconducting or have lower critical temperature than Nb. There are several approaches to model such defects. Defects which are known to be insulators can be modeled by adding such insulating domains into the simulation with appropriate boundary conditions (see Sec. 7.3.1). Metallic inclusions, areas with suppressed  $T_c$  or the effect of nonzero temperature, can be specified through modulations of the superconductor critical temperature. For that purpose one can define dimensionless pinning coefficients  $\epsilon(\vec{r}, T)$  [204–209] which can range from  $\epsilon(\vec{r}, T) = 0$  (strong order parameter suppression) to  $\epsilon(\vec{r}, T) = 1$  (full superconductivity). The effects of spatial variation of the mean free path  $l(\vec{r})$  (or effective mass  $m_*$ ) can be specified through the diffusion

coefficient at the defect location  $D_d(\vec{r})$ :

$$\eta \frac{\partial \Delta}{\partial t} = \frac{D_d(\vec{r})}{D_{cl}} (\vec{\nabla} - \vec{A})^2 \Delta + \epsilon(\vec{r}, T) \Delta - |\Delta|^2 \Delta \quad , \quad (7.53)$$

$$\sigma \frac{\partial \vec{A}}{\partial t} = \frac{1}{2i} (\Delta^* \vec{\nabla} \Delta - \Delta \vec{\nabla} \Delta^*) - |\Delta|^2 \vec{A} - \frac{D_{cl}}{D_d(\vec{r})} \kappa^2 \vec{\nabla} \times \vec{\nabla} \times \vec{A} \quad , \quad (7.54)$$

where

$$\epsilon(\vec{r}, T) = f_a(T, T_c(\vec{r})) = 1 - \frac{T}{T_{c_d}(\vec{r})} \quad . \quad (7.55)$$

Here subscript  $_d$  stands for "defect",  $_{cl}$  stands for clean and  $T_{c_0}$  is bulk critical temperature. We model the defect through a spatially varying  $T_{c_d}(\vec{r}) < T_c$  and  $T_{c_d} \rightarrow T_c$  far from the defect. These pinning coefficients dictate the maximum possible value for the superconducting gap  $\Delta(\vec{r}, T)$  at a given location and temperature in the absence of external magnetic field and :

$$|\Delta(\vec{r}, T)|^2 \leq \epsilon(\vec{r}, T) = \begin{cases} 1 - \frac{T}{T_{c_d}(\vec{r})} & \text{for } T \leq T_{c_d} \\ 0 & \text{for } T > T_{c_d} \end{cases} \quad . \quad (7.56)$$

One could also consider the spatial variation in temperature ( $T = T(\vec{r})$ ) due to local heating or externally applied heating (like that produced by laser illumination [210–212]) but in my models the temperature is constant and homogeneous everywhere.

One can calculate the vortex pinning potential created by this kind of disorder using the method outlined in reference [202]. Consider a point defect at the origin, which means the defect extends on a scale smaller than the coherence length, hence perturbs  $T_c$  or  $l$  only locally. This will lead to a small change in the total free energy of the superconductor. Using Eq. (7.13)

$$\delta F_{tot} = \int_V d^3r \left( \delta\alpha_\Delta \Delta_\infty^2 + \frac{\delta\beta_\Delta}{2} \Delta_\infty^4 + \delta\gamma \hbar^2 |\vec{\nabla} \Delta_\infty|^2 \right) , \quad (7.57)$$

where  $\delta\alpha_\Delta = \delta\alpha_\Delta(\vec{r})$ ,  $\delta\beta_\Delta = \delta\beta_\Delta(\vec{r})$  and  $\delta\gamma = \delta\gamma(\vec{r})$  represent small position dependent changes in the phenomenological GL parameters, and the integral stands for integration over the whole volume of the superconductor. Now consider the same scenario with a vortex line directed along  $\hat{z}$  at location  $\vec{u}(z) = u_x(z)\hat{x} + u_y(z)\hat{y}$  relative to the defect location. The change in the total energy will be

$$\delta F_{tot} = \int_V d^3r \left( \delta\alpha_\Delta \Delta_v^2(\vec{r} - \vec{u}) + \frac{\delta\beta_\Delta}{2} \Delta_v^4(\vec{r} - \vec{u}) + \delta\gamma \hbar^2 |\vec{\nabla} \Delta_v(\vec{r} - \vec{u})|^2 \right) , \quad (7.58)$$

where  $\Delta_v$  is the GL solution for the order parameter around a vortex, given by  $\Delta_v(\vec{r}) = \frac{r e^{i\theta}}{\sqrt{r^2 + 2\xi^2}} \Delta_\infty$  [156, p.79]. The vortex pinning potential  $U_p(\vec{r})$ , is the free energy difference between these two cases: namely the vortex being at position  $\vec{r}$  and the

vortex not being there. Hence using [Eq. \(7.57\)](#) and [Eq. \(7.58\)](#):

$$\begin{aligned}
U_p(\vec{u}(z)) = & - \int d^2r \left[ \delta\alpha_\Delta (\Delta_\infty^2 - \Delta_v^2(\vec{r} - \vec{u}(z))) + \right. \\
& \left. + \frac{\delta\beta_\Delta}{2} (\Delta_\infty^4 - \Delta_v^4(\vec{r} - \vec{u}(z))) - \delta\gamma\hbar^2 |\vec{\nabla}\Delta_v(\vec{r} - \vec{u}(z))|^2 \right] .
\end{aligned} \tag{7.59}$$

The simplest defect to model is a point defect (inside the superconductor), defined as a defect with spatial extent smaller than the coherence length (for example oxygen defects). Consider a point defect which locally suppresses  $T_c$  such that  $\delta\alpha_\Delta = A\delta(r)$  is now a Dirac delta function at the origin (and I take  $\delta\beta_\Delta = 0$  for simplicity). Then:

$$\begin{aligned}
U_p(\vec{u}(z)) = & - \int d^2r \left[ \delta\alpha_\Delta (\Delta_\infty^2 - \Delta_v^2(\vec{r} - \vec{u}(z))) \right] = \\
= & -A(\Delta_\infty^2 - \Delta_v^2(-\vec{u}(z))) = -\frac{2A\xi^2}{u(z)^2 + 2\xi^2} = -\frac{U_0}{u(z)^2 + 2\xi^2} ,
\end{aligned} \tag{7.60}$$

where  $U_0$  is the potential depth per unit length in the  $\hat{z}$  direction. This is very similar to the pinning potential used in [\[72\]](#) and [\[213\]](#).

### 7.3.4 TDGL in COMSOL

COMSOL multiphysics simulation software [\[214\]](#) can be used to solve the TDGL equations in both 2D and 3D domains [\[184, 215\]](#). The main advantage of COMSOL is



the intuitive interface of the software and automatic algorithm optimization. A critical comparison of COMSOL and ANSYS simulation software was previously performed [216], where the authors showed that COMSOL can complete the simulation 10 times faster while reaching similar results. The accuracy of the software has been validated by other researchers as well [217, 218]. COMSOL has an easy learning curve enabling researchers to use the TDGL model as a tool without spending too much effort on algorithm development [219].

The General Form Partial Differential Equation is one of the equations best suited to be solved by COMSOL multiphysics simulation software and is given as:

$$d \frac{\partial \vec{u}}{\partial t} + \vec{\nabla} \cdot \vec{\Pi} = \vec{F} \quad . \quad (7.61)$$

Here  $\vec{F}$  is the driving term vector,  $d$  is the inertia tensor,  $\vec{u}$  is a column vector of all unknowns and  $\vec{\Pi}$  is a column vector function of  $\vec{u}$ . I can rewrite Eq. (7.53) and Eq. (7.54) to be in this form. Redefine  $\Delta$  and  $\vec{A}$  as:

$$\Delta = v_1 + i v_2 \quad , \quad (7.62)$$

where  $v_1$  and  $v_2$  are real functions of position and time.

$$\vec{A} = A_1 \hat{x} + A_2 \hat{y} + A_3 \hat{z} \quad , \quad (7.63)$$

where  $A_1$ ,  $A_2$  and  $A_3$  are real functions of position and time representing the magnitudes of the components of  $\vec{A}$  in the  $\hat{x}$ ,  $\hat{y}$ ,  $\hat{z}$  directions.

We thus have 5 independent unknown variables, and 5 equations (2 from Eq. (7.53), real and imaginary; 3 from Eq. (7.54), 3 vector components). After some simple mathematical rearrangement I get an equation of the form of Eq. (7.61), where:

$$d_a = \begin{bmatrix} \frac{D_{cl}}{D_d} \mathcal{D}_1 & 0 & 0 & 0 & 0 \\ 0 & \frac{D_{cl}}{D_d} \mathcal{D}_1 & 0 & 0 & 0 \\ 0 & 0 & \sigma \mathcal{D}_2 & 0 & 0 \\ 0 & 0 & 0 & \sigma \mathcal{D}_2 & 0 \\ 0 & 0 & 0 & 0 & \sigma \mathcal{D}_2 \end{bmatrix}, \quad (7.64)$$

$$\vec{u} = \begin{bmatrix} v_1 \\ v_2 \\ A_1 \\ A_2 \\ A_3 \end{bmatrix}, \quad (7.65) \quad \vec{\Pi} = \begin{bmatrix} -v_{1x} & -v_{1y} & -v_{1z} \\ -v_{2x} & -v_{2y} & -v_{2z} \\ 0 & A_{2x} - A_{1y} & A_{3x} - A_{1z} \\ A_{1y} - A_{2x} & 0 & A_{3y} - A_{2y} \\ A_{1z} - A_{3x} & A_{2z} - A_{3y} & 0 \end{bmatrix}, \quad (7.66)$$

$$\vec{F} = \begin{bmatrix} (A_{1x} + A_{2y} + A_{3z})v_2 + 2(A_1v_{2x} + A_2v_{2y} + A_3v_{2z}) - (A_1^2 + A_2^2 + A_3^2)v_1 + \mathcal{E}v_1 \\ -(A_{1x} + A_{2y} + A_{3z})v_1 - 2(A_1v_{1x} + A_2v_{1y} + A_3v_{1z}) - (A_1^2 + A_2^2 + A_3^2)v_2 + \mathcal{E}v_2 \\ \mathcal{D}_2[(v_1v_{2x} - v_2v_{1x}) - (v_1^2 + v_2^2)A_1] \\ \mathcal{D}_2[(v_1v_{2y} - v_2v_{1y}) - (v_1^2 + v_2^2)A_2] \\ \mathcal{D}_2[(v_1v_{2z} - v_2v_{1z}) - (v_1^2 + v_2^2)A_3] \end{bmatrix}, \quad (7.67)$$

where  $\mathcal{D}_1 = \eta$ ,  $\mathcal{D}_2 = \frac{1}{\kappa^2} \frac{D_d}{D_{cl}}$ ,  $\mathcal{E} = \frac{D_{cl}}{D_d} [f_\alpha(T, T_c(\vec{r})) - (v_1^2 + v_2^2)f_\beta(T, T_c(\vec{r}))]$  and  $v_{1x}$  stands for  $\frac{\partial v_1}{\partial x}$ ,  $A_{2z}$  stands for  $\frac{\partial A_2}{\partial z}$  and so on.

The boundary conditions at the superconductor-vacuum interface are as follows:

$$\vec{\Pi} \cdot \hat{n} = 0 \quad \text{on} \quad \partial\Omega, \quad (7.68)$$

$$\vec{A} \cdot \hat{n} = 0 \quad \text{on} \quad \partial\Omega, \quad (7.69)$$

and

$$\vec{\nabla} \times \vec{A} = \vec{\nabla} \times \vec{A}_{ext} \quad \text{on} \quad \partial\Omega \quad . \quad (7.70)$$

For all the simulations presented in this work, the time-dependent study in the COMSOL Multiphysics software was used. The Direct-MUMPS solver with the default parameters was used as the general solver and time-stepping was performed using the Backward Differentiation Formula (BDF) solver. The maximum time-step was constrained to 1. The free tetrahedral mesh was used.

## 7.4 Two-Domain TDGL and Inclusion of Superconducting Screening

After reviewing some previously published TDGL simulations [184, 186, 207], I noticed that usually Eq. (7.70) is enforced on the boundary of the superconductor. However this implies that the superconducting screening current has no effect on the magnetic field at the boundary and beyond the superconducting domain. This is physically incorrect for the situations of interest to us, be it a magnetic dipole above the superconductor case or the case of a point defect on the surface of an SRF cavity. The effect of screening currents is crucial when one is trying to simulate such spatially nonuniform external magnetic field, and the resulting nonlinear response of the superconductor.

To include the important physics of screening, my simulation is divided into

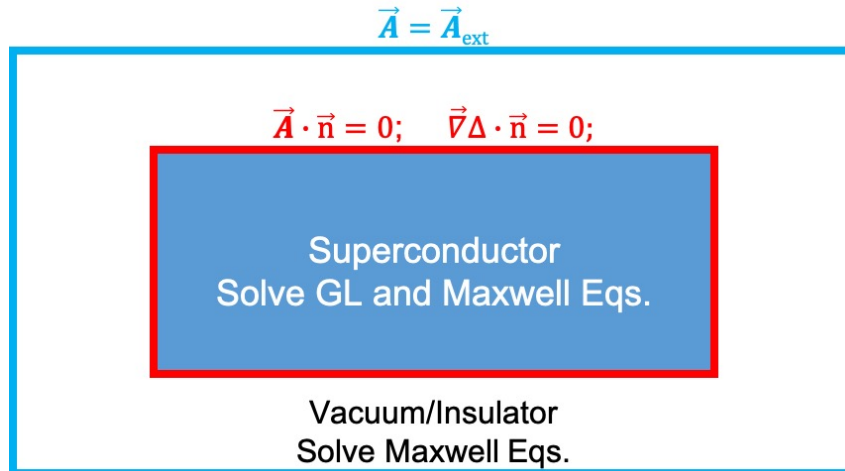


Fig. 7.4 Schematic view of the superconductor and vacuum domains and boundary conditions in my COMSOL simulations.

two domains: Superconductor and Vacuum (Fig. 7.4). The full coupled GL equations are solved in the superconductor domain, while only Maxwell's equations are solved in the vacuum domain, with appropriate boundary conditions at the interface. Any finite value of  $\vec{A} \cdot \vec{n}$  or  $\vec{\nabla} \Delta \cdot \vec{n}$  would lead to a finite current passing through the superconductor-vacuum boundary (red box in Fig. 7.4), which is nonphysical, hence Eq. (7.68) and Eq. (7.69) are enforced at the superconductor/vacuum interface. Any externally applied magnetic field is introduced by placing a boundary condition on the outer boundary of the vacuum domain (Eq. (7.70)). The vacuum domain is assumed to be large enough that at the external boundary (blue box in Fig. 7.4) the magnetic field generated by the superconductor is negligible. Fig. 7.4 schematically summarizes this scenario.

Now I examine several key examples where it is crucial to include the screening response of the superconductor to capture the interesting physics. Through these two

examples our approach to solving the TDGL equations is validated.

#### 7.4.1 Superconducting sphere in a uniform magnetic field

First consider the classic problem of a superconducting sphere immersed in a uniform magnetic field. Assume that the superconductor remains in the Meissner state. It is known from the exact solution to this problem that there will be an enhancement of the magnetic field at the equatorial surface of the superconducting sphere due to the magnetic flux that is expelled from the interior of the sphere. To test this approach to solving the TDGL equations I created a model of this situation in COMSOL. Then the response was simulated using the two-domain method, and the well-established standard single domain method. Later I compared both results with the exact analytical solution for the magnetic field profile [220].

Fig. 7.5 shows the GL simulation of a superconducting sphere subjected to a uniform static external magnetic field. The boundaries of the spheres are shown with the dashed lines, where the smaller sphere is the superconducting sphere, and the larger sphere is the vacuum domain. The colors represent the amplitude of the  $\hat{z}$ -component of the applied magnetic field in the  $y$ - $z$  plane passing through the common center of the spheres. Black lines show the streamline plot of magnetic field in the same  $y$ - $z$  plane. The streamline plot is defined as collection of lines that are tangent everywhere to the instantaneous vector field, in this case to the direction of the magnetic field. The simulation was initialized in a field free configuration and the external magnetic field was applied at  $t = 0$ . The simulation was iterated for  $t = 1000\tau_j$  time steps after

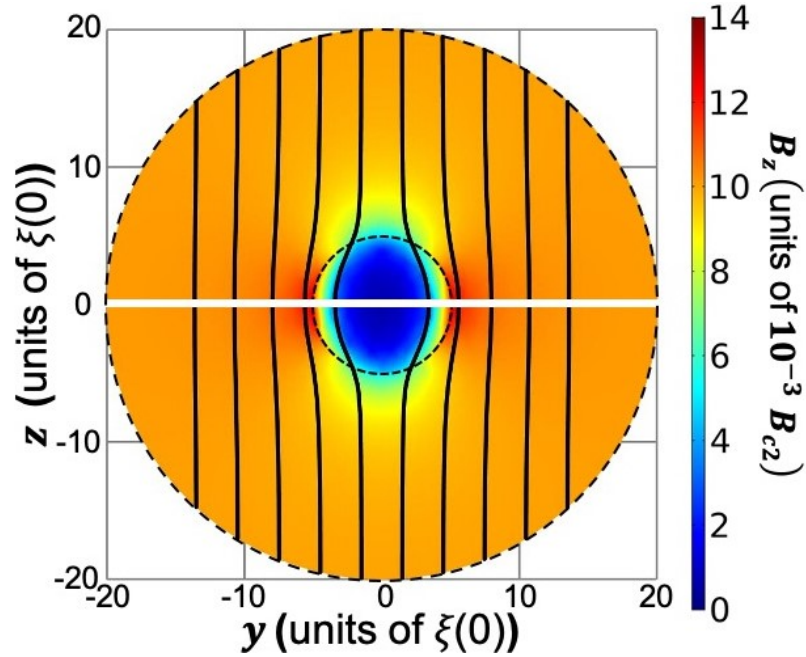


Fig. 7.5 Plot of TDGL two-domain solution for  $z$  component of magnetic field in a plane through the center of the sphere in and around a superconducting sphere in the Meissner state subjected to a uniform static external magnetic field in the  $z$ -direction. The dashed lines show the boundaries of the spheres, with the smaller sphere being the superconducting sphere with diameter  $10\xi(0)$  and the larger sphere being the vacuum domain with diameter  $40\xi(0)$ . The solution is obtained for temperature  $T = 0$ , GL parameter  $\kappa = 1$  and external magnetic field  $\vec{B}_{applied} = 10 \times 10^{-3} B_{c2} \hat{z}$ . Black lines show the streamline plot of magnetic field, while the color represents the value of magnetic field component  $B_z$ . The white line indicates the equator, and the magnetic field along the white line is shown in Fig. 7.6.

which the changes in  $|\Delta|^2$  were  $< 0.1\%$  per iteration.

To test the reproducibility of the result, I later repeated the simulation, but this time I increased the external magnetic field linearly in time from zero to  $0.01B_{c2}$  between time 0 and  $500\tau_j$ . After this, the simulation was again iterated for  $t = 1000\tau_j$  time steps. The results of these two simulations were identical.

Eq. (7.68) and Eq. (7.69) were enforced on the spherical superconductor-vacuum boundary ( $r = 5\xi(0)$ ) in both cases. When the two-domain method was used, the GL equations were solved in the inner sphere ( $r < 5\xi(0)$ ) and only Maxwell's equations were solved in the vacuum domain ( $5\xi(0) < r < 20\xi(0)$ ). Eq. (7.70) was enforced at the outer boundary of the simulation ( $r = 20\xi(0)$ ). When the single domain simulation method was used, Eq. (7.70) was enforced at the inner boundary of the simulation ( $r = 5\xi(0)$ ) and the vacuum domain was not utilized.

The top plot in Fig. 7.6 shows the profile of the z-component of magnetic field ( $B_z$ ) along a line through the center of the sphere, in a plane perpendicular to the externally applied magnetic field (white line in Fig. 7.5) calculated from the single domain simulation, the two-domain simulation and the analytic result. Inside the sphere, the magnetic field profile calculated from the single domain simulation and the two-domain simulation are very similar although not identical. The bottom plot in Fig. 7.6 shows the difference between the TDGL simulation results and the analytic solution. The field deep inside the sphere is strongly suppressed by the screening currents. This can also be seen from the color-map in Fig. 7.5. The blue region inside the sphere corresponds to the fully shielded portion of the sphere. However, there is a region outside the sphere around the equator where the magnetic field is enhanced



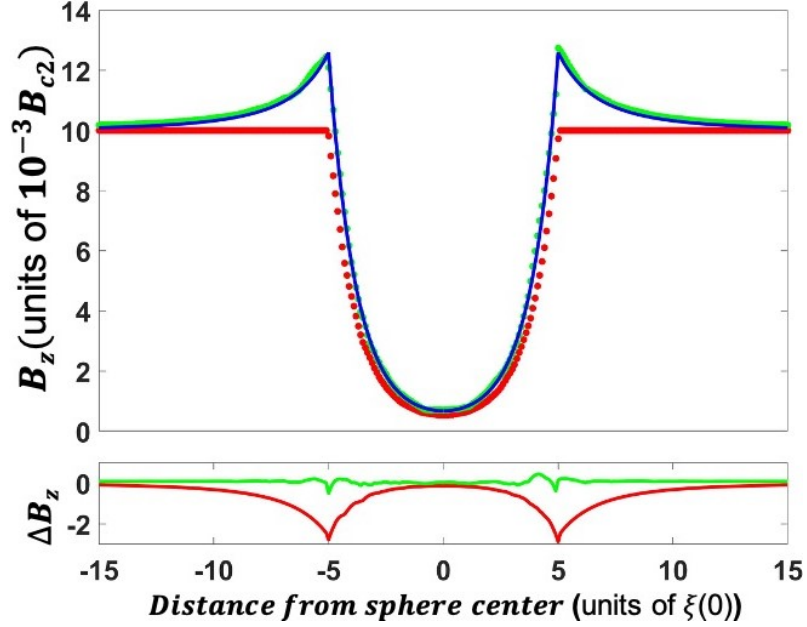


Fig. 7.6 Top: Magnetic field  $\hat{z}$ -component ( $B_z$ ) profile through the center of sphere (white line in Fig. 7.5). The results of a single domain TDGL model are shown in red, a two-domain TDGL model in green, and the analytic solution is shown as a blue solid line. Bottom: The difference between a two-domain TDGL model and the analytic solution is shown in green and the difference between single domain TDGL model and the analytic solution is shown in red. The biggest difference is observed at the surface.

(red color in Fig. 7.5).

At the surface of the sphere the magnetic field calculated from the two-domain model reproduces the exact analytic solution, while the single domain model fails to account for the enhancement of magnetic field on the equator of the sphere. This disparity between the single domain model and analytic solution is caused by the treatment of the boundary conditions. In the single domain model, Eq. (7.70) is enforced at the superconductor-vacuum interface, which completely ignores the effect of screening currents. Thus a two-domain model should be used for any problem where screening and the magnetic field profile at the surface of the superconductor is important.

## 7.4.2 Point magnetic dipole above a semi-infinite superconductor

To ensure that I can accurately simulate the screening currents produced by a spatially nonuniform magnetic field, I numerically simulated the case of a static point magnetic dipole placed at a height of  $h_{dp} = 1\xi(0)$  above the surface of a semi-infinite superconductor. The superconducting domain and vacuum domain are simulated inside two coaxial cylinders with equal radius  $R = 8\xi(0)$  with common axis along the  $\hat{z}$  direction of the Cartesian coordinate system. The origin of this coordinate system is located on the superconductor surface immediately below the dipole. The thickness of the superconducting domain is  $h_{sc} = 10\xi(0)$  and the height of the vacuum domain is  $h_{vac} = 5\xi(0)$ . The GL parameter  $\kappa$  is set to 1.

The surface magnetic fields produced by the dipole are assumed to be below the lower critical field  $H_{c1}$ , so that the superconductor remains in the Meissner state. The simulation was started with a superconductor in the uniform Meissner state and the dipole field equal to 0. Then, at time  $t = 0$ , the dipole magnetic field is turned on, and the simulation is iterated in time until the relative tolerance of  $\frac{\partial u}{u} < 0.001$  is achieved for all the variables in the column vector of all unknowns  $u$  (Eq. (7.61)). At this point the static solution to the problem is obtained. Later the simulation was repeated with external magnetic field linearly increasing with time over  $t = 0 - 500\tau_j$  time interval before reaching a set constant value. The results of these two simulations were identical.

I compared my TDGL results for the distribution of the surface screening current

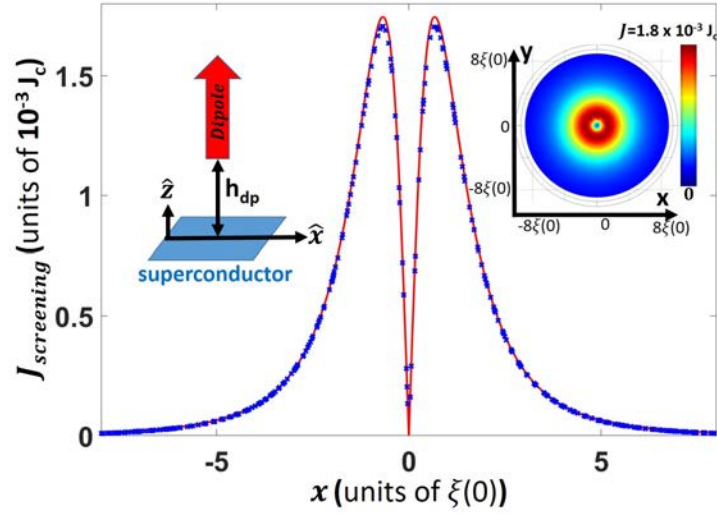


Fig. 7.7 The magnitude of the superconducting screening current density at the surface  $J_{screening}$  as a result of a perpendicular magnetic dipole placed  $h_{dp} = 1\xi(0)$  above the superconductor vs the horizontal distance from the dipole location obtained from GL simulation (blue  $\times$ ) and numerical solution for the same scenario obtained from Ref. [221] (red solid line). Left inset shows a schematic of the dipole over the superconductor, while the right inset shows the top view of the surface current distribution calculated by GL, which is azimuthally symmetric.

density  $\vec{J}_{screening}(x, y)$  to numerical results obtained by Melnikov [221] for the case of a perpendicular magnetic dipole. Fig. 7.7 shows a comparison of the calculated screening current profiles. Both results show that there is a circulating screening current centered directly below the dipole. Also note that the screening current reaches zero at the outer boundary of the simulation. This indicates that a sufficiently large domain was chosen for simulation and no finite size effects are expected. There is a very good agreement between the two-domain GL simulation result and numerical results obtained by Melnikov, in the low magnetic field limit where there are no vortices (Fig. 7.7). This, and the previous result, serve to validate my two-domain approach to properly capturing the screening response of the superconductor.

# 8

---

## TDGL Modeling of the Near-Field Magnetic Microwave Microscope

---

In [Chapters 4](#) and [5](#) I described our microwave (MW) magnetic microscope and some experimental data which can't be fit using the models discussed in [Chapter 6](#). In this chapter I will present the TDGL simulation of the probe-sample interaction. Even in the absence of defects, vortex semiloops can penetrate into a superconductor subjected to a strong rf magnetic field, generating nonlinear rf response [[20](#), [69](#)].

The TDGL equations were described in great detail in [Chapter 7](#). However, one needs to keep in mind that TDGL is not a microscopic theory, thus some of the parameters of the model are difficult to determine precisely for a given material of interest. For this reason I focus on semi-quantitative results and use the phenomenological TDGL equations mainly to give insight into the signals created by our near-field microwave microscope, and to study rf vortex penetration into the surfaces of SRF cavities.

## 8.1 Magnetic Dipole

The rf magnetic field produced by the magnetic writer probe sitting on top of a sample is very similar to the magnetic field produced by a horizontal point magnetic dipole with normalized magnetic moment  $M_{dp}(t)\|\hat{x}$  placed at a height  $h_{dp}$  above the sample. The normalized vector potential produced by such a dipole in free space is given by [222]:

$$\vec{A}_{dp}(x, y, z, t) = \frac{M_{dp}(t)}{(x^2 + y^2 + (z - h_{dp})^2)^{3/2}} \left( -(z - h_{dp})\hat{y} + y\hat{z} \right) \quad , \quad (8.1)$$

where the origin of the coordinate system is on the superconductor surface immediately below the dipole. While this is very different from a uniform and parallel magnetic field inside an actual SRF cavity, the dynamics of the vortex semiloops created by this field should be very similar.

The superconducting domain and vacuum domain are simulated inside two coaxial cylinders with equal radius  $R$  (see Fig. 8.1) with common axis along the  $\hat{z}$  direction of the Cartesian coordinate system. The thickness of the superconducting domain is  $h_{sc}$  and the height of the vacuum domain is  $h_{vac}$  in normalized units.

The boundary condition Eq. (7.70) is enforced at the top of the vacuum domain, whereas a  $\vec{B} = 0$  boundary condition is enforced at the bottom and the sides of the superconducting domain, since it is expected that the superconducting currents due to the Meissner state will fully shield the externally applied magnetic field before it reaches the outer boundary of the superconductor.

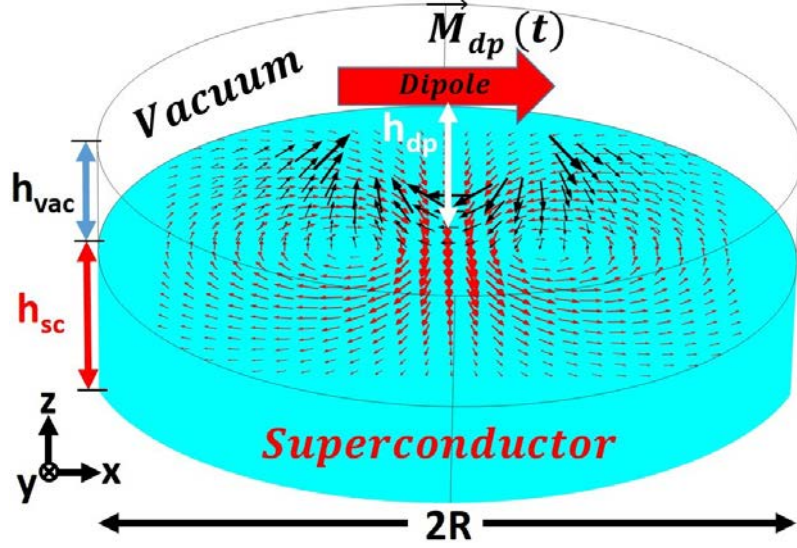


Fig. 8.1 TDGL simulation setup for an oscillating horizontal magnetic dipole  $\vec{M}_{dp}(t)$  at fixed height  $h_{dp}$  above the superconductor surface. The magnetic probe is approximated as an oscillating point magnetic dipole parallel to the surface. Red Arrows: Surface currents on the horizontal (xy) superconductor/vacuum interface as calculated from the self-consistent TDGL equations. Black Arrows: Externally applied magnetic field on a vertical plane (xz) perpendicular to the superconductor surface and including the dipole.

The interaction between the probe and the sample was modeled by solving the TDGL equations. In the simulation, we specify  $M_{dp}(t)$  indirectly through the the magnetic field experienced at the origin (on the superconductor surface immediately below

the dipole)  $\vec{B}_0(t) = \vec{\nabla} \times \vec{A}_{dp}(0, 0, 0, t) = -\frac{M_{dp}(t)}{h_{dp}^3} \hat{x}$ , where  $M_{dp}(t) = M_{dp}(0) \sin(\omega t)$ .

The driving rf magnetic field profile is specified through the analytic equation for the magnetic vector potential of a point dipole (Eq. (8.1)), therefore the dipole itself can be placed either inside the vacuum domain  $h_{vac} > h_{dp}$  or beyond it  $h_{vac} < h_{dp}$  without affecting the accuracy of the simulation.  $h_{vac}$  is chosen to be large enough to be consistent with Eq. (7.70) at the top of the vacuum domain.

The choice of material parameters is discussed in Sec. 7.3.2. The period of the

dipole rf magnetic field was chosen to be  $\frac{2\pi}{\omega} = 200\tau_j$ . The GL parameter  $\kappa = 1$  [54] and  $\eta$  is on the order of unity (parameters summarized in Table 8.1). It should be noted that the relaxation time  $\tau_j \sim ps$  with  $\eta \sim 1$  is "fast" in the sense that the order parameter will quickly follow any variations in rf field or current.

The spatial distribution of the magnetic field at the surface of the superconductor is set through the value for the dipole height  $h_{dp}$ . While the driving rf magnetic field is specified through the analytic equation Eq. (8.1), the goal is to reproduce the actual spatial distribution produced by the magnetic writer head at the surface of the superconductor, which was provided by the manufacturer Sec. 4.5.2. To produce a similar spatial distribution of the magnetic field, we set the dipole height to the  $300nm - 500nm$  range which corresponds to  $h_{dp}$  of  $8 - 12\xi(0)$  in normalized units.

## 8.2 Vortex semiloops

Consider a dipole that oscillates sinusoidally in time with frequency  $\omega$ . In this section we calculate the response of the superconductor to this external inhomogeneous and time-dependent magnetic field. Our objective is to describe a spatially-inhomogeneous microwave frequency stimulus of the superconducting surface. In this section a uniform superconductor domain with no defects is considered. The simulation is started with the order parameter having a uniform value of  $\Delta = \Delta_\infty$  everywhere. At time  $t = 0$  the externally applied magnetic field is turned on. Then

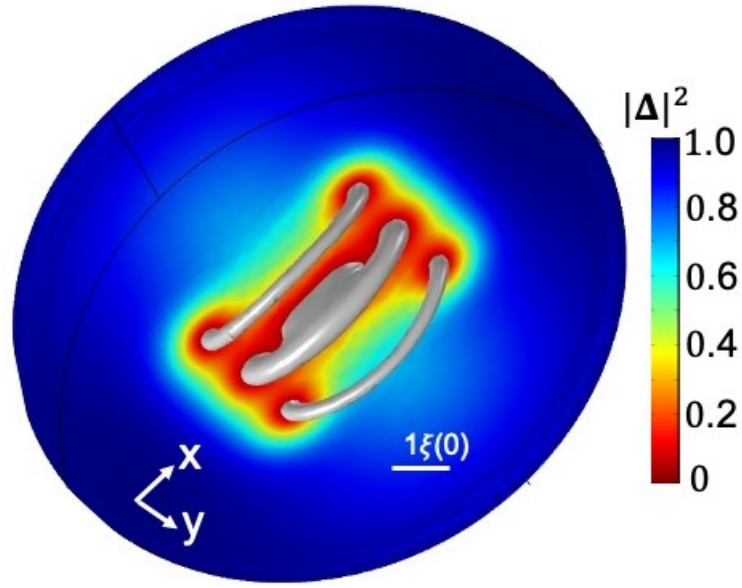


Fig. 8.2 Snapshot of 3 vortex semiloops at time  $t = 73\tau_j$  during the rf cycle of period  $200\tau_j$ . In this view, one is looking from inside the superconducting domain into the vacuum domain. Plots of  $|\Delta|^2$  are evaluated at the superconductor surface for an oscillating parallel magnetic dipole above the superconductor. The three-dimensional silver surfaces (corresponding to  $|\Delta|^2 = 0.005$ ) show the emergence of vortex semiloops. The simulation parameters are given in [Table 8.1](#).

the simulation is run for several rf cycles to reach the steady state solution.

[Fig. 8.2](#) shows the results for such a simulation and the parameters are given in [Table 8.1](#). In this view, the viewer is looking from inside the superconducting domain into the surface of the superconductor. As the time progresses the value of the local rf magnetic field amplitude  $|\vec{B}_0(t)|$  increases eventually exceeding the value of vortex nucleation field at a given temperature  $H_v(T)$ . At first, a domain forms just below the probe where the superconducting order parameter is suppressed by the externally applied magnetic field and screening currents. Later in rf period, when the rf magnetic field amplitude decreases back to zero, this "suppressed domain" diminishes and the vortex semiloops emerge from it. In [Fig. 8.2](#) three well-defined examples of such



vortex semiloops are illustrated by the three-dimensional silver surface corresponding to  $|\Delta|^2 = 0.005$ . In this case, the simulation was run for 3 driving periods to stabilize and the results shown in Fig. 8.2 are from the 4<sup>th</sup> driving period. In the upcoming sections, I will describe the time evolution of these vortex semiloops, their dynamics as a function of rf field amplitude and friction coefficient, and their interaction with point defects embedded inside the superconductor.

Parameter Name	Symbol	Scale	Fig. 8.2	Fig. 8.3	Fig. 8.4	Fig. 8.5	Fig. 8.6	Fig. 8.7	Fig. 8.8
Temperature	$T$	$T_c$	0	0.6	0.9	0.6	0.9	0.85	6.5
Applied RF field amplitude	$B_0$	$B_{c2}$	0.75	0.55	0.3	0.46-0.84	0.3	0.3	0.4
Period of Applied RF field	$2\pi/\omega$	$\tau_0$	200	200	200	200	200	200	200
Dipole height	$h_{dp}$	$\lambda_0$	8	8	12	8	12	12	12
Radius of the simulation domain	$R$	$\lambda_0$	12	35	60	20	60	40	5-50
Height of superconducting domain	$h_{sc}$	$\lambda_0$	6	20	50	8	50	25	30
Height of vacuum domain	$h_{vac}$	$\lambda_0$	3	20	25	4	25	15	15
Ginzburg-Landau parameter	$\kappa$	1	1	1	1	1	1	1	1
Ratio of characteristic time scales	$\eta$	1	1.675	1	0.2	1	0.05-5.79	0.5	1.675

Table 8.1 Values of parameters used for TDGL simulations of the oscillating magnetic dipole above the superconductor.

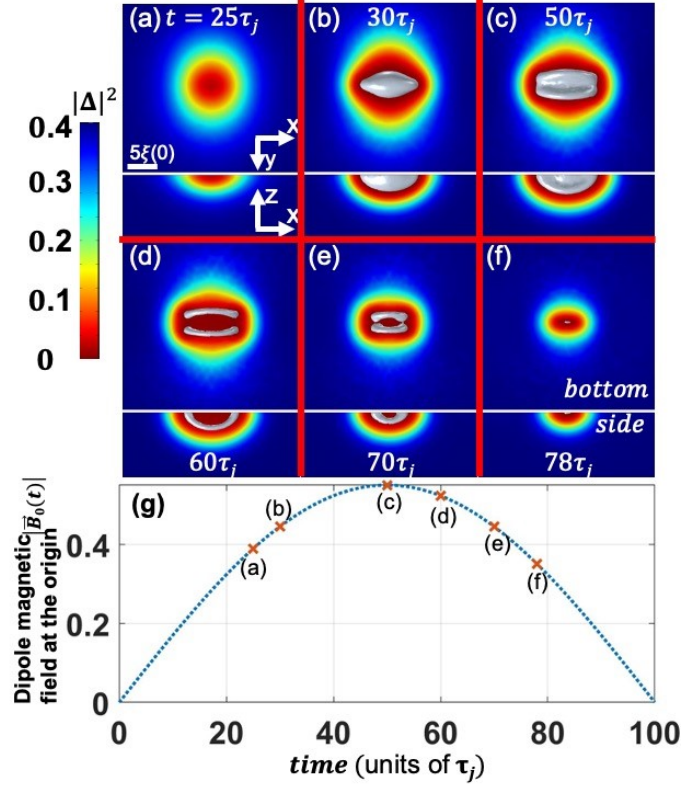


Fig. 8.3 Summary of TDGL solution for an oscillating parallel magnetic dipole above a superconducting surface. (a)-(f) Plots of  $|\Delta|^2$  evaluated at the superconductor surface at different times for an oscillating parallel magnetic dipole above the superconductor. In the top part of each panel, one is looking from inside the superconducting domain into the vacuum domain, whereas in the bottom part of each panel, one is looking at the  $x$ - $z$  cross-section plane towards the  $+y$  axis.  $\vec{M}_{dp}(t)$  is chosen such that  $\vec{B}_0(t) = 0.55\sin(\omega t)\hat{x}$ . The three-dimensional silver surfaces (corresponding to  $|\Delta|^2 = 0.005$ ) show the emergence of vortex semiloops. (g)  $|\vec{B}_0|$  at the surface vs time during the first half of the rf cycle. Red crosses correspond to field values for snapshots (a)-(f). The simulation parameters are given in Table 8.1.

### 8.3 The evolution of vortex semiloops with time

The main goal of the simulation described in the previous section was to illustrate vortex semiloops, as such the simulation was performed at  $T = 0$  and in a very small domain. To study the time evolution of this vortex semiloops a similar simulation was performed at a higher temperature and a larger simulation domain.

Fig. 8.3 shows results for this simulation, illustrating the order parameter space and time dependence, and the parameters of simulation are given in Table 8.1. The simulation was run for 5 driving periods to stabilize, and the results shown in Fig. 8.3 are from the 6<sup>th</sup> driving period. We see that as  $\vec{B}_0(t)$  increases a suppressed  $|\Delta|^2$  domain (red region) forms at the superconductor surface immediately below the dipole. At  $t = 50\tau_j$  the magnetic field reaches its peak value and the suppressed superconducting region reaches its deepest point inside the superconducting domain illustrated by the silver surface in Fig. 8.3(c). Later ( $t > 50\tau_j$ ), the amplitude of the external driving magnetic field decreases, the suppressed  $|\Delta|^2$  domain rapidly diminishes and vortex semiloops spontaneously emerge, become well-defined (Fig. 8.3(d),(e)), then move back towards the surface and vanish there before the end of the first half of the rf cycle. In the second part of the rf cycle, the same process is repeated but now antivortex-semiloops enter the superconducting domain. The full solution animated over time is available online as supplemental material to Ref. [20]. In this particular scenario vortices and anti-vortices never meet, unlike the situation discussed in [104].

Fig. 8.4 shows another simulation result with the same period but otherwise with a different set of parameters (listed in Table 8.1). Here the dipole is further away from the surface, at  $h_{dp} = 12\xi(0)$  and the temperature is set to  $T = 0.9T_c$ . Three dimensional silver contour surfaces correspond to  $|\Delta|^2 = 0.005$ . The two-dimensional screening currents (white arrows) and two-dimensional order parameter (colors) are plotted in the  $yz$ -plane. Three vortex semiloops are clearly visible in this  $x = 0$  cross-section cut. We see that the vortex semiloops penetrated somewhat deeper into the superconductor than the suppressed order parameter domain.

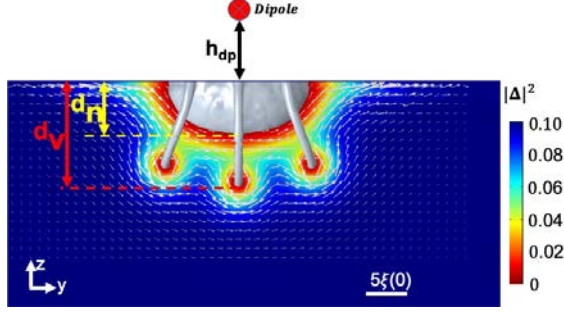


Fig. 8.4 Plots of  $|\Delta|^2$  (color) and  $\vec{J}_{surf}$  (arrows) evaluated at the two dimensional  $x = 0$  plane inside the superconductor at  $t = 50\tau_j$  for an oscillating parallel magnetic dipole above the superconductor. White arrows indicate the currents induced inside the superconducting domain. The three-dimensional silver surfaces (corresponding to  $|\Delta|^2 = 0.005$ ) show the emergence of vortex semiloops and the suppressed superconducting domain. All model parameters are listed in [Table 8.1](#)

## 8.4 The evolution of vortex semiloops with rf field amplitude

One can also study the effect of the applied rf field amplitude, defined through  $|\vec{B}_0|$ , on the number and the dynamics of vortex semiloops. [Fig. 8.5](#) shows the bottom view of the order parameter on the surface of the superconducting domain for different values of the applied rf magnetic field amplitude, all at the same point in the rf cycle ( $t = 50\tau_j$  and  $\vec{B}_0(t)$  at its peak value). As expected, the number of vortex semiloops increase with increasing  $|\vec{B}_0|$ . Once  $|\vec{B}_0| = 0.6$  is reached, a normal state  $|\Delta|^2 = 0$  domain emerges at the origin, as opposed to a suppressed  $|\Delta|^2$  domain observed at lower rf field amplitudes. The simulation is performed with  $T = 0.6T_c$ ,  $h_{dp} = 8\xi(0)$  and  $\eta = 1$ . The full solution as a function of peak applied magnetic field amplitude is available online as supplemental material to Ref. [\[20\]](#).

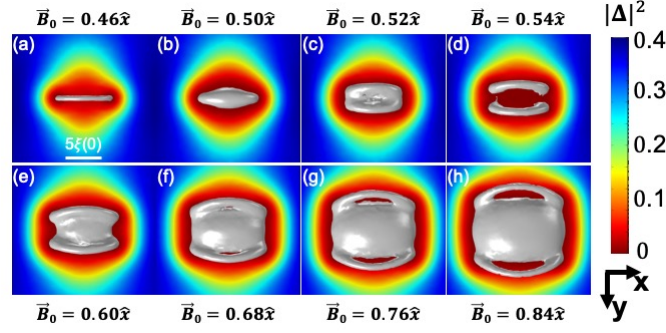


Fig. 8.5 a-h) Plots of  $|\Delta|^2$  evaluated at the superconductor surface at  $t = 50\tau_j$  for an oscillating parallel magnetic dipole above the superconductor as a function of dipole strength. In this view, one is looking from inside the superconducting domain into the vacuum domain. The maximum amplitude of applied rf field is shown as  $|\vec{B}_0|$ . The silver three-dimensional surfaces correspond to  $|\Delta|^2 = 0.005$  and show the suppressed order parameter domain and the vortex semiloops. The parameters of the simulation are listed in Table 8.1.

## 8.5 The dependence of rf vortex dynamics on the friction coefficient $\eta$

As we discussed in Sec. 7.3.2 the friction coefficient  $\eta$  depends on the purity of the material which is defined through the value of the mean-free-path  $l$ . Furthermore, different materials will have a different effective superfluid density  $n_s^*$  which also leads to tunable  $\eta$ . The parameter  $\eta$  governs the dynamics of the order parameter and vector potential relaxation. However one should remember that there is a limiting value for the friction coefficient  $\eta \leq \eta_0 = 5.79$  (see Eq. (7.52)) [162, 188].

In this section I entertain the possibility that  $\eta$  can be tuned in the range of  $\eta = 0 - 5.79$ . Fig. 8.6 shows the maximum extent of the rf vortex semiloop excursion ( $d_v$ , defined in Fig. 8.4) and maximum extent of suppressed order parameter ( $d_n$ , defined in Fig. 8.4) over the full rf cycle, as a function of  $\eta$ . In the case of vortex

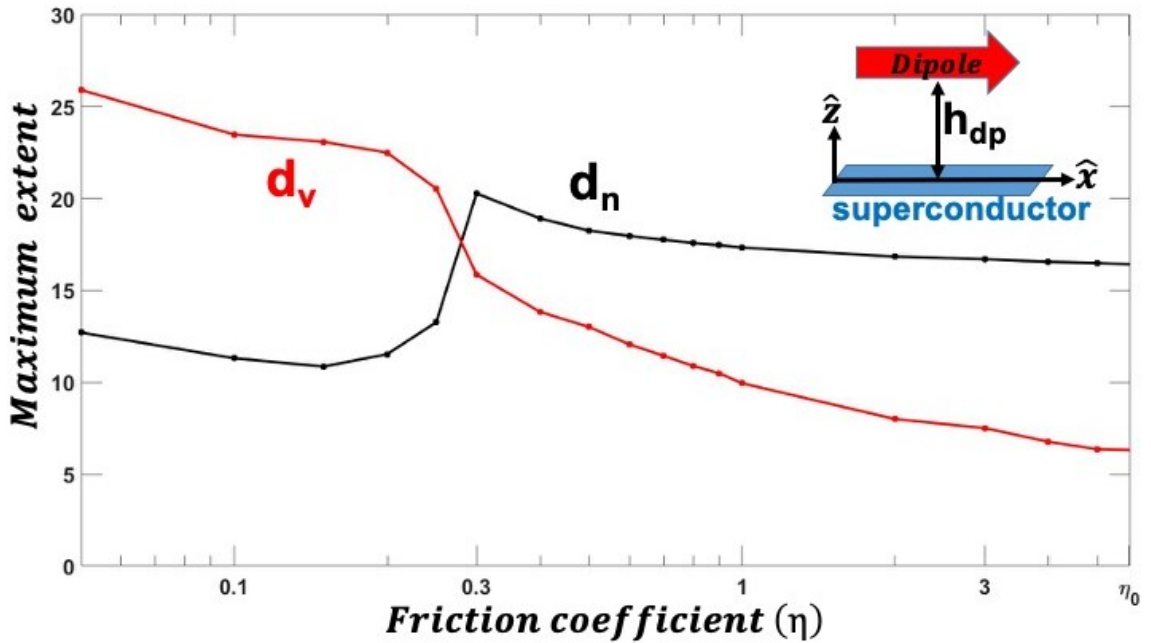


Fig. 8.6 Plot of the maximum extent (in units of  $\xi(0)$ ) of excursion for the vortex semiloop  $d_v$  and the maximum extent for the suppressed superconductor domain  $d_n$  in an rf cycle as a function of friction coefficient  $\eta$  (log scale). The TDGL equations are solved at  $T = 0.9T_c$  for a parallel magnetic dipole above the superconductor. The full list of simulation parameters is given in Table 8.1.

semiloop excursion, lower  $\eta$  values lead to nucleation of vortex semiloops earlier in the rf cycle, and that reach deeper into the superconductor. This in turn provides additional channels for magnetic field penetration, effectively reducing the size of the suppressed superconducting domain (decreasing  $d_n$  for  $\eta < 0.3$  in Fig. 8.6).

As the  $\eta$  value increases the maximum vortex excursion distance  $d_v$  becomes smaller than the suppressed superconducting domain depth  $d_n$ . In this case the vortex semiloops simply can't detach from the suppressed superconductor domain resulting in an effectively larger domain of reduced order parameter. We identify the vortices in this case by regions of small radius of curvature on the surface of suppressed order

parameter, as shown in Fig. 8.7(b) and (c), for example.

When the friction coefficient is increased further, the time scale for the relaxation of the order parameter  $\tau_\Delta$  approaches/or exceeds the period of the rf field. In this case, no vortex semiloops develop, because there is simply not enough time within the rf cycle for the vortex to nucleate. In this limit, the superconductor responds to a time averaged value of the magnetic field  $\langle \vec{B}^2(t) \rangle$ , instead of following the rf magnetic field adiabatically [36]. The only effect of the rf magnetic field in this scenario is the formation of a suppressed  $|\Delta|^2$  domain at the superconductor surface immediately below the dipole, similar to Fig. 8.3.(b). For large  $\eta$  this region of suppressed  $|\Delta|^2$  is also reduced in size.

## 8.6 The effect of localized defects on rf vortex semiloops

Here I want to examine the effect of a single point-like defect on rf vortex nucleation in a bulk sample. The procedure to model a defect was discussed in Sec. 7.3.3. A simple defect can be created, for example by defining a Gaussian-in-space domain with suppressed superconducting critical temperature  $T_{cd}$ , where  $0 < T_{cd} < T_c$ :

$$\epsilon(\vec{r}, T) = 1 - \frac{T}{1 - (1 - T_{cd}) e^{-\frac{(x-x_d)^2}{2\sigma_x} - \frac{(y-y_d)^2}{2\sigma_y} - \frac{(z-z_d)^2}{2\sigma_z}}}, \quad (8.2)$$

where  $(x_d, y_d, z_d)$  are the central coordinates of the defect,  $\sigma_x, \sigma_y, \sigma_z$  are the standard deviations in the 3 coordinate directions, and  $T > T_{cd}$  all expressed in normal-

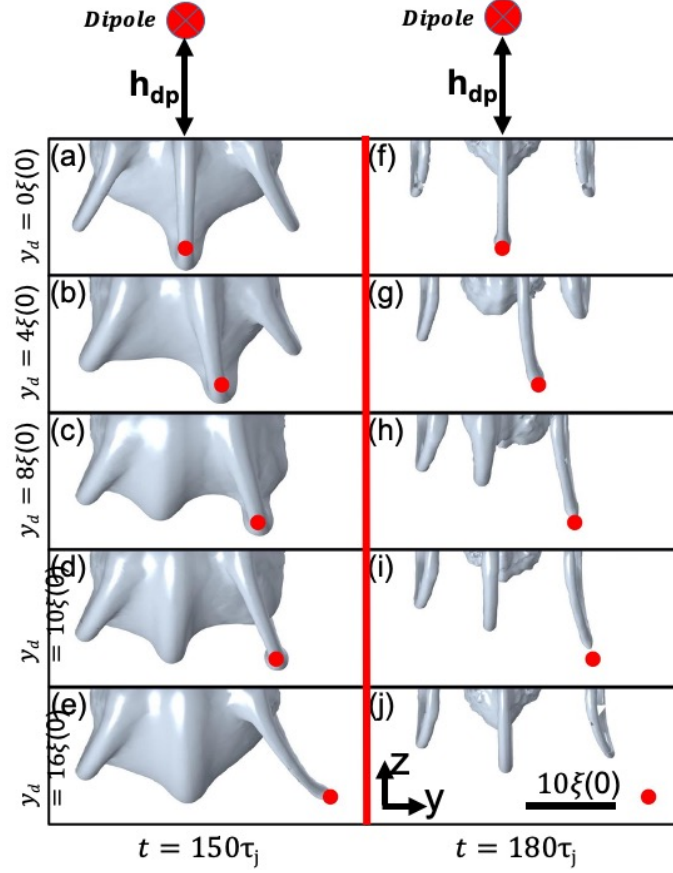


Fig. 8.7 Summary of TDGL solutions for an oscillating parallel magnetic dipole above a superconducting surface in the presence of a localized defect at  $\vec{r}_d = 0\hat{x} + y_d\hat{y} - 12\hat{z}$ , where  $y_d$  is varied from 0 to  $16\xi(0)$ . (a)-(e) Plots of vortex semiloops in the  $y$ - $z$  cross-section plane below the dipole illustrated with a three-dimensional silver surface (corresponding to  $|\Delta|^2 = 0.003$ ) at time  $t = 150\tau_j$ , when the applied magnetic field reaches its peak amplitude. (f)-(j) Plots of vortex semiloops at time  $t = 180\tau_j$ . The defect is denoted by the red dot to the right of the center.  $\vec{M}_{dp}(t)$  is chosen such that  $\vec{B}_0(t) = 0.30\sin(\omega t)\hat{x}$ . The full list of simulation parameters is given in [Table 8.1](#).

ized values. [Fig. 8.7](#) shows a simulation which was done with parameters given in [Table 8.1](#). A localized defect with  $\sigma_x = \sigma_y = \sigma_z = \sqrt{2}$  and  $T_{cd} = 0.2T_c$  is located at  $\vec{r}_d = 0\hat{x} + y_d\hat{y} - 12\hat{z}$ , where  $y_d$  is varied from 0 to  $20\xi(0)$ , to represent a localized defect that is centered at a depth of 12 coherence lengths ( $\xi(0)$ ) below the surface and offset various distances from the oscillating dipole. We observed very similar vor-



tex semiloops in the time domain evolution as those shown above. However, one of the vortex semiloops is now attracted towards the defect location (shown as red dot in Fig. 8.7 and is distorted in shape. Furthermore, the vortex attracted by the defect remains inside the superconductor longer compared to the other vortex semiloops. Note that the semiloop disappears at the end of each half of the rf cycle, hence the pinning potential of this defect is not strong enough to trap the vortex semiloop, only to modify the rf behaviour. The strength of the defect depends both on its critical temperature  $T_{cd}$  and size.

## 8.7 Fitting the third harmonic data

These simulations have proven very useful in understanding the measured third-harmonic response of Nb materials subjected to intense localized rf magnetic fields. In all the cases described in the previous section, the superconducting gap  $|\Delta|^2$  and the vector potential  $\vec{A}$  are first retrieved from the simulation. Using Eq. (7.42) the screening super-current is calculated for each point in space and time. The response magnetic field  $\vec{B}_{sc}(t)$  generated by said currents at the location of the dipole is calculated using the Biot-Savart law. This calculation is simplified due to the symmetric nature of the problem. At the location of the dipole, magnetic field produced by the superconductor is only in the  $\hat{x}$  direction. The third-harmonic response  $V_{3\omega}(B_0)$  recovered at the location of the dipole is obtained through Fourier transformation of the calculated time-dependent response magnetic field  $\vec{B}_{sc}(t)$ . Later the TDGL-derived

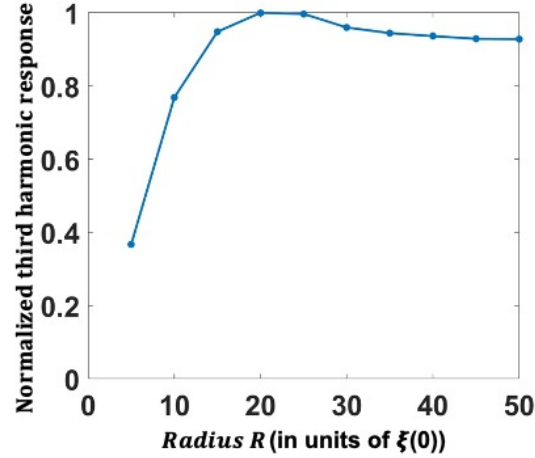


Fig. 8.8 The third harmonic response  $B_{3\omega}(B_0)$  normalized by the maximum value vs the radius of the simulation domain  $R$ . Note that  $h_{sc}$  and  $h_{vac}$  are varied proportionally with  $R$ . The parameters of the simulation are listed in Table 8.1.

third-harmonic voltage  $V_{3\omega}$  was compared with the third-harmonic response measured from experiment.

Many simulations were performed by varying temperature  $T$ , rf magnetic field  $B_0$ , dipole height  $h_{dp}$  and friction coefficient  $\eta$ . The radius of the simulation domain  $R$ , the height of the superconductor domain  $h_{sc}$  and the height of the vacuum domain  $h_{vac}$  control the geometry, and some finite size effects can be seen for  $R < 30\xi(0)$  (Fig. 8.8). However, at sufficiently high values of  $R$ ,  $h_{sc}$  and  $h_{vac}$ , the third harmonic response  $V_{3\omega}$  is independent of the simulation size. Note that larger geometry size leads to larger meshes and longer run times due to limited computational power.

$V_{3\omega}(B_0)$  as a function of the peak magnetic moment of the dipole shows the following behaviour. Harmonic response is small for smaller values of dipole magnetic moments but increases rapidly above an onset magnetic moment value, reaches a peak value and then slowly decreases back to a finite value, which depends on temperature,

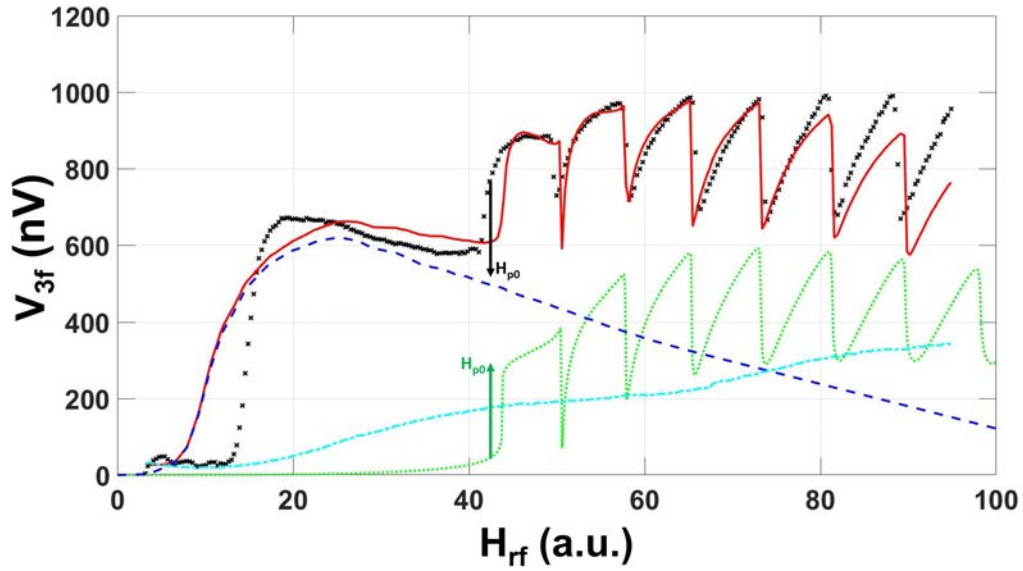


Fig. 8.9 Third-harmonic response  $V_{3f}$  data from Sample 1 at  $T = 5.1K$  and  $f = 2.2GHz$  (black  $\times$  markers). Also shown are the time-dependent Ginzburg-Landau fit with  $H_{dp} = 12$  (blue dashed line), probe background (cyan dotted line), RSJ fit with  $I_c R = 58.3\mu V$  (green dashed-dotted line) (see Sec. 6.1), and complete fit obtained by vector complex addition (red solid line).

height of the dipole and friction coefficient  $\eta$ . Note that this evolution is very similar to the low  $H_{rf} < H_{p0}$  part of the Nb on Cu sample data shown in Fig. 6.7 of Chapter 6 and re-plotted here (Fig. 8.9).

In total the data shown in Fig. 8.9 have contributions from a nonlinear response generated by the current-biased junction, intrinsic low-field nonlinearity modeled by TDGL, and a temperature-independent probe background. First, the steps discussed in Chapter 6 for fitting the RSJ model are followed. Later, complex vector addition of all three contributions is performed for a full fit (Fig. 8.9).

In conclusion, the TDGL model can be used to describe the "pedestal" low-field non-periodic part of the third harmonic data measured from Nb samples, however no

periodic response was observed from this model within the range of parameters that were used in our simulations.

# 9

---

## Vortex-Semiloops inside SRF cavities

---

In [Chapter 8](#), I examined the dynamics of vortex semiloops created by a point magnetic dipole, as it is relevant to the magnetic microscopy experiment presented in [Chapter 4](#). In this section I will address the more general case which is appropriate for SRF applications, a uniform parallel rf magnetic field ( $\vec{B}(t) = B_0 \sin(\omega t) \hat{x}$ ) above the superconductor in the presence of a single defect on the surface. Additionally, I will explore some other dynamic generalizations of GL theory, beyond the TDGL approach that was presented in [Sec. 7.2](#) and utilized in [Chapter 8](#).

### 9.1 Numerical simulation of SRF cavity surface fields

The interior surface of an SRF cavity was simulated using the two-domain simulation method described in [Sec. 7.4](#). In order to have truly uniform field in the numerical simulation, the boundary between superconductor and vacuum is simulated as an infinite plane. The superconducting domain and vacuum domain are simulated

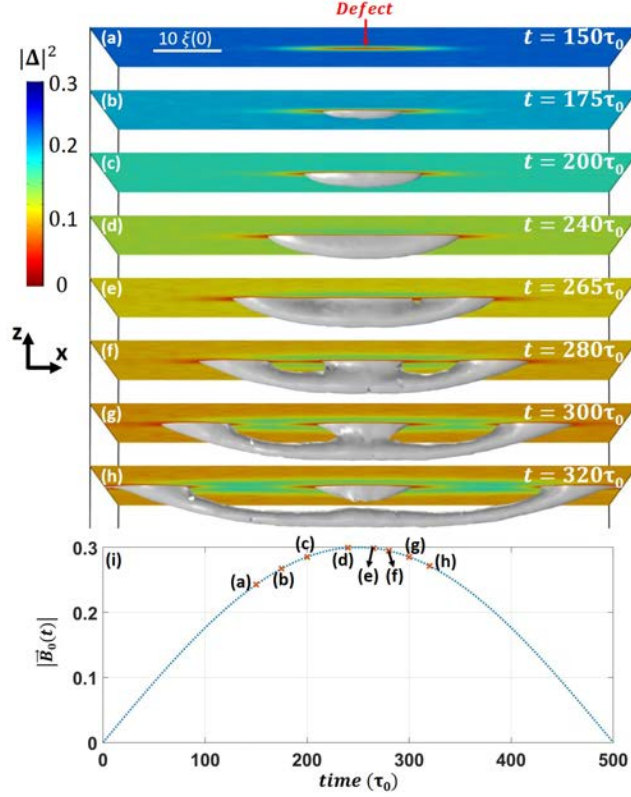


Fig. 9.1 (a)-(h) Plots of vortex semiloops illustrated with a silver surface (corresponding to  $|\Delta|^2 = 0.005$ ) at different times for parallel rf magnetic field in the  $\hat{x}$  direction above the superconductor. A localized defect is placed at the origin ( $\vec{r}_d = 0\hat{x} + 0\hat{y} + 0\hat{z}$ ) and defined using Eq. (8.2) with  $\sigma_x = 6$  and  $\sigma_y = \sigma_z = 1$  and  $T_{cd} = 0.1$ . The color shows the order parameter magnitude  $|\Delta|^2$  on the superconducting surface. (i)  $|\vec{B}_0|$  at the surface vs time during the first half of the rf cycle. Red crosses correspond to field values for snapshots (a)-(h). The simulation was performed for  $\kappa = 1$ ,  $\eta = 1$ ,  $B_0 = 0.3B_{c2}$  and  $2\pi/\omega = 1000\tau_j$ . Note that this is a transient solution rather than a steady state solution.

inside 2 rectangular blocks instead of the cylindrical domain used in Chapter 8. The block dimensions are  $L = 80\xi_0$  (along the field direction) and width  $W = 60\xi_0$ . The height of the superconducting domain is  $h_{sc} = 20\xi_0$ , and the height of the vacuum domain is  $h_{vac} = 10\xi_0$ . The vacuum domain is placed on top of the superconducting domain. To mimic the infinite domain periodic boundary conditions are applied in the  $\pm\hat{x}$  and  $\pm\hat{y}$  directions both for  $\Psi$  and  $\vec{A}$ .

Fig. 9.1 shows the solution for the order parameter in the case of externally applied rf magnetic field parallel to the surface of the superconductor along the  $\hat{x}$  axis direction. A localized defect (modeled with Eq. (8.2)) is placed on the surface at the origin ( $\vec{r}_d = 0\hat{x} + 0\hat{y} + 0\hat{z}$ ) with  $\sigma_x = 6$  and  $\sigma_y = \sigma_z = 1$  and  $T_{cd} = 0.1$ . The simulation was performed for  $\kappa = 1$ ,  $\eta = 1$ ,  $B_0 = 0.3B_{c2}$  and  $2\pi/\omega = 1000\tau_0$ .

A *transient* solution starting from the zero field Meissner state is studied in this case. A vortex semiloop penetrates into the superconducting domain at the site of the defect as the rf field amplitude increases [223]. We consider vortex semiloops as a unique type of vortex, distinctly different from parallel line vortices [132]. When the amplitude of magnetic field is increased beyond that used in Fig. 9.1, we observe that arrays of parallel line vortices nucleate into the superconductor. While no defect was required to create vortex semiloops with the magnetic dipole source, a surface defect is required to create such a vortex when parallel field is applied. The solution shown in Fig. 9.1 is an initial transient solution, i.e. the simulation is not run for several cycles to reach the steady state condition. When the vortex semiloop reaches the boundary of the simulation in the field direction the results become nonphysical due to artificial pinning of the vortex semiloop by the boundaries. This finite size effect is currently limiting our ability to perform full rf parallel field simulation. Nevertheless, the transient solution shown in Fig. 9.1 may give some insight into the development of vortex semiloops in SRF cavities [69], and will be pursued later in this chapter.

## 9.2 "Slow" TDGL

Until now I only utilized TDGL to study rf vortex dynamics. But Gor'kov had limited the use of TDGL to gapless superconductors, or to materials with magnetic impurities. However, for fully gapped superconductors like pure Nb, there are nominally no magnetic or other types of pair-breakers and the relevance of the original TDGL theory is called into question [36]. In this case, one must rely on inelastic phonon-electron interactions to achieve equilibrium of the quasiparticle distribution. In his book [36], Tinkham claims that the electron-phonon scattering time  $\tau_E$  is very slow compared to the time scales defined by TDGL, namely  $\tau_\Delta$  and  $\tau_j$ . In this limit one can treat  $\tau_\Delta$  and  $\tau_j$  as being so short that the order parameter and currents simply respond instantaneously to changes in externally applied fields. In this case one can simply use the static GL equations with an effective temperature  $T^*$ . The effective temperature arises due to the existence of non-equilibrium quasi-particles. This effective temperature is given via the following equation:

$$k_B(T^* - T) = \frac{\pi}{4} \tau_E \frac{\partial \Delta}{\partial t} \quad . \quad (9.1)$$

Using this effective temperature in the static GL equation (Eq. (7.14)) gives an alternative time-generalized version of GL, which I refer to as "Slow" TDGL (expressed in



normalized form):

$$\eta \left( \frac{2\tau_E \Delta}{\hbar} \right) \frac{\partial \Delta}{\partial t} = (\vec{\nabla} - i\vec{A})^2 \Delta + f_\alpha \Delta - f_\beta |\Delta|^2 \Delta \quad . \quad (9.2)$$

The main difference between TDGL Eq. (7.40) and "Slow" TDGL Eq. (9.2) is that in "Slow" TDGL the relaxation time for the order parameter is enhanced by a factor of

$$\tau_{\Delta}(Slow-TDGL)/\tau_{\Delta}(TDGL) = \frac{2\tau_E \Delta}{\hbar}$$

from the one given by TDGL. More importantly, the relaxation time for the order parameter depends on the magnitude of the order parameter  $|\Delta|$ , thus the relaxation rate is different inside the superconducting vortex or at the surface of the cavity. I will not be directly utilizing this slow-TDGL model in my simulations, because, as we will see in the next section, this "slow" version of TDGL is one limiting form of a substantially generalized TDGL model.

### 9.3 Generalized TDGL (gTDGL) equations

It is well known that a superconductor with a finite energy gap will have a singularity in the spectral function at the gap frequency. This singularity is the reason that Gor'kov and Eliashberg limited their treatment of TDGL to gapless superconductors. There are two important energy scales to be considered when deriving the TDGL

equations, one on the order of  $k_B T$  and another on the order of  $|\Delta|$ . In the original derivation of the TDGL equations, only gapless superconductors were considered, hence all physics and interactions happening at energy scales other than  $k_B T$  were neglected. In a superconductor with a finite gap, interactions on the order of  $|\Delta|$  can make significant contributions when terms involving energy integrals are considered together with the spectral function singularity mentioned before [224].

In order to extend the validity of the TDGL formalism to gapped superconductors, a generalized version of TDGL (gTDGL) was proposed [181, 225]. As Larkin and Ovchinnikov pointed out in Ref. [161], the energy relaxation time of electrons  $\tau_E$  in metals is much longer than the average scattering time  $\tau_s = l/v_F$ , hence even weak electric fields can lead to large changes in the electron energy distribution. The superconducting energy gap and the current density strongly depend on the shape of this distribution function. Watts-Tobin and Kramer were able to show that in a dirty limit superconductor, one can derive the phenomenological equations which account for both a finite superconducting energy gap and finite inelastic electron-phonon scattering time.

Superconductors in the dirty limit, with a finite inelastic electron-phonon scattering time  $\tau_E$  subject to  $\sqrt{D\tau_E} \ll \xi$  (or  $\tau_E \ll \tau_\Delta$ , for Nb this condition is met for  $T_c - T < 0.72K$ ) can be better studied using gTDGL [181]. gTDGL does not require strong limitations such as a large concentration of magnetic impurities and/or gapless superconductivity [158], but it does require  $T \approx T_c$  for Nb.

The gTDGL equations can be written as follows [158, 164, 181, 225]:

$$\begin{aligned}
\nu(0)\tau_{GL}(0)\frac{T_c}{T}\frac{1}{\sqrt{1+(\Gamma|\Delta|)^2}}\left(\frac{\partial}{\partial t}+\frac{1}{2}\Gamma^2\frac{\partial|\Delta|^2}{\partial t}+\frac{i}{\hbar}e_*\Phi\right)\Delta = \\
-\gamma\hbar^2\left(\vec{\nabla}-\frac{ie_*}{\hbar}\vec{A}\right)^2\Delta-\alpha_\Delta(\vec{r},T)\Delta-\beta_\Delta(\vec{r},T)|\Delta|^2\Delta, \tag{9.3}
\end{aligned}$$

where  $\Gamma = \frac{2\tau_E}{\hbar}$  is the inverse of an inelastic electron-phonon scattering energy scale. Also note the extra  $T_c/T$  term on the left when compared to Eq. (7.32). While this introduces a small correction to Eq. (7.32), it is insignificant as  $T \rightarrow T_c$ . The authors of this equation themselves conclude that the  $(\Gamma|\Delta|)^2$  term is not very significant, so the use of the original and simpler TDGL equations, but with a reduced  $\tau_{GL}$  value to simulate the effect of finite  $\Gamma$ , is justified [225]. A more detailed derivation of these equations can be found in Ref. [225]. For a proper historical background see Ref.[224].

For consistency  $\Gamma$  has to be non-dimensionalized as  $\tilde{\Gamma} = \frac{2\tau_E\Delta_\infty(0)}{\hbar}$  and the gTDGL equations should be written using the dimensionless quantities introduced in

Sec. 7.3.1 (and dropping " $\sim$ "):

$$\frac{\eta}{\sqrt{1+(\Gamma|\Delta|)^2}} \left( \frac{\partial}{\partial t} + \frac{\Gamma^2}{2} \frac{\partial |\Delta|^2}{\partial t} \right) \Delta = (\vec{\nabla} - i\vec{A})^2 \Delta + f_\alpha \Delta - f_\beta |\Delta|^2 \Delta, \quad (9.4)$$

where  $\eta \equiv \frac{\tau_\Delta}{\tau_j}$ . The gTDGL equation is a truly generalized equation, in the sense that both the TDGL and the "slow" TDGL equations can be recovered in appropriate limits. When  $\Gamma = 0$  (i.e. strong inelastic scattering) the singularity of the density of states at the gap edge is totally smeared out and the original TDGL equation Eq. (7.32) is recovered. On other hand when  $\Gamma \gg 1$  (i.e. slow quasiparticle energy relaxation) one recovers the "slow" TDGL equation Eq. (9.2):

$$\frac{\eta}{\sqrt{1+(\Gamma|\Delta|)^2}} \left( \frac{\partial}{\partial t} + \frac{\Gamma^2}{2} \frac{\partial |\Delta|^2}{\partial t} \right) \Delta = \begin{cases} \eta \frac{\partial \Delta}{\partial t} & \text{for } \tau_E \ll \hbar/|\Delta| \ (\Gamma \ll 1) \\ \eta \left( \frac{2\tau_E \Delta}{\hbar} \right) \frac{\partial \Delta}{\partial t} & \text{for } \tau_E \gg \hbar/|\Delta| \ (\Gamma \gg 1). \end{cases} \quad (9.5)$$

## 9.4 Relaxation times for amplitude and phase of $\Delta$

The normalized  $\Gamma$  parameter for SRF Nb can be computed by simply using the numbers from [Table 7.1](#):

$$\Gamma = \frac{2\tau_E}{\hbar/\Delta_\infty(0)} = \sqrt{\eta_0} \frac{\tau_E}{\tau_{GL}} = 30.78 \quad . \quad (9.6)$$

Note that it is difficult to experimentally measure  $\tau_E$ , as such  $\Gamma$  has generally been used as a fitting parameter in the literature [[164](#)]. In the end, all of these models are phenomenological models.

$\Gamma$  is associated with enhanced nonlinearity in the TDGL equations by increasing the relaxation time for the *amplitude* of the order parameter, while decreasing it for the *phase* of the order parameter. Writing the order parameter in terms of magnitude and phase,  $\Delta = |\Delta| e^{i\theta}$ , the time dependent term on the left hand side of [Eq. \(9.4\)](#) can be rewritten as follows:

$$\eta \sqrt{1 + (\Gamma |\Delta|)^2} \frac{\partial |\Delta|}{\partial t} e^{i\theta} + i \frac{\eta |\Delta| e^{i\theta}}{\sqrt{1 + (\Gamma |\Delta|)^2}} \frac{\partial \theta}{\partial t} \quad . \quad (9.7)$$

leading to two distinct relaxation times:  $\tau_{|\Delta|} = \eta \sqrt{1 + (\Gamma |\Delta|)^2}$  and  $\tau_\theta = \frac{\eta}{\sqrt{1 + (\Gamma |\Delta|)^2}}$  for the magnitude and phase of the order parameter, respectively. [Fig. 9.2](#) shows these two time scales as a function of  $|\Delta|$  for dimensionless  $\Gamma = 30.78$ . Note that when  $|\Delta| \rightarrow 0$  (for example inside the vortex core) one recovers the single TDGL relaxation

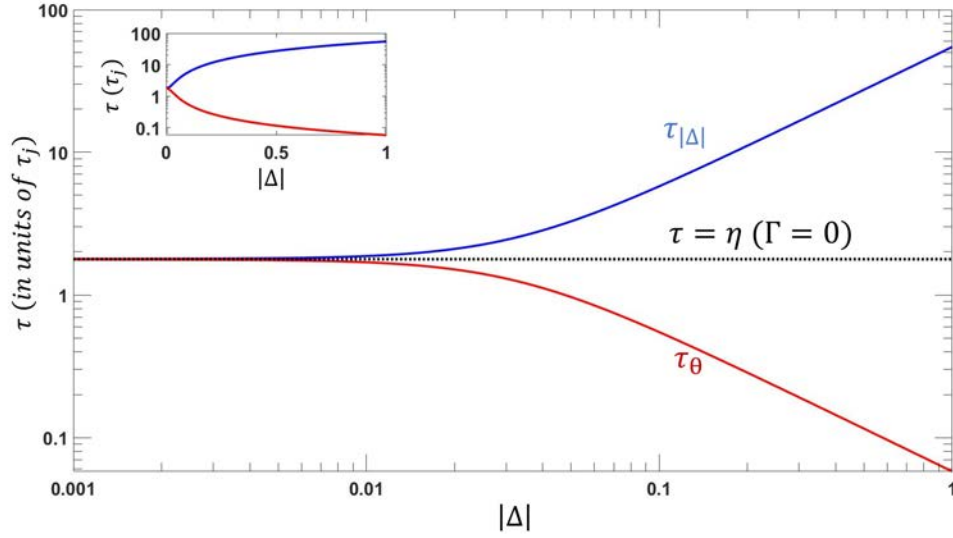


Fig. 9.2 Relaxation times  $\tau_{|\Delta|}$  (blue) and  $\tau_\theta$  (red) vs normalized gap  $|\Delta|$ , for the case of Nb in the dirty limit with  $\eta = 1.78$  and  $\Gamma = 30.78$ . Inset shows the same plot vs linear  $|\Delta|$ . This illustrates that the phase of the order parameter will relax more quickly than the amplitude whenever  $|\Delta|$  is large. Note that as  $|\Delta| \rightarrow 1$ ,  $\tau_{|\Delta|}/\tau_\theta \rightarrow 1 + \Gamma^2 \sim 10^3$ .

time, but as  $|\Delta| \rightarrow 1$ , the  $\Gamma |\Delta|$  term dominates the time dynamics of the full equation. As  $|\Delta| \rightarrow 1$ ,  $\tau_{|\Delta|}/\tau_\theta \rightarrow 1 + \Gamma^2 \sim 10^3$  which causes an issue for any numerical simulation efforts. It is computationally challenging to simulate the physics that happens in such vastly different timescales. For that reason in my simulations I simply assume

$\tau_\theta = 0$ . However, this does not mean that  $\frac{\partial \theta}{\partial t}$  is zero, it merely means that the relaxation of the phase happens so quickly that one can regard it as instantaneous, hence

$$\tau_\theta \frac{\partial \theta}{\partial t} = 0.$$

The vortices are expected to nucleate into the superconductor when the magnetic field exceeds  $H_{c1}$ . However in reality, superconductors can remain vortex-free up to a superheating field  $H_{sh} > H_{c1}$  due to the interaction of the vortices with the screening currents on the surface of the superconductor. This creates a surface barrier for

vortex nucleation, which is known as the Bean-Livingston surface barrier [226]. While  $H_{c1}$  is an intrinsic parameter of a material,  $H_{sh}$  strongly depends on the geometry of the surface, and is defined as the field at which the Bean-Livingston barrier vanishes. The superheating field of an SRF cavity is the key parameter that limits the cavity's peak accelerating gradient, as such many theoretical works are devoted to calculate  $H_{sh}$  [227–229].

Longer relaxation times  $\tau_{|\Delta|}$  would mean that a longer time is needed to nucleate a vortex since a vortex involves creation of a suppressed  $\Delta$  region. This would imply that one can temporarily apply magnetic field higher than  $H_{c1}$ , and even  $H_{sh}$  (both of which are conventionally measured with static magnetic field), and still retain a full Meissner state, introducing an extra **time** barrier on top of the Bean-Livingston surface barrier. This should increase the vortex-penetration field of a superconductor at rf frequencies. Unless the instantaneous magnetic field  $B_{rf}(t)$  exceeds the critical field for a sufficiently long time, the vortex simply can't nucleate.

Fig. 9.3 shows the relaxation times  $\tau_{|\Delta|}$ ,  $\tau_j$  and  $\tau_{GL}$  in Nb as a function of temperature, calculated for various values of inelastic phonon-electron scattering time  $\tau_E$  and mean free path  $l$ . The GL timescale  $\tau_{GL}$  does not depend on impurity concentration and its temperature dependence was derived by Gor'kov and Eliashberg to

be  $\tau_{GL}(T) = \frac{\pi\hbar}{8k_B(T_c - T)}$  (see Sec. 7.2). On other hand, the impurity concentration can change the characteristic time for the relaxation of magnetic vector potential  $\tau_j$  which depends on the value of the normal state conductance. Fig. 9.3 shows the temperature dependence of  $\tau_j(T) = \mu_0\lambda(T)^2\sigma_n$ , where  $\sigma_n = 2e^2\nu(0)v_F l/3$  is the normal

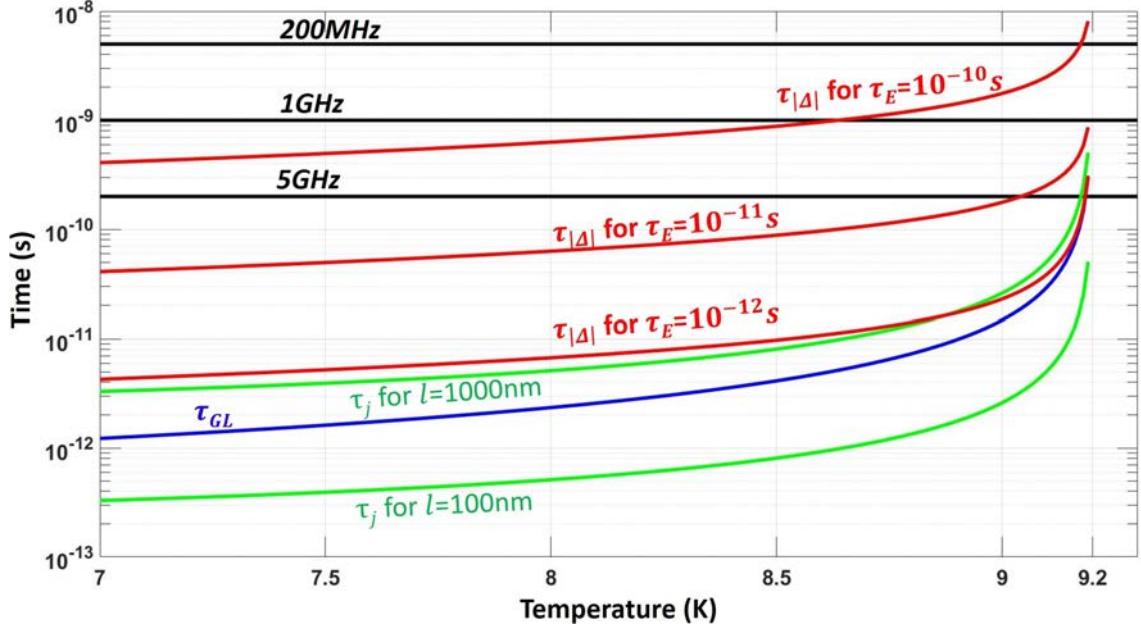


Fig. 9.3 Relaxation times  $\tau_{GL}$  (blue),  $\tau_{|\Delta|}$  (red) and  $\tau_j$  (green) vs temperature for Nb with  $T_c = 9.2$  K. Also shown are periods corresponding to rf excitations with 200 MHz, 1GHz and 5 GHz frequencies.

state conductivity. In Fig. 9.3  $\tau_j(T)$  is calculated for  $l = 100nm$  and  $l = 1000nm$ , which are the values of mean-free path appropriate for SRF Nb. The temperature dependence of the penetration depth  $\lambda(T)$  is defined through temperature kernels  $f_\alpha(T)$  and  $f_\beta(T)$  as  $\lambda(T) = \lambda(0)\sqrt{f_\beta(T)/f_\alpha(T)}$ , where I used  $\lambda(0) = 39nm$ . Here temperature kernels  $f_\alpha(T) = \frac{T_c^2 - T^2}{T_c^2 + T^2}$  and  $f_\beta(T) = \frac{T_c^4}{(T_c^2 + T^2)^2}$  are used since they provide good agreement with experimental data on SRF cavities down to  $T = 3K$  [230]. Finally,  $\tau_{|\Delta|}(T) = \tau_{GL}(T)\sqrt{1 + (2\tau_E\Delta(T)/\hbar)^2}$  contains both the temperature dependence of  $\tau_{GL}(T)$  and superconducting gap  $\Delta(T)$ , assuming that  $\tau_E$  is temperature independent. Fig. 9.3 shows the temperature dependence of  $\tau_{|\Delta|}(T)$  calculated for  $\tau_E = 10^{-12}s$ ,  $\tau_E = 10^{-11}s$  and  $\tau_E = 10^{-10}s$ . Here I use a high temperature approximation for the temperature dependence of the superconducting gap



$\Delta(T) = \frac{1.74}{2}\Delta(0)\sqrt{f_\alpha(T)/f_\beta(T)}$  with  $\Delta(0) = 1.55\text{meV}$ . The periods of rf excitations with  $f = 200\text{ MHz}$ ,  $f = 1\text{ GHz}$  and  $f = 5\text{ GHz}$  frequencies are also shown. It is evident from Fig. 9.3 that as  $T \rightarrow T_c$  the time scale  $\tau_{|\Delta|}$  approaches and even exceeds the period of rf excitation. Consequently, one needs to consider the time dynamics of vortex nucleation and cannot extrapolate the results of DC critical field measurements to high frequencies. On the other hand, at low temperatures the dc values of  $H_{sh}$  are likely appropriate.

One can calculate the following naive estimate for the frequency dependence of the rf critical field  $H_{c1}(\omega)$ . Consider an rf field in the form  $H(t) = H_{rf} \sin \omega t$ , where  $f = \omega/2\pi$  is the frequency and  $H_{rf} > H_{c1}(\omega = 0)$ . The time when the instantaneous field first exceeds the dc critical field  $H_{c1}(\omega = 0)$  is  $\omega t_1 = \sin^{-1}(H_{c1}(\omega = 0)/H_{rf})$ . The instantaneous field remains above  $H_{c1}(\omega = 0)$  until  $\omega t_2 = \pi - \omega t_1$ . In line with my previous discussion I postulate that in order for a vortex to nucleate the condition  $t_2 - t_1 \geq \tau_{|\Delta|}$  should be satisfied. This leads to an analytic equation for the frequency dependence of the critical field  $H_{c1}(\omega)$ :

$$H_{c1}(\omega) = \frac{H_{c1}(\omega = 0)}{\sin \left[ \frac{\pi}{2} - \frac{\omega \tau_{|\Delta|}}{2} \right]}, \quad (9.8)$$

which assumes  $\omega \tau_{|\Delta|} < \pi$ . Very large enhancement of the frequency-dependent  $H_{c1}$  are predicted. This dependence is plotted in Fig. 9.4. This estimate will lose validity as  $\omega \rightarrow 1/\tau_{|\Delta|}$ , since in the high-frequency regime the superconductor will start

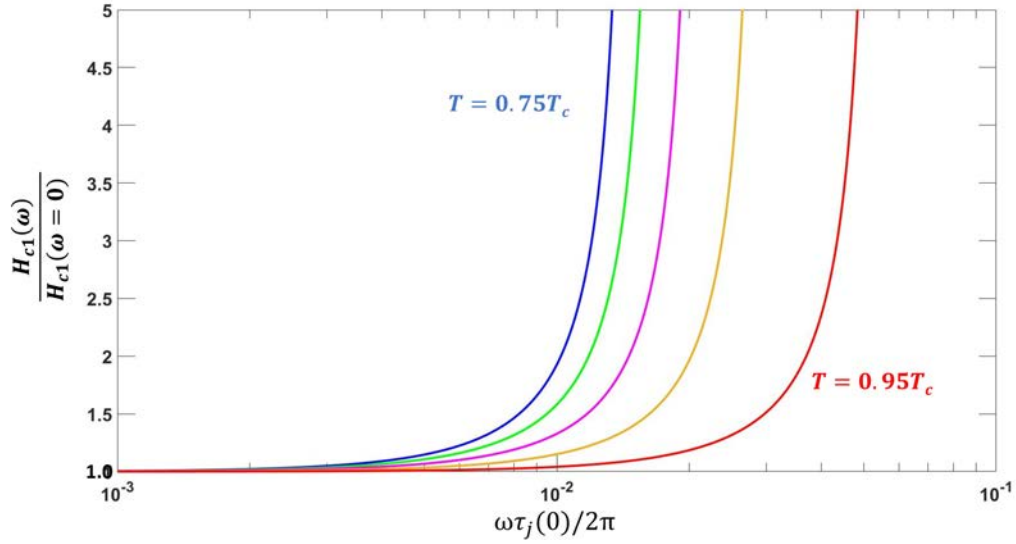


Fig. 9.4 The frequency dependence of the critical field  $H_{c1}(\omega)$  calculated using Eq. (9.8) for  $T/T_c = 0.75, 0.80, 0.85, 0.90$  and  $0.95$ . Here  $\tau_j(0)/\tau_{|\Delta|}(T) = 0.027, 0.031, 0.038, 0.053$  and  $0.097$  with  $\Delta(T)/\Delta(0) = \frac{1.74}{2} [1 - (T/T_c)^4]$ . This calculation is performed for  $\Gamma = 30.78$  and  $\eta = 1.78$ .

responding to the time-averaged value of magnetic field [36].

One should also note that I am ignoring the fact that the order parameter will be suppressed due the applied rf magnetic field even for  $H(t) < H_{c1}(\omega = 0)$ , which will reduce  $H_{c1}(\omega)$ . Overall, this exercise is not a numerical estimate for the enhancement of the  $H_{c1}(\omega)$  or a prediction of a new phenomenon, it is only intended as a mental exercise for the reader to highlight the difference between DC and RF behaviour and to underscore the importance of studying the response of superconductors in the appropriate regime. In the end, if the effect of the "time gap" was as massive as shown in Fig. 9.4, it would have been proven experimentally by now.

## 9.5 The dependence of Vortex Dynamics on Inelastic Scattering $\Gamma$

To study the effects of the inelastic electron-phonon scattering parameter  $\Gamma$ , a gTDGL simulation of the interior surface of the SRF cavity was created, similar to that shown in Fig. 9.1. The superconducting domain was simulated as a block with  $L = 120\xi(0)$ ,  $W = 30\xi(0)$  and  $h_{sc} = 15\xi(0)$ . The vacuum domain was simulated as a separate block with  $h_{vac} = 5\xi(0)$  placed on top of the superconducting domain. A single defect is located on the surface and a parallel rf magnetic field is applied. Here we study the properties of the rf vortex semiloops as a function of inelastic scattering in the Nb. The simulation was performed at  $T = 0.7T_c$ ,  $B_0 = 0.35B_{c2}$ ,  $2\pi/\omega = 5000\tau_0$ ,  $\kappa = 1.5$  and  $\eta = 1$ . The simulation is run for 3 rf cycles to reach the steady state solution. Fig. 9.5 shows a snapshot of this simulation at  $t = 4200\tau_0$  which corresponds to the time when the vortex semiloop penetrates deepest into the superconductor within the rf cycle for all values of  $\Gamma$  used in this simulation. Vortex semiloops are illustrated with a silver surface (corresponding to  $|\Delta|^2 = 0.075$ ). As evident from this figure, the depth to which vortex semiloops penetrate into the superconductor depends on the value of the  $\Gamma$  parameter, with larger  $\Gamma$  corresponding to vortex semiloops remaining closer to the surface.

One of the dissipation mechanisms in superconductors is the dissipation due to moving vortices. As such, materials with larger  $\Gamma$  parameter values would result in less dissipation due to the smaller distance travelled by the vortex semiloop in an RF cycle.

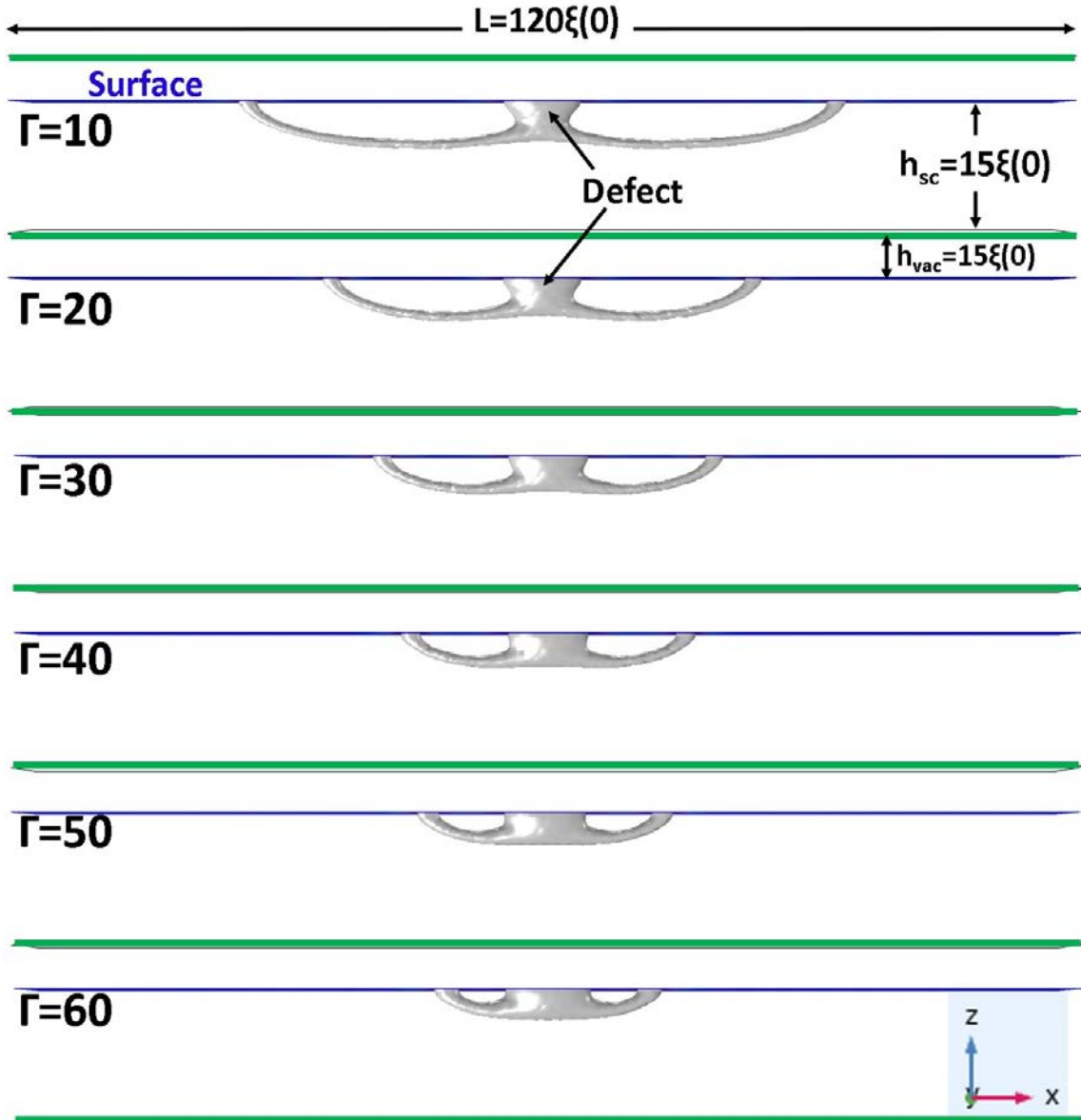


Fig. 9.5 Snapshots at  $t = 4200\tau_0$  of vortex semiloops illustrated with a silver surface (corresponding to  $|\Delta|^2 = 0.075$ ) simulated with different values of  $\Gamma = \frac{2\tau_E\Delta_\infty(0)}{\hbar}$  for parallel rf magnetic field in the  $\hat{x}$  direction above the superconductor. The blue line represents the free superconducting surface. The green line represents the boundaries of each simulation. A localized defect is placed on the surface at the origin ( $\vec{r}_d = 0\hat{x} + 0\hat{y} + 0\hat{z}$ ) and defined using Eq. (8.2) with  $\sigma_x = 4$  and  $\sigma_y = \sigma_z = 2$  and  $T_{cd} = 0.2$ . The simulation was performed for  $\kappa = 1.5$ ,  $\eta = 1$ ,  $B_0 = 0.35B_{c2}$ ,  $T = 0.7T_c$  and  $2\pi/\omega = 5000\tau_0$ .

Recently, an investigation of nitrogen doped Nb by scanning tunneling spectroscopy was performed by Lechner *et al.* [178]. The authors found that there is an 8% probability to find a spot with large Dynes fitting parameter value  $\Gamma_{Dynes} > 1.75\Delta(0)$  on the surface of a baseline Nb sample, whereas the largest value of the Dynes fitting parameter measured on the surface of a nitrogen doped Nb is  $\Gamma_{Dynes} = 0.5\Delta(0)$ . Large Dynes parameter values are associated with the smearing of the superconducting gap. And as I discussed in [Chapter 7](#), it is more appropriate to treat superconductors with a smeared gap, or gapless superconductors, with the standard TDGL model, which corresponds to using gTDGL with  $\Gamma = 0$ . By the transitive property, we can say that a larger Dynes fitting parameter value corresponds to a small value of  $\Gamma$ . Vortices can nucleate much faster at locations with smaller  $\Gamma$  values, hence the elimination of such locations could at least partially explain the recent success of nitrogen doped and nitrogen infused SRF cavities, which show higher  $Q$ -factors and higher accelerating gradients  $E_{acc}$  when compared to baseline Nb SRF cavities. [231].

Clearly, the  $\Gamma$  parameter has a strong effect on the nucleation of vortex semiloops. One can simultaneously increase both the  $Q$ -factor and the peak accelerating gradient of the cavity ( $E_{acc}$ ) by increasing the value of the  $\Gamma$  parameter on the surface, and eliminating the locations with suppressed values of  $\Gamma$ . Researchers in the SRF community are already considering several alternative superconductors that can be coated on the inner surface of the Nb cavity to increase the vortex nucleation field. The values of  $T_c$  and  $H_{c1}$  are usually given as the main consideration when these materials are chosen. My preliminary results presented in this chapter show that the value of the  $\Gamma$  parameter in these new materials should receive a similar consideration.

# 10

## Surface Imaging Efforts

The next step for our Near-Field Magnetic Microscope is demonstrating the ability to raster scan over the samples and to create images of nonlinear response. As was discussed in [Chapter 4](#), the surface defects and inhomogeneities on the surface of the superconductors will locally suppress  $J_{NL}$  and thus should generate stronger harmonic response (see [Eq. \(4.2\)](#)). Thus 2-dimensional maps of surface third-harmonic response should clearly show the location of these surface defects (see [Fig. 10.1](#) for the principle of the imaging method). In this chapter I will summarize the preliminary

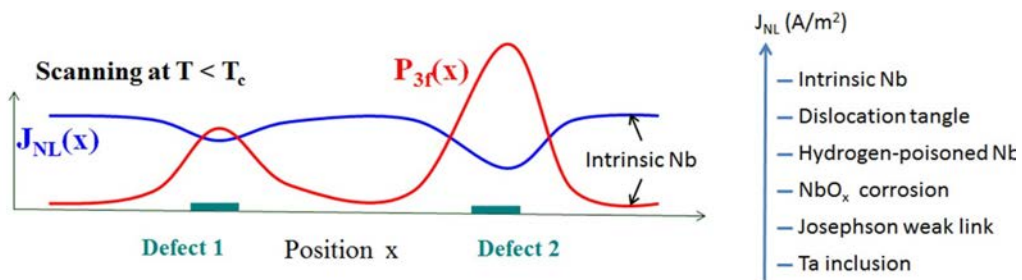


Fig. 10.1 Schematic illustration of the variation in nonlinear scaling current density  $J_{NL}$  (blue) and third-harmonic response  $P_{3f}$  (red) due to the local surface defects. The schematic hierarchy of  $J_{NL}$  attributed to some well-known defects is shown on the right side arrow. This figure is partially reproduced from [104].

scanning results and the experience gained so far.

## 10.1 2D scans of the $Bi_2Sr_2CaCu_2O_{8+x}$ sample

The first attempt to produce 2-dimensional maps of third-harmonic response was made inside the Desert Cryogenics wafer-probe station used by my predecessors. This setup was equipped with 3 stepper motors, one on each Cartesian axis, that can be used to scan the magnetic writer probe over the surface of the sample with  $0.5\mu m$  steps. For the detailed description of this setup please see [104, p.35 and p.145]).

A Bismuth strontium calcium copper oxide ( $Bi_2Sr_2CaCu_2O_{8+x}$ ) (a.k.a BSCCO and pronounced "bisko") sample was provided by the Kenneth Burch's group at Boston College. The sample was prepared using a mechanical exfoliation technique. Fig. 10.2 shows an optical image of the sample. It had a superconducting transition temperature  $T_c = 102$  K, obtained from the onset of third-harmonic response  $P_{3f}(T)$  that was measured during the cool down.

Fig. 10.3 shows the spatially-resolved images of the nonlinear response of the BSCCO flake sample at  $T = 89.5$  K,  $f = 4.975$  GHz and  $P_f = -6$  dBm input power. The measurement was performed across the edge of the sample shown in Fig. 10.2. I was able to measure a 10 dB difference in nonlinearity response while scanning perpendicular to and across the edge of the sample.

With this image we successfully demonstrate our ability to map-out the third-harmonic response. The measured third-harmonic response is consistent across a large

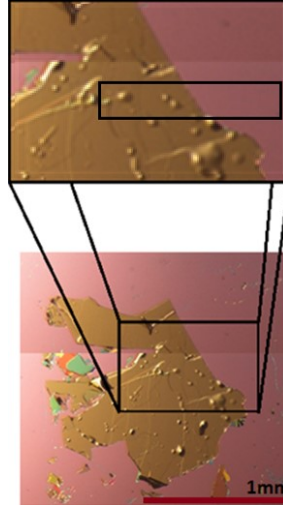


Fig. 10.2 Optical microscope image of the measured BSCCO flake sample. The scanned area is shown by a black box in the inset, and the third-harmonic power image is shown in Fig. 10.3.

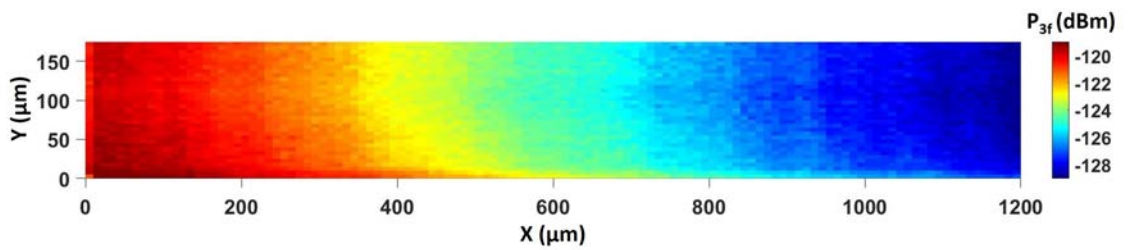


Fig. 10.3 Scanned Image of BSCCO sample at  $T = 89K$  at applied power  $P_f = -6dBm$  and frequency  $f = 4.975$  GHz. Colorbar shows the third-harmonic response  $P_{3f}$  in dBm. The scanned area is shown as a black box in Fig. 10.2.

surface area ( $1200\mu m \times 200\mu m$ ) and shows large contrast (10dB or 10 times) between the sample and the substrate.



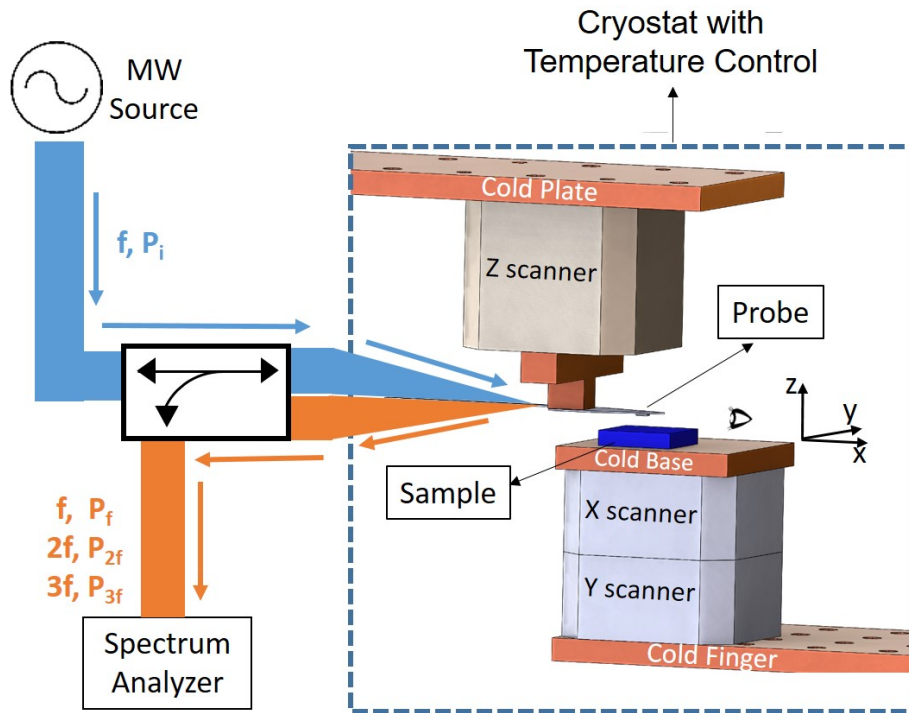


Fig. 10.4 Schematic of the experimental setup for raster scanning and imaging of nonlinear response. The probe is attached to an Attocube z-axis cryogenic piezo scanner, directly above the superconducting sample which rests on top of a Cold Base attached to an Attocube xy cryogenic scanner. The coldbase is thermally anchored to the cold plate of the cryostat. The eye icon indicates the point from which images shown in Fig. 10.9 are captured. As described in Chapter 4, a microwave (MW) source is used to generate an rf signal and feed it to the magnetic writer probe. The sample response magnetic field is coupled back to the probe and measured with a spectrum analyzer.

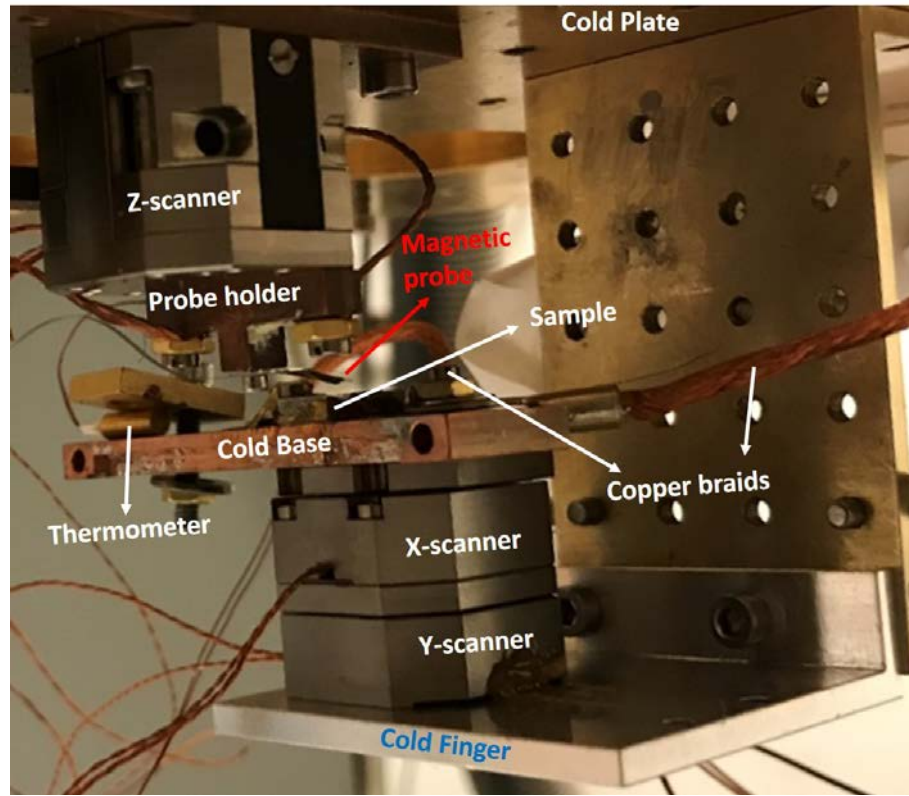


Fig. 10.5 A picture of the experimental setup for raster scanning and imaging of nonlinear response. The probe is attached to an Attocube z-axis cryogenic piezo scanner, directly above the superconducting sample, which rests on top of a Cold Base attached to an Attocube xy cryogenic scanner. The coldbase is thermally anchored to the cold plate of the cryostat by means of copper braids. To strengthen the thermal link vacuum grease (Apiezon N Grease) is applied between the sample and the Cold Base, and also between the Y-scanner and the Cold Finger.

## 10.2 Attocube positioning system

A low temperature positioning system was purchased from Attocube. The system consists of 3 individual piezo material-based linear nanopositioners ( $2 \times \text{ANPx101/RES/LT}$  and  $1 \times \text{ANPz101/RES/LT}$ ) controlled by a  $\text{ANC350/3/RES}$  Piezo Motion Controller. Each positioner has a built-in resistive encoder which can be used to read-out the current position of the positioner with  $200\text{nm}$  accuracy. Each positioner has a  $5000\mu\text{m}$  travel range. The stick-slip mechanism is used for the motion. This positioning system was later integrated into the Entropy Dry Pulsed Tube cryostat.

[Figs. 10.4](#) and [10.5](#) show the schematic diagram and a photograph of the microscope. The ANPz101 nanopositioner was used as a stand alone scanner for the Z-axis direction. The magnetic writer head is attached to the z-axis scanner using a custom built OFHC copper holder. The ANPx101 nanopositioners were mounted on top of each other to create an XY scanner. A base plate which is thermally anchored to the cold plate of the cryostat is mounted on the free surface of the XY scanner. The sample rests on top of this base plate. The sample is moved in the X and Y directions by the XY axis scanner. The probe-sample separation is controlled by the Z-axis scanner. The rf measurement procedure is the same as that described in [Chapter 4](#), along with the terminology for the magnetic writer probe pieces.

## 10.3 Probe Z-scan over Sample

Our attempts to create a Tuning Fork based probe-sample separation control were not successful (see [Appendix B](#)). Hence we decided that the probe should be pushed against the surface and dragged across the surface of the sample to create 2D-surface images. To interpret the resulting 2D-surface image of third-harmonic response, one should be able to decouple the features caused by the topography of the sample and the features created by other parameters at the surface which are relevant to SRF applications. Additionally one needs to identify the optimal Z-position at which the 2D-surface images have the highest quality. Hence, one needs to study the probe-sample interaction as a function of Z-position.

First the magnetic writer probe-sample interaction was studied at room temperature. [Fig. 10.6](#) shows magnified optical images of the magnetic writer probe approaching the flat sample. We see that as the probe approaches the sample it starts to bend after touching the sample. At this point the writer pole of the magnetic writer probe (see [Figs. 4.5](#) and [4.6](#)) is still far away from the sample. As the Z-scanner pushes the probe closer to the sample it reaches the point when the probe lays flat on the sample ([Fig. 10.6\(e\)](#)). Usually this is the best position to perform fixed-point measurements discussed in [Chapters 4](#) and [5](#). Also this is the configuration in which all 2-dimensional scans are performed. If the probe is pushed further it causes a deformation in the support frame and the writer pole detaches from the sample (see [Fig. 10.6\(f\)](#)). Thus there is a narrow window of Z-positions (on the order of  $500\mu m$ ) where the probe-sample

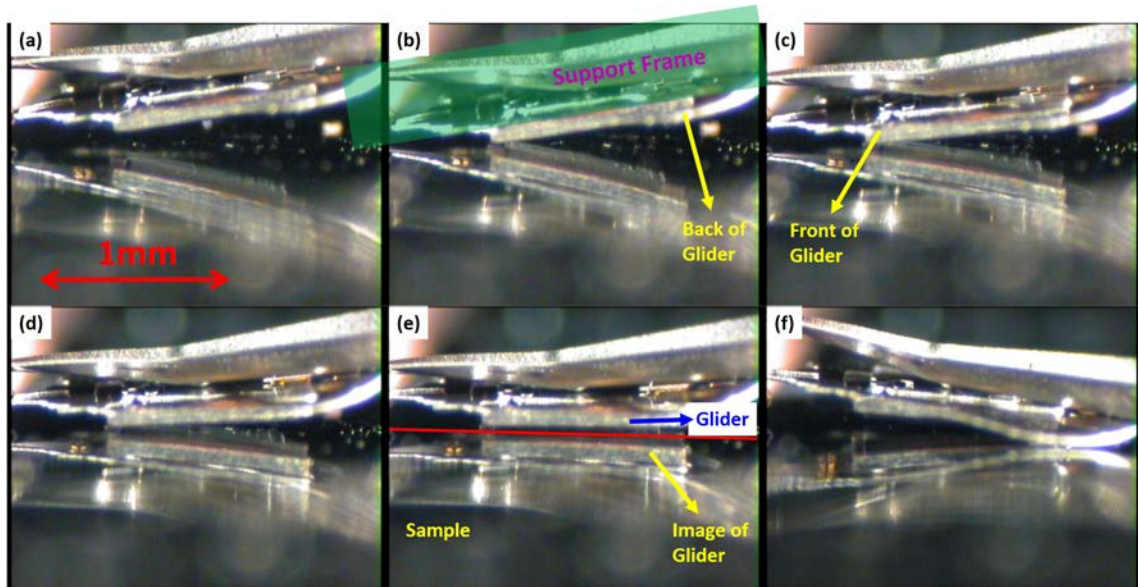


Fig. 10.6 Optical images of the probe as it approaches the sample: (a) when probe is away from the sample; (b),(c),(d) when probe is barely touching the sample; (e) when probe is laying flat on the sample; and (f) when the Z-scanner is pushed too far and the front of the probe where the writer pole is located moves away from the sample. Reflection of the probe from the sample can be used to infer the probe-sample separation. The surface of the sample is shown by the red line in (e).

interaction is optimal.

The bulk Nb sample which was described in [Chapter 5](#) as Sample 2, was imaged in this way. [Figs. 10.7](#) and [10.8](#) show the low temperature third-harmonic response  $P_{3f}$  vs the position of the Z-axis scanner as measured from the built-in resistive encoder. Both Z-scans were measured at the same x-y location but at different frequencies. Note that larger Z-position values correspond to the Z-scanner moving forward and the probe approaching the sample at room temperature for the same run. [Fig. 10.9](#) shows optical images of the probe approaching this sample. We see that when  $Z < 2000\mu\text{m}$  the probe is away from the sample ([Fig. 10.9\(a\)](#)). In this case the  $P_{3f}$  is nearly constant both as a function of temperature and position. A small apparent temperature depen-

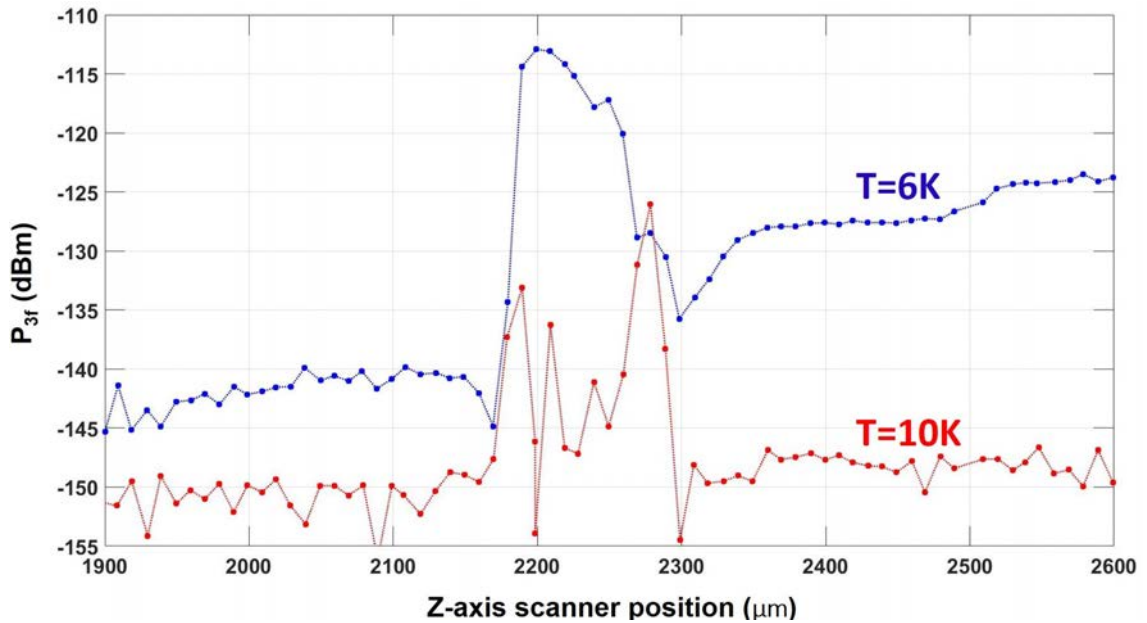


Fig. 10.7 Third-harmonic response  $P_{3f}$  vs the position of the Z-axis scanner measured in the superconducting state (blue curve measured at  $T = 6\text{K}$ ) and the normal state (red curve measured at  $T = 10\text{K}$ ). Below  $Z < 2000\mu\text{m}$  the probe is far away from the sample and the measured third-harmonic response can be attributed to the probe itself. For  $2000\mu\text{m} < Z < 2300\mu\text{m}$  the probe starts deforming and we have noisy spikes in  $P_{3f}(Z)$  both in the superconducting and normal states. Above  $Z > 2300\mu\text{m}$  the probe lays flat against the sample and we measure consistent and temperature dependent third-harmonic response. The data is measured on a Bulk Nb (Sample 2 in Chapter 5) at frequency of  $f = 1.49\text{GHz}$  and  $P_f = -5\text{dBm}$  input power.

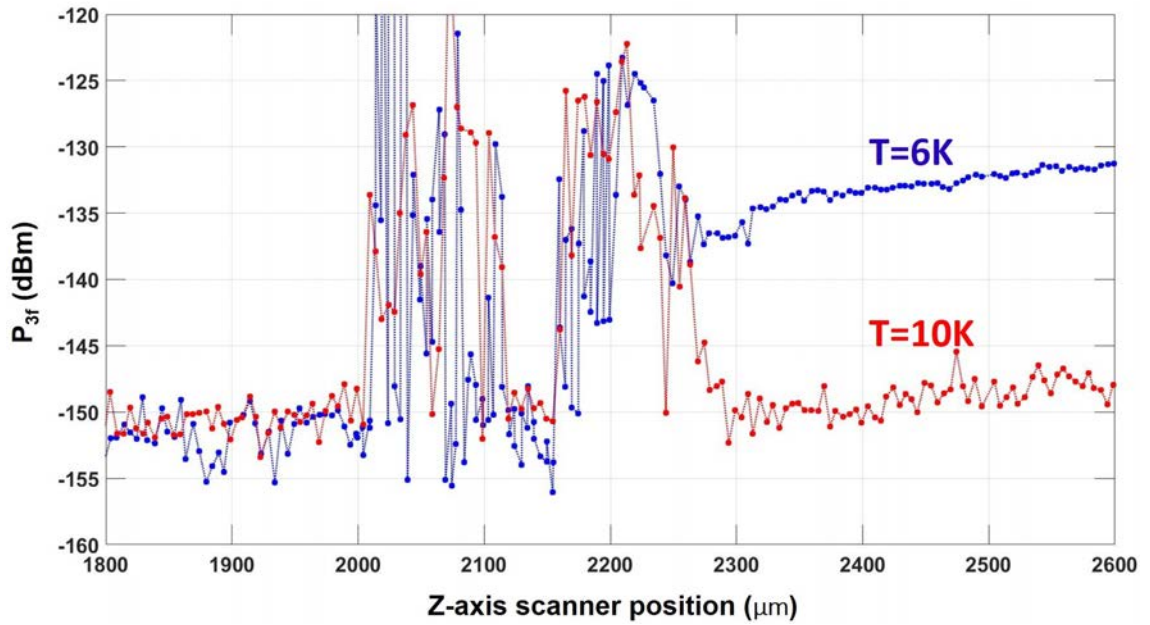


Fig. 10.8 Third-harmonic response  $P_{3f}$  vs the position of the Z-axis scanner measured in the superconducting state (blue curve measured at  $T = 6K$ ) and the normal state (red curve measured at  $T = 10K$ ). Below  $Z < 2000\mu\text{m}$  the probe is far away from the sample and the measured third-harmonic response can be attributed to the probe itself. For  $2000\mu\text{m} < Z < 2300\mu\text{m}$  the probe starts deforming and we have noisy spikes in  $P_{3f}(Z)$  both in the superconducting and normal states. Above  $Z > 2300\mu\text{m}$  the probe lays flat against the sample and we measure consistent and temperature dependent third-harmonic response. The data is measured on a Bulk Nb (Sample 2 in Chapter 5) at frequency of  $f = 1.8\text{GHz}$  and  $P_f = -5\text{dBm}$  input power.





Fig. 10.9 Optical images of the probe as it approaches the sample at room temperature: (a) when  $Z = 1900\mu m$  and probe is away from the sample. (b) when  $Z = 2200\mu m$  and the probe is barely touching the sample. (c) when  $Z = 2600\mu m$  and the probe is laying flat on the sample. In these pictures one is looking from the location denoted with an eye icon in Fig. 10.4.

dence for  $Z < 2150\mu m$  in Fig. 10.7 is insignificant since it corresponds to  $< 1\%$  of the nonlinear response power measured for  $Z > 2500\mu m$  at  $T = 6K$ . Once  $Z > 2000\mu m$  is reached, the probe starts barely touching the sample (Fig. 10.9(b)). In this regime the probe is being affected by the vibration in the cryostat (due to the active pulsed tube and vacuum pump). It is also being continuously deformed as the z positioner moves forward. The sample is entering and exiting the probe's field of view in an uncontrolled fashion. This results in noisy peaks and dips in  $P_{3f}(Z)$  both in the superconducting state ( $T = 6K$ ) and the normal state ( $T = 10K$ ) as shown in Figs. 10.7 and 10.8. Once the Z position is increased further to  $Z > 2300\mu m$ , the probe is now in good contact with the sample (Fig. 10.9(c)) and reproducible  $P_{3f}(Z)$  data can be measured. The  $P_{3f}(T)$  measured from this sample in this regime was shown in Fig. 5.6, where the third-harmonic response emerges sharply below  $T < 9.2K$  confirming the fact that the measured response is generated by the superconducting sample.



## 10.4 XZ-scan

The Z-scan described in the previous section is then repeated at an array of X-positions to produce a 2-dimensional (XZ) scan of the sample third-harmonic response. Fig. 10.10 shows the 2-dimensional (XZ) scan of the bulk Nb sample. The third-harmonic response  $P_{3f}$  is measured at frequency  $f = 1.49GHz$ , temperature of  $T = 6K$  and  $P_f = -5dBm$  input power. The measurement is performed in the following fashion: first the Z position is changed from  $Z = 3000\mu m$  to  $Z = 1500\mu m$  in  $20\mu m$  steps. Once  $Z = 1500\mu m$  is reached, where the probe is away from the sample, the X position is increased by  $10\mu m$  and the probe is returned to  $Z = 3000\mu m$ . This process ensures that the probe is not damaged by sliding it in the X-direction while it is being pushed hard against the sample. The sample (shown in the inset of Fig. 10.10) had a tilt which can be seen in the scanned image as well. The nonlinear response is localized to  $1600\mu m < X < 4000\mu m$  from which we can deduce that those are the locations of the sample edges. There is a sharp contrast change in  $P_{3f}$  at  $X = 2510\mu m$  which we don't yet understand. The image was later digitally rotated  $13^\circ$  in the counterclockwise direction. Later, the part of the data that is shown as bounded by 2 white lines in Fig. 10.10 was averaged and plotted in Fig. 10.11. While the data in Fig. 10.11 is presented in a logarithmic scale and in dBm units, the actual averaging was done in the linear power scale. From Fig. 10.11 we can estimate the width of the sample at the location of the scan to be  $2.94mm$ , assuming that the drop in  $\langle P_{3f} \rangle(X)$  at  $X = 0$  and  $X = 2940\mu m$  corresponds to the edges of the sample.

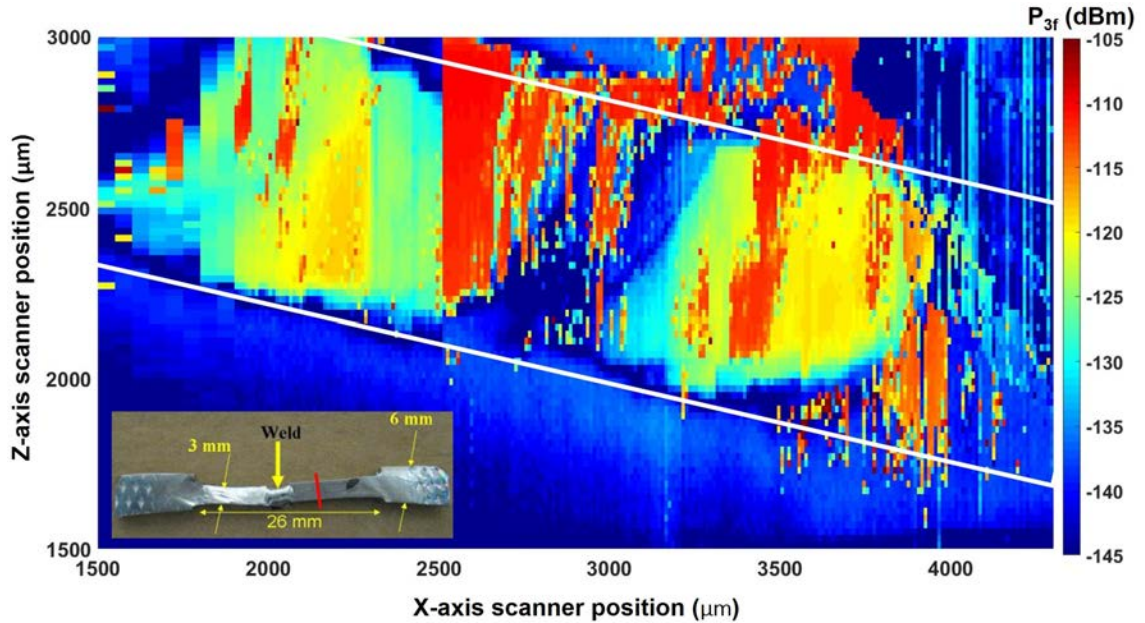


Fig. 10.10 2-dimensional (XZ) scan of the bulk Nb sample (Sample 2 in Chapter 5). The third-harmonic response  $P_{3f}$  is measured at a frequency of  $f = 1.49\text{GHz}$ , temperature of  $T = 6\text{K}$  and  $P_f = -5\text{dBm}$  input power. The image was taken by scanning in Z and rastering in X. The data in the area bounded by two white line was averaged and is plotted in Fig. 10.11. The inset show the picture of the sample where the location of the scan is shown with a red line.

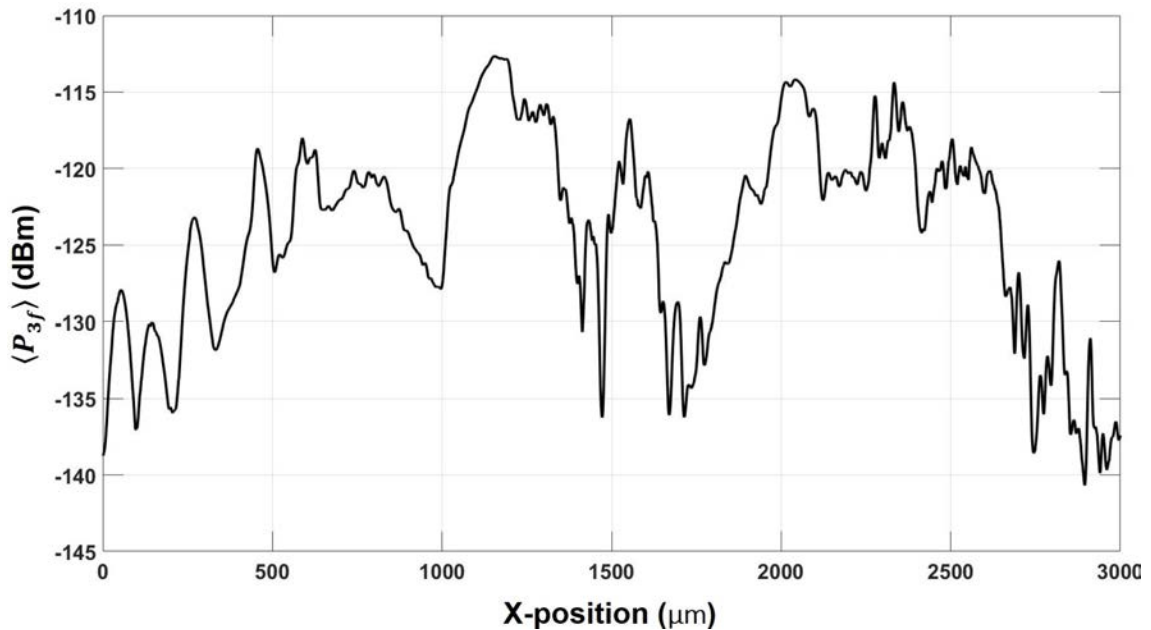


Fig. 10.11 Third harmonic response averaged over the area bounded by the white lines in Fig. 10.10. The data is presented in a logarithmic scale in dBm units but the averaging is performed in the linear scale.

Since we now know the boundaries of the sample, the surface tilt was re-imaged at higher input power. Fig. 10.12 shows the third-harmonic response  $P_{3f}$  that was measured over the same line shown in the inset of Fig. 10.10 at  $P_f = 0\text{dBm}$  input power. However now the measurement order was reversed: first the X position is changed from  $X = 3000\mu\text{m}$  to  $X = 1500\mu\text{m}$  in  $50\mu\text{m}$  steps. Once  $X = 1500\mu\text{m}$  is reached the Z position is increased by  $50\mu\text{m}$  and the probe is returned to  $X = 3000\mu\text{m}$ . Here we recover the same tilt shown in Fig. 10.10. An interesting feature of both measurements is the fact that the nonlinear response reaches its lowest value at or near the surface of the sample. A good explanation for this would be the destructive interference between the sample nonlinear response and that generated by the probe itself, as seen by my predecessors with the magnetic writer microwave microscope (It is discussed in section III.c of Ref. [128]).

## 10.5 Line Scans over a grain boundary in Bulk Nb

A bi-crystal bulk Nb tensile sample was provided by Tom Bieler's group at Michigan State University. The sample has a prominent grain boundary (GB) with  $53^\circ$  misorientation angle between the grains. A picture of this sample and an SEM image of the grain boundary are shown in Fig. 10.13. Further details about the sample (GB6-10) preparation can be found in Ref.[232].

Fig. 10.14 shows the line scan of third-harmonic voltage across the GB. The data was acquired by scanning in the X-direction at a constant  $Z = 1588\mu\text{m}$  value. This

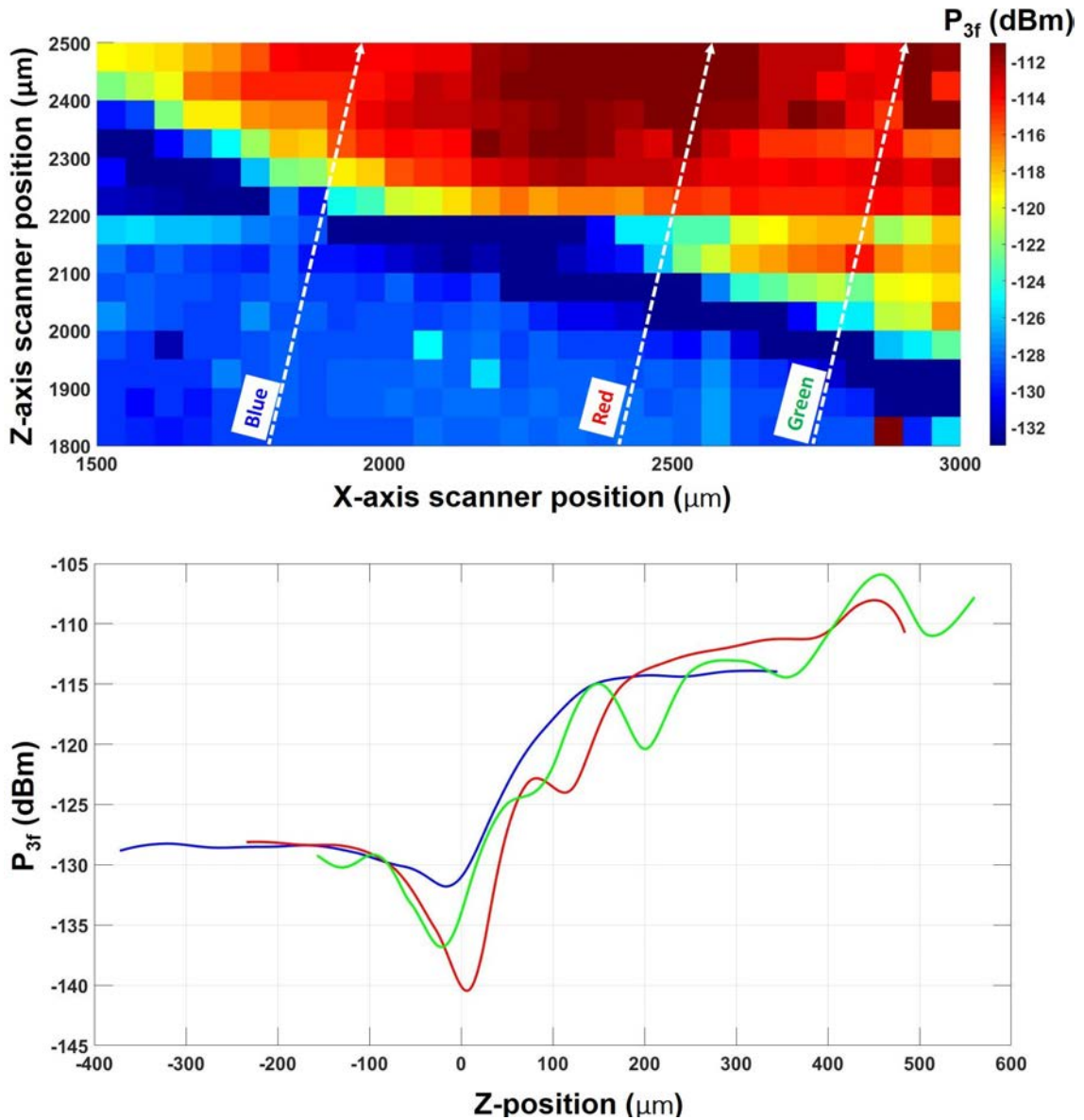


Fig. 10.12 Top: 2-dimensional (XZ) scan of the bulk Nb sample. The third-harmonic response  $P_{3f}$  is measured at frequency of  $f = 1.49\text{GHz}$ , temperature  $T = 6\text{K}$  and  $P_f = 0\text{dBm}$  input power. In this case the X value is scanned while the Z value is rastered. Bottom: Line scans along the lines shown in the top panel. The new Z-direction is  $13^\circ$  tilted compared to the top panel. Dips in  $P_{3f}(Z)$  around  $Z=0$  are the result of the destructive interference between the sample nonlinear response and that generated by the probe itself.

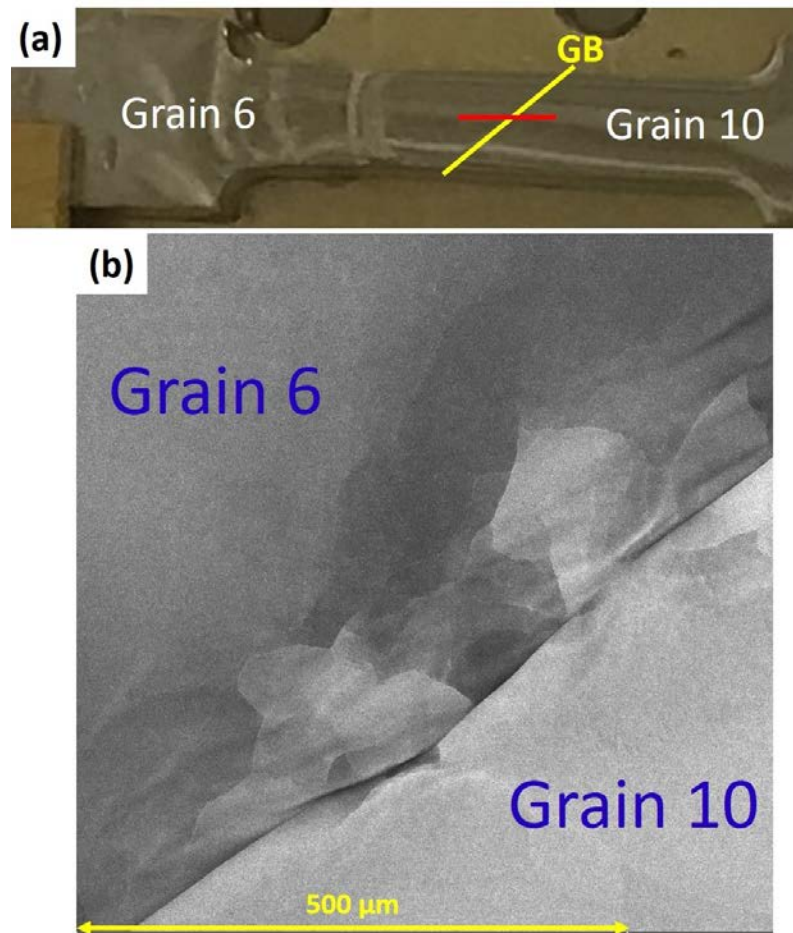


Fig. 10.13 (a) Picture of the bi-crystal bulk Nb tensile sample. Yellow line shows the location of the grain boundary and the red line shows an approximate location where the line scan shown in Fig. 10.14 was measured. (b) SEM image of the grain boundary.

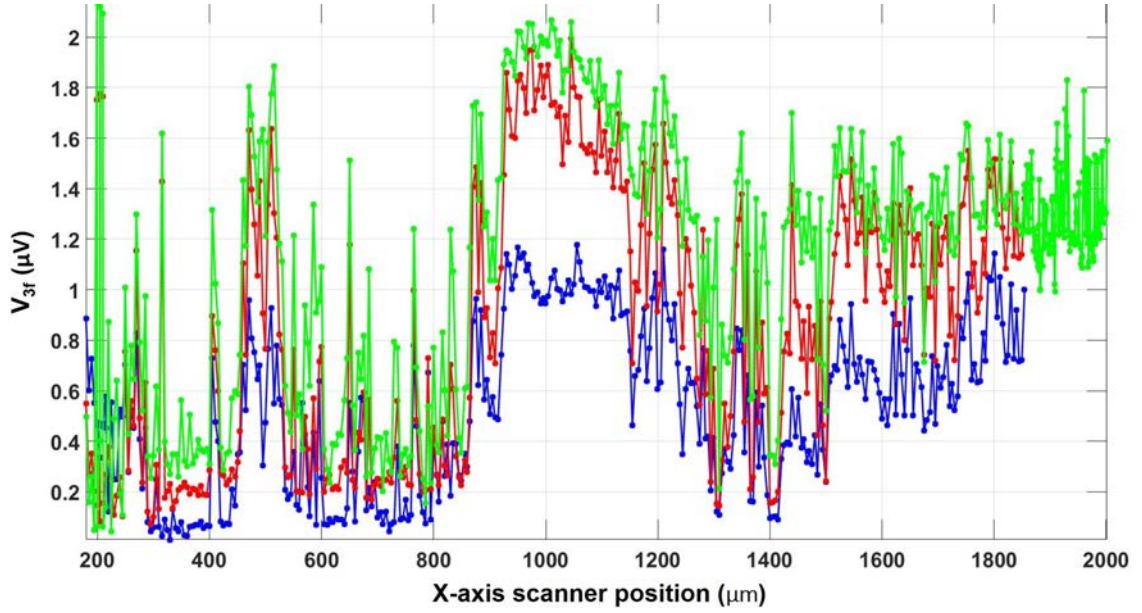


Fig. 10.14 Third-harmonic response  $V_{3f}$  vs the position of the X-axis scanner measured at frequency of  $f = 5.845\text{GHz}$  and temperature  $T = 4.5\text{K}$ . The measurement is performed simultaneously at 3 different input rf amplitudes:  $H_{rf} = 200\text{a.u.}$  (blue),  $H_{rf} = 400\text{a.u.}$  (red) and  $H_{rf} = 600\text{a.u.}$  (green).

value of  $Z$  corresponds to the probe laying flat against the sample as was inferred from the  $P_{3f}(Z)$  measurement. The third-harmonic voltage  $V_{3f}(X)$  measured at three different input rf amplitudes  $H_{rf}$  shows a peak around  $X = 1100\mu\text{m}$  which roughly corresponds to the location of the GB. The peak in  $V_{3f}$  is localized to about  $400\mu\text{m}$ , whereas the lateral extent of the GB itself is about  $10\mu\text{m}$ . This might indicate that other defects associated with the GB extend out to greater distances, suppressing the nonlinearity current density scale, and enhancing  $V_{3f}$ .



## 10.6 Conclusion

In conclusion, I provide several proof of principle level results on surface imaging of non-linear response with the magnetic writer probe. I found that there is an optimal range of Z-positioner values which can be used to perform 2-dimensional scans. Additionally I measured the third harmonic response from a GB and observed a peak in  $V_{3f}$  as we have expected. We also identified several limitations of the imaging capabilities of the microscope. Most importantly the samples should be flat with minimal surface roughness and tilt, as we have only rudimentary probe-sample distance control.

The setup can be improved by implementing 2 key changes. Firstly the scanners which I am using right now are in fact positioners and are not designed for nm precision measurements. An actual XYZ scanner system, such as those used in cryogenic STM/AFM, can significantly improve the resolution and performance of our microscope. Also, perhaps an alternative sample-probe separation control method should be designed. One can either measure capacitance between the probe and the sample, or attach mirrors to the probe and use an optical interferometer to measure the precise location of the probe. Finally, several samples with known defect structures should be measured to characterize our system.

# 11

---

## Microwave Surface Impedance measurements using the Parallel Plate Resonator

---

Measuring the London penetration depth and surface resistance of a superconductor is very important when one considers using said superconductors in high-frequency applications. The measured temperature dependence of the penetration depth and surface resistance can be used to extract several key parameters like the zero temperature penetration depth  $\lambda(T = 0)$ , superconducting order parameter  $\Delta(T)$ , critical temperature  $T_c$ , quasi-particle scattering time  $\tau$ , and the pairing symmetry of the material. In superconductors, the pairing symmetry refers to the symmetry of the bounded Cooper pair wave function. Conventional phonon-mediated pairing superconductors like Nb, have an s-wave symmetry, whereas most Rare-earth Barium Copper Oxide (ReBCO) high temperature superconductors (a.k.a. cuprates) generally have a d-wave symmetry. The pairing symmetry of the superconductor also defines the temperature dependence of its surface resistance. The low-temperature surface resistance of an s-wave superconductor (neglecting the residual resistance discussed



in [Chapter 2](#)) has an exponential dependence on temperature ( $R_s \propto \exp\left[-\frac{\Delta}{k_B T}\right]$ , see [Eq. \(2.1\)](#)) whereas a d-wave superconductor has the power law dependence ( $R_s \propto T^2$ ). Specifically for SRF purposes, where the low surface resistance is of the utmost importance, only s-wave superconductors can be used. The pairing symmetry of a new material can be quickly checked by fitting  $\lambda(T)$  in the low temperature limit to the following equation [[233–235](#)]:

$$\frac{\lambda(T)}{\lambda(0)} = \left[ 1 - \left( \frac{T}{T_c} \right)^p \right]^{-1/2} \quad \begin{array}{l} \text{For s-wave } p = 2 \\ \text{For d-wave } p = 4/3 \end{array} \quad (11.1)$$

As I discussed in [Chapter 2](#), when a new material is being considered for SRF or any other high-frequency applications, it is often costly and/or difficult to fabricate a full cavity for testing. There is growing interest in surface characterization techniques that can be used on flat thin film and bulk superconducting samples. Another approach involves creating a superconducting test cavity where one side of the cavity is replaced with the sample of interest [[236](#)]. This approach still requires large samples (10 cm diameter). Additionally the MW losses on the cavity walls can be comparable or sometimes even greater than the losses due to the sample. Hence this method can only provide an estimate on the surface resistance of the sample.

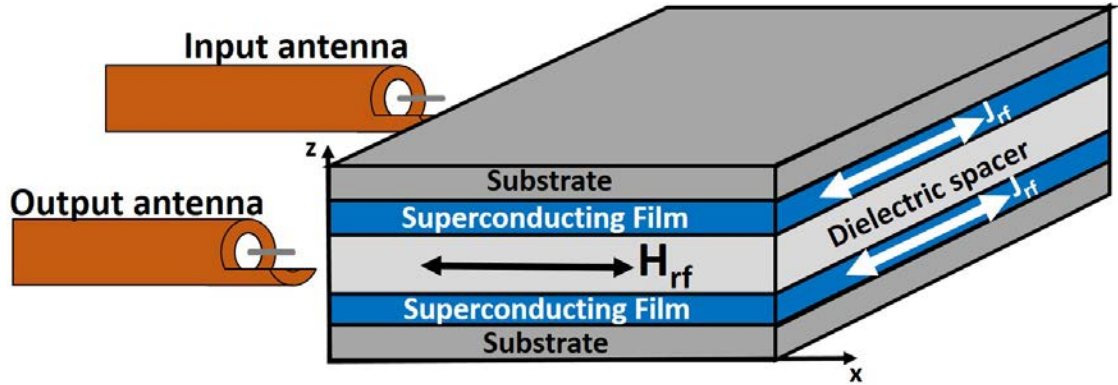


Fig. 11.1 Schematic of the Parallel Plate Resonator. A dielectric spacer is sandwiched between two nominally identical superconducting films. Arrows show the rf magnetic fields  $H_{rf}$  (black) and surface currents  $J_{rf}$  (white) corresponding to the  $TEM_{01}$  mode. The coupling to the PPR is achieved by bringing 2 antennas close to the edge of the PPR. The antennas are made by exposing a short part of the inner conductor and a portion of the outer conductor of a coaxial cable. Schematic diagram not to scale.

## 11.1 Parallel Plate Resonator

In our lab, we used the surface characterization method originally proposed by Taber [237]. In this approach, a dielectric spacer is placed between two flat and nominally identical superconductors forming a parallel plate resonator (PPR) as shown in Fig. 11.1. No direct electrical contacts are made to the superconducting samples, preserving the open-circuit boundary conditions at the edges.

The TEM modes of the PPR can be excited by positioning 2 antennas near the two corners of a PPR. Antennas are capacitively coupled to the PPR and the coupling strength can be tuned by varying the physical distance between the antennas and the PPR. The antennas are made by exposing a short part of the inner conductor and a portion of the outer conductor of a coaxial cable. Other antenna designs like a

microstrip line [238] or moon-shaped antenna [239] have been used by other authors.

The dimensions of the films used in the PPR are on the order of  $\sim 1\text{cm}$ , whereas the thickness of the dielectric spacer is  $< 500\mu\text{m}$ . Due to the thin height of the PPR, the waves inside the PPR can be considered to be quasi-2D. Also, the fringing fields on the edges of the PPR can be ignored when calculating the resonant frequencies of the PPR. Consider a rectangular PPR resonator with length  $L$ , width  $W$  and dielectric constant  $\epsilon_r$ . The  $\hat{x}$ ,  $\hat{y}$ ,  $\hat{z}$  axes are aligned with the edges of the PPR with one of its corners coinciding with the origin, as shown in Fig. 11.1. The electric field distribution and the resonant frequency of the transverse electromagnetic (TEM) modes for this PPR can be written as:

$$\vec{E} = E_0 \cos\left(\frac{n\pi}{L}\hat{x}\right) \cos\left(\frac{m\pi}{W}\hat{y}\right) \hat{z} \quad \text{and} \quad (11.2)$$

$$f_0 = \frac{c}{2\sqrt{\epsilon_r}} \sqrt{\left(\frac{n}{L}\right)^2 + \left(\frac{m}{W}\right)^2},$$

where  $n$  and  $m$  are the mode indices ( $n, m \geq 0$ ,  $n+m \geq 1$  and  $n, m \in \mathbb{Z}$ ),  $c$  is the speed of light and the superconducting samples are modeled as perfect conductors. To avoid mode degeneracy, it is best to avoid square ( $L = W$ ) samples. In fact, the exact shape of the sample is not crucial for the measurement and will result in slightly different electric distributions than the one given in Eq. (11.2).

A Keysight (model N5242A) Vector Network Analyzer (VNA) was used to measure the complex transmission  $S_{21}(f)$  through the cavity. The measured temperature

dependence of the resonant frequency  $f_{res}$  stems from the temperature dependence of the penetration depth  $\lambda(T)$ , and can be written as [240]:

$$\frac{f_{res}(T)}{f_0} = \left[ 1 + 2 \frac{\lambda(T)}{d} \coth \left( \frac{t}{\lambda(T)} \right) \right]^{-1/2} \quad (11.3)$$

where  $d$  is the thickness of the dielectric spacer,  $t$  is the thickness of the superconducting sample and  $f_0$  is the resonant frequency corresponding to a perfect conductor (i.e.  $\lambda = 0$ ). Note that for extracting a value of  $\lambda(0)$  this method requires that a functional form of the penetration depth temperature dependence is known beforehand (like in Eq. (11.1)). A better approach to determine  $\lambda(T)$  is to vary the thickness of the dielectric spacer  $d$  at a constant temperature [239, 241].

The total energy lost during the oscillation can be obtained from the quality factor of the resonance. This loss is caused by the resistive loss on the surface of the superconductor, dielectric loss in the spacer, and the radiation loss from the edges of the PPR. The total loss can be reduced by placing the PPR inside a conductive cavity. In this case, the total loss can be written as [237]:

$$1/Q = \underbrace{c_{rad}d}_{\text{Radiation Loss}} + \underbrace{\tan\delta}_{\text{Dielectric Loss}} + \frac{R_s}{\underbrace{\pi\mu_0 f_{res}d}_{\text{Superconductor Loss}}}, \quad (11.4)$$

where  $c_{rad}$  is the radiation loss coefficient,  $\tan\delta$  is the loss tangent of the dielectric spacer, and  $R_s$  is the assumed uniform surface resistance of the sample. As evident from the equation above, when a thin dielectric spacer is used, loss due to the su-

perconductor dominates. Again, the ideal approach to obtaining the absolute surface resistance is to systematically vary the thickness of the dielectric spacer  $d$ . Nevertheless, at any temperature,  $R_s < \frac{\pi\mu_0 f_{res} d}{Q}$  provides an upper bound on the surface resistance.

The antennas should be weakly coupled to the PPR so that the loaded quality factor and unloaded quality factor are nearly identical. For more details on the loaded and unloaded quality factors and the coupling strength of the antenna please see [Sec. 3.6](#).

## 11.2 Experimental Setup

[Fig. 11.2\(a\)](#) shows a picture of the PPR located inside the cavity, which is made out of gold-plated OFHC copper. The dielectric posts are used to press and hold the samples together. Later, this cavity is attached to a dipping probe and inserted into a liquid helium dewar (see [Fig. 11.2\(a\)](#) and (b)). The dipping probe is made out of a stainless steel tube that houses rf coaxial cables and dc wiring running from the top of the probe ([Fig. 11.2\(c\)](#)) to the cavity([Fig. 11.2\(a\)](#)). A thermometer and a heater are installed on this cavity to monitor and control the temperature. Alternatively, the dipping probe can be moved up and down relative to the liquid helium surface to sweep the temperature, which is the case for the measurements presented here. The relief valve shown at the bottom of [Fig. 11.2\(c\)](#) is used to relieve the helium gas

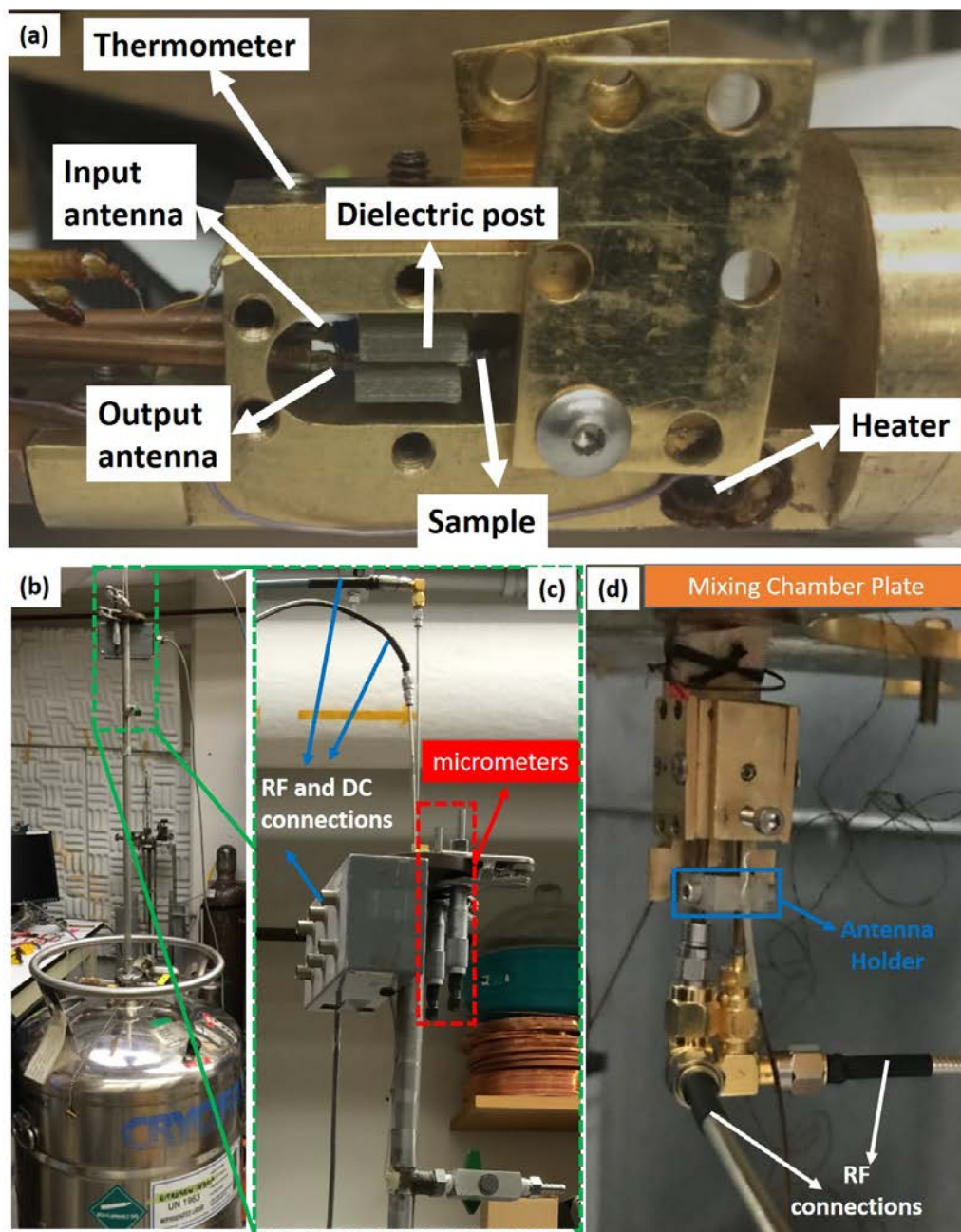


Fig. 11.2 Picture of the experimental setup. (a) PPR inside the copper cavity. Two dielectric posts are used to keep the samples together. Coupling antennas enter the cavity from two small holes on the left side. A thermometer and a heater are installed to monitor and control the temperature. The cavity housing the PPR is attached to the end of the dipping probe. (b) The dipping probe is inserted into the liquid helium dewar. (c) Top part of the dipping probe. Micrometers are installed to precisely move the rf coaxial cables up or down, which moves the antennas away or towards the sample, hence tuning the coupling strength of the antennas to the PPR. A relief valve is installed to relieve the helium gas pressure build up. (d) The cavity housing the PPR is attached to the mixing chamber plate of the dilution fridge shown in Fig. 3.5 of Chapter 3. An aluminium holder is designed to hold the antennas at the desired position. Alternatively, the cavity can be attached to the cold plate of the dry pulsed-tube cryostat shown in Fig. 4.11 of Chapter 4.

pressure build up inside the dewar and the probe. If the dipping probe is removed from the dewar, water from ambient air around the setup can condense on the sample surface, damaging the sample. The same valve is used to supply a constant flow of dry nitrogen gas to preserve the sample surface from contamination during the warmup. The micrometers on the top of the probe are used to fine tune the coupling strength to the PPR by controlling the separation between the antenna and PPR. This allows one to modify the coupling at any temperature.

The dipping probe method has several disadvantages. Firstly the base temperature of the setup is  $4.2K$ , which is not sufficiently cold to study many interesting superconductors. Secondly, the moment the PPR is immersed below the liquid helium surface, liquid helium flows between the samples resulting in a noticeable discontinuity in the PPR resonant frequency. Lastly, nowadays liquid helium is an expensive and increasingly scarce commodity [242], and in our Lab we have decided to move away from liquid helium. To address these shortcomings, the PPR was moved inside the dilution fridge (see Fig. 11.2(d)). The cavity was mounted on the mixing chamber and an aluminium holder was used to hold the antennas at a fixed position. Using this new approach, we gained the ability to measure the superconducting samples down to  $100mK$  temperatures, although losing the ability to adjust the coupling strength of the antennas *in-situ*.

One feature of using a cavity to host the PPR is that it will have resonant modes of its own. The measured complex transmission  $S_{21}(f)$  will show both the cavity modes and PPR modes. Also, if a cavity mode happens to be in the vicinity of the PPR mode in the frequency spectrum, these two modes can couple to each other. Such interaction

will add skew to the PPR resonance distorting it from a standard Lorentzian curve predicted by the lumped element model of a single isolated resonator [243]. Since the metallic cavity is lossier than the superconducting sample, the PPR modes tend to be sharper, due to their higher quality factor. Furthermore, the intrinsic properties of a superconductor are strongly temperature dependent, thus the resonant frequency of the PPR mode will have strong dependence on temperature variation. Additionally the quality factor of the PPR peak is power dependent due to the nonlinearity associated with the superconducting state. These properties can be used to distinguish the PPR modes from the cavity modes.

To study the surface impedance one needs to extract the resonant frequency and quality factor from transmission data  $S_{21}(f)$ . To aid with this process, one should design the cavity and PPR such that the cavity modes and PPR modes do not overlap. Additionally the PPR modes can be shifted up and down in frequency by utilizing dielectric spacers with different dielectric constants  $\epsilon_r$ .

### 11.3 Boron doped diamond sample

Diamond is the hardest known natural material. Diamond is also an excellent electrical insulator but with a very high thermal conductivity ( $2200W/m \cdot K$  at room temperature), in fact Diamond is a better thermal conductor than copper. These properties make usage of diamond in electronic applications very appealing. Recently, it was discovered that the Boron-doped Diamond (B-diamond) exhibits superconductiv-



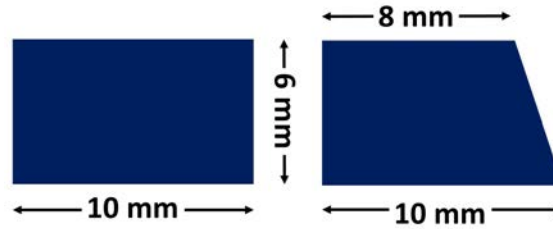


Fig. 11.3 The shape of the B-diamond sample.

ity above liquid helium temperatures, both in bulk [244] and thin-film forms [245]. Early transport measurements showed a high upper critical value of  $H_{c2}(0) = 2.7T$  on bulk B-diamond samples and  $H_{c2}(0) = 11.62T$  in B-diamond films deposited using the Chemical Vapor Deposition (CVD) technique [246]. Later, Mandal *et al.* demonstrated that a Superconducting Quantum Interference Device (SQUID) made of B-diamond can operate in a 4 Tesla field [247].

One of the key advantages of using diamond in electronics is the fact that by controlling the dopant type and doping concentration one can create an insulator, a semiconductor (both p and n type), or a superconductor, all using the same starting material. For instance, Watanabe *et al.* demonstrated that they could create very uniform vertical SNS Josephson junctions solely with B-diamond by carefully controlling the doping concentration during the deposition of the thin-film [248].

The high thermal conductivity and high stiffness of diamond might eventually capture the interest of the SRF community as well. However, currently the costs associated with the production of B-diamond thin-films prohibits its usage in any of the large scale applications. Nevertheless, with a PPR setup at our disposal, and owing to the fact that there is no literature available on the microwave performance

of B-doped diamond, we proceeded with the following measurement. A B-diamond thin-film sample was provided by Ramachandra Rao's group at the Indian Institute of Technology Madras. A  $1.5\mu\text{m}$  thick film with  $7.8 \times 10^{21}/\text{cm}^3$  Boron doping concentration was deposited on a silicon substrate using the hot filament chemical deposition technique [249, 250]. The critical temperature of the film was obtained from dc resistivity measurement to be  $T_c = 7.0\text{K}$  [251], which corresponds to the temperature where resistance goes to zero. It has been shown that  $T_c$  vs Boron doping is a dome-shaped curve in the noncrystalline B-diamond films [252]. This film has nearly the optimum dopant concentration for superconductivity. However these films are known to be granular [245, 253–257] and inhomogeneous on the sub-micron length scale.

The sample had an irregular shape, and was cut into two pieces to form a PPR. The dimensions of the sample are shown in Fig. 11.3. A  $d = 500\mu\text{m}$  thick quartz ( $\text{SiO}_2$ ) spacer was used as a dielectric spacer. The sample was first measured inside liquid helium using the dipping probe. Fig. 11.4 shows the amplitude of the measured transmission through the PPR at 3 different temperatures. As the temperature is increase both the resonant frequency and quality factor shift to lower values. The rapid shift of the resonance frequency as a function of temperature indicates that these are the PPR modes.

Later the PPR setup was moved to the dry pulsed-tube Entropy cryostat shown in Fig. 4.11 of Chapter 4. The same PPR formed with the B-diamond sample with a  $d = 500\mu\text{m}$  thick quartz ( $\text{SiO}_2$ ) dielectric spacer was measured down to a temperature of 2.8 K. It was observed that one needs to wait for up to 10 minutes at each temperature point for the sample to reach an equilibrium temperature. This is caused

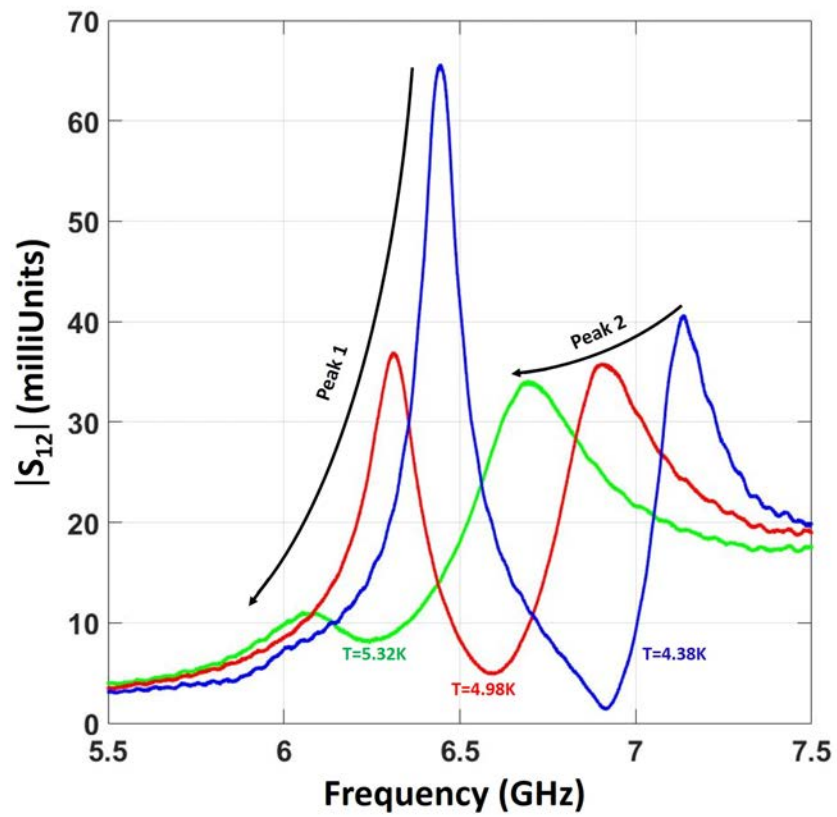


Fig. 11.4 Transmission through the cavity housing the B-diamond PPR,  $|S_{12}|$  as a function of frequency, measured by the VNA at  $T = 4.38K$ ,  $T = 4.98K$  and  $T = 5.32K$  in the dipping probe.

by low thermal conductivity of the teflon posts and the lack of helium vapor that was present in the dipping probe setup. Finally, the PPR setup was moved inside a BlueFors dilution fridge (see Fig. 11.2(d)) where measurements down to mK temperatures were made. But in this case the dielectric quartz dielectric spacer was replaced with a  $430\mu\text{m}$  thick sapphire spacer.

Only the PPR peaks which do not extensively overlap with a cavity mode and have  $Q > 20$  were studied closely. Both the data measurement inside the dipping probe and the Entropy cryostat showed 2 PPR peaks each which met this criteria. The data measurement inside the BlueFors dilution fridge had only 1 PPR peak that met my criteria. The model and the fitting procedure that is used to extract  $f_{res}(T)$  and  $Q(T)$  from this measurements is discussed in the next section.

## 11.4 Extracting $f_{res}$ and $Q$ from the transmission data

An ideal resonator can be modeled as an RLC circuit where each element is connected in series. The complex transmission coefficient of an RLC circuit in the weak coupling limit and ignoring external measurement effects is given by [243]

$$S_{12}(f) = \frac{S_{peak}}{1 + iQ \left( \frac{f}{f_{res}} - \frac{f_{res}}{f} \right)}, \quad (11.5)$$

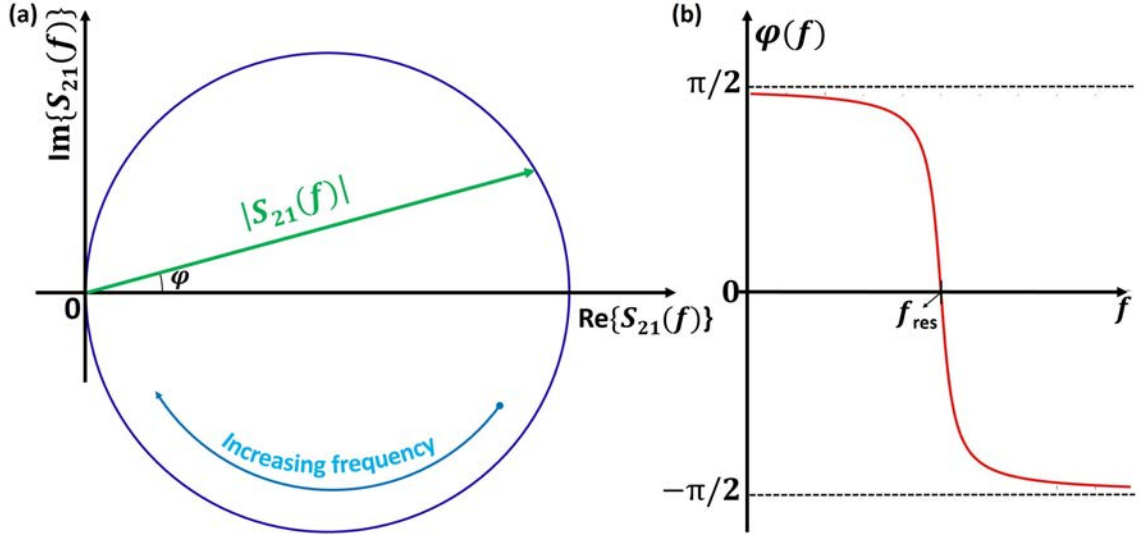


Fig. 11.5 (a) Complex plane plot of the ideal resonator transmission  $S_{12}(f)$  (blue circle) calculated using Eq. (11.5). The diameter of this circle is equal to  $S_{peak}$ . The length of the green arrow connecting the origin with a data point on the circle is equal to the measured amplitude of the transmission  $|S_{21}(f)|$ . The phase of the resonance  $\phi$  which is defined as the angle between the real axis and the line connecting the origin with a particular point is shown in (b) (red solid line). At the resonant frequency  $Re\{S_{21}(f_{res})\} = S_{peak}$  and  $\phi(f_{res}) = 0$ .

where  $S_{peak} = |S_{12}(f_{res})|$  and  $i = \sqrt{-1}$ . This equation holds in the limit of weak coupling, i.e.  $\beta_1, \beta_2 \ll 1$ , where  $\beta_1$  and  $\beta_2$  are the coupling strength of the input and output antennas. Fig. 11.5 shows the complex plane plot of  $S_{12}(f)$  calculated using Eq. (11.5). The complex function  $S_{12}(f)$  forms a circle with a diameter  $S_{peak} = 2\sqrt{\beta_1\beta_2}$  centered at  $(S_{peak}/2, 0)$ . Eq. (11.5) can be used to derive the following analytic equation for the phase of the resonance

$$\phi(f) = \tan^{-1} \left[ Q \left( \frac{f_{res}}{f} - \frac{f}{f_{res}} \right) \right] \simeq \tan^{-1} \left[ 2Q \left( 1 - \frac{f}{f_{res}} \right) \right], \quad (11.6)$$

where the approximation is valid when  $f \simeq f_{res}$ . Fig. 11.5(b) shows the phase of the resonance  $\phi$  vs frequency.

Some real world measurement effects like the crosstalk between the cables/antennas and the phase shift introduced because the calibration plane is a finite distance away from the coupling ports can cause corruption to the data. These effects result in the translation and rotation of the measured  $S_{12}(f)$  data in the complex plane, away from the simple resonance shown in Fig. 11.5. There are several methods that can be used to extract the resonance frequency and quality factor from transmission  $S_{12}(f)$  data. The summary and head to head comparison of these methods can be found in Ref.[243], where the authors show that the most accurate method to extract the  $f_{res}$  and  $Q$  from  $S_{12}(f)$  is the "Phase vs frequency fit".

#### 11.4.1 Phase vs frequency fit

This method can account for the corruption to the data caused by the real world measurement effects. Fig. 11.6 illustrates the steps involved in the phase vs frequency fit method, which can be summarized as follows: First, the frequency range for the peak is identified from  $|S_{12}(f)|$  data (see Fig. 11.6(a)). Fig. 11.6(b) shows the phase of  $S_{12}(f) = |S_{12}(f)|e^{i\phi(f)}$ . To use this data first we need to unwind it's phase  $\phi(f)$  (by adding  $\pm 2\pi$  to the raw measured phase). Later the linear in frequency background phase variation that is the result of phase delay caused by the un-calibrated coaxial cables is removed, resulting in the clean phase vs frequency data shown in Fig. 11.6(c). Fig. 11.6(d) shows the processed  $S_{12}(f)$  data (blue) in the complex  $S_{12}$  plane. A point

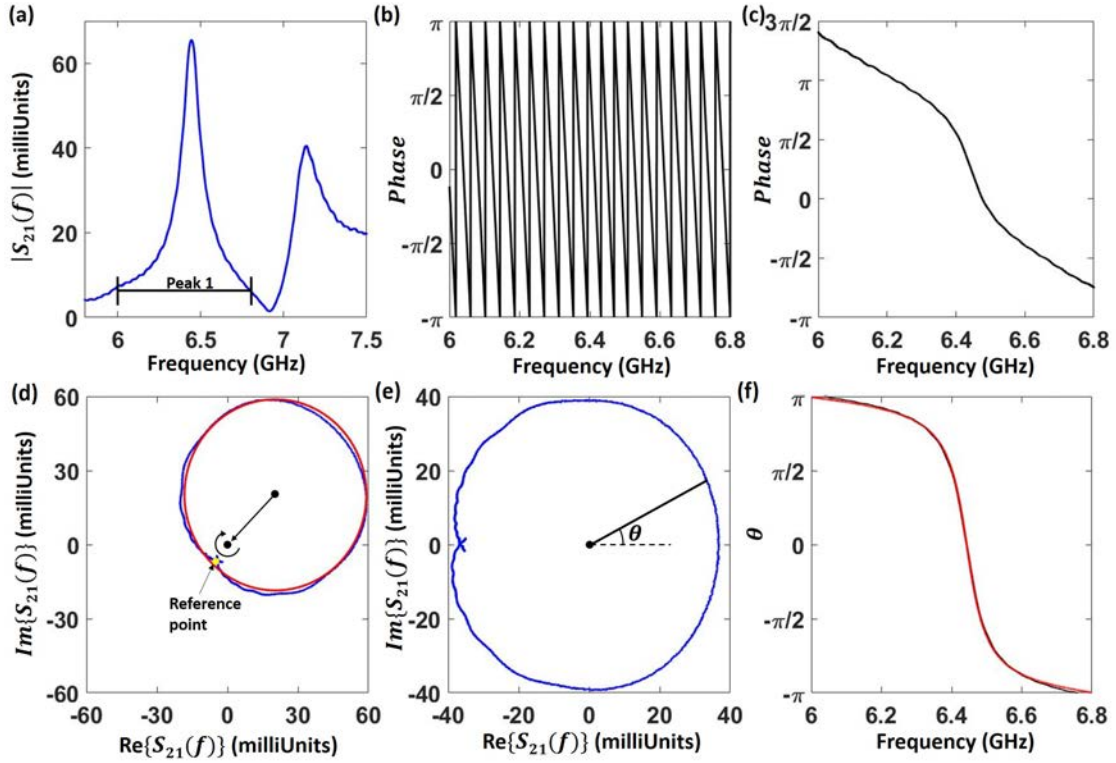


Fig. 11.6 The steps of an Phase vs frequency fit method. Measured amplitude and phase of  $S_{12}(f)$  is shown in (a) and (b) respectively. (c) shows the Phase of the  $S_{12}(f)$  after unwinding and background subtraction. (d) Complex plane plot of  $S_{12}(f)$  (blue) and a circle fit (red) to it after the phase unwinding. Yellow circle shows the coordinates of  $S_{ref}$  and the arrows indicate the translation and rotation performed to arrive at the data shown in (e). (e) Complex plane plot of  $S_{12}(f)$  after the translation to and rotation around the origin. (f) (Black) The phase of the "clean"  $S_{12}(f)$  data shown in (e) and the Eq. (11.8) fit to this data with  $Q = 78$ ,  $f_{res} = 6.444$  GHz and  $\theta_0 = -0.048$  (red).

in the complex  $S_{12}$  plane midway between the first and last  $S_{12}(f)$  data points is chosen as the reference point  $S_{ref}$  (yellow circle). This represents an approximation to the off-resonance S-parameter value. A circle (red circle in Fig. 11.6(d)) is then fit to the data with the following weight assigned to each data point,

$$W_i = |S_{12}(f_i) - S_{ref}|^2 \quad (11.7)$$

This weighting convention ensures that the points closer to the resonance peak (which is on the circle opposite to  $S_{ref}$ ) have highest weight. As the next step, the data is first moved and then rotated such that  $Im\{S_{ref}\} = 0, Re\{S_{ref}\} < 0$  and the center of the fit circle coincides with the origin of the complex  $S_{12}$  plane (see Fig. 11.6(e)). This removes all the external alterations to the data besides the noise. Fig. 11.6(f) shows the clean phase of  $S_{12}$  data extracted from Fig. 11.6(e). Finally, Eq. (11.8) is fit to this "cleaned" phase vs frequency data using three parameters:

$$\theta(f) = \theta_0 + 2 \tan^{-1} \left[ 2Q \left( 1 - \frac{f}{f_{res}} \right) \right] . \quad (11.8)$$

Here,  $f_{res}$  is the resonance frequency,  $Q$  is the quality factor and  $\theta_0$  is an offset needed to account for the errors associated with the choice of  $S_{ref}$ .

#### 11.4.2 Multi-peak fit

The phase vs frequency fit method is a very accurate method. However, it works best when a PPR peak  $|S_{12}(f)|$  can be isolated from other signals. When multiple PPR peaks are located very close to each other in the frequency spectrum, the peak shapes becomes distorted, as in the 2<sup>nd</sup> peak in Fig. 11.4. In this case I propose an alternative fitting approach. The phase of the  $S_{12}(f)$  data is unwrapped as was previously discussed. Then the number of peaks  $N$  contributing to the signal is identified. The measured  $S_{12}(f)$  data is the result of complex addition of transmission that can be attributed to each individual peak and the background transmission due



to real world measurement effects discussed above. The real and imaginary part of the background transmission can be modeled as  $Re \{S_{12,bg}(f)\} = x_1 + x_2f$  and  $Im \{S_{12,bg}(f)\} = y_1 + y_2f$  respectively. Parameters  $x_1, x_2, y_1, y_2$  account for the cross-talk between the cables and between the antennas. The contribution of each peak to the real and imaginary parts of  $S_{12}(f)$  is  $r \{1 + \cos[\theta(f)]\}$  and  $r \sin[\theta(f)]$ , respectively, as derived from Eq. (11.5). Here  $r$  is the radius of each peak (see Fig. 11.5(a)) and  $\theta(f)$  is the phase shown in Fig. 11.6(e), both of which are measured from the center of the circle formed by the individual resonances in the complex  $S_{12}$  plot. The  $S_{12,bg}$  only accounts for the translation of the peaks in the complex plane. In order to account for the rotation of each resonance peak in the complex plane, an additional phase offset  $\theta_0$  is introduced. Putting this all together, Eq. (11.9) contains all of these contributions and is fit to the entirety of the  $S_{12}(f)$  data:

$$\begin{aligned}
 Re \{S_{12}(f_i)\} &= x_1 + x_2f_i + \sum_{j=1}^N r_j \{1 + \cos[\theta_j(f_i)]\} \quad , \\
 Im \{S_{12}(f_i)\} &= y_1 + y_2f_i + \sum_{j=1}^N r_j \sin[\theta_j(f_i)] \quad , \\
 \theta_j(f_i) &= \theta_{0j} + 2 \tan^{-1} \left[ 2Q_j \left( 1 - \frac{f_i}{f_{res,j}} \right) \right] \quad .
 \end{aligned} \tag{11.9}$$

Here  $i$  and  $j$  are indices for the data points and the peak number, respectively; and  $f_{res,j}$  and  $Q_j$  are the resonant frequency and the quality factor of each peak ( $j$  runs from 1 to  $N$ ). In total for a dataset with  $N$  peaks there are  $4N + 4$  independent parameters to be fitted. Fig. 11.7 shows a  $N = 3$  peak fit to  $S_{12}(f)$  data performed

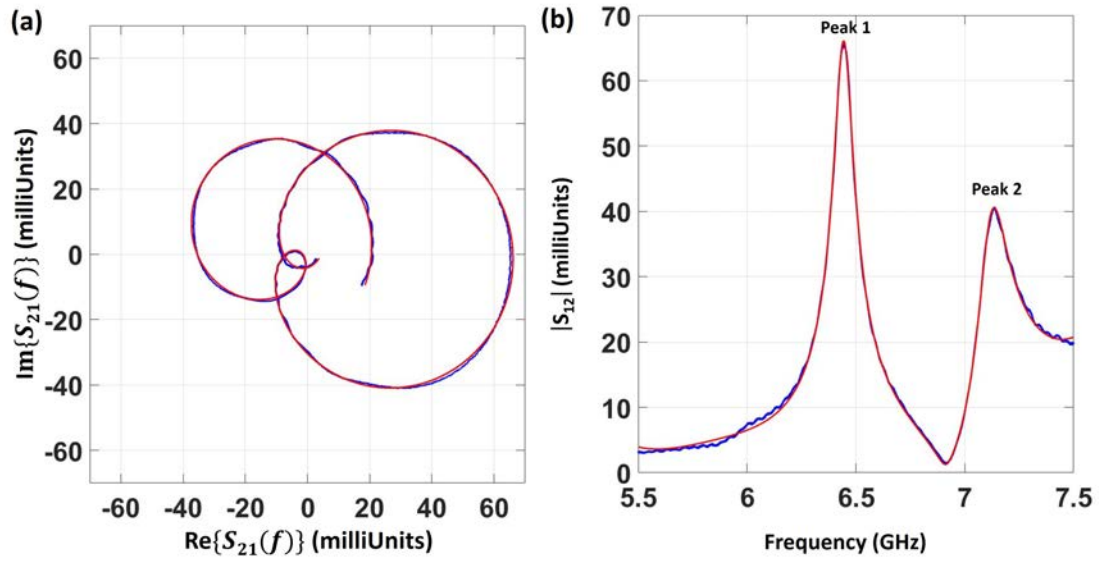


Fig. 11.7 Multi-peak fit to  $S_{12}(f)$  data using Eq. (11.9) with  $N = 3$ :  $f_{res,peak1} = 6.443$  GHz and  $Q_{peak1} = 69$ ;  $f_{res,peak2} = 7.115$  GHz and  $Q_{peak2} = 52$ ;  $f_{res,peak3} = 8.532$  GHz and  $Q_{peak3} = 5.2$ . Data collected from Boron-doped diamond PPR at  $T = 4.38$  K in the dipping probe.

using Eq. (11.9). The third peak in this fit corresponds to a low-Q cavity mode, which acts as a complex frequency dependent background to the 2 PPR peaks shown in Fig. 11.7. The existence of this low-Q cavity mode was deduced from a separate measurement with a wider frequency window under identical conditions.

## 11.5 Results

### 11.5.1 Penetration depth

The procedure described in the previous section was repeated for each temperature providing  $f_{res}(T)$  and  $Q(T)$  for the B-diamond films. Fig. 11.8 shows frequency

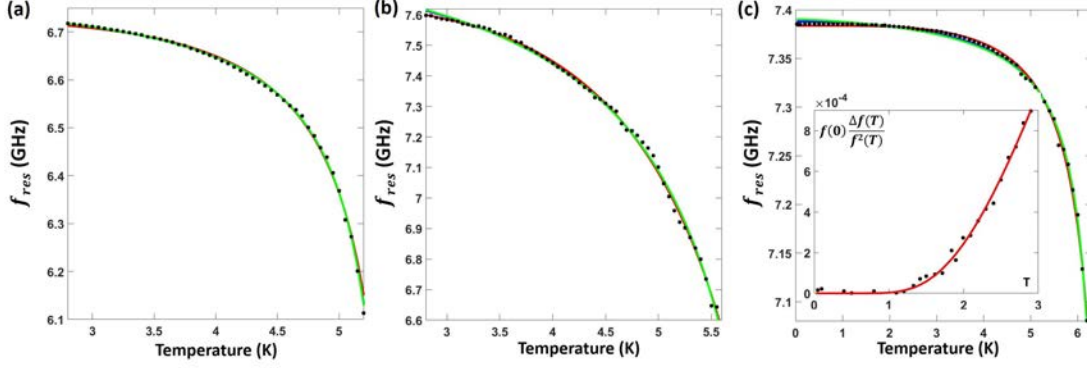


Fig. 11.8 Temperature dependence of the resonant frequency  $f_{res}(T)$  extracted from PPR measurement on B-diamond films inside the (a),(b) Entropy cryostat with  $500\mu\text{m}$  Quartz dielectric spacer (two modes measured simultaneously) and (c) dilution fridge with  $430\mu\text{m}$  Sapphire dielectric spacer. Also shown are fits to the data using Eqs. (11.1) and (11.3) with  $p = 2$  (blue),  $p = 4$  (red),  $p = 4/3$  (green). Inset in (c) shows the quantity  $f_{res}(0)\Delta f_{res}(T)/f_{res}^2(T)$  vs temperature, which is proportional to  $\Delta\lambda/\lambda(0)$ . Solid red line is the fit to the data using Eq. (11.10) with  $\Delta(0) = 812\mu\text{eV}$ .

shift data for several PPR modes. The first thing to note about the data in Fig. 11.8 is the unusually large range of frequency shift of the modes, on the order of 1 GHz. Given the large dielectric spacer thickness ( $d = 500\mu\text{m}$ ) this implies that the change in the penetration depth  $\Delta\lambda(T)$  is unusually large. Eq. (11.3) can be fit to  $f_{res}(T)$  data to extract an estimate of the zero temperature penetration depth  $\lambda(0)$  and the critical temperature  $T_c$ . However one first needs to find out the functional form of  $\lambda(T)$  to be used in the fit. For this purpose the data measured inside the Entropy pulse tube cryostat and the BlueFors Dilution fridge was fit using Eqs. (11.1) and (11.3) with  $p = 2$ ,  $p = 4$  and  $p = 4/3$ . Fig. 11.8 show the results of these fits and the variance of the fits are listed in Table 11.1.

Additionally one can look at the low temperature ( $T < T_c/3$ ) behaviour of  $f_{res}(T)$ , where  $\Delta\lambda(T)/\lambda(0) \propto \Delta f_{res}(T)/f_{res}^2(T)$ . Here  $\Delta f_{res}(T) = f_{res}(T) - f_{res}(0)$ .

In this regime,  $\Delta\lambda(T)$  for an s-wave superconductor has an exponential dependence on temperature [235]:

$$\Delta\lambda(T) \equiv \lambda(T) - \lambda(0) = \lambda(0) \sqrt{\frac{\pi\Delta(0)}{2k_B T} \exp\left(-\frac{\Delta(0)}{k_B T}\right)}, \quad (11.10)$$

while  $\Delta\lambda(T)$  for a clean d-wave superconductor has linear in temperature dependence  $\Delta\lambda(T) = a\lambda(0)k_B T/\Delta(0)$  [258]. Inset of Fig. 11.8(c) shows the temperature dependence of

$f_{res}(0)\Delta f_{res}(T)/f_{res}^2(T)$  in the low temperature limit ( $T < 3K$ ). The low temperature part of  $f_{res}(T)$  was fit using Eqs. (11.3) and (11.10) (see solid red line in the inset of Fig. 11.8(c)), which yielded  $\Delta(0) = 812\mu eV$  and  $\lambda(0) = 1.78\mu m$ .

Dataset	$\frac{\lambda(T)}{\lambda(0)} = \left[1 - \left(\frac{T}{T_c}\right)^p\right]^{-1/2}$		
	$p = 2$	$p = 4$	$p = 4/3$
Peak 1 measured in Entropy Cryostat	$1.59 \times 10^{-5}$	$1.4 \times 10^{-5}$	$3.06 \times 10^{-5}$
Peak 2 measured in Entropy Cryostat	$1.78 \times 10^{-4}$	$1.43 \times 10^{-4}$	$1.95 \times 10^{-4}$
PPR Peak measured in Bluefors DR	$8.09 \times 10^{-6}$	$7.15 \times 10^{-6}$	$1.23 \times 10^{-5}$

Table 11.1 The variance  $\langle (f_{meas}(T) - f_{fit}(T))^2 \rangle$  of the fits shown in Fig. 11.8.

Given the exponential temperature dependence of  $f_{res}(0)\Delta f_{res}(T)/f_{res}^2(T)$  shown in Fig. 11.8(c) and the  $p = 4$  fit having the lowest variance in Table 11.1, I conclude that B-diamond is an s-wave superconductor and we are obligated to fit the

$f_{res}(T)$  data to the full BCS s-wave temperature dependence up to near  $T_c$ . Previous specific heat, Hall effect, upper critical field, and resistivity measurements on bulk B-diamond samples have also hinted that the conventional electron-phonon mechanism is responsible for the emergence of superconductivity in B-diamond [259]. Additionally STM measurements showed that single-crystal B-doped diamond was an s-wave BCS superconductor with a superconducting gap to critical temperature ratio of  $\Delta(0)/k_B T_c = 1.74$  [255]. Using  $\Delta(0) = 812\mu V$  obtained from the low temperature  $f_{res}(T)$  data extracted from the Boron doped diamond PPR measurement inside the dilution fridge, and  $T_c = 6.45K$  extracted from the full temperature fit to the same data, the superconducting gap to critical temperature ratio is calculated to be  $\Delta(0)/k_B T_c = 1.48$  somewhat less than 1.764 which is expected from weak-coupled BCS theory (see Eq. (1.15) in Chapter 1). However we believe that our film is a heavily doped nanocrystalline material, and not a doped single crystal. Previous work on nanocrystalline Boron-doped diamond films by scanning tunneling spectroscopy showed a similar value for the gap ratio ( $0.63 < \frac{\Delta(0)}{k_B T_c} < 1.54$ ) [260]. The authors of that work attributed this to an inverse proximity effect whereby the granular aspect of the sample created a range of gap values at the nanoscale. Therefore the  $\lambda(0)$  value that we extract is likely that of a composite granular material.

Finally all 5 data sets taken on the B-diamond films were fit to Eqs. (11.1) and (11.3) with  $p = 4$ . The summary of the fits is given in Table 11.2. Surprisingly the critical temperatures extracted from two separate modes within the same measurement (lines 2-3 and 4-5 in Table 11.2) do not match. This suggests that the sample

Measurement date	Dielectric spacer	Setup	Temperature range (K)	$f_0$ (GHz)	$\lambda(0)$ ( $\mu\text{m}$ )	$T_c$ (K)
02/10/2015	500 $\mu\text{m}$ Quartz	Dipping Probe	4.4-5.84	6.70	4.40	5.69
02/10/2015	500 $\mu\text{m}$ Quartz	Dipping Probe	4.4-5.84	8.44	11.05	6.46
03/27/2017	500 $\mu\text{m}$ Quartz	Entropy Cryostat	2.8-5.55	6.97	5.19	5.60
03/27/2017	500 $\mu\text{m}$ Quartz	Entropy Cryostat	2.8-5.55	9.53	14.41	6.66
07/03/2017	430 $\mu\text{m}$ Sapphire	Bluefors DR	0.025-6.20	7.52	3.42	6.45
07/03/2017	430 $\mu\text{m}$ Sapphire	Bluefors DR <sup>†</sup>	0.025-3.00	7.43	1.78	-

Table 11.2 Summary of fits to data taken with PPR measurements on Boron-doped diamond films. † Low temperature limit part of the data only.

may be inhomogeneous since the two modes send rf current through different parts of the films. Also, I observed that the choice of the temperature range used for the fitting significantly affects the result of the fitting. If the lowest temperature data point in the dilution fridge measurement is omitted from the fit and the fit is repeated, with each omission the value of the extracted zero temperature penetration depth continuously decreases from  $\lambda(0) = 3.42\mu\text{m}$  to  $\lambda(0) = 2.52\mu\text{m}$ ; On other hand, if the highest temperature data point is omitted from the fit and the fit is repeated, with each omission the value of the extracted zero temperature penetration depth initially increases from  $\lambda(0) = 3.42\mu\text{m}$  to  $\lambda(0) = 6.6\mu\text{m}$  when the highest temperature used for the fit is 4.7 K, afterwards the extracted  $\lambda(0)$  decreases down to  $\lambda(0) = 1.8\mu\text{m}$ . This may explain the large variation in the fitting parameters listed in [Table 11.2](#). These measurements were performed in 3 different setups with a different constraints on base temperature, hence both the dipping probe and Entropy cryostat measurements contain only

a portion of the data that is needed to accurately determine  $\lambda(0)$ .

The dilution fridge measurement covers the widest temperature range, thus can be considered most accurate determination of the penetration depth, with  $\lambda(0) = 3.42\mu m$ . The extracted zero temperature penetration depth for this measurement is significantly larger than the values reported for other conventional superconductors, which range between  $50nm - 500nm$  [261–264]. However it is not very surprising since B-diamond is a low-carrier density material, and similar to the cuprate superconductors, the superconducting state is created by doping an insulator. An order of magnitude estimate for the zero temperature penetration depth can be obtained using the following equation from Sec. 1.2.2 (using conventional values for  $e_*$  and  $m_*$ ) and the stated carrier density from the Rao group:

$$\lambda(0) = \sqrt{\frac{m_*}{\mu_0 n_s e_*^2}} = \sqrt{\frac{m_*}{\mu_0 \cdot 7.8 \times 10^{21} cm^{-3} e_*^2}} = 60.2nm,$$

which is much shorter than the value that we measured. The disparity between the measured value and the theoretical estimate can be caused by a higher effective mass of the Cooper pair than  $2m_e$  as I discussed in Sec. 7.3.2.

An estimate for the zero temperature penetration depth of a granular superconductor can be obtained using Eq. (11.11) which is valid in the local limit [57]:

$$\lambda(0) = 105nm \times \sqrt{\frac{\rho_n \quad 1K}{1\mu\Omega cm \quad T_c}} . \quad (11.11)$$

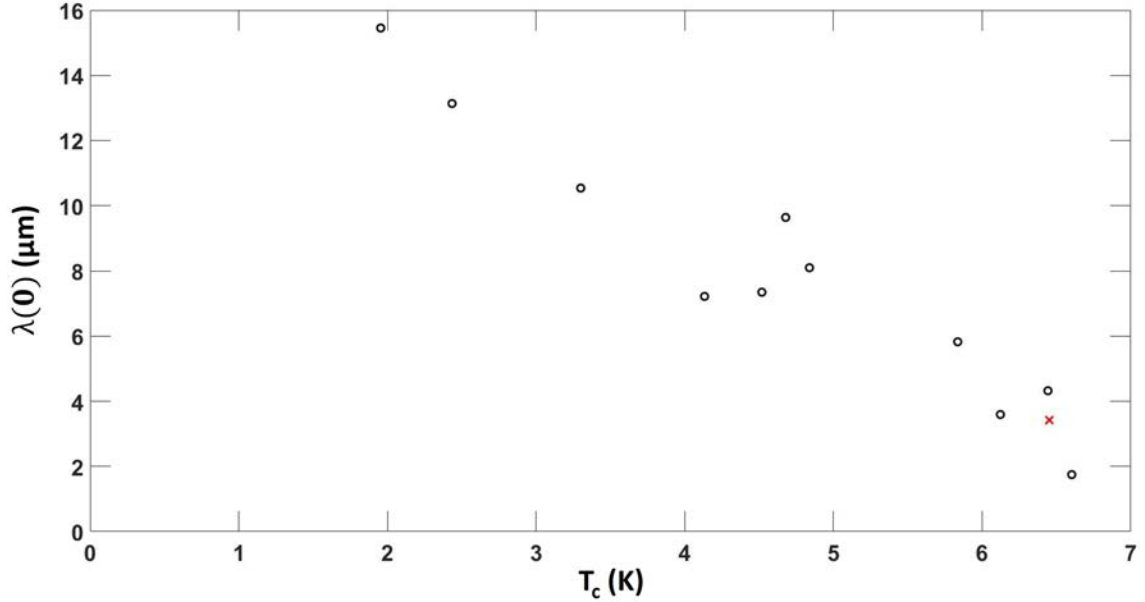


Fig. 11.9 Estimated zero temperature penetration depth  $\lambda(0)$  for various B-diamond films calculated using Eq. (11.11) (black  $\circ$ ). The normal state resistivity  $\rho_n$  and the critical temperature  $T_c$  was taken from the data published in Ref.[252]. The red  $\times$  shows the value of the penetration depth extracted from my B-diamond PPR measurement inside the dilution fridge.

Here  $\rho_n$  is the normal state resistivity of the film measured at a temperature just above the  $T_c$ . The dc transport measurements on several B-diamond films with various Boron doping concentrations was performed by the same group who provided us with the sample [252]. The  $\rho_n$  and  $T_c$  values for these films were plugged into Eq. (11.11) to calculate an estimated value of the zero temperature penetration depth  $\lambda(0)$  shown in Fig. 11.9. The value of the penetration depth extracted from my B-diamond PPR measurement inside the dilution fridge is shown as the red  $\times$  in Fig. 11.9 for comparison. Evidently, the value for the penetration depth extracted from the B-diamond film PPR measurements is aligned with the values of the penetration depth extracted from the dc transport measurements on similar films.



### 11.5.2 Surface resistance

The measured quality factor can be used to estimate the surface resistance of the boron doped diamond using Eq. (11.4). Since the dielectric loss and the radiation loss are not precisely known, the calculated value provides an upper limit on the surface resistance. Fig. 11.10 shows the effective surface resistance  $R_s(T) = \frac{\pi\mu_0 f_{res}(T)d}{Q(T)}$  extracted from the dilution fridge measurement of the B-diamond film (Note that finite thickness corrections are not included here). The temperature dependence of this data in the low temperature limit ( $T < T_c/2$ ) was fit using  $R_s(T) = R_{BCS}(T) + R_0$ , where the  $R_{BCS}$  is the BCS surface resistance (Eq. (2.1)) and  $R_0$  accounts for the assumed temperature independent dielectric loss and radiation loss (solid red line in Fig. 11.10). The log-linear plot of  $R_s(T) - R_0$  and  $R_{BCS}$  fit vs  $T_c/T$  are shown in the inset of Fig. 11.10.

## 11.6 Conclusion

In this chapter, I present the preliminary results from our efforts to measure the complex surface impedance of the superconducting Boron-doped Diamond films, using the PPR technique. Using the multi-peak fit method presented in Sec. 11.4.2 I extracted the resonance frequencies and quality factors of the PPR peaks despite the fact that those peaks were partially overlapping with the nearby cavity modes in the frequency domain. Without this method, one would have to redo the measurement

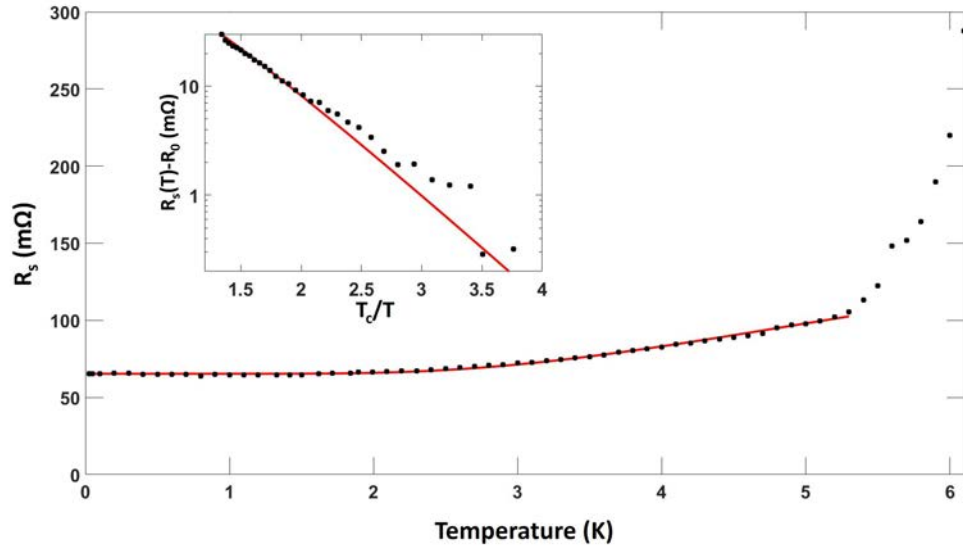


Fig. 11.10 Upper bound on the surface resistance  $R_s$  of the boron doped diamond film. Data taken at a frequency of  $f = 7.52$  GHz (black stars). Also shown is the  $R_s(T) = R_{BCS}(T) + R_0$  fit to the low temperature part of the data ( $T < 5.4$  K) with  $R_0 = 65.3\text{m}\Omega$ ,  $\sigma_n = 4.02 \times 10^5\text{S/m}$  and  $\Delta(0) = 1.34\text{meV}$  used as fitting parameters (red solid line). Here  $\lambda(0) = 3.42\mu\text{m}$  from Sec. 11.5.1 was used for the value of the penetration depth. Inset shows the  $R_s(T) - R_0$  vs  $T_c/T$  in log-linear scale.

with a different dielectric spacer in order to decouple the PPR modes from the peaks associated with the cavity modes.

Using the PPR technique, I measured the penetration depth of the B-diamond films in the entire temperature range where the films are in the superconducting state. As far as I am aware, this is the first-ever attempt to measure the penetration depth of this material. The values of the zero temperature penetration depths extracted from the 3 measurements (and tabulated in Table 11.2) are large when compared to other conventional superconductors. One possible explanation for the high value of the penetration depth that we measured on the B-diamond films is that these films are highly granular, giving rise to a large effective screening length due to a combina-

tion of Meissner and Josephson screening. This is consistent with numerous previous studies showing granular behaviour in nanocrystalline B-doped diamond films [253, 256, 257, 260, 265]. The effective penetration depth of polycrystalline and nanocrystalline superconductors can be estimated using the Laminar Model [266], where the superconductor is modeled as an array of identical superconducting grains separated by a thin non-superconducting grain boundary. The grains are coupled to each other through Josephson coupling. The effective penetration depth of such superconductors strongly depends on the coupling strength between the grain, approaching the intrinsic value of the penetration depth of the grains in the strong coupling limit. Additionally the effective penetration depth strongly depends on the grain size and can be 2 orders of magnitude larger than the intrinsic penetration depth in the small grain size limit. If this is the case for B-doped diamond film, the temperature dependence of  $\lambda(T)$  will be influenced by the temperature dependence of the Josephson penetration depth at the grain boundary  $\lambda_J(T)$ . This may help explain the strong dependence of the extracted  $\lambda(0)$  on the temperature range used in the fitting that I discussed in [Sec. 11.5.1](#).

Similarly large values of penetration depth are observed in other amorphous and granular superconductors:  $\lambda(0) > 0.51\mu m$  in  $\text{Mo}_3\text{Si}$  [267],  $\lambda_l(0) = 0.575\mu m$  in  $\text{TiN}$  [268],  $\lambda(0) = 0.645\mu m$  in  $\text{Mo-Ge}$  [269],  $\lambda(0) > 0.65\mu m$  in  $\text{Nb}_3\text{Ge}$  [267] and  $\lambda(0) = 1.2\mu m$  in granular aluminium film [270]. Additionally, as the value of the penetration depth exceeds the thickness of the film  $t$ , the effective penetration depth

is enhanced due to finite size effects ( $\lambda \rightarrow \frac{\lambda^2}{t}$  (see [Eq. \(11.3\)](#) and Refs. [271, 272]).

Such large values of penetration depth measured in B-diamond films make B-diamond an appealing material to be used in applications where large inductance is needed, such as microwave kinetic inductance detectors (MKID) or Superconducting Microresonator Bolometers [57].

# 12

---

## Conclusion and Outlook

---

In this thesis, I presented a complete set of experimental techniques and theoretical tools that I utilized to characterize the surface of SRF grade Nb cavity samples at microwave frequencies.

In [Chapter 3](#) I present the system we built to measure full-size SRF cavities at mK temperatures. The setup includes a novel liquid nitrogen precooling system and a cheap, yet effective magnetic shielding solution. This setup will be utilized by future generations of researchers in the Anlage Lab to measure the surface resistance of SRF cavities in otherwise inaccessible temperature ranges, and understand the origins of residual resistance in SRF cavities.

In [Chapter 4](#) I presented the Near-Field Magnetic MW Microscope, a tool that can be used to study the MW response of new superconducting materials that are being considered for usage in SRF applications, without the need to fabricate a full cavity. The nonlinear response data measured on SRF grade Nb and presented in [Chapter 5](#) shows an abundance of features in both the  $P_{3f}(T)$  and  $V_{3f}(H_{rf})$  data. The numerical RCSJ model that I developed and presented in [Chapter 6](#) provides an

accurate explanation for the periodicity in  $V_{3f}(H_{rf})$ . Using this model I was able to confirm and experimentally validate the existence of weak-links on the surface of Nb. Additionally, we can extract the  $T_c$  and the BCS gap  $\Delta(0)$  around these weak-links. We show that the BCS gap is suppressed at the location of the weak-link. The existence of such locations with the suppressed gap or even no gap was known from point-contact tunneling (PCT) spectroscopy measurements [273]. One of the key advantages of our technique is the fact that unlike PCT, the Near-Field Magnetic MW Microscope is insensitive to a thin insulating layer of  $\text{Nb}_2\text{O}_5$  which is known to be present on the surface of any SRF grade Nb samples. Finally, in [Chapter 10](#) I present the preliminary 2D-scan results and a line-scan over a grain boundary where we see the peak in  $P_{3f}$  as expected.

In [Chapters 7](#) and [8](#) I present the an analysis of vortex semiloops created by my magnetic writer probe. The nonlinear response generated by these vortices and the one measured from the experiment are in good agreement. This means that our Near-Field Magnetic MW Microscope can be used to create 2D maps of the local vortex nucleation field  $H_v(x, y)$ . Later, in [Chapter 9](#), I show that similar vortex semiloops can be created by small surface defects in the interior of SRF cavities. While illustrations of such vortex semiloops exist in the literature, this is the first full scale 3D-simulation of such vortices to the best of my knowledge. As a last step, in [Sec. 9.4](#) I describe the importance of considering several relaxation times and not anticipating a certain RF performance based on the DC measurement results. As my simulations indicate, there exists a time-barrier for vortex nucleation, similar to the Bean-Livingston barrier, that can shield the interior of the SRF cavity from magnetic vortices at sufficiently high

frequencies.

In [Chapter 11](#) I present the PPR technique, that can be used to measure the temperature dependent complex surface impedance of a thin film sample at GHz frequencies. This tool can be used to study the next generation of SIS multilayer film structures for use as SRF coatings, for example.

# APPENDIX A

---

## Magnetic Microscope Operation Manual

---

Here I provide a step by step instruction on how to correctly operate the Near-Field Magnetic MW Microscope described in [Sec. 4.6](#).

### A.1 Connecting to the writer head

First, one has to electrically connect the microwave source to the magnetic writer head. This can be achieved by soldering an SMA RF coaxial connector (Digi-Key P/N: SAM9950-ND) to the soldering pads at the end of the magnetic writer probe transmission line (pads 3 and 4 in [Fig. 4.5.\(b\)](#)). Alternatively, the RF connector can be soldered to the pins of a socket adapter (Digi-Key P/N: A881AR-ND) which has soldering pads that match the ones on the probe. It is important to use a lead-free solder, as lead is a superconductor with  $T_c = 7.2\text{K}$  and can generate nonlinear response that would contaminate the data.

To check the connection one should measure the resistance between the inner



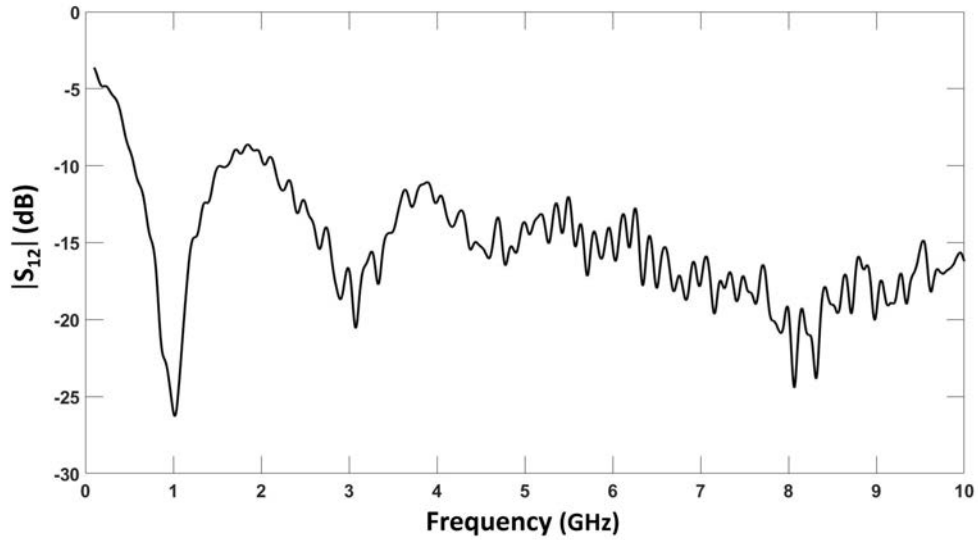


Fig. A.1 The reflection coefficient  $S_{11}(f)$  of the probe measured with a VNA at room temperature.

and the outer conductors of the SMA connector, which should result in a  $\simeq 6\Omega$  resistance at room temperature. Note that at cryogenic temperatures this resistance will decrease to  $\simeq 1\Omega$ . Additionally, one can measure the reflection coefficient  $S_{11}(f)$  of the probe using a Vector Network Analyzer (VNA).  $S_{11}(f)$  should have broad dips similar to the ones shown in [Figs. A.1](#) and [A.2](#).

## A.2 Choosing the measurement frequency

The magnetic writer probes used in this thesis ("Dragonfly" probe by Western Digital Corporation and typical perpendicular writer heads made by Seagate Technology) are designed to operate best in the 1-2 GHz frequency window. However, my

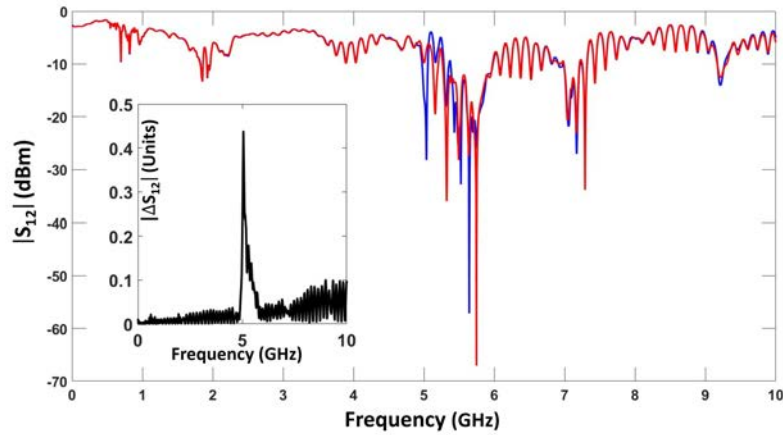


Fig. A.2 The reflection coefficient  $S_{11}(f)$  of the probe measured at  $T = 88\text{K}$  (blue) and  $T = 107\text{K}$  (red), below and above the  $T_c$  of the sample. In this measurement the probe is in contact with the BSCCO sample described in Sec. 10.1. The inset shows the amplitude of the complex difference  $\Delta S_{12}$  between these two measurements.

experience with these probes shows that there is an additional frequency window at 4-5.5GHz where I observed good coupling between the probe and the sample.

There are two methods employed to find the optimal measurement frequency. First the reflection coefficient  $S_{11}(f)$  of the probe is measured at two temperatures, one below and one above the critical temperature of the sample. The difference between these two reflection coefficients  $\Delta S_{12}(f) = |S_{12}(T = 88\text{K}) - S_{12}(T = 107\text{K})|$  can be attributed to the transition of the sample into the superconducting state and the frequency which corresponds to the maximum difference is the optimal frequency. For example, in Fig. A.2 the optimal frequency is  $f = 4.975\text{GHz}$ . Note that with newer versions of the probe that were made by Seagate Technology after 2016  $\Delta S_{12}(f)$  can be immeasurably small.

Another method is to perform a similar comparison, but with the third-harmonic

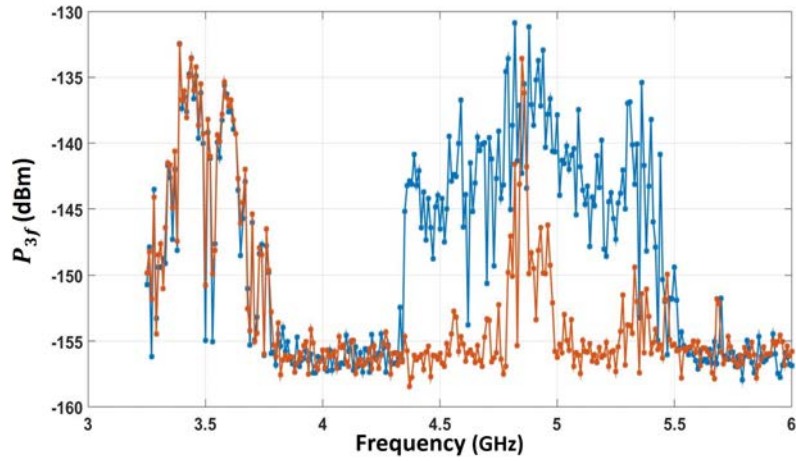


Fig. A.3 Third-harmonic response  $P_{3f}(f)$  measured on a bulk Nb sample at  $T = 8\text{K}$  (blue) and  $T = 10\text{K}$  (orange) below and above  $T_c$ . There is enhanced third harmonic response measured in the  $4.3\text{GHz} < f < 5.5\text{GHz}$  frequency window when the sample goes into the superconducting state.

response. Again,  $P_{3f}(f)$  is measured using the spectrum analyzer (for measurement setup refer to Fig. 4.13) at two temperatures, one below and one above the critical temperature of the sample. Fig. A.3 shows the third harmonic response  $P_{3f}$  vs frequency measured on a bulk Nb sample at  $T = 8\text{K}$  and  $T = 10\text{K}$ . Clearly, there is enhanced third harmonic response measured in the  $4.3\text{GHz} < f < 5.5\text{GHz}$  frequency window and in superconducting state. In this example  $f = 4.38\text{GHz}$  is chosen as the optimal measurement frequency.

## A.3 Finding optimal parameters

As I already discussed, each probe has its own optimal working frequency. In addition, as was described in [Sec. 10.3](#), there exist an optimal Z-position for measurement as well. Furthermore, there is the range of optimal excitation powers for the measurement, since if the input power is too low  $P_f < -40\text{dBm}$  the nonlinear response is very weak and below the noise floor of the spectrum analyzer, whereas if the input power is too high  $P_f > 10\text{dBm}$  the nonlinear response from the probe will overwhelm the signal from the sample. Adding to the challenge sometimes the  $T_c$  of the sample is unknown hence one doesn't know what range of temperatures to use for the measurement. The main question is how should one optimize all 4 parameters: Z-position, frequency input power and temperature?

Here is the method I utilized. First I do a quick survey of all parameters by performing quick measurements with a subset of parameters. For example for a Nb sample, I do measurements at  $T = 4\text{K}$ ,  $T = 6\text{K}$ ,  $T = 8\text{K}$  and  $T = 10\text{K}$ . For input power I use  $P_f = -5\text{dBm}$  and  $P_f = -15\text{dBm}$ , which from my experience is neither too high nor too low. Scanning the frequency is a bit more tricky. First I scan the 1 GHz to 2.2 GHz frequency window in 100 MHz steps. Additionally I scan the 4 GHz to 5.5 GHz window, again with 100 MHz steps. Note that to switch between these two windows, one has to physically change the low-pass and high-pass filters in [Fig. 4.13](#). And finally I perform a Z-position scan with  $20\mu\text{m}$  steps over the predetermined Z-position window. This window is determined at room temperature by identifying Z-

position values at which the probe is fully away from the sample (see Fig. 10.6(a)), and the probe is fully engaged with the sample (see Fig. 10.6(e)).

Later the data is analyzed to find the optimal frequency and Z-position for the measurement. Then one can proceed with  $P_{3f}$  vs temperature and input power measurement by scanning in input power and rastering in temperature.

## APPENDIX B

---

### Tuning Fork based Probe-Sample Distance Control

---

Here I summarize an attempt to develop a probe-sample separation feedback control to enable reproducible 2D scanning of the superconducting samples with the magnetic write head. This method was based on Tuning Fork (TF) Atomic Force Microscopy (AFM). In a TF AFM a sharp tip is attached to a TF made of a piezoelectric material such as quartz. An electrical signal can be used to drive this tuning fork to oscillate on its resonant frequency. When the tip is brought very close to the sample surface, it periodically contacts the surface. This interaction results in a shift in the resonant frequency which depends linearly on the tip-sample separation.

In our setup a commercially available Tuning Fork Sensor Controller from NanoAndMore [274] was used. I then integrated a Magnetic Writer onto the tuning fork in a well-known q-plus sensor design [275]. In this design one prong of the TF is fixed to a large substrate (in our case a large piece of MACOR ceramic) and the probe is attached to the other prong (see Fig. B.1). This arrangement allows one to use relatively large/massive probes.

The unloaded TF was first measured and found to have  $f_{res} = 99,922$  Hz and

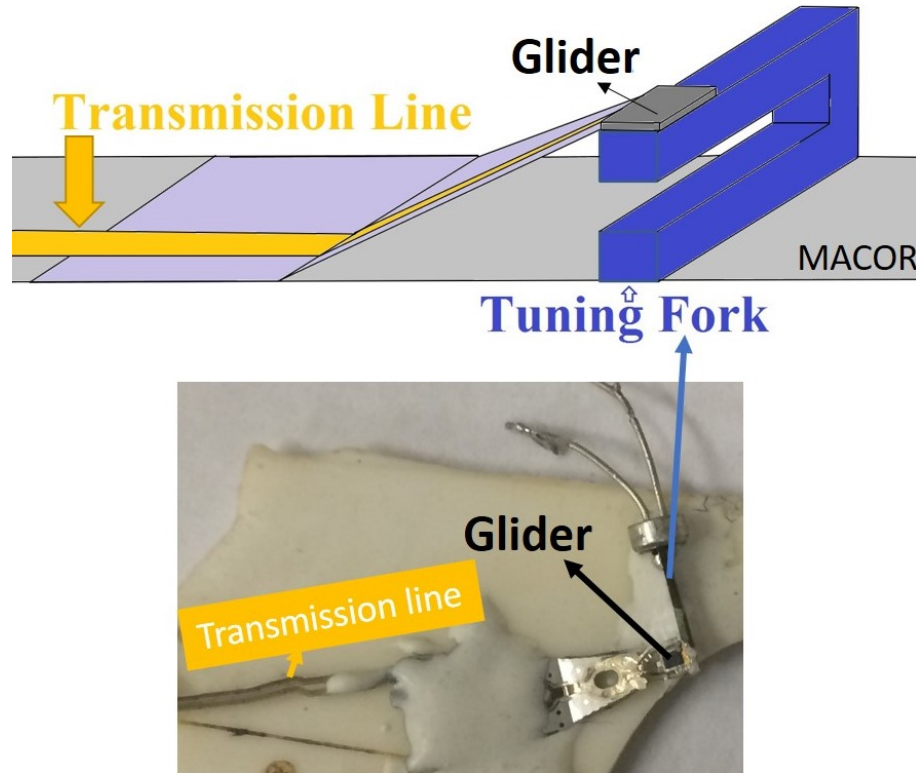


Fig. B.1 Magnetic writer head attached to a quartz Tuning Fork in a q-plus sensor design.

$Q = 2675$ . The Magnetic writer head was then attached to the TF in a q-plus sensor design. The resonant frequency and the quality factor of this sensor was measured to be  $f_{res} = 21,018$  Hz and  $Q = 106$  (see Fig. B.2). Such a low quality factor is reasonable given the size and mass of the magnetic writer head. We then encountered the following challenges:

1. The quality factor of the sensor is very low to the point that the controller cannot drive it to self-resonance. This can potentially be remedied by removing unnecessary parts of the probe.
2. The triangular frame hosting the transmission line acts like a mechanical anchor on the TF. An alternative electrical connection to the head is needed.

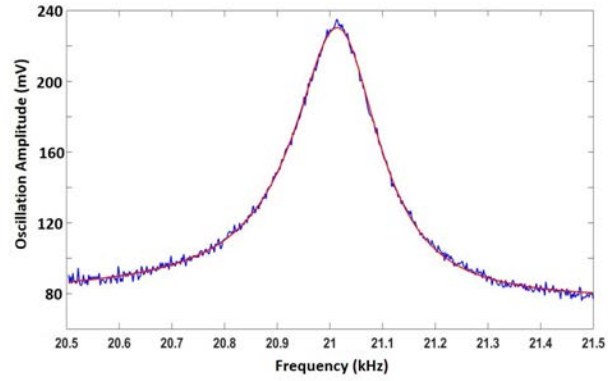


Fig. B.2 Fundamental tone of the sensor shown in Fig. B.1. Data shown in blue and a Lorentzian fit with  $f_{res} = 21,018$  Hz and  $Q = 106$  is shown in red.

3. The size of the actual writer pole is very small compared to the size of the probe (see Figs. 4.5 and 4.6). For this sensor to work the probe and the sample have to be extremely flat and perfectly aligned. Otherwise the writer pole will not come close enough to the sample to create a strong enough current and generate nonlinear response.



---

## Bibliography

---

- [1] D. van Delft and P. Kes, “The discovery of superconductivity,” [Physics Today](#) **63**, 38 (2010) (cited on pp. 1, 2).
- [2] R. de Bruyn Ouboter, “Heike Kamerlingh Onnes’s Discovery of Superconductivity,” [Scientific American](#) **276**, 98 (1997) (cited on p. 1).
- [3] Heike Kamerlingh Onnes, “Further experiments with liquid helium. H. On the electrical resistance of pure metals etc. VII. The potential difference necessary for the electric current through mercury below 4.19 K,” [Commun. Phys. Lab. Univ. Leiden](#) **133a** (1914) (cited on p. 2).
- [4] Heike Kamerlingh Onnes, “Further experiments with liquid helium. C. On the change of electric resistance of pure metals at very low temperatures etc. IV. The resistance of pure mercury at helium temperatures,” [Commun. Phys. Lab. Univ. Leiden](#) **120b** (1911), reprinted in *Proc. K. Ned. Akad. Wet.* 13, 1274 (1911). (Cited on p. 2).
- [5] Heike Kamerlingh Onnes, “Further experiments with Liquid Helium G. On the electrical resistance of Pure Metals etc. VI. On the Sudden Change in the Rate at which the Resistance of Mercury Disappears,” [Commun. Phys. Lab. Univ. Leiden](#) **122b** (1911), reprinted in *Proc. K. Ned. Akad. Wet.* 14, 113 (1911). (Cited on p. 2).

- [6] A. Einstein, “Die Plancksche Theorie der Strahlung und die Theorie der spezifischen Wärme,” [Annalen der Physik](#) **327**, 180 (1907) (cited on p. 2).
- [7] D. Goodstein and J. Goodstein, “Richard Feynman and the History of Superconductivity,” [Physics in Perspective](#) **2**, 30 (2000) (cited on pp. 2, 15, 16).
- [8] Heike Kamerlingh Onnes, “Sur les resistances electriques,” in [Proceedings, First Solvay Conference on Physics in Brussels](#) (1911) (cited on p. 2).
- [9] N. Straumann, “On the first Solvay Congress in 1911,” [European Physical Journal H](#) **36**, 379 (2011) (cited on p. 2).
- [10] Heike Kamerlingh Onnes, “Further experiments with liquid helium. II. On the electrical resistance etc. (continues). VIII. The sudden disappearance of the ordinary resistance of tin, and the super conductive state of lead,” [Commun. Phys. Lab. Univ. Leiden](#) **133d** (1914), reprinted in Proc. K. Ned. Akad. Wet. 16, 673 (1914). (Cited on p. 3).
- [11] R. P. Feynman, *Feynman Lectures on Physics Vol III*, edited by R. P. Feynman, R. B. Leighton, and M. Sands (Addison-Wesley, 1965), available at [https://www.feynmanlectures.caltech.edu/III\\_toc.html](https://www.feynmanlectures.caltech.edu/III_toc.html) (cited on pp. 4, 13).
- [12] W. Meissner and R. Ochsenfeld, “Ein neuer Effekt bei Eintritt der Supraleitfähigkeit,” [Naturwissenschaften](#) **21**, 787 (1933) (cited on p. 4).
- [13] C. Gorter and H. Casimir, “On supraconductivity I,” [Physica](#) **1**, 306 (1934) (cited on p. 5).

- [14] C. Gorter and H. Casimir, “The thermodynamics of the superconducting state,” *Z. Tech. Phys* **15**, 539 (1934) (cited on p. 5).
- [15] F. London and H. London, “Supraleitung und diamagnetismus,” *Physica* **2**, 341 (1935) (cited on pp. 6, 122).
- [16] F. London, H. London, and F. A. Lindemann, “The electromagnetic equations of the supraconductor,” *Proceedings of the Royal Society of London. Series A - Mathematical and Physical Sciences* **149**, 71 (1935) (cited on pp. 6, 122).
- [17] H. London and F. A. Lindemann, “Phase-equilibrium of supraconductors in a magnetic field,” *Proceedings of the Royal Society of London. Series A - Mathematical and Physical Sciences* **152**, 650 (1935) (cited on pp. 6, 122).
- [18] L. D. Landau and V. L. Ginzburg, “On the theory of superconductivity,” *Soviet Physics-JETP* **20**, 1064 (1950) (cited on pp. 8, 122).
- [19] F. London, “On the Problem of the Molecular Theory of Superconductivity,” *Phys. Rev.* **74**, 562 (1948) (cited on pp. 8, 11, 122).
- [20] B. Oripov and S. M. Anlage, “Time-dependent Ginzburg-Landau treatment of rf magnetic vortices in superconductors: Vortex semiloops in a spatially nonuniform magnetic field,” *Phys. Rev. E* **101**, 33306 (2020) (cited on pp. 9, 147, 163, 170, 171).
- [21] L. P. Gor’kov, “Microscopic derivation of the Ginzburg-Landau equations in the Theory of Superconductivity,” *Soviet Physics-JETP* **36(9)**, 4 (1959) (cited on pp. 9, 126–128, 132, 135).

- [22] A. B. Pippard and W. L. Bragg, “An experimental and theoretical study of the relation between magnetic field and current in a superconductor,” [Proceedings of the Royal Society of London. Series A. Mathematical and Physical Sciences](#) **216**, 547 (1953) (cited on p. 10).
- [23] B. S. Deaver and W. M. Fairbank, “Experimental Evidence for Quantized Flux in Superconducting Cylinders,” [Phys. Rev. Lett.](#) **7**, 43 (1961) (cited on p. 11).
- [24] R Doll and M Näbauer, “Experimental Proof of Magnetic Flux Quantization in a Superconducting Ring,” [Phys. Rev. Lett.](#) **7**, 51 (1961) (cited on p. 11).
- [25] *Applied Superconductivity and Cryoscience Group, University of Cambridge, Department of Materials Science and Metallurgy*, <https://ascg.msm.cam.ac.uk/> (cited on p. 12).
- [26] A. A. Abrikosov, “The magnetic properties of superconducting alloys,” [Journal of Physics and Chemistry of Solids](#) **2**, 199 (1957) (cited on pp. 13, 122, 134).
- [27] J. Bardeen and M. J. Stephen, “Theory of the Motion of Vortices in Superconductors,” [Phys. Rev.](#) **140**, A1197 (1965) (cited on pp. 13, 147).
- [28] N. B. Kopnin, “Vortex dynamics and mutual friction in superconductors and Fermi superfluids,” [Reports on Progress in Physics](#) **65**, 1633 (2002) (cited on pp. 13, 147, 148).
- [29] B. D. Josephson, “Possible new effects in superconductive tunnelling,” [Physics Letters](#) **1**, 251 (1962) (cited on pp. 13, 122).

- [30] J. Schmalian, “Failed Theories of Superconductivity,” [Modern Physics Letters B 24, 2679 \(2010\)](#) (cited on p. 16).
- [31] A. Einstein, “Theoretische Bemerkungen zur Supraleitung der Metalle,” (1922), English translation is available on <https://arxiv.org/abs/physics/0510251> (cited on p. 16).
- [32] C. A. Reynolds, B. Serin, W. H. Wright, and L. B. Nesbitt, “Superconductivity of Isotopes of Mercury,” [Phys. Rev. 78, 487 \(1950\)](#) (cited on p. 16).
- [33] E. Maxwell, “Isotope Effect in the Superconductivity of Mercury,” [Phys. Rev. 78, 477 \(1950\)](#) (cited on p. 16).
- [34] J. Bardeen and D. Pines, “Electron-Phonon Interaction in Metals,” [Phys. Rev. 99, 1140 \(1955\)](#) (cited on p. 17).
- [35] L. N. Cooper, “Bound Electron Pairs in a Degenerate Fermi Gas,” [Phys. Rev. 104, 1189 \(1956\)](#) (cited on p. 17).
- [36] M. Tinkham, *Introduction to Superconductivity*, 2nd ed. (Dover Publications, Inc., Mineola, New York, 2004) (cited on pp. 17, 35, 119, 126, 135, 142–144, 174, 183, 193).
- [37] B. Mitrović, H. G. Zarate, and J. P. Carbotte, “The ratio  $\frac{2\Delta_0}{k_B T_c}$  within Eliashberg theory,” [Phys. Rev. B 29, 184 \(1984\)](#) (cited on p. 20).
- [38] P. Seidel, ed., *Applied Superconductivity: Handbook on Devices and Applications*, Vol. 2 (WILEY-VCH Verlag GmbH & Co. KGaA, 2015) (cited on p. 21).

- [39] *Technological applications of superconductivity*. McGraw-Hill Concise Encyclopedia of Physics. (2002), <https://encyclopedia2.thefreedictionary.com/Technological+applications+of+superconductivity>, Accessed: 2020-04-30 (cited on p. 21).
- [40] ATLAS Collaboration, "Observation of a new particle in the search for the standard model higgs boson with the atlas detector at the lhc," *Physics Letters B* **716**, 1 (2012) (cited on p. 22).
- [41] ATLAS and CMS collaborations, "CERN experiments observe particle consistent with long-sought Higgs boson," *July 4, 2012 Press Release* (cited on p. 22).
- [42] ATLAS and CMS collaborations, "New results indicate that particle discovered at CERN is a Higgs boson," *March 14, 2013 Press Release* (cited on p. 22).
- [43] M. K. Gaillard, P. D. Grannis, and F. J. Sciulli, "The standard model of particle physics," *Rev. Mod. Phys.* **71**, S96 (1999) (cited on p. 22).
- [44] B. Barish and J. E. Brau, "The International Linear Collider," *International Journal of Modern Physics A* **28**, 1330039 (2013) (cited on pp. 22, 23).
- [45] O. M. Gomez, *Five mysteries the standard model can't explain*, Symmetry Magazine, (2018) <https://www.symmetrymagazine.org/article/five-mysteries-the-standard-model-cant-explain> (visited on 04/03/2020) (cited on p. 22).
- [46] B. Greene, *How the Higgs Boson was found*, Smithsonian Magazine, (2013) <https://www.smithsonianmag.com/science-nature/how-the-higgs-boson-was-found-4723520/> (visited on 04/03/2020) (cited on p. 22).

- [47] P. Bambade *et al.*, “The International Linear Collider: A Global Project,” [Technical Report \(2019\)](#), doi: 10.2172/1527401 (cited on p. 23).
- [48] B. Barish, *Superconducting RF Cavities and Future Particle Accelerators*, Applied Superconductivity Conference (ASC), (2018) <https://ieeetv.ieee.org/conference-highlights/superconducting-rf-cavities-future-particle-accelerators> (cited on p. 23).
- [49] *Fermilab ILC–SRF R&D webpage*, <https://ilc.fnal.gov/ilc-srf.html> (cited on p. 24).
- [50] T. Behnke, J. E. Brau, B. Foster, J. Fuster, M. Harrison, J. M. Paterson, M. Peskin, M. Stanitzki, N. Walker, and H. Yamamoto, “The international linear collider technical design report-volume 1: Executive summary,” [ArXiv preprint: 1306.6327 \(2013\)](#) (cited on p. 23).
- [51] B. Aune *et al.*, “Superconducting TESLA cavities,” [Physical Review Special Topics - Accelerators and Beams](#) **3**, 092001 (2000) (cited on pp. 23, 24, 27, 28, 49, 117).
- [52] *International Linear Collider reference design report vol 3: accelerator p 157*, [http://ilcdoc.linearcollider.org/record/6321/files/ILC\\_RDR\\_Volume\\_3-Accelerator.pdf](http://ilcdoc.linearcollider.org/record/6321/files/ILC_RDR_Volume_3-Accelerator.pdf), Accessed: 2019-03-01, 2007 (cited on p. 23).
- [53] *International linear collider website*, <https://ilchome.web.cern.ch/ilc/facts-and-figures>, Accessed: 2019-03-01 (cited on p. 23).
- [54] W Singer, “SRF Cavity Fabrication and Materials,” [CERN Yellow Report CERN-2014-005](#), edited by R. Bailey, 171 (2015) (cited on pp. 24, 166).

- [55] J. P. Turneaure, J. Halbritter, and H. A. Schwettman, “The surface impedance of superconductors and normal conductors: The Mattis-Bardeen theory,” [Journal of Superconductivity](#) **4**, 341 (1991) (cited on p. 26).
- [56] A. Gurevich, “Theory of RF superconductivity for resonant cavities,” [Superconductor Science and Technology](#) **30**, 034004 (2017) (cited on pp. 26, 33, 140, 145, 148).
- [57] J. Zmuidzinas, “Superconducting Microresonators: Physics and Applications,” [Annual Review of Condensed Matter Physics](#) **3**, 169 (2012) (cited on pp. 26, 238, 243).
- [58] H. Padamsee, J. Knobloch, and T. Hays, *RF Superconductivity for Accelerators*, 2nd ed. (WILEY-VCH Verlag GmbH & Co. KGaA, Mörlenbach, Germany, 2008) (cited on pp. 28, 55).
- [59] S. Calatroni, M. Arzeo, S. Aull, M. Himmerlich, P. Costa Pinto, W. Vollenberg, B. Di Girolamo, P. Cruikshank, P. Chiggiato, D. Bajek, S. Wackerow, and A. Abdolvand, “Cryogenic surface resistance of copper: Investigation of the impact of surface treatments for secondary electron yield reduction,” [Phys. Rev. Accel. Beams](#) **22**, 63101 (2019) (cited on p. 28).
- [60] D. J. Goldie and S. Withington, “Non-equilibrium superconductivity in quantum-sensing superconducting resonators,” [Superconductor Science and Technology](#) **26**, 15004 (2012) (cited on p. 28).



- [61] T. Kubo and A. Gurevich, “Field-dependent nonlinear surface resistance and its optimization by surface nanostructuring in superconductors,” [Phys. Rev. B](#) **100**, 064522 (2019) (cited on pp. 28, 135).
- [62] A. Romanenko and D. I. Schuster, “Understanding Quality Factor Degradation in Superconducting Niobium Cavities at Low Microwave Field Amplitudes,” [Phys. Rev. Lett.](#) **119**, 264801 (2017) (cited on pp. 28, 33).
- [63] A. Romanenko, R. Pilipenko, S. Zorzetti, D. Frolov, M. Awida, S. Belomestnykh, S. Posen, and A. Grassellino, “Three-Dimensional Superconducting Resonators at  $T < 20$  mK with Photon Lifetimes up to  $\tau = 2$  s,” [Phys. Rev. Applied](#) **13**, 34032 (2020), doi: 10.1103/PhysRevApplied.13.034032 (cited on p. 28).
- [64] A. Gurevich and T. Kubo, “Surface impedance and optimum surface resistance of a superconductor with an imperfect surface,” [Phys. Rev. B](#) **96**, 184515 (2017) (cited on pp. 29, 35, 37, 135).
- [65] R. C. Dynes, V. Narayanamurti, and J. P. Garno, “Direct Measurement of Quasiparticle-Lifetime Broadening in a Strong-Coupled Superconductor,” [Phys. Rev. Lett.](#) **41**, 1509 (1978) (cited on pp. 29, 36, 135).
- [66] J. Knobloch, “The “Q disease“ in Superconducting Niobium RF Cavities,” [AIP Conference Proceedings](#) **671**, 133 (2003), doi: 10.1063/1.1597364 (cited on p. 30).
- [67] J. Halbritter, P. Kneisel, and K. Saito, “Additional Losses in High Purity Niobium Cavities related to Slow Cooldown and Hydrogen Segregation,” in [6th rf superconductivity workshop](#) (1993) (cited on pp. 30, 31).

- [68] F. Barkov, A. Romanenko, and A. Grassellino, “Direct observation of hydrides formation in cavity-grade niobium,” [Phys. Rev. ST Accel. Beams](#) **15**, 122001 (2012) (cited on p. 30).
- [69] A. Gurevich and G. Ciovati, “Dynamics of vortex penetration, jumpwise instabilities, and nonlinear surface resistance of type-II superconductors in strong RF fields,” [Phys. Rev. B](#) **77**, 104501 (2008) (cited on pp. 32, 33, 163, 182).
- [70] P. Dhakal, G. Ciovati, and A. Gurevich, “Flux expulsion in niobium superconducting radio-frequency cavities of different purity and essential contributions to the flux sensitivity,” [Phys. Rev. Accel. Beams](#) **23**, 23102 (2020) (cited on p. 32).
- [71] M. Martinello, M. Checchin, A. Grassellino, O. Melnychuk, S. Posen, A. Romanenko, D. A. Sergatskov, and J. F. Zasadzinski, “Trapped Flux Surface Resistance Analysis for Different Surface Treatments,” in [Proceedings, 17th International Conference on RF Superconductivity \(SRF2015\)](#), MOPB015 (cited on p. 32).
- [72] M. Checchin, M. Martinello, A. Grassellino, A. Romanenko, and J. F. Zasadzinski, “Electron mean free path dependence of the vortex surface impedance,” [Superconductor Science and Technology](#) **30**, 34003 (2017) (cited on pp. 32, 145, 151).
- [73] A. Romanenko, A. Grassellino, O. Melnychuk, and D. A. Sergatskov, “Dependence of the residual surface resistance of superconducting radio frequency

- cavities on the cooling dynamics around  $T_c$ ,” [J. Appl. Phys](#) **115**, 184903 (2014) (cited on p. 32).
- [74] M. Ge, G. Wu, D. Burk, J. Ozelis, E. Harms, D. A. Sergatskov, D. Hicks, and L. D. Cooley, “Routine characterization of 3D profiles of SRF cavity defects using replica techniques,” [Superconductor Science and Technology](#) **24**, 35002 (2010) (cited on p. 32).
- [75] Y. Iwashita, Y. Tajima, and H. Hayano, “Development of high resolution camera for observations of superconducting cavities,” [Phys. Rev. ST Accel. Beams](#) **11**, 93501 (2008) (cited on pp. 32, 33).
- [76] J. Knobloch, H. Muller, and H. Padamsee, “Design of a high speed, high resolution thermometry system for 1.5 GHz superconducting radio frequency cavities,” [Review of Scientific Instruments](#) **65**, 3521 (1994) (cited on p. 32).
- [77] A. Canabal, J. D. Bowyer, P. Chacon, N. A. Gillespie, M. A. Madrid, and T. Tajima, “Development of a temperature mapping system for 1.3-GHz 9-cell SRF cavities,” in [2007 IEEE Particle Accelerator Conference \(PAC\)](#) (2007), pp. 2406–2408 (cited on p. 32).
- [78] K Watanabe, “Review of optical inspection methods and results,” in [Proceedings, 14th international conference on rf superconductivity](#) (SRF, 2009), TUOBAU01 (cited on pp. 32, 33).
- [79] T. Kubo, “Magnetic field enhancement at a pit on the surface of a superconducting accelerating cavity,” [Progress of Theoretical and Experimental Physics](#) **2015**, 073G01 (2015) (cited on p. 33).

- [80] H. Safa, D. Moffat, B. Bonin, and F. Koechlin, “Advances in the purification of niobium by solid state gettering with titanium,” [Journal of Alloys and Compounds](#) **232**, 281 (1996) (cited on p. 33).
- [81] O. Malyshev, K. Dumbell, A. Gurevich, L. Gurrán, N. Pattalwar, S. Pattalwar, and R. Valizadeh, “First Results of Magnetic Field Penetration Measurements on Multilayer S-I-S Structures,” in [Proceedings 7th international particle accelerator conference \(ipac 2016\)](#): (2016), WEPMB057, doi: 10.18429/JACoW-IPAC2016-WEPMB057 (cited on p. 33).
- [82] X. Zhao, G. Ciovati, and T. R. Bieler, “Characterization of etch pits found on a large-grain bulk niobium superconducting radio-frequency resonant cavity,” [Phys. Rev. ST Accel. Beams](#) **13**, 124701 (2010) (cited on p. 33).
- [83] Y. Trenikhina, A. Romanenko, J. Kwon, J.-M. Zuo, and J. F. Zasadzinski, “Nanos-structural features degrading the performance of superconducting radio frequency niobium cavities revealed by transmission electron microscopy and electron energy loss spectroscopy,” [Journal of Applied Physics](#) **117**, 154507 (2015) (cited on p. 33).
- [84] A. V. Gurevich, “Multiscale mechanisms of SRF breakdown,” [Physica C: Superconductivity and its Applications](#) **441**, 38 (2006) (cited on p. 33).
- [85] S. Posen and D. L. Hall, “Nb<sub>3</sub>Sn superconducting radiofrequency cavities: fabrication, results, properties, and prospects,” [Superconductor Science and Technology](#) **30**, 33004 (2017) (cited on p. 34).

- [86] A. Gurevich, “Enhancement of rf breakdown field of superconductors by multilayer coating,” *Applied Physics Letters* **88**, 12511 (2006) (cited on p. 34).
- [87] *Low temperature properties of materials*, [https://uspas.fnal.gov/materials/10MIT/Lecture\\_1.2.pdf](https://uspas.fnal.gov/materials/10MIT/Lecture_1.2.pdf) (cited on p. 38).
- [88] *Metglas data sheet*, <https://metglas.com/wp-content/uploads/2017/09/SDS-for-Metglas-2605SA1-2605HB1M-and-2605SC.pdf> (cited on p. 46).
- [89] G. Wu, S. Aderhold, S. K. Chandrasekaran, A. Crawford, A. Grassellino, C. Grimm, J. Ozelis, D. A. Sergatskov, and A. Vostrikov, “Magnetic Foils for SRF Cryomodule,” in *Proceedings, 17th International Conference on RF Superconductivity (SRF2015): Whistler, Canada, September 13-18, 2015* (2015), TUPB099 (cited on p. 46).
- [90] C. Häussler, J Oppenländer, and N Schopohl, “Nonperiodic flux to voltage conversion of series arrays of dc superconducting quantum interference devices,” *Journal of Applied Physics* **89**, 1875 (2001) (cited on p. 47).
- [91] J. Knobloch, “Basic Concepts of Measurements Made on Superconducting RF Cavities,” *Cornell University, SRF Group, internal report SRF 910927-07* (1991) (cited on p. 51).
- [92] T. Powers, “Theory and Practice of Cavity RF Test Systems,” English, in *Proceedings, 12th International Conference on RF Superconductivity (SRF2005): Ithaca, Canada, New York, July 10-15, 2005* (2005) (cited on p. 51).
- [93] G Binnig, H Rohrer, C. Gerber, and E Weibel, “Surface Studies by Scanning Tunneling Microscopy,” *Phys. Rev. Lett.* **49**, 57 (1982) (cited on p. 64).

- [94] H. K. Wickramasinghe, “Progress in scanning probe microscopy,” [Acta Materialia](#) **48**, 347 (2000) (cited on p. 64).
- [95] J. D. Jackson, *Classical Electrodynamics* (Wiley, 1999) (cited on p. 65).
- [96] S. M. Anlage, D. E. Steinhauer, B. J. Feenstra, C. P. Vlahacos, and F. C. Wellstood, “Near-Field Microwave Microscopy of Materials Properties,” in [Microwave Superconductivity](#), edited by H. Weinstock and M. Nisenoff (Springer Netherlands, Dordrecht, 2001), pp. 239–269 (cited on p. 65).
- [97] S. M. Anlage, V. V. Talanov, and A. R. Schwartz, “Principles of Near-Field Microwave Microscopy,” in [Scanning probe microscopy: electrical and electromechanical phenomena at the nanoscale](#), edited by S. Kalinin and A. Gruverman (Springer New York, New York, NY, 2007), pp. 215–253 (cited on p. 65).
- [98] D. I. Mircea, “Measurements of doping-dependent microwave nonlinear response in cuprate superconductors,” [PhD dissertation \(University of Maryland, 2007\)](#) (cited on pp. 66, 71).
- [99] Y. Cho and K. Ohara, “Higher-order nonlinear dielectric microscopy,” [Applied Physics Letters](#) **79**, 3842 (2001) (cited on p. 67).
- [100] T. Dahm and D. J. Scalapino, “Theory of microwave intermodulation in a high- $T_c$  superconducting microstrip resonator,” [Applied Physics Letters](#) **69**, 4248 (1996), doi: 10.1063/1.116960 (cited on pp. 67, 68).
- [101] B. A. Willemsen, K. E. Kihlstrom, T. Dahm, D. J. Scalapino, B. Gowe, D. A. Bonn, and W. N. Hardy, “Microwave loss and intermodulation in  $Tl_2Ba_2CaCu_2O_y$  thin films,” [Phys. Rev. B](#) **58**, 6650 (1998) (cited on p. 67).

- [102] S.-C. Lee and S. M. Anlage, "Spatially-resolved nonlinearity measurements of  $\text{YBa}_2\text{Cu}_3\text{O}_{7-\delta}$  bicrystal grain boundaries," [Applied Physics Letters](#) **82**, 1893 (2003) (cited on pp. 68, 70).
- [103] S.-C. Lee, "Measurements of Doping-Dependent Microwave Nonlinearities in High-Temperature Superconductors," [PhD dissertation \(University of Maryland, 2004\)](#) (cited on pp. 68, 71).
- [104] T. Tai, "Measuring Electromagnetic Properties of Superconductors in High and Localized RF Magnetic Field," [PhD dissertation \(University of Maryland, 2013\)](#) (cited on pp. 68, 71, 74, 170, 197, 198).
- [105] S.-C. Lee, M. Sullivan, G. R. Ruchti, S. M. Anlage, B. S. Palmer, B. Maiorov, and E. Osquiguil, "Doping-dependent nonlinear Meissner effect and spontaneous currents in high- $T_c$  superconductors," [Phys. Rev. B](#) **71**, 14507 (2005) (cited on pp. 68, 91, 105).
- [106] J. C. Booth, L. R. Vale, and R. H. Ono, "On-wafer measurements of nonlinear effects in high temperature superconductors," [IEEE Transactions on Applied Superconductivity](#) **11**, 1387 (2001) (cited on p. 68).
- [107] D. E. Oates, Y. D. Agassi, and B. H. Moeckly, "Intermodulation Distortion and Nonlinearity in  $\text{MgB}_2$ : Experiment and Theory," [IEEE Transactions on Applied Superconductivity](#) **17**, 2871 (2007) (cited on pp. 69, 70).
- [108] D. E. Oates, "Overview of Nonlinearity in HTS: What We Have Learned and Prospects for Improvement," [Journal of Superconductivity and Novel Magnetism](#) **20**, 3 (2007) (cited on p. 69).

- [109] D. I. Mircea, H. Xu, and S. M. Anlage, “Phase-sensitive harmonic measurements of microwave nonlinearities in cuprate thin films,” *Phys. Rev. B* **80**, 144505 (2009) (cited on pp. 71, 93).
- [110] T. Tai, B. G. Ghamsari, and S. M. Anlage, “Modeling the nanoscale linear response of superconducting thin films measured by a scanning probe microwave microscope,” *J. Appl. Phys* **115**, 203908 (2014) (cited on p. 71).
- [111] S Granz, M Conover, J Guzman, W Cross, P Harlee, and T Rausch, “Perpendicular Interlaced Magnetic Recording,” *IEEE Transactions on Magnetics* **55**, 1 (2019) (cited on p. 73).
- [112] B. Stipe, “The Magnetic Hard Disk Drive - How Information is Stored in the Cloud,” in APS March Meeting (2018), Presented at the annual APS March Meeting, Los Angeles, CA, March 5-9 2018, available online at <https://www.youtube.com/watch?v=faUZZLSwdKA> (cited on p. 74).
- [113] M. R. Koblischka, J. D. Wei, and U. Hartmann, “High-frequency properties of stray fields emanating from hard disk writer poles up to 2GHz,” *Journal of Magnetism and Magnetic Materials* **322**, 1694 (2010) (cited on p. 74).
- [114] I. Jakobi, P. Neumann, Y. Wang, D. Bhaktavatsala, R. Dasari, F. E. Hallak, M. A. Bashir, M. Markham, A. Edmonds, D. Twitchen, and J. Wrachtrup, “Measuring broadband magnetic fields on the nanoscale using a hybrid quantum register,” *Nature Nanotech* **12**, 67 (2017) (cited on pp. 74, 78).
- [115] H Jonathon Mamin, “New life for hard-disk write heads,” *Nature Nanotech* **12**, 5 (2017) (cited on pp. 74, 78).



- [116] S. Russek, I. Haygood, E. Edwards, M. Schneider, A. Fox, P. Dresselhaus, P. Hopkins, W. Rippard, and S. Benz, “High Resolution Imaging of Supercurrents with Magnetic Recording Heads,” in [2018 Applied Superconductivity Conference](#) (ASC, 2018), 4EOr2A–02 (cited on p. 74).
- [117] W. Si, Y. Hong, Z. Bai, Y. Huang, F. Liu, H. Zhang, Z. Jikou, X. Yang, Y. Yao, I. Zana, *et al.*, *Process for manufacturing a perpendicular magnetic recording writer pole with nonmagnetic bevel*, 2014, US Patent 8,628,672 available online at <https://patents.google.com/patent/US8628672B1/en>. (Cited on pp. 78, 79).
- [118] S. Narayana, *Stray field shielding for perpendicular magnetic recording write head*, 2016, US Patent 9,269,378 available online at <https://patents.google.com/patent/US9269378B2/en>. (Cited on pp. 78, 79).
- [119] E. C. Stoner and E. P. Wohlfarth, “A mechanism of magnetic hysteresis in heterogeneous alloys,” [Philosophical Transactions of the Royal Society of London. Series A, Mathematical and Physical Sciences](#) **240**, 599 (1948) (cited on p. 80).
- [120] G. Terenziani, S. Calatroni, and A. Ehasarian, “Niobium Coatings for Superconducting RF Applications by HIPIMS,” in [Proceedings 4th international conference on fundamentals and industrial applications of hipims](#): (2012), doi: 10.13140/2.1.2837.9846 (cited on pp. 88, 89).
- [121] T. Junginger, S. Calatroni, A. Sublet, G. Terenziani, T. Prokscha, Z. Salman, A. Suter, T. Proslie, and J. F. Zasadzinski, “A low energy muon spin rotation and point contact tunneling study of niobium films prepared for superconducting

- cavities,” [Superconductor Science and Technology](#) **30**, 125013 (2017), doi: 10.1088/1361-6668/aa8926 (cited on pp. 88, 89).
- [122] T. R. Bieler, N. T. Wright, F. Pourboghrat, C. C. Compton, K. T. Hartwig, D. C. Baars, A. Zamiri, S. Chandrasekaran, P. Darbandi, H. Jiang, E. Skoug, S. Balachandran, G. E. Ice, and W. Liu, “Physical and mechanical metallurgy of high purity Nb for accelerator cavities,” [Phys. Rev. ST Accel. Beams](#) **13**, 031002 (2010) (cited on pp. 88, 95, 96).
- [123] D. C. Baars, “Investigation of active slip systems in high purity single crystal Nb,” [PhD dissertation \(Michigan State University, 2013\)](#), page 110 (cited on pp. 88, 96).
- [124] P. Dhakal, S. Chetri, S. Balachandran, P. J. Lee, and G. Giovati, “Effect of low temperature baking in nitrogen on the performance of a niobium superconducting radio frequency cavity,” [Phys. Rev. Accel. Beams](#) **21**, 32001 (2018) (cited on pp. 88, 101).
- [125] S. Wilde, R. Valizadeh, O. B. Malyshev, G. B. G. Stenning, T. Sian, and B. Chesca, “Dc Magnetometry of Nb Thin Film Superconductors deposited using High Power Impulse Magnetron Sputtering,” [Phys. Rev. Accel. Beams](#) **21**, 73101 (2018) (cited on pp. 88, 101).
- [126] A.-M. Valente-Feliciano, “Development of SRF thin film materials for monolayer/multilayer approach to increase the performance of SRF accelerating structures beyond bulk Nb,” [PhD dissertation \(University of Paris, 2014\)](#) (cited on pp. 88, 103, 117).

- [127] A. Anders, “Tutorial: Reactive high power impulse magnetron sputtering (R-HiPIMS),” [Journal of Applied Physics](#) **121**, 171101 (2017) (cited on p. 89).
- [128] T. Tai, X. X. Xi, C. G. Zhuang, D. I. Mircea, and S. M. Anlage, “Nonlinear Near-Field Microwave Microscope for RF Defect Localization in Superconductors,” [IEEE Transactions on Applied Superconductivity](#) **21**, 2615 (2011) (cited on pp. 93, 210).
- [129] T. Tai, B. G. Ghamsari, T. R. Bieler, and S. M. Anlage, “Nanoscale nonlinear radio frequency properties of bulk Nb: Origins of extrinsic nonlinear effects,” [Phys. Rev. B](#) **92**, 134513 (2015) (cited on pp. 95, 108, 117).
- [130] T. Tai, B. G. Ghamsari, and S. M. Anlage, “Nanoscale Electrodynamic Response of Nb Superconductors,” [IEEE Transactions on Applied Superconductivity](#) **23**, 7100104 (2013) (cited on p. 105).
- [131] H. Ito, H. Hayano, T. Kubo, T. Saeki, R. Katayama, Y. Iwashita, H. Tongu, R. Ito, T. Nagata, and C. Z. Antoine, “Lower critical field measurement of NbN multilayer thin film superconductor at KEK,” [ArXiv preprint: 1907.03410](#) (2019) (cited on p. 106).
- [132] C. Z. Antoine, M. Aburas, A. Four, F. Weiss, Y. Iwashita, H. Hayano, S. Kato, T. Kubo, and T. Saeki, “Optimization of tailored multilayer superconductors for RF application and protection against premature vortex penetration,” [Superconductor Science and Technology](#) **32**, 085005 (2019), doi: 10.1088/1361-6668/ab1bf1 (cited on pp. 106, 182).

- [133] J. Halbritter, “On the oxidation and on the superconductivity of niobium,” [Applied Physics A](#) **43**, 1 (1987) (cited on pp. 107, 108, 119).
- [134] J. Halbritter, “Transport in superconducting niobium films for radio frequency applications,” [Journal of Applied Physics](#) **97**, 83904 (2005) (cited on p. 107).
- [135] K. E. Yoon, D. N. Seidman, C. Z. Antoine, and P. Bauer, “Atomic-scale chemical analyses of niobium oxide/niobium interfaces via atom-probe tomography,” [Applied Physics Letters](#) **93**, 132502 (2008) (cited on p. 107).
- [136] C Nico, T Monteiro, and M. P. F. Graça, “Niobium oxides and niobates physical properties: Review and prospects,” [Progress in Materials Science](#) **80**, 1 (2016) (cited on p. 107).
- [137] A. M. Portis, *Electrodynamics of High-Temperature Superconductors* (World Scientific, Singapore, 1993) (cited on p. 108).
- [138] L. M. Xie, J. Wosik, and J. C. Wolfe, “Nonlinear microwave absorption in weak-link Josephson junctions,” [Phys. Rev. B](#) **54**, 15494 (1996) (cited on p. 108).
- [139] J. McDonald and J. R. Clem, “Microwave response and surface impedance of weak links,” [Phys. Rev. B](#) **56**, 14723 (1997) (cited on pp. 108, 109).
- [140] Z. Zhai, P. V. Parimi, and S. Sridhar, “Nonlinear microwave impedance of short and long Josephson junctions,” [Phys. Rev. B](#) **59**, 9573 (1999) (cited on p. 108).
- [141] A. Sheikhzada and A. V. Gurevich, “Nonlinear dynamics of Josephson vortices in a film screen under dc and ac magnetic fields,” [Physica C: Superconductivity and its Applications](#) **506**, 59 (2014) (cited on p. 108).

- [142] B. Oripov, T. R. Bieler, G. Ciovati, S. Calatroni, P. Dhakal, T. Junginger, O. B. Malyshev, G. Terenziani, A.-M. Valente-Feliciano, R. Valizadeh, S. Wilde, and S. M. Anlage, “High-Frequency Nonlinear Response of Superconducting Cavity-Grade Nb Surfaces,” [Physical Review Applied](#) **11**, 64030 (2019) (cited on p. 108).
- [143] H. Xin, D. E. Oates, S. Sridhar, G. Dresselhaus, and M. S. Dresselhaus, “Observation of individual Josephson vortices in  $\text{YBa}_2\text{Cu}_3\text{O}_{7-\delta}$  bicrystal grain-boundary junctions,” [Phys. Rev. B](#) **61**, R14952 (2000) (cited on p. 108).
- [144] S.-C. Lee, S.-Y. Lee, and S. M. Anlage, “Microwave nonlinearities of an isolated long  $\text{YBa}_2\text{Cu}_3\text{O}_{7-\delta}$  bicrystal grain boundary,” [Phys. Rev. B](#) **72**, 24527 (2005) (cited on p. 108).
- [145] V. Ambegaokar and A. Baratoff, “Tunneling Between Superconductors,” [Phys. Rev. Lett.](#) **10**, 486 (1963) (cited on p. 119).
- [146] V. Ambegaokar and A. Baratoff, “Erratum to Tunneling Between Superconductors,” [Phys. Rev. Lett.](#) **11**, 104 (1963) (cited on p. 119).
- [147] T. Proslir, J. F. Zasadzinski, L. D. Cooley, C. Z. Antoine, J. Moore, J. Norem, M. Pellin, and K. E. Gray, “Tunneling study of cavity grade Nb: Possible magnetic scattering at the surface,” [Applied Physics Letters](#) **92**, 212505 (2008) (cited on pp. 119, 135).
- [148] J. Wei, G. Sheet, and V. Chandrasekhar, “Possible microscopic origin of large broadening parameter in point Andreev reflection spectroscopy,” [Applied Physics Letters](#) **97**, 62507 (2010) (cited on p. 119).

- [149] D. A. Jacobson, “Ginzburg-Landau Equations and the Josephson Effect,” [Phys. Rev. \*\*138\*\*, A1066 \(1965\)](#) (cited on p. [122](#)).
- [150] V. L. Ginzburg and L. D. Landau, “On the Theory of Superconductivity,” in [On superconductivity and superfluidity: a scientific autobiography](#) (Springer Berlin Heidelberg, 2009), pp. 113–137 (cited on p. [123](#)).
- [151] L. P. Gor’kov, “Theory of superconducting alloys in a strong magnetic field near the critical temperature,” [Soviet Physics-JETP \*\*37\*\*, 1407 \(1960\)](#) (cited on pp. [126](#), [128](#)).
- [152] M. Cyrot, “Ginzburg-Landau theory for superconductors,” [Reports on Progress in Physics \*\*36\*\*, 103 \(1973\)](#) (cited on pp. [126](#), [128](#), [131](#)).
- [153] P. G. D. Gennes, *Superconductivity of Metals and Alloys* (Perseus Books Group, Boulder, Colorado, 1999) (cited on pp. [126](#), [134](#), [139](#)).
- [154] J. Bardeen, L. N. Cooper, and J. R. Schrieffer, “Microscopic Theory of Superconductivity,” [Phys. Rev. \*\*106\*\*, 162 \(1957\)](#) (cited on pp. [127](#), [137](#)).
- [155] J. Bardeen, L. N. Cooper, and J. R. Schrieffer, “Theory of Superconductivity,” [Phys. Rev. \*\*108\*\*, 1175 \(1957\)](#) (cited on pp. [127](#), [137](#)).
- [156] A. Larkin and A. Varlamov, *Theory of Fluctuations in Superconductors*, 1st ed., International Series of Monographs on Physics (Oxford University Press, 2005) (cited on pp. [129](#), [131](#), [132](#), [150](#)).

- [157] Željko L. Jelić, “Emergent vortex phenomena in spatially and temporally modulated superconducting condensates,” [PhD dissertation \(University of LIEGE, 2018\)](#) (cited on p. [131](#)).
- [158] N. B. Kopnin, *Theory of Nonequilibrium Superconductivity (International Series of Monographs on Physics)* (Oxford University Press, USA, 2001) (cited on pp. [131](#), [132](#), [134](#), [136](#), [137](#), [147](#), [185](#), [186](#)).
- [159] I. S. Aranson, N. B. Kopnin, and V. M. Vinokur, “Dynamics of vortex nucleation by rapid thermal quench,” [Phys. Rev. B \*\*63\*\*, 184501 \(2001\)](#) (cited on p. [131](#)).
- [160] L. Tewordt, “Gap Equation and Current Density for a Superconductor in a Slowly Varying Static Magnetic Field,” [Phys. Rev. \*\*132\*\*, 595 \(1963\)](#) (cited on pp. [132](#), [134](#)).
- [161] A. I. Larkin and Y. N. Ovchinnikov, “Nonlinear effects during the motion of vortices in superconductors,” [Soviet Physics-JETP \*\*73\*\*, 299 \(1977\)](#) (cited on pp. [132](#), [185](#)).
- [162] A. Schmid, “A time dependent Ginzburg-Landau equation and its application to the problem of resistivity in the mixed state,” [Physik der kondensierten Materie \*\*5\*\*, 302 \(1966\)](#) (cited on pp. [132](#), [135–137](#), [172](#)).
- [163] K. H. Bennemann and J. B. Ketterson, eds., *The Physics of Superconductors: Conventional and High- $T_c$  Superconductors*, 1st ed., Vol. 1 (Springer-Verlag Berlin Heidelberg, 2003) (cited on p. [132](#)).
- [164] D. Y. Vodolazov, F. M. Peeters, M. Morelle, and V. V. Moshchalkov, “Masking effect of heat dissipation on the current-voltage characteristics of a mesoscopic

- superconducting sample with leads,” [Phys. Rev. B 71, 184502 \(2005\)](#) (cited on pp. [132](#), [186](#), [188](#)).
- [165] N. N. Bogoliubov, “A new method in the theory of superconductivity. I,” [Sov. Phys. JETP 34\(7\), 58 \(1958\)](#) (cited on p. [134](#)).
- [166] N. N. Bogoliubov, “A new method in the Theory of Superconductivity. III,” [Sov. Phys. JETP 34\(7\), 73 \(1958\)](#) (cited on p. [134](#)).
- [167] P. G. D. Gennes, “Boundary Effects in Superconductors,” [Rev. Mod. Phys. 36, 225 \(1964\)](#) (cited on pp. [134](#), [139](#)).
- [168] A. A. Abrikosov, L. P. Gor’kov, and I. E. Dzyaloshinski, *Methods of Quantum Field Theory in Statistical Physics*, edited by R. A. Silverman, 2nd ed., Dover Books on Physics (Dover Publications, 1975) (cited on p. [134](#)).
- [169] L. P. Gor’kov, “On the energy spectrum of Superconductors,” [Soviet Physics-JETP 34\(7\), 735 \(1958\)](#) (cited on p. [134](#)).
- [170] G. Eilenberger, “Transformation of Gorkov’s Equation for Type II Superconductors into Transport-Like Equations,” [Zeitschrift for Physik 214, 195 \(1968\)](#) (cited on p. [134](#)).
- [171] H. Ehrenreich, F. Seitz, and D. Turnbull, *Solid State Physics*, 1st, Advances in Research and Applications, Vol. 37 (Academic Press, 1983) (cited on p. [134](#)).
- [172] K. D. Usadel, “Generalized Diffusion Equation for Superconducting Alloys,” [Phys. Rev. Lett. 25, 507 \(1970\)](#) (cited on p. [134](#)).



- [173] M. G. Flokstra, “Proximity effects in superconducting spin-valve structures,” [PhD dissertation \(Leiden University, 2010\)](#) (cited on p. 134).
- [174] L. P. Gor’kov and G. M. Eliashberg, “Generalization of the Ginzburg-Landau equations for non-stationary problems in the case of alloys with paramagnetic impurities,” [Soviet Physics-JETP 27, 328 \(1968\)](#) (cited on pp. 135, 137).
- [175] R. C. Dynes, J. P. Garno, G. B. Hertel, and T. P. Orlando, “Tunneling Study of Superconductivity near the Metal-Insulator Transition,” [Phys. Rev. Lett. 53, 2437 \(1984\)](#) (cited on p. 135).
- [176] J. F. Zasadzinski, “Tunneling spectroscopy of conventional and unconventional superconductors,” in *The Physics of Superconductors*, Vol. 1, edited by K. H. Bennemann and J. B. Ketterson (Springer, Berlin, 2003) Chap. 8, p. 591 (cited on p. 135).
- [177] A. V. Balatsky, I. Vekhter, and J.-X. Zhu, “Impurity-induced states in conventional and unconventional superconductors,” [Rev. Mod. Phys. 78, 373 \(2006\)](#) (cited on p. 135).
- [178] E. M. Lechner, B. D. Oli, J. Makita, G. Giovati, A. V. Gurevich, and M. Iavarone, “Electron Tunneling and X-Ray Photoelectron Spectroscopy Studies of the Superconducting Properties of Nitrogen-Doped Niobium Resonator Cavities,” [Phys. Rev. Applied 13, 44044 \(2020\)](#) (cited on pp. 136, 196).
- [179] H. Rogalla, *100 Years of Superconductivity* (Taylor & Francis, 2011) (cited on p. 136).

- [180] L. D. Landau and I. M. Khalatnikov, “On the anomalous absorption of sound near a second order transition point,” in *Collected Papers of L.D. Landau*, edited by D. T. Haar (Gordon and Breach, Science Publishers, 1965) Chap. 82, pp. 626–629 (cited on p. 136).
- [181] L. Kramer and R. J. Watts-Tobin, “Theory of Dissipative Current-Carrying States in Superconducting Filaments,” *Phys. Rev. Lett.* **40**, 1041 (1978) (cited on pp. 136, 140, 185, 186).
- [182] A. D. Hernández and D. Domínguez, “Surface barrier in mesoscopic type-I and type-II superconductors,” *Phys. Rev. B* **65**, 144529 (2002) (cited on pp. 137, 140).
- [183] J. Fleckinger-Pelle and H. G. Kaper, “Gauges for the Ginzburg-Landau equations of superconductivity,” in *International Congress on Industrial and Applied Mathematics* (Argonne National Lab, 1995), available at <https://www.osti.gov/servlets/purl/191594>. (Cited on p. 138).
- [184] T. S. Alstrøm, M. P. Sørensen, N. F. Pedersen, and S. Madsen, “Magnetic Flux Lines in Complex Geometry Type-II Superconductors Studied by the Time Dependent Ginzburg-Landau Equation,” *Acta Applicandae Mathematicae* **115**, 63 (2011) (cited on pp. 138–140, 151, 155).
- [185] C. W. Robson, K. A. Fraser, and F. Biancalana, “Giant ultrafast Kerr effect in superconductors,” *Phys. Rev. B* **95**, 214504 (2017) (cited on p. 138).
- [186] W. D. Gropp, H. G. Kaper, G. K. Leaf, D. M. Levine, M. Palumbo, and V. M. Vinokur, “Numerical Simulation of Vortex Dynamics in Type-II Superconduc-

- tors,” [Journal of Computational Physics](#) **123**, 254 (1996) (cited on pp. 140, 147, 155).
- [187] A. D. Hernández, A. López, and D. Domínguez, “Anisotropic ac dissipation at the surface of mesoscopic superconductors,” [Applied Surface Science](#) **254**, 69 (2007) (cited on p. 140).
- [188] A. I. Blair and D. P. Hampshire, “Time-Dependent Ginzburg-Landau Simulations of the Critical Current in Superconducting Films and Junctions in Magnetic Fields,” [IEEE Transactions on Applied Superconductivity](#) **28**, 8000205 (2018) (cited on pp. 140, 172).
- [189] B. W. Maxfield and W. L. Mclean, “Superconducting Penetration Depth of Niobium,” [Phys. Rev.](#) **139**, A1515 (1965) (cited on p. 142).
- [190] L. E. Williamson, S. J. and Valby, “Nonlocal Characteristics of the Bulk Upper Critical Field of Niobium,” [Phys. Rev. Lett.](#) **24**, 1061 (1970) (cited on p. 142).
- [191] Neil W. Ashcroft; N. David Mermin, *Solid State Physics* (Harcourt College Publishers, Fort Worth, TX, 1976) (cited on p. 142).
- [192] S. B. Kaplan, C. C. Chi, D. N. Langenberg, J. J. Chang, S. Jafarey, and D. J. Scalapino, “Quasiparticle and phonon lifetimes in superconductors,” [Phys. Rev. B](#) **14**, 4854 (1976) (cited on p. 142).
- [193] D. B. Liarte, S. Posen, M. K. Transtrum, G. Catelani, M. Liepe, and J. P. Sethna, “Theoretical estimates of maximum fields in superconducting resonant radio frequency cavities: stability theory, disorder, and laminates,” [Superconductor Science and Technology](#) **30**, 033002 (2017) (cited on p. 142).

- [194] A. R. Jana, A. Kumar, V. Kumar, and S. B. Roy, “Influence of material parameters on the performance of niobium based superconducting RF cavities,” [ArXiv preprint: 1703.07985 \(2018\)](#) (cited on p. 142).
- [195] T. M. Mishonov, “Technique for measuring the Cooper-pair velocity, density, and mass using Doppler splitting of the plasmon resonance in low-dimensional superconductor microstructures,” [Phys. Rev. B 50, 4004 \(1994\)](#) (cited on p. 144).
- [196] T. M. Mishonov, “Theory of Cooper-pair mass spectroscopy by the current-induced contact-potential difference,” [Phys. Rev. B 50, 4009 \(1994\)](#) (cited on p. 144).
- [197] T. M. Mishonov and A. Varonov, “Nanotechnological Structure for Observation of Current Induced Contact Potential Difference and Creation of Effective Cooper Pair Mass-Spectroscopy,” [ArXiv preprint: 2003.04637 \(2020\)](#) (cited on p. 144).
- [198] D. C. Mattis and J. Bardeen, “Theory of the Anomalous Skin Effect in Normal and Superconducting Metals,” [Phys. Rev. 111, 412 \(1958\)](#) (cited on p. 145).
- [199] J. I. Gittleman and B. Rosenblum, “Radio-Frequency Resistance in the Mixed State for Subcritical Currents,” [Phys. Rev. Lett. 16, 734 \(1966\)](#) (cited on pp. 147, 148).
- [200] J. I. Gittleman and B. Rosenblum, “The Pinning Potential and High-Frequency Studies of Type-II Superconductors,” [Journal of Applied Physics 39, 2617 \(1968\)](#) (cited on pp. 147, 148).

- [201] M. Golosovsky, Tsindlekht M., and D. Davidov, “High-frequency vortex dynamics in  $\text{YBa}_2\text{Cu}_3\text{O}_7$ ,” [Superconductor Science and Technology](#) **9**, 1 (1996) (cited on p. 147).
- [202] G. Blatter, M. V. Feigel’man, V. B. Geshkenbein, A. I. Larkin, and V. M. Vinokur, “Vortices in high-temperature superconductors,” [Rev. Mod. Phys.](#) **66**, 1125 (1994) (cited on pp. 147, 148, 150).
- [203] R. Hübener, *Magnetic Flux Structures in Superconductors*, 1st ed. (Springer, Berlin, Heidelberg, 2001) (cited on p. 147).
- [204] I. A. Sadovskyy, A. E. Koshelev, C. L. Phillips, D. A. Karpeyev, and A Glatz, “Stable large-scale solver for Ginzburg–Landau equations for superconductors,” [Journal of Computational Physics](#) **294**, 639 (2015) (cited on p. 148).
- [205] R. Geurts, M. V. Milošević, and F. M. Peeters, “Second generation of vortex-antivortex states in mesoscopic superconductors: Stabilization by artificial pinning,” [Phys. Rev. B](#) **79**, 174508 (2009) (cited on p. 148).
- [206] A. D. Hernández and D. Domínguez, “Dissipation spots generated by vortex nucleation points in mesoscopic superconductors driven by microwave magnetic fields,” [Phys. Rev. B](#) **77**, 224505 (2008) (cited on p. 148).
- [207] S. Miyamoto and T. Hikihara, “Dynamical behavior of fluxoid and arrangement of pinning center in superconductor based on TDGL equation,” [Physica C: Superconductivity and its Applications](#) **417**, 7 (2004) (cited on pp. 148, 155).

- [208] A. Aftalion, E. Sandier, and S. Serfaty, “Pinning phenomena in the Ginzburg-Landau model of superconductivity,” [Journal des Mathematiques Pures et Appliquees](#) **80**, 339 (2001) (cited on p. 148).
- [209] A. Presotto, E. Sardella, A. L. Malvezzi, and R. Zadorosny, “Dynamical regimes of ultrafast kinematic vortices in the resistive state of mesoscopic superconductors,” [ArXiv preprint: 1910.04893](#) (2019) (cited on p. 148).
- [210] Ž. L. Jelić, M. V. Milošević, J Van De Vondel, and A. V. Silhanek, “Stroboscopic phenomena in superconductors with dynamic pinning landscape,” [Scientific Reports](#) **5**, 14604 (2015) (cited on p. 149).
- [211] G. Ciovati, S. M. Anlage, C. Baldwin, G. Cheng, R. Flood, K. Jordan, P Kneisel, M. Morrone, G. Nemes, L. Turlington, H. Wang, K. Wilson, and S. Zhang, “Low temperature laser scanning microscopy of a superconducting radio-frequency cavity,” [Review of Scientific Instruments](#) **83**, 034704 (2012) (cited on p. 149).
- [212] G. Ciovati, S. M. Anlage, and A. V. Gurevich, “Imaging of the Surface Resistance of an SRF Cavity by Low-Temperature Laser Scanning Microscopy,” [IEEE Transactions on Applied Superconductivity](#) **23**, 3500506 (2013) (cited on p. 149).
- [213] L. Embon, Y. Anahory, A. Suhov, D. Halbertal, J. Cuppens, A. Yakovenko, A. Uri, Y. Myasoedov, M. L. Rappaport, M. E. Huber, A. Gurevich, and E. Zeldov, “Probing dynamics and pinning of single vortices in superconductors at nanometer scales,” [Scientific Reports](#) **5**, 7598 (2015) (cited on p. 151).
- [214] *COMSOL Multiphysics Simulation Software*, <https://www.comsol.com/> (cited on p. 151).

- [215] L. Peng and C. Cai, "Finite Element Treatment of Vortex States in 3D Cubic Superconductors in a Tilted Magnetic Field," [Journal of Low Temperature Physics](#) **188**, 39 (2017) (cited on p. 151).
- [216] D. Salvi, D. Boldor, J. Ortego, G. M. Aita, and C. M. Sabliov, "Numerical modeling of continuous flow microwave heating: A critical Comparison of COMSOL and ANSYS," [Journal of Microwave Power and Electromagnetic Energy](#) **44**, 187 (2010) (cited on p. 152).
- [217] G. Gomes, "Comparison between COMSOL and RFSP-IST for a 2-D Benchmark Problem," in Proceedings, COMSOL Conference (Hannover 2008) (cited on p. 152).
- [218] M. Cardiff and P. K. Kitanidis, "Efficient solution of nonlinear, underdetermined inverse problems with a generalized PDE model," [Computers and Geosciences](#) **34**, 1480 (2008) (cited on p. 152).
- [219] Q. Du, "Finite element methods for the time-dependent Ginzburg-Landau model of superconductivity," [Computers and Mathematics with Applications](#) **27**, 119 (1994) (cited on p. 152).
- [220] E. A. Matute, "On the superconducting sphere in an external magnetic field," [American Journal of Physics](#) **67**, 786 (1999) (cited on p. 157).
- [221] A. S. Mel'nikov, Y. N. Nozdrin, I. D. Tokman, and P. P. Vysheslavtsev, "Experimental investigation of a local mixed state induced by a small ferromagnetic particle in YBaCuO films: Extremely low energy barrier for formation of vortex-antivortex pairs," [Phys. Rev. B](#) **58**, 11672 (1998) (cited on p. 162).

- [222] T. Chow, *Introduction to Electromagnetic Theory: A Modern Perspective*, 1st ed. (Jones & Bartlett Publishers., Boston, 2006) Chap. 4, pp. 146–150 (cited on p. 164).
- [223] A. Gurevich, “Maximum screening fields of superconducting multilayer structures,” *AIP Advances* **5**, 17112 (2015) (cited on p. 182).
- [224] C.-R. Hu, “New set of time-dependent Ginzburg-Landau equations for dirty superconductors near  $T_c$ ,” *Phys. Rev. B* **21**, 2775 (1980) (cited on pp. 185, 186).
- [225] R. J. Watts-Tobin, Y Krähenbühl, and L. Kramer, “Nonequilibrium theory of dirty, current-carrying superconductors: phase-slip oscillators in narrow filaments near  $T_c$ ,” *Journal of Low Temperature Physics* **42**, 459 (1981) (cited on pp. 185, 186).
- [226] C. P. Bean and J. D. Livingston, “Surface Barrier in Type-II Superconductors,” *Phys. Rev. Lett.* **12**, 14 (1964) (cited on p. 190).
- [227] M. K. Transtrum, G. Catelani, and J. P. Sethna, “Superheating field of superconductors within Ginzburg-Landau theory,” *Phys. Rev. B* **83**, 094505 (2011) (cited on p. 190).
- [228] D. B. Liarte, M. K. Transtrum, and J. P. Sethna, “Ginzburg-Landau theory of the superheating field anisotropy of layered superconductors,” *Phys. Rev. B* **94**, 144504 (2016) (cited on p. 190).



- [229] V. Ngampruetikorn and J. A. Sauls, “Effect of inhomogeneous surface disorder on the superheating field of superconducting RF cavities,” [Phys. Rev. Research](#) **1**, 012015 (2019) (cited on p. 190).
- [230] K. Saito, “Theoretical critical field in RF application,” in [Proceedings, 11th workshop on rf superconductivity](#) (SRF2003, 2003), moo02 (cited on p. 191).
- [231] P. Dhakal, “Nitrogen Doping and Infusion in SRF Cavities: A Review,” [ArXiv preprint: 2005.03149](#) (2020) (cited on p. 196).
- [232] M. Wang, S. Balachandran, T. Bieler, S. Chetri, C. Compton, P. Lee, and A. Polyanskii, “Investigation of the Effect of Strategically Selected Grain Boundaries on Superconducting Properties of SRF Cavity Niobium,” in [18th international conference on rf superconductivity](#) (2018), THPB026 (cited on p. 210).
- [233] B. Mühlshlegel, “Die thermodynamischen Funktionen des Supraleiters,” [Zeitschrift für Physik](#) **155**, 313 (1959) (cited on p. 216).
- [234] M. Prohammer and J. P. Carbotte, “London penetration depth of d-wave superconductors,” [Phys. Rev. B](#) **43**, 5370 (1991) (cited on p. 216).
- [235] R. Prozorov and R. W. Giannetta, “Magnetic penetration depth in unconventional superconductors,” [Superconductor Science and Technology](#) **19**, R41 (2006) (cited on pp. 216, 235).
- [236] O. Malyshev, G. Burt, P. Goudket, L. Gurrán, T. Jones, E. Jordan, D. Malyshev, S. Pattalwar, and R. Valizadeh, “Test Cavity and Cryostat for SRF Thin Film Evaluation,” in [6th international particle accelerator conference](#) (2015), WEPHA052 (cited on p. 216).

- [237] R. C. Taber, “A parallel plate resonator technique for microwave loss measurements on superconductors,” [Review of Scientific Instruments](#) **61**, 2200 (1990) (cited on pp. 217, 219).
- [238] M. S. Pambianchi, “Microwave Surface Impedance Investigation of the Superconducting Proximity Effect in Superconductor/Normal-Metal Bilayer Structures,” [PhD dissertation \(University of Maryland, 1995\)](#) (cited on p. 218).
- [239] A. Y. Basovich, R. K. Belov, V. A. Markelov, L. A. Mazo, S. A. Pavlov, V. V. Talanov, and A. V. Varganov, “Parallel-plate resonator of variable spacer thickness for accurate measurements of surface impedance of high- $T_c$  superconductive films,” [Journal of Superconductivity](#) **5**, 497 (1992) (cited on pp. 218, 219).
- [240] F. Gao, M. V. Klein, J. Kruse, and M. Feng, “Mode Coupling in Superconducting Parallel Plate Resonator in a Cavity with Outer Conductive Enclosure,” [IEEE Transactions on Microwave Theory and Techniques](#) **44**, 944 (1996) (cited on p. 219).
- [241] V. V. Talanov, L. V. Mercaldo, and S. M. Anlage, “Measurement of the absolute penetration depth and surface resistance of superconductors using the variable spacing parallel plate resonator,” [IEEE Transactions on Applied Superconductivity](#) **9**, 2179 (1999) (cited on p. 219).
- [242] J. S. Carmin Chappell, *The worldwide helium shortage affects everything from mris to rockets-here is why*, CNBC, (2019) <https://www.cnbc.com/2019/06/21/helium-shortage-why-the-worlds-supply-is-drying-up.html> (visited on 05/17/2020) (cited on p. 222).

- [243] P. J. Petersan and S. M. Anlage, “Measurement of resonant frequency and quality factor of microwave resonators: Comparison of methods,” [Journal of Applied Physics](#) **84**, 3392 (1998) (cited on pp. 223, 227, 229).
- [244] E. A. Ekimov, V. A. Sidorov, E. D. Bauer, N. N. Mel’nik, N. J. Curro, J. D. Thompson, and S. M. Stishov, “Superconductivity in diamond,” [Nature](#) **428**, 542 (2004) (cited on p. 224).
- [245] Y. Takano, M. Nagao, I. Sakaguchi, M. Tachiki, T. Hatano, K. Kobayashi, H. Umezawa, and H. Kawarada, “Superconductivity in diamond thin films well above liquid helium temperature,” [Applied Physics Letters](#) **85**, 2851 (2004) (cited on pp. 224, 225).
- [246] Y. Takano, “Superconductivity in CVD diamond films,” [Journal of Physics: Condensed Matter](#) **21**, 253201 (2009) (cited on p. 224).
- [247] S. Mandal, T. Bautze, O. A. Williams, C. Naud, É. Bustarret, F. Omnès, P. Rodière, T. Meunier, C. Bäuerle, and L. Saminadayar, “The Diamond Superconducting Quantum Interference Device,” [ACS Nano](#) **5**, 7144 (2011) (cited on p. 224).
- [248] M. Watanabe, R. Kanomata, S. Kurihara, A. Kawano, S. Kitagoh, T. Yamaguchi, Y. Takano, and H. Kawarada, “Vertical SNS weak-link Josephson junction fabricated from only boron-doped diamond,” [Phys. Rev. B](#) **85**, 184516 (2012) (cited on p. 224).
- [249] D. Kumar, M. Chandran, and M. S. Ramachandra Rao, “Effect of boron doping on first-order Raman scattering in superconducting boron doped diamond films,” [Applied Physics Letters](#) **110** (2017) (cited on p. 225).

- [250] M. Abdel-Hafiez, D. Kumar, R. Thiyagarajan, Q. Zhang, R. T. Howie, K. Sethupathi, O. Volkova, A. Vasiliev, W. Yang, H. K. Mao, and M. S. Rao, “High-pressure behavior of superconducting boron-doped diamond,” [Physical Review B](#) **95**, 1 (2017) (cited on p. 225).
- [251] T. Venkatesan, personal communication, Oct. 9, 2014 (cited on p. 225).
- [252] D. Kumar, M. Chandran, D. K. Shukla, D. M. Phase, K. Sethupathi, and M. S. Ramachandra Rao, “ $T_c$  suppression and impurity band structure in overdoped superconducting Boron-doped diamond films,” [Physica C: Superconductivity and its Applications](#) **555**, 28 (2018) (cited on pp. 225, 239).
- [253] N. Dubrovinskaia, G. Eska, G. A. Sheshin, and H. Braun, “Superconductivity in polycrystalline boron-doped diamond synthesized at 20GPa and 2700K,” [Journal of Applied Physics](#) **99**, 33903 (2006) (cited on pp. 225, 242).
- [254] M. Nesládek, D. Tromson, C. Mer, P. Bergonzo, P. Hubik, and J. J. Mares, “Superconductive B-doped nanocrystalline diamond thin films: Electrical transport and Raman spectra,” [Applied Physics Letters](#) **88**, 232111 (2006) (cited on p. 225).
- [255] B. Sacépé, C. Chapelier, C. Marcenat, J. Kacmarcik, T. Klein, M. Bernard, and E. Bustarret, “Tunneling Spectroscopy and Vortex Imaging in Boron-Doped Diamond,” [Phys. Rev. Lett.](#) **96**, 97006 (2006) (cited on pp. 225, 236).
- [256] B. L. Willems, G. Zhang, J. Vanacken, V. V. Moshchalkov, I. Guillamon, H. Suderow, S. Vieira, S. D. Janssens, K. Haenen, and P. Wagner, “In/extrinsic granular-

- ity in superconducting boron-doped diamond,” [Physica C: Superconductivity](#) **470**, 853 (2010) (cited on pp. 225, 242).
- [257] L. Li, J. Zhao, Z. Hu, B. Quan, J. Li, and C. Gu, “Low-temperature electrical transport in B-doped ultrananocrystalline diamond film,” [Applied Physics Letters](#) **104**, 182602 (2014) (cited on pp. 225, 242).
- [258] P. J. Hirschfeld and N. Goldenfeld, “Effect of strong scattering on the low-temperature penetration depth of a d-wave superconductor,” [Phys. Rev. B](#) **48**, 4219 (1993) (cited on p. 235).
- [259] V. A. Sidorov, E. A. Ekimov, S. M. Stishov, E. D. Bauer, and J. D. Thompson, “Superconducting and normal-state properties of heavily hole-doped diamond,” [Phys. Rev. B](#) **71**, 60502 (2005) (cited on p. 236).
- [260] F. Dahlem, P. Achatz, O. A. Williams, D. Araujo, E. Bustarret, and H. Courtois, “Spatially correlated microstructure and superconductivity in polycrystalline boron-doped diamond,” [Phys. Rev. B](#) **82**, 33306 (2010) (cited on pp. 236, 242).
- [261] T. J. Greytak and J. H. Wernick, “The penetration depth in several hard superconductors,” [Journal of Physics and Chemistry of Solids](#) **25**, 535 (1964) (cited on p. 238).
- [262] S. M. Anlage and D.-H. Wu, “Magnetic penetration depth measurements in cuprate superconductors,” [Journal of Superconductivity](#) **5**, 395 (1992) (cited on p. 238).
- [263] R. Prozorov, R. W. Giannetta, A. Carrington, P. Fournier, R. L. Greene, P. Gup-  
tasarma, D. G. Hinks, and A. R. Banks, “Measurements of the absolute value

- of the penetration depth in high- $T_c$  superconductors using a low- $T_c$  superconductive coating,” [Applied Physics Letters 77, 4202 \(2000\)](#) (cited on p. 238).
- [264] K Hashimoto, T Shibauchi, T Kato, K Ikada, R Okazaki, H Shishido, M Ishikado, H Kito, A Iyo, H Eisaki, S Shamoto, and Y Matsuda, “Microwave Penetration Depth and Quasiparticle Conductivity of  $\text{PrFeAsO}_{1-y}$  Single Crystals: Evidence for a Full-Gap Superconductor,” [Phys. Rev. Lett. 102, 17002 \(2009\)](#) (cited on p. 238).
- [265] G. Zhang, M. Zeleznik, J. Vanacken, P. W. May, and V. V. Moshchalkov, “Metal–Bosonic Insulator–Superconductor Transition in Boron-Doped Granular Diamond,” [Phys. Rev. Lett. 110, 77001 \(2013\)](#) (cited on p. 242).
- [266] T. L. Hylton and M. R. Beasley, “Effect of grain boundaries on magnetic field penetration in polycrystalline superconductors,” [Physical Review B 39, 9042 \(1989\)](#) (cited on p. 242).
- [267] R. Wördenweber, P. H. Kes, and C. C. Tsuei, “Peak and history effects in two-dimensional collective flux pinning,” [Phys. Rev. B 33, 3172 \(1986\)](#) (cited on p. 242).
- [268] M. R. Vissers, J. Gao, D. S. Wisbey, D. A. Hite, C. C. Tsuei, A. D. Corcoles, M. Steffen, and D. P. Pappas, “Low loss superconducting titanium nitride coplanar waveguide resonators,” [Applied Physics Letters 97, 232509 \(2010\)](#) (cited on p. 242).

- [269] N. Missert, “Superconducting Transition in Amorphous Molybdenum-Germanium Ultrathin Films and Multilayers,” PhD dissertation (Stanford University, 1989), p. 110 (cited on p. 242).
- [270] R. W. Cohen and B. Abeles, “Superconductivity in Granular Aluminum Films,” *Phys. Rev.* **168**, 444 (1968) (cited on p. 242).
- [271] A. I. Gubin, K. S. Il’in, S. A. Vitusevich, M Siegel, and N Klein, “Dependence of magnetic penetration depth on the thickness of superconducting Nb thin films,” *Phys. Rev. B* **72**, 64503 (2005) (cited on p. 242).
- [272] N. Klein, H. Chaloupka, G. Müller, S. Orbach, H. Piel, B. Roas, L. Schultz, U. Klein, and M. Peiniger, “The effective microwave surface impedance of high  $T_c$  thin films,” *Journal of Applied Physics* **67**, 6940 (1990) (cited on p. 242).
- [273] N. R. Groll, G. Ciovati, A. Grassellino, A. Romanenko, J. F. Zasadzinski, and T. Proslie, “Insight into bulk niobium superconducting RF cavities performances by tunneling spectroscopy,” *ArXiv preprint: 1805.06359* (2018) (cited on p. 245).
- [274] *Nano and More USA – Tuning fork sensor controller website*, <https://www.nanoandmore.com/tuning-fork-sensor-controller>, Accessed: 2020-05-23 (cited on p. 253).
- [275] F. J. Giessibl, “Advances in atomic force microscopy,” *Rev. Mod. Phys.* **75**, 949 (2003) (cited on p. 253).

# Bakhrom Oripov



2671 Avenir Place, Apt 1342, Vienna, VA 22180, USA  
bakhromtjk@gmail.com • +1 (571) 201-2286 • <https://www.bakhromtjk.com/>  
<https://www.linkedin.com/in/bakhromtjk/>

## SUMMARY

- Enthusiastic and self-motivated scientist with 6 years of experience in condensed matter physics with strong analytical and problem solving skills as demonstrated by 2 peer-reviewed publications and 16 conference report presentations.
- Excellent team player and builder of scientific collaborations demonstrated by the peer reviewed scientific publications with 11 coauthors from 4 leading National Laboratories around the world.
- Strong leadership skills and experience supervising junior scientists. Mentor to 6 current and prospective PhD student students from Tajikistan.

## WORK EXPERIENCE



### Quantum Materials Center, University of Maryland

- Graduate Research Assistant Jun 2014 – Aug 2020  
In collaboration with scientists from several DOE National labs investigated the material limitations of Superconducting Radio-Frequency cavities (SRF) which are used in next-generation particle accelerators using various experimental techniques.
  - Characterized the defects on the surface of SRF-grade Nb samples using the Near-field Magnetic Microwave Microscopy
  - Developed a superconducting RF cavity testing facility to measure the residual losses at very low temperatures down to 50mK
  - Studied the dynamics of vortex-antivortex semiloops inside a superconductor using time-dependent Ginzburg Landau model and COMSOL Multiphysics simulation software
  - Measured the surface resistance and absolute value of London penetration depth of a Boron-doped diamond thin film superconductor using parallel plate resonator technique
  - Assisted with the writing of a \$450,000 proposal which was successfully funded
  - Mentored 3 undergraduate students and 1 first year graduate student

### Institute for Research in Electronics and Applied Physics, University of Maryland

- Graduate Research Assistant Jan 2014 – Jun 2014
  - Project: Built a Frequency-resolved optical gating (FROG) device for femtosecond laser pulse characterization



## EDUCATION



### University of Maryland, College Park, Maryland, USA

- Ph.D. in Physics Aug 2013 – Aug 2020
  - Thesis: Superconducting RF Materials Science through Near-Field Magnetic Microscopy
  - Adviser: Prof. Steven Anlage



### Boğaziçi University, Istanbul, Turkey






- B.S. in Physics (Honors List) Aug 2008 – Jul 2012

## PUBLICATIONS

- [2] B. Oripov and S. Anlage, "Time-dependent Ginzburg-Landau treatment of RF Magnetic Vortices in Superconductors: Vortex-Semiloops in a Spatially Nonuniform Magnetic Field", **Physical Review E** **101**, 033306 (2020)
- [1] B. Oripov *et al*, "High-Frequency Nonlinear Response of Superconducting Cavity-Grade Nb Surfaces", **Physical Review Applied** **11**, 064030 (2019)



**SKILLS AND QUALIFICATIONS**

- Research and analysis
- Experimental Design
- Data Analysis
- Numerical Modeling
- Remote Control of Hardware
- Scientific writing
- Team building and leadership
- Project Management
- Presentations and Public Speaking
- Measurement automation
- Scientific Instruments Designed or Operated:
  - Dilution Refrigerator
  - Cryogenic Probe Station
  - Ultra-high Vacuum (UHV) systems
  - Scanning Electron Microscope (SEM)
  - Scanning Probe Microscope (AFM, STM)
  - Superconducting RF cavities
  - Parallel Plate and dielectric resonators
  - Magnetic Field Shielding
  - Cryogenic Cryostat
  - Lock-in Amplifier
  - Network Analyzers
  - Spectrum Analyzer
  - Laser Systems
  - Piezo Based Scanning Systems
  - Wire bonding
  - Milling machine
- Computer skills:
  - Scientific Computing
  - COMSOL Multiphysics Modeling Software
  - High Frequency Structure Simulator (HFSS)
  - Solidworks 3D Modeling
  - Code Optimization for Parallel Computation
  - C language
  - MATLAB
  - Mathematica
  - Python
  - L<sup>A</sup>T<sub>E</sub>X
- Languages:  English •  Russian •  Turkish •  Tajik •  Persian

**TEACHING EXPERIENCE****University of Maryland**, College Park, MD, USA

- Teaching Assistant, Department of Physics Aug 2013 – Dec 2013
  - Led weekly discussion sections and hands-on laboratory sessions.
  - Proctored and graded exams.
  - Held weekly office hours.

**State Educational Institution-Lyceum for Gifted Students**, Dushanbe, Tajikistan

- Physics Olympiad Team Mentor & Physics Teacher Aug 2012 – Jun 2013
  - Selected and prepared students to represent Tajikistan in various International Physics Olympiads
  - Traveled with the Physics Olympiad team as team leader
  - Taught physics classes
  - Planned and organized hands-on activities that encourage active student participation: mousetrap car race, spaghetti bridge, water rocket etc.

**AWARDS & SCHOLARSHIPS**

- Bronze Medal, 39<sup>th</sup> International Physics Olympiad (IPhO), Vietnam Jul 2008
- Bronze Medal, 9<sup>th</sup> Asian Physics Olympiad (APhO), Mongolia Apr 2008
- Bronze Medal, 4<sup>th</sup> Zhautykov Physics Olympiad (ZPhO), Kazakhstan Apr 2008
- Gold Medal, Tajikistan Nationwide Physics Olympiad, Tajikistan Mar 2008
- Honorable Mention, 38<sup>th</sup> International Physics Olympiad (IPhO), Iran Jul 2007
- Honorable Mention, 8<sup>th</sup> Asian Physics Olympiad (APhO), China Apr 2007

**PROFESSIONAL AFFILIATIONS & ACTIVITIES**

- Paper Reviewer for Applied Physics Letters Journal 2017 – Present
- Member of American Physical Society 2013 – Present
- Referee for Universal Project Olympiad 2017 – Present
- Referee for Tajikistan Science Project Olympiad 2013
- Bookkeeper at Tajik American Cultural Association 2013 – 2019

**CONFERENCE  
TALKS  
& PRESENTATIONS**

- [11] B. Oripov and S. Anlage, “High Frequency Near-Field Magnetic Microscopy ,” at *National Institute of Standards and Technology (NIST) High Frequency Scanning Probe Microscopy Workshop* , Boulder, Colorado, Dec 2019.
- [10] B. Oripov and S. Anlage, “Microwave Microscopy of Materials Limitations of Superconducting RF Cavities,” in *Cryogenic Engineering Conference and International Cryogenic Materials Conference*, Hartford, Connecticut, Jul 2019.
- [9] B. Oripov and S. Anlage, “Microwave Microscopy of Materials Limitations of Superconducting RF Cavities,” at *American Physics Society March Meeting*, Boston, Massachusetts, Mar 2019.
- [8] B. Oripov, G. Ciovatti and S. Anlage, “SRF Cavity Residual Losses at mK Temperatures,” at *51<sup>st</sup> Applied Superconductivity Conference*, Seattle, Washington, Nov 2018.
- [7] B. Oripov and S. Anlage, “Microscopic Investigation of Materials Limitations of Superconducting RF Cavities,” at *51<sup>th</sup> Applied Superconductivity Conference*, Seattle, Washington, Nov 2018.
- [6] B. Oripov and S. Anlage, “Study of RF flux penetration on Nb for SRF Applications,” in *American Physics Society March Meeting*, Los Angeles, California, Mar 2018.
- [5] B. Oripov, S. Bae, T. Tai and S. Anlage, “Near-Field Nonlinear Microwave Microscopy of Superconductors,” at *Radio Frequency Scanning Probe Microscopy Workshop*, Boulder, Colorado, Nov 2017.
- [4] B. Oripov and S. Anlage, “Extreme and Local Electrodynamic Measurement of Nb for SRF Applications,” at *50<sup>th</sup> Applied Superconductivity Conference*, Denver, Colorado, Sep 2016.
- [3] B. Oripov and S. Anlage, “Extreme Electrodynamic and Local Harmonic Measurement of Nb Thin Films,” at *7<sup>th</sup> International Workshop on Thin Films and New Ideas for Pushing the Limits of RF Superconductivity*, Jefferson Lab, Newport News, Virginia, Jul 2016.
- [2] B. Oripov, T.Tai and S. Anlage, “Extreme and Local 3<sup>rd</sup> Harmonic Response of Niobium (Nb) SC,” at *American Physics Society March Meeting*, Baltimore, Maryland, Mar 2016.
- [1] B. Oripov, T.Tai and S. Anlage, “Microscopic Investigation of Materials Limitations of Superconducting RF Cavities,” Poster presented at: *17<sup>th</sup> International Conference on RF Superconductivity*, Whistler, British Columbia, Canada, Sep 2015.

**CO-AUTHORED  
CONFERENCE  
PRESENTATIONS**

- [7] B. Oripov and S. Anlage, “Microscopic Investigation Of Materials Limitations of Superconducting RF Cavities,” Talk given by S. Anlage at *TESLA Technology Collaboration*, European Organization for Nuclear Research (CERN), Geneva, Switzerland, Feb 2020.
- [6] B. Oripov, G. Ciovatti and S. Anlage, “Superconducting Radio Frequency Cavity Residual Losses at mK Temperatures,” Poster presented by S. Anlage at: *19<sup>th</sup> International Conference on RF Superconductivity*, Dresden, Germany, Jul 2019.
- [5] B. Oripov and S. Anlage, “High-Frequency Nonlinear Response of Superconducting Cavity-Grade Nb Surfaces,” Poster presented by S. Anlage at: *19<sup>th</sup> International Conference on RF Superconductivity*, Dresden, Germany, Jul 2019.
- [4] B. Oripov and S. Anlage, “Microscopic Investigation of Materials Limitations of Superconducting RF Cavities,” Talk given by S. Anlage at *8<sup>th</sup> International Workshop on Thin Films and New Ideas for Pushing the Limits of RF Superconductivity*, Laboratori Nazionali di Legnaro, Padua, Italy, Oct 2018.
- [3] B. Oripov and S. Anlage, “Measurements of local nonlinear rf response of superconductors using a scanned magnetic microwave microscope” Talk given by S. Anlage at *14<sup>th</sup> International Workshop of High-Temperature Superconductors in High Frequency Field*, Zao-Onsen, Yamagata, Japan, Jun 2018.
- [2] B. Oripov, S. Bae, T. Tai and S. Anlage, “Near-Field Nonlinear Microwave Microscopy of Superconductors,” Talk given by S. Anlage at *Radio Frequency Scanning Probe Microscopy Workshop*, Boulder, Colorado, Nov 2017.
- [1] B. Oripov and S. Anlage, “Study of RF flux penetration on Nb for SRF Applications,” Talk given by S. Bae at *American Physics Society March Meeting*, New Orleans, Louisiana, Mar 2017.